



HAL
open science

Thermomagnetic Convection in Ferrofluids: Finite Element Approximation and Application to Transformer Cooling

Raphaël Zanella

► **To cite this version:**

Raphaël Zanella. Thermomagnetic Convection in Ferrofluids: Finite Element Approximation and Application to Transformer Cooling. Fluid mechanics [physics.class-ph]. Université Paris Saclay (COmUE), 2018. English. NNT: 2018SACLS501 . tel-02014586

HAL Id: tel-02014586

<https://theses.hal.science/tel-02014586>

Submitted on 11 Feb 2019

HAL is a multi-disciplinary open access archive for the deposit and dissemination of scientific research documents, whether they are published or not. The documents may come from teaching and research institutions in France or abroad, or from public or private research centers.

L'archive ouverte pluridisciplinaire **HAL**, est destinée au dépôt et à la diffusion de documents scientifiques de niveau recherche, publiés ou non, émanant des établissements d'enseignement et de recherche français ou étrangers, des laboratoires publics ou privés.

Thermomagnetic Convection in Ferrofluids: Finite Element Approximation and Application to Transformer Cooling

Thèse de doctorat de l'Université Paris-Saclay
préparée à l'Université Paris-Sud

Ecole doctorale n°579 Sciences mécaniques et énergétiques, matériaux et
géosciences (SMEMAG)
Spécialité de doctorat : Mécanique des fluides

Thèse présentée et soutenue à Orsay, le 14 décembre 2018, par

RAPHAËL ZANELLA

Composition du Jury :

M. Frédéric Mazaleyrat Professeur, ENS Paris-Saclay (SATIE)	Président
M. Philippe Marty Professeur, Université Grenoble Alpes (LEGI)	Rapporteur
M. Rachid Touzani Professeur, Université Clermont Auvergne (LMBP)	Rapporteur
M. Yvan Avenas Maître de Conférences, Grenoble INP (G2ELAB)	Examineur
M. Xavier Mininger Professeur, Université Paris-Sud (GeePs)	Examineur
M. Olivier Moreau Ingénieur Chercheur, EDF R&D (EDF Lab Paris-Saclay)	Examineur
Mme Caroline Nore Professeur, Université Paris-Sud (LIMSI)	Directrice de thèse
M. Frédéric Bouillault Professeur, Université Paris-Sud (GeePs)	Co-directeur de thèse (Invité)
M. Jean-Luc Guermond Professeur, Université Texas A&M (Dépt de Mathématiques)	Co-encadrant (Invité)

Remerciements

Je voudrais ici remercier les nombreuses personnes qui m'ont aidé à mener à bien ce travail de thèse. Pour commencer, je remercie mes encadrants Caroline Nore, Frédéric Bouillault et Jean-Luc Guermond pour m'avoir donné la chance de me former à la recherche sur ce sujet. J'ai pu profiter pleinement de leur expérience en modélisation et en simulation numérique, et effectuer une expérience très enrichissante de plus d'un an à la *Texas A&M University* (TAMU).

Je tiens à remercier les membres du jury de leur intérêt pour mon travail, à commencer par les rapporteurs Philippe Marty et Rachid Touzani qui ont accepté de lire le manuscrit. Merci également aux examinateurs Yvan Avenas, Frédéric Mazaleyrat, Xavier Mininger et Olivier Moreau pour leur présence, et leurs questions, à la soutenance. Je remercie en particulier Xavier pour son implication et ses nombreux conseils tout au long de la thèse.

Je souhaiterais aussi remercier les autres collaborateurs avec qui j'ai pu échanger au cours de la thèse. Un grand merci à Loic Capanera pour sa disponibilité et son aide, toujours efficace, pour le développement du code à TAMU. Merci à Ignacio Tomas de TAMU pour ses nombreuses explications sur les éléments finis. Merci à Nicola Puigmal, Amel Nait Djoudi, Sleimane Nasser El Dine et Eric Berthelot du GeePs pour la réalisation des essais expérimentaux, les simulations numériques complémentaires et les discussions à ce sujet. Merci à Anne Sergent et Patrick Le Quéré du LIMSIS d'avoir partagé leur connaissances sur la convection naturelle. Enfin, merci à l'équipe informatique du LIMSIS pour leur aide en général.

Si les compétences scientifiques et techniques sont importantes, l'ambiance qui peut régner dans le laboratoire l'est aussi. Pour cela, je souhaiterais remercier l'ensemble des doctorants ou post-doctorants du LIMSIS que j'ai pu rencontrer : Can, Shreyas, Marko, Elie, Andrés, Julien, Wen, Antoine, Ismail, Mebarek, Ziad, Guy, Song, Ye, Raksmy. Je remercie aussi les membres du GeePs avec qui je suis parti en conférence en Corée notamment. Merci également à Andrea Bonito de TAMU pour les foots et les *Friday beers*.

Enfin, merci à mes amis, vieux et nouveaux, pour les bons moments. Et pour finir, merci à ma famille, et en particulier à mes parents, pour leur soutien.

Contents

1	Introduction	9
1.1	Context and motivation	9
1.2	Objectives	10
1.3	Outline of the manuscript	10
2	Bibliography study on ferrofluids	13
2.1	Generalities	13
2.1.1	Definition	13
2.1.2	Composition	14
2.1.3	Stability	15
2.1.4	Applications	18
2.2	Modeling	18
2.2.1	Magnetic properties	19
2.2.2	Governing equations	21
2.2.3	Thermophysical properties	24
2.3	Thermomagnetic convection	27
2.3.1	Thermomagnetic instability	27
2.3.2	Literature review	29
2.3.3	Conclusive remarks	32
2.4	Transformer cooling	34
2.4.1	Cooling performance	34
2.4.2	Suitability as insulating liquid	36
2.5	Conclusion of the chapter	37
3	New developments in SFEMaNS: ferrohydrodynamics applications	39
3.1	Physical setting	39
3.1.1	Geometry	39
3.1.2	Equations	40
3.2	Numerical method	43
3.2.1	Fourier representation	43
3.2.2	Finite element approximation spaces	44
3.2.3	Time-marching algorithm	45
3.3	Validation	49
3.3.1	Nondimensionalized equations	50
3.3.2	Magnetostatics	53
3.3.3	Temperature computation in solid regions	57
3.3.4	Kelvin magnetic body force	60
3.3.5	Robin boundary conditions	63
3.3.6	Temperature-dependent viscosity	65
3.3.7	Helmholtz magnetic body force	67
3.3.8	Pyromagnetic coefficient term in the temperature equation	71

3.4	Conclusion of the chapter	73
4	Thermomagnetic convection in an oil bath heated by a solenoid	75
4.1	Article published in IEEE Transaction on Magnetics	76
4.2	Additional comments	80
4.2.1	Experimental setup	80
4.2.2	Governing equations	80
4.2.3	Physical properties	80
4.2.4	Mesh choice	81
4.2.5	Comparison with another experiment	82
4.2.6	Interface conditions on the magnetic field	82
4.2.7	Focus on the convective flow	83
4.2.8	Presence of oscillations in the regular oil case	85
4.2.9	Time evolution of the velocity field in the magnetic oil case	85
4.3	Complementary discussion	87
4.3.1	Visualization of the magnetic body force	87
4.3.2	Three-dimensional study	90
4.3.3	Use of a temperature-dependent viscosity	94
4.3.4	Comparison of the Kelvin and Helmholtz force models	95
4.4	Conclusion of the chapter	97
5	Realistic ferrofluid thermophysical properties	99
5.1	Article published in Journal of Magnetism and Magnetic Materials	100
5.2	Complementary discussion	121
5.2.1	Experimental setup	121
5.2.2	Physical properties	121
5.2.3	Experiment vs. numerics using pure transformer oil	121
5.2.4	Numerical simulations with ferrofluid	125
5.2.5	Experiment vs. numerics using transformer oil-based ferrofluid	129
5.3	Improvement of the ferrofluid modeling	130
5.3.1	Temperature-dependent saturation magnetization of the magnetic nanoparticles	130
5.3.2	Complete temperature equation of ferrofluids	132
5.3.3	Limit of the linear magnetic material approximation	134
5.4	Conclusion of the chapter	135
6	Thermomagnetic convection in a transformer	137
6.1	Transformer principle	137
6.1.1	Simplified transformer	137
6.1.2	Absence of load	137
6.1.3	Presence of a load	139
6.1.4	Superimposed coils	139
6.2	Physical problem and modeling	140
6.2.1	The considered electromagnetic system	140
6.2.2	Modeling	141
6.3	Regular oil vs. magnetic oil cooling	144
6.3.1	Time evolutions	145
6.3.2	Temperature and velocity fields	146
6.3.3	Magnetic field	148
6.3.4	Three-dimensional study	149
6.4	Variations of the model	149
6.4.1	Tank magnetic permeability	150

6.4.2	Curie temperature	150
6.4.3	Size of the tank	151
6.4.4	Distance between the coils	152
6.5	Conclusion of the chapter	153
7	Conclusion	155
7.1	Outcome	155
7.2	Perspectives	156
8	Résumé en français	159
8.1	Introduction	159
8.2	Etude bibliographique sur les ferrofluides	160
8.2.1	Généralités	160
8.2.2	Modélisation	160
8.2.3	Convection thermomagnétique	161
8.2.4	Refroidissement des transformateurs	162
8.3	Nouveaux développements dans SFEMaNS	163
8.3.1	Problème physique	163
8.3.2	Méthode numérique	164
8.4	Convection thermomagnétique dans un bain d'huile	166
8.4.1	Modélisation du problème	166
8.4.2	Avantage du refroidissement par ferrofluide	167
8.4.3	Comparaison des modèles de force de Kelvin et de Helmholtz	168
8.5	Vraies propriétés thermophysiques du ferrofluide	169
8.5.1	Adaptation du modèle	169
8.5.2	Résultats avec les propriétés modifiées	169
8.5.3	Amélioration de la modélisation du ferrofluide	170
8.6	Convection thermomagnétique dans un transformateur	171
8.6.1	Modélisation du problème	171
8.6.2	Refroidissement par huile classique versus par ferrofluide	172
8.7	Conclusion	173
8.7.1	Bilan	173
8.7.2	Perspectives	174
A	Governing equations in fluid mechanics	175
A.1	General equations	175
A.1.1	Continuity equation	175
A.1.2	Momentum equation	176
A.1.3	Energy equation	177
A.1.4	Theorem of the kinetic energy	178
A.1.5	Internal energy and temperature equations	179
A.2	Incompressible Navier-Stokes equations	179
A.2.1	Continuity equation	180
A.2.2	Momentum equation	180
A.2.3	Temperature equation	180
A.3	Newtonian fluid under Boussinesq approximation	180
A.3.1	Applicability of the approximation	180
A.3.2	Governing equations	181

B	Approximations using Taylor expansions in SFEMaNS	183
B.1	Backward Difference Formula of second order (BDF2)	183
B.2	Time extrapolation of second order	183
B.3	Time extrapolation of first order	183
C	Additional convergence tests	185
C.1	Magnetostatics	185
C.2	Kelvin magnetic body force	185
C.2.1	Linear law of magnetic susceptibility	186
C.2.2	Periodic solution	187
C.2.3	Periodic solution with non-zero pressure	189
C.2.4	Inverse law of magnetic susceptibility	190
C.3	Temperature-dependent viscosity	192
C.3.1	Polynomial temperature	192
C.3.2	Exponential temperature	195
D	Preparatory study for the design of the experiment	199
D.1	Modeling	199
D.2	Results	201
E	Transformer case: estimation of the convection coefficient in the absence of heat transfer fins	203
E.1	Theory	203
E.2	Computations	204
E.3	Conclusion	206
	Bibliography	207

Chapter 1

Introduction

1.1 Context and motivation

Transformers are electrical devices used to modify the voltage between two branches of an electrical network for efficiency purpose. The conversion process is based on a ferromagnetic circuit that transfers the electrical energy from one circuit to another through the magnetic flux generated by the alternating currents. The process generates heat, in particular due to the Joule effect in the windings. To maintain the temperature at a reasonable level, and therefore improve the lifetime of the transformer, the largest transformers are immersed in an insulating liquid. This liquid, mineral oil mostly, is used to cool the system as well as to electrically insulate it from the exterior.

The cooling of the immersed transformers is based on the forced or natural convection taking place in the insulating liquid. Several research groups have proposed to enhance heat transfer in transformers by taking advantage of the leakage magnetic flux in the insulating liquid [1, 2, 3, 4]. Their approach relies on the use of transformer oil seeded by magnetic nanoparticles. Such a mixture is called a ferrofluid and has the particularity of exhibiting both fluidic and magnetic properties. In these specific fluids, the presence of an applied magnetic field and a temperature gradient can generate a convective phenomenon called thermomagnetic convection, in addition to the thermogravitational convection, which improves the heat transfer from the hot to the cold area.

Enhancing heat transfer in transformers may have several advantages: to extend the transformer lifetime, to reduce the tank size and the oil volume, to remove the pumps or the fans used to generate forced convection (requiring an energy input and producing noise). Another advantage that we are particularly interested in is the use of vegetable transformer oil. Scientists have recently studied this environment-friendly alternative to the mineral transformer oil [5, 6, 7, 8, 9]. Vegetable oils are more biodegradable and have a lower flammability than mineral oil but their cooling performance is lower due to their large viscosity. If the addition of magnetic nanoparticles can compensate this drawback, vegetable oils will become more competitive.

Nevertheless, the advantage of adding magnetic nanoparticles for transformer cooling is not obvious. We can wonder whether thermomagnetic convection will arise in such a system, i.e., whether the conditions of appearance are satisfied. If so, the question is if the thermomagnetic convection and the thermogravitational convection will work together or, on the contrary, if they will have opposite effects on the flow of ferrofluid, cancelling the benefit of natural convection. Moreover, the magnetic nanoparticles in a ferrofluid do not only introduce thermomagnetic convection, they also modify the thermophysical properties of the fluid: the density, the specific heat, the thermal conductivity, the viscosity and the thermal expansion coefficient are changed depending on the volume fraction of nanoparticles. For instance, the thermal conductivity and the viscosity are larger, which

have positive and negative influences on heat transfer, respectively. The question of the impact of this aspect of ferrofluids needs to be addressed as well. Finally, the effect of the ferrofluid on the temperature in the system should not be assessed only qualitatively but also quantitatively, to truly state on the relevance of such a mixture.

In order to address this problem, we propose a numerical modeling approach using the in-house parallel code SFEMaNS (Spectral/Finite Element for Maxwell and Navier-Stokes) for axisymmetric geometries, using a spectral decomposition in the azimuthal direction and Lagrange finite elements in the meridian plane. After several developments in SFEMaNS, the code is first applied to the case of an experimental setup. It consists in a coil immersed in a cylindrical tank, which is a simplified model of an immersed transformer. The numerical results can therefore be cross-validated with the experimental ones (temperature measured at various points). The code is then applied to the case of an actual transformer to verify whether the benefit of ferrofluids can be extended to this industrial application.

1.2 Objectives

The final goal of the PhD is to assess the benefit of transformer oil-based ferrofluid compared to pure transformer oil in terms of cooling performance. Nevertheless, other objectives need to be achieved on the way. The study of ferrofluids, referred to as ferrohydrodynamics, is a wide field involving fluid mechanics, thermodynamics and electromagnetism. The convection of ferrofluids is therefore governed by a strongly coupled set of partial differential equations. The problem considered in this PhD - the cooling of an electromagnetic system by a ferrofluid - is a challenge in terms of modeling and of numerical methods. Here is the list of objectives for this PhD:

1. to propose a realistic model (governing equations, magnetic and thermophysical fluid properties modeling) for the natural convection of ferrofluids;
2. to adapt the SFEMaNS code to solve the complete set of governing equations for such problem;
3. to validate the model against the experimental results on the setup with the immersed coil;
4. to assess and to understand the advantage of ferrofluid compared to regular fluid for the cooling of electromagnetic systems.

1.3 Outline of the manuscript

The manuscript is composed of seven chapters, including the introduction and the conclusion. In addition, a substantial summary in French is presented after the conclusion.

Chapter 1 - Introduction. We introduce the topic of transformer cooling using ferrofluid, the motivations for such a study and the work program of this PhD.

Chapter 2 - Bibliography study on ferrofluids. We present the ferrofluids, the common modeling of these specific fluids proposed in the literature and the main results of relevant studies, regarding our objectives, on thermomagnetic convection and transformer cooling by ferrofluid.

Chapter 3 - New developments in SFEMaNS: ferrohydrodynamics applications. We describe the code used for this PhD. The ferrofluid typical problem that can now address the SFEMaNS code is first described. The numerical method is then presented, putting forward the adaptations of the numerical schemes performed during the PhD to solve this kind of problem. The convergence tests on manufactured solutions validating each new development are finally shown.

Chapter 4 - Thermomagnetic convection in an oil bath heated by a solenoid. We present a first series of results obtained with simulations on the experimental setup. The thermo-hydrodynamical model (no magnetic interactions) is validated against experimental temperature data obtained with pure transformer oil. We show that the use of ferrofluid can reduce the maximum temperature in the system by a few degrees and try to understand the thermomagnetic convection mechanism by studying the ferrofluid flow and the magnetic body force. A key result of this chapter is the comparison of the thermomagnetic convection effect when using different magnetic body forces (Kelvin and Helmholtz models).

Chapter 5 - Realistic ferrofluid thermophysical properties. We present another series of results obtained with simulations on a second experimental setup. The major change with respect to Chapter 4 is the improvement of the ferrofluid model, here taking into account the impact of the magnetic nanoparticles on the thermophysical properties. Another change is the adaptation of the model due to the use of an aluminium tank in the experimental setup. The thermo-hydrodynamical model is once again validated against an experiment using pure transformer oil, but a comparison with an experiment using transformer oil-based ferrofluid is also carried out. We show that the thermomagnetic convection and the change of thermophysical properties both have a positive impact on the ferrofluid cooling efficiency. We also improve the magnetic modeling of the ferrofluid by considering the temperature-dependence of the nanoparticle magnetic properties.

Chapter 6 - Thermomagnetic convection in a transformer. We present a third series of results obtained with simulations on an electromagnetic system close to a 40 kV transformer. The cooling performances provided by transformer oil and transformer oil-based ferrofluid are compared. We try to understand the positive influence of the ferrofluid and the limit of the modeling.

Chapter 7 - Conclusion. We summarize the results obtained during the PhD and present possible perspectives to extend this work.

Chapter 8 - Résumé en français. We summarize the seven previous chapters in French.

Chapter 2

Bibliography study on ferrofluids

In this chapter, we present the ferrofluids and their study for heat transfer applications. The first section is a general presentation of ferrofluids (definition, composition, stability, applications). The second section details the common modeling of ferrofluids in the literature, focusing on their magnetic properties, their governing equations and their thermophysical properties. Thermomagnetic convection, the specific phenomenon of ferrofluids leading to heat transfer enhancement, is detailed in the third section. Finally, the fourth section presents the past works on the use of ferrofluids as insulating liquid in electrical transformers to improve the cooling efficiency.

2.1 Generalities

2.1.1 Definition

A magnetic fluid cannot be found in the natural state. As a matter of fact, no magnetic substance has a fusion temperature smaller than its Curie temperature, the temperature above which the magnetic properties become negligible. It is nevertheless possible to manufacture such liquids. According to the definition of Rosensweig [10, p. 7], ferrofluids, also called magnetic fluids, are suspensions constituted of a liquid carrier seeded by magnetic particles of nanometric size (diameter typically between 3 and 15 nm).

The particularity of ferrofluids is that they present both magnetic and fluidic properties. The interactions between the magnetic nanoparticles and the molecules of the liquid carrier are such that the liquid carrier follows the magnetic nanoparticles in their movement when they react to an applied magnetic field. Thus, the whole mixture behaves as a single phase fluid with magnetic properties [11]. A typical manifestation of ferrofluid magnetism is the spike-shape structure forming at the surface of a ferrofluid in the presence of an applied magnetic field, the spikes following the magnetic field lines. Figure 2.1 shows the behavior of a ferrofluid in the presence of an electromagnet, placed above, for instance. When the electromagnet is activated, the ferrofluid is attracted toward it and the spike-shape structure at the surface is formed.

Ferrofluids must be distinguished from magnetorheological fluids, which are suspensions of magnetic particles of micrometric size. Magnetorheological fluids can become highly viscous when a magnetic field is applied. They are used in some suspensions of vehicles so that the suspension stiffness can be adapted [13]. Ferrofluids are a particular case of nanofluids. Nanofluids are suspensions of nanoparticles (often metallic but not necessarily magnetic) and are thoroughly studied for heat transfer applications, see the review of Wen et al. [14] for instance.

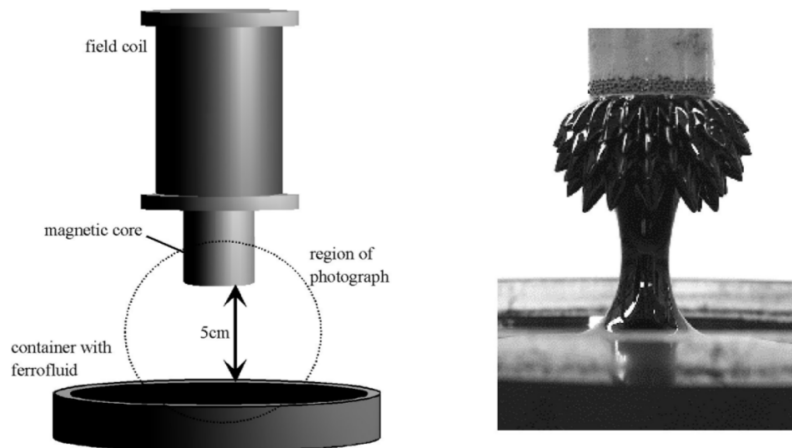


Figure 2.1: Interaction between a ferrofluid layer and an electromagnet. From [12].

2.1.2 Composition

Magnetic nanoparticles

Let us recall the main categories of magnetic behaviors. We introduce the magnetization, which represents the density of magnetic moments carried by the atoms in a material (unit: A/m), defined by

$$\mathbf{M}(P) = \frac{\sum_{i=1}^N \mathbf{m}_i}{\Delta V}, \quad (2.1)$$

where ΔV is a mesoscopic volume centred in a point P and $\mathbf{m}_i, \forall i \in [1, N]$, are the atomic magnetic moments in ΔV . In most materials, the atomic magnetic moments have random directions in the absence of an applied magnetic field, so that the magnetization is zero. When the material is in the presence of an applied magnetic field, the atomic magnetic moments tend to become collinear to it. The magnetization takes thus a non-zero value. If the magnetization has the direction of the applied magnetic field, the material is said to be paramagnetic; if the magnetization has the opposite direction, the material is said to be diamagnetic. Other materials present a non-zero magnetization even in the absence of an applied magnetic field. The atomic magnetic moments interact between them, which spontaneously produces a general alignment. These materials are said to be ferromagnetic. Note that all ferromagnetic materials become paramagnetic or diamagnetic above a temperature called the Curie temperature [15, pp. 182-183].

A ferromagnetic material is partitioned into microscopic domains, called Weiss domains, in which the atomic magnetic moments have the same direction (the boundaries between the Weiss domains are called Bloch walls). If the material is not magnetized, the general direction of the atomic magnetic moments may vary from one Weiss domain to another, so that the magnetic moment of the whole sample is zero [16, pp. 87-88].

The magnetic nanoparticles in a ferrofluid are made of ferromagnetic materials such as iron, nickel and cobalt, of their compounds and alloys, or of their oxides (iron oxides mostly). A widely used material is magnetite (Fe_3O_4). The magnetic nanoparticles in a ferrofluid have such a small size that they are composed of a unique Weiss domain. The atomic magnetic moments in the magnetic nanoparticle have thus the same direction and the magnetic nanoparticle always carries a non-zero magnetic moment [11, 17, 18, 19].

Liquid carrier

There exists a wide range of liquid carriers¹ such as water, oil or kerosene. In organic liquid carriers (like oil), a surfactant, oleic acid mostly, is added to create a layer around the nanoparticles and avoid their agglomeration by steric repulsion. The surfactant is not necessary in water-based ferrofluids, which use ionic repulsion [18, 19]. Repulsion mechanisms are detailed next.

Ferrofluids are obtained by various methods such as grinding [20] or chemical precipitation [21], see more in [10, pp. 38-44].

2.1.3 Stability

A good ferrofluid is supposed to be stable, i.e., to keep a uniform density of nanoparticles. While an applied magnetic field, the gravity and attraction forces between the nanoparticles (magnetic dipole interactions and van der Waals interactions) tend to destabilize the suspension by sedimentation or agglomeration, the Brownian motion (random movement of fine particles in a liquid carrier [22]) and the steric or ionic repulsion keep the nanoparticles in suspension and spaced. The stability of the ferrofluid depends on the balance of the energies associated to each destabilizing or stabilizing mechanism. With theoretical calculations, Rosensweig [10, pp. 34-38] and Odenbach [12, pp. 8-12] show that the nanoparticle diameter needs to be of order 10 nm for the suspension to be stable.

Stability regarding an applied magnetic field

The magnetic nanoparticles are attracted toward the region where the magnetic field intensity is the strongest. The Brownian motion will counterbalance the sedimentation of the nanoparticles there if their thermal energy is sufficient. The thermal energy of one nanoparticle is

$$E_T = k_B T, \quad (2.2)$$

where k_B is the Boltzmann constant and T is the temperature in Kelvin. At the scale of the fluid, the nanoparticles can be seen as magnetic dipoles of magnetic moment \mathbf{m} . The magnetic potential energy of a nanoparticle in a magnetic field \mathbf{H} is defined by

$$E_H = -\mu_0 \mathbf{m} \cdot \mathbf{H}, \quad (2.3)$$

where μ_0 is the magnetic permeability of vacuum. The energy needed to move a nanoparticle away from the region where the magnetic field intensity $H = \|\mathbf{H}\|$ is the strongest is

$$\Delta E_H = \mu_0 m H_{\max}, \quad (2.4)$$

where H_{\max} is the maximum magnetic field intensity. The stability condition is $\Delta E_H < E_T$ and can be written

$$\mu_0 m H_{\max} < k_B T. \quad (2.5)$$

Assuming that the nanoparticle is spherical and of diameter d , the intensity of its magnetic moment is

$$m = \frac{\pi M_{s,p} d^3}{6}, \quad (2.6)$$

where $M_{s,p}$ is the saturation magnetization of the constitutive material. We replace m in (2.5) by using (2.6). The Brownian motion will avoid sedimentation due to an applied magnetic field if the nanoparticle diameter stays under a critical value:

$$d < \left(\frac{6k_B T}{\pi \mu_0 M_{s,p} H_{\max}} \right)^{\frac{1}{3}}. \quad (2.7)$$

¹Also called base fluids.

Stability regarding the gravity

The nanoparticles are metallic and would sediment at the bottom of the solution without the Brownian motion. The thermal energy must be strong enough to enable the nanoparticles to move freely from the bottom to the top of the solution. The difference of potential energy associated with the reduced weight (sum of the gravity and the Archimedes forces) of a nanoparticle between the top and the bottom of the solution is

$$\Delta E_p = (\rho_p - \rho_{bf})Vgh, \quad (2.8)$$

where ρ_p is the density of the nanoparticle, ρ_{bf} is that of the base fluid, V is the volume of the nanoparticle, g is the gravity and h is the height of ferrofluid. The condition of stability is $\Delta E_p < E_T$ and can be written

$$(\rho_p - \rho_{bf})Vgh < k_B T. \quad (2.9)$$

The nanoparticle volume can be expressed with the diameter:

$$V = \frac{\pi d^3}{6}. \quad (2.10)$$

We replace V in (2.9) by using (2.10). For the Brownian motion to counterbalance the gravity, the nanoparticle diameter must be smaller than a second critical value:

$$d < \left(\frac{6k_B T}{\pi(\rho_p - \rho_{bf})gh} \right)^{\frac{1}{3}}. \quad (2.11)$$

Stability regarding the magnetic dipole interactions

The nanoparticles generate attractive magnetic forces on each other due to the magnetic dipole interactions. Agglomeration must be avoided because it creates clusters of nanoparticles and leads to their sedimentation. The approach is quasi identical to that used in the applied magnetic field case, except that we consider the movement of one nanoparticle in the magnetic field generated by another one. Two nanoparticles 1 and 2, whose centers of gravity are localized by \mathbf{r}_1 and \mathbf{r}_2 , will naturally get closer to each other in order to minimize their magnetic dipole interaction energy

$$E_{dd} = -\frac{\mu_0}{4\pi} \left(3 \frac{(\mathbf{m}_1 \cdot \mathbf{r}_{12})(\mathbf{m}_2 \cdot \mathbf{r}_{12})}{r_{12}^5} - \frac{\mathbf{m}_1 \cdot \mathbf{m}_2}{r_{12}^3} \right), \quad (2.12)$$

where \mathbf{m}_i is the magnetic moment carried by the dipole i and $\mathbf{r}_{12} = \mathbf{r}_2 - \mathbf{r}_1$ is the vector between the centers of gravity. This quantity is the magnetic potential energy of the nanoparticle 2 in the magnetic field generated by the nanoparticle 1. We use the simplified notation $r = r_{12}$ and we introduce the angles between the magnetic moments and \mathbf{r}_{12} : $a_1 = \widehat{(\mathbf{r}_{12}, \mathbf{m}_1)}$ and $a_2 = \widehat{(\mathbf{r}_{12}, \mathbf{m}_2)}$. With these parameters, the magnetic dipole interaction energy is given by

$$E_{dd} = -\frac{\mu_0 m^2}{4\pi r^3} (2 \cos(a_1) \cos(a_2) - \sin(a_1) \sin(a_2)). \quad (2.13)$$

For a fixed distance r , this quantity is minimum when $a_1, a_2 = 0$ [2π] or when $a_1, a_2 = \pi$ [2π] (see Figure 2.2), i.e., when the magnetic dipoles are collinear to \mathbf{r}_{12} and have the same direction. Assuming that the magnetic dipoles satisfy this condition, the magnetic dipole interaction energy reaches its minimum when the nanoparticles are in contact, i.e.,

when $r = d$. The magnetic moment intensity can be replaced by using (2.6) and we obtain the following expression:

$$E_{dd}^{min} = -\frac{\pi\mu_0 M_{s,p}^2 d^3}{72}. \quad (2.14)$$

The opposite of this quantity is the energy needed to separate the nanoparticles. The stability condition is $-E_{dd}^{min} < 2E_T$ (thermal energy of two nanoparticles) and can be written

$$\frac{\pi\mu_0 M_{s,p}^2 d^3}{144} < k_B T. \quad (2.15)$$

For the stability condition to be true, the diameter of the nanoparticles must be weaker than a third critical value:

$$d < \left(\frac{144 k_B T}{\pi\mu_0 M_{s,p}^2} \right)^{\frac{1}{3}}. \quad (2.16)$$

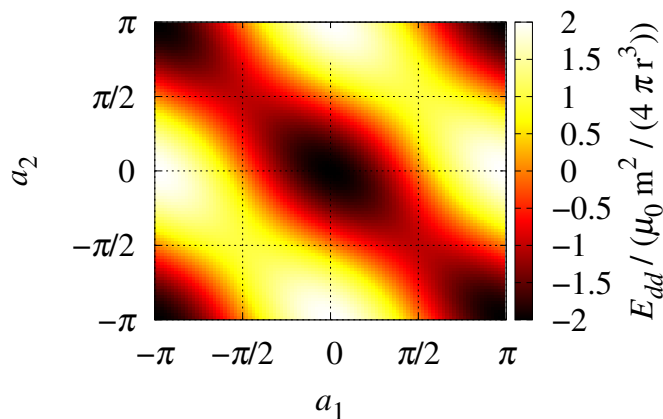


Figure 2.2: Normalized magnetic dipole interaction energy in (2.13) with respect to the angles a_1 and a_2 , when the distance r is fixed.

Stability regarding the van der Waals interactions

The nanoparticles also generate forces from electrical origin, called van der Waals forces, on each other. We consider two nanoparticles whose centers of gravity are separated by a distance r . We introduce $\delta = r - d$, the distance between the surfaces of the nanoparticles, and $l = 2\delta/d$. According to the results of Hamaker [23] on the interactions of van der Waals between spherical particles, the van der Waals interaction energy is

$$E_{vdW} = -\frac{A}{6} \left(\frac{2}{l^2 + 4l} + \frac{2}{(l + 2)^2} + \ln \left(\frac{l^2 + 4l}{(l + 2)^2} \right) \right), \quad (2.17)$$

where A is a constant that depends on the volume fraction of nanoparticles and the constitutive material. The van der Waals interaction energy goes to infinity when the distance between the nanoparticles goes to zero (or $l \rightarrow 0$). As a matter of fact, the first term, of order l^{-2} , dominates the logarithm. The thermal energy can thus not counterbalance the van der Waals interaction energy once there is contact. In organic carrier liquids, the nanoparticles are covered by a surfactant to avoid contacts. The surfactant is constituted of long chained molecules which heads are absorbed at the surface of the nanoparticles and which tails are used as repulsive barriers, see Figure 2.3. In water-based ferrofluids, the nanoparticles are electrically charged at the surface, which attract water molecules to create a repulsive barrier as well.

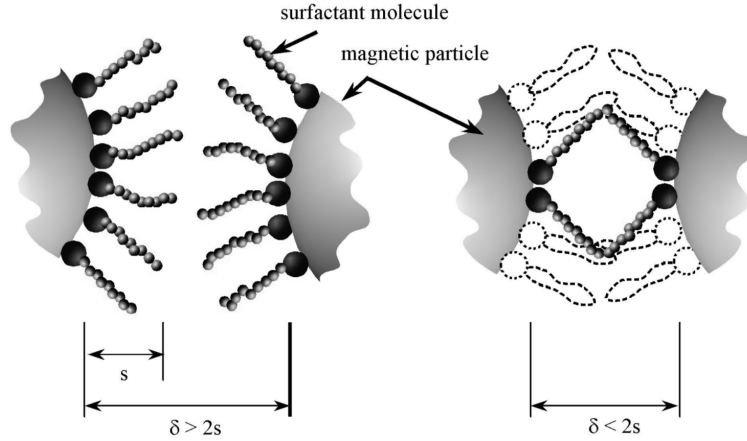


Figure 2.3: Mechanism of steric repulsion. The surfactant of thickness s avoids mechanically that two nanoparticles come too close, once the distance between the surfaces δ becomes smaller than $2s$. From [12].

Numerical values

We consider the representative example presented in [10, pp. 34-38]: a ferrofluid containing magnetite nanoparticles in the presence of the magnetic field generated by a magnet of average power. The parameters of the problem are $H_{\max} = 8 \times 10^4$ A/m, $M_{s,p} = 4.46 \times 10^5$ A/m, $T = 298$ K, $h = 5 \times 10^{-2}$ m and $\rho_p - \rho_{bf} = 4300$ kg/m³. The physical constants are $k_B = 1.38 \times 10^{-23}$ J.K⁻¹, $\mu_0 = 4\pi \times 10^{-7}$ N.A⁻² and $g = 9.81$ m/s² [24]. The maximum diameters of the nanoparticles given by (2.7), (2.11) and (2.16) are:

- 5.6 nm for the stability regarding the magnetic field generated by the magnet;
- 15.5 nm for the stability regarding the gravity;
- 9.1 nm for the stability regarding the magnetic dipole interactions.

The values given by the energy-based approach are consistent with the size of nanoparticles in actual ferrofluids.

2.1.4 Applications

Ferrofluid have applications in various domains. Ferrotec company [25] sells ferrofluids and ferrofluid-based technologies. Marketed applications of ferrofluids include audio speakers and liquid seals, see Figure 2.4. In audio speakers, the ferrofluid, attracted by the magnetic field of the coil, creates a layer of high thermal conductivity around it, enhancing heat dissipation. Liquid seals of ferrofluid are used in rotary shafts. The magnetic field of a permanent magnet maintains the ferrofluid seal around the shaft. Other applications have been or are still being investigated: accelerometer or inclinometer [26, 27], micro-pump [28], bio-medical applications such as drug targeting or hyperthermia [29, pp. 327-358], transformer cooling [30].

2.2 Modeling

In the literature, ferrofluids are generally modeled as continuous media with homogeneous properties. In this section, we present the modeling of their magnetization, discuss their governing equations and report classical laws for their thermophysical properties.

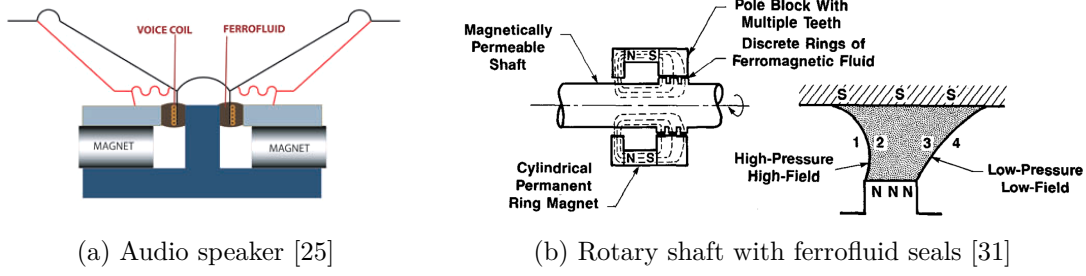


Figure 2.4: Industrial ferrofluid applications.

2.2.1 Magnetic properties

Owing to the low concentrations of magnetic nanoparticles, the magnetic dipole interactions are weak and ferrofluids exhibit super-paramagnetic behavior. The magnetic moments carried by the nanoparticles change direction relatively to the applied magnetic field. In the absence of an applied magnetic field, the magnetic moments are uniformly distributed in all directions. They compensate each other and the magnetization is zero. In the presence of an applied magnetic field, the magnetic moments tend to align in the same direction. The stronger the magnetic field intensity, the stronger the alignment. Above a critical value of the magnetic field intensity, all magnetic moments are aligned with the magnetic field. The ferrofluid magnetization intensity has then reached the saturation magnetization

$$M_s = \phi M_{s,p}, \quad (2.18)$$

where ϕ is the volume fraction of the ferromagnetic material and $M_{s,p}$ is its saturation magnetization. The temperature has an influence on the ferrofluid magnetization in the presence of an applied magnetic field of average intensity. Thermal agitation perturbs the magnetic moments alignment. The higher the temperature, the lower the ferrofluid magnetization intensity [10, pp. 55-61].

The magnetization intensity of a ferrofluid is given by Langevin's law, which takes into account the effects of the magnetic field and of the temperature:

$$M = M_s L(\xi) = M_s \left(\coth(\xi) - \frac{1}{\xi} \right), \quad (2.19)$$

with ξ defined by

$$\xi = \frac{\mu_0 m H}{k_B T}, \quad (2.20)$$

where μ_0 is the magnetic permeability of vacuum, m is the intensity of the magnetic moment carried by one nanoparticle, H is the intensity of the magnetic field, k_B is the Boltzmann constant, T is the temperature (in Kelvin) and L is the function of Langevin. By replacing m in (2.20) with (2.6), the parameter ξ can also be formulated as

$$\xi = \frac{\pi \mu_0 M_{s,p} d^3 H}{6 k_B T}. \quad (2.21)$$

Figure 2.5 presents the graph of the function of Langevin, which is a strictly increasing function of the parameter ξ . Thus, when ξ increases because H increases, M increases. Reversely, when ξ decreases because T increases, M decreases. The function of Langevin satisfies

$$\lim_{\xi \rightarrow \infty} L(\xi) = 1. \quad (2.22)$$

It means that, for strong values of the magnetic field intensity ($\xi \gg 1$), the magnetization intensity reaches the saturation magnetization M_s , as previously explained. The function

of Langevin also has the following Taylor expansion close to 0:

$$L(\xi) = \frac{\xi}{3} + o(\xi). \quad (2.23)$$

It means that, for weak values of the magnetic field intensity ($\xi \ll 1$), the magnetization intensity is proportional to H and can be simplified into

$$M = \chi_i H, \quad (2.24)$$

where χ_i is the initial magnetic susceptibility defined by

$$\chi_i = \frac{\pi\mu_0\phi M_{s,p}^2 d^3}{18k_B T}. \quad (2.25)$$

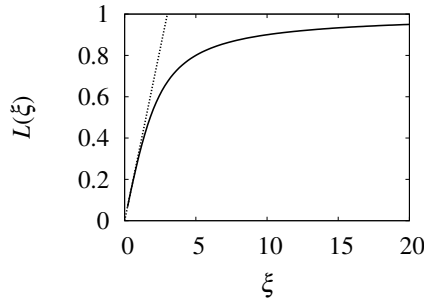


Figure 2.5: Langevin's function (dashed line: linearization $\xi/3$ close to 0).

Note that in actual ferrofluids the nanoparticles follow a distribution of sizes. Chatreil et al. [32] described the equations taking into account the distribution of the nanoparticle sizes. Denoting by d_m the median diameter and by x the ratio d/d_m , the ferrofluid magnetization intensity is given by

$$M = M_s \int_0^\infty L(\xi) f(x) dx, \quad (2.26)$$

where ξ is the parameter in (2.21), which is also a function of x , and f is the distribution function. The initial magnetic susceptibility is given by

$$\chi_i = \frac{\pi\mu_0\phi M_{s,p}^2 d_m^3}{18k_B T} \int_0^\infty x^3 f(x) dx. \quad (2.27)$$

The distribution of sizes can be approximated by a log-normal distribution function. Figure 2.6 shows the distribution of size of an actual ferrofluid produced by Sophie Neveu at PHENIX lab (Sorbonne University).

Figure 2.7a presents the theoretical evolution of a ferrofluid magnetization intensity as a function of the magnetic field intensity, illustrating parameters M_s and χ_i (simply denoted by χ there). In the following, we consider that (2.24) is always true; the initial magnetic susceptibility is called magnetic susceptibility and denoted by χ . To show the relevance of Langevin's law, Figure 2.7b presents the magnetization curve of a ferrofluid constituted of magnetite in transformer oil, with a volume fraction of 1.2%, measured in [2].

Ferrofluids are said to be super-paramagnetic because the parameter ξ is much greater than that of regular paramagnetic materials. As a matter of fact, in (2.20), m is the intensity of the magnetic moment of a whole nanoparticle while it is that of an atomic magnetic moment in a regular paramagnetic material. Consequently, in ferrofluids, the saturation

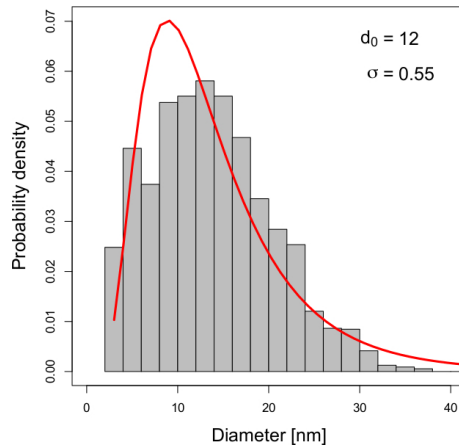
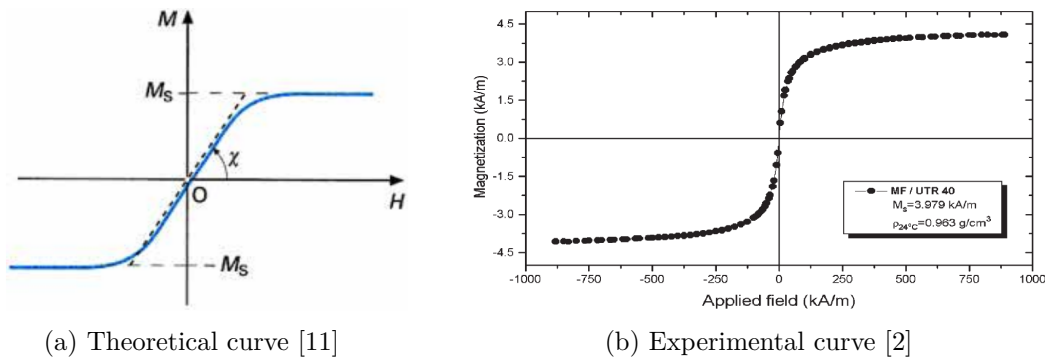


Figure 2.6: Log-normal distribution of the nanoparticle sizes in a ferrofluid.



(a) Theoretical curve [11]

(b) Experimental curve [2]

Figure 2.7: Theoretical and experimental magnetization curves of a ferrofluid.

magnetization is reached for relatively weak values of the magnetic field intensity and the initial susceptibility is much stronger than in regular paramagnetic materials [11].

Magnetization relaxation refers to the way the magnetization adapts to the change of the magnetic field direction. There are two mechanisms of relaxation in a ferrofluid. With the Brownian relaxation, the magnetic moment carried by a nanoparticle stays rooted inside it and the nanoparticle rotates. With the Néel relaxation, the magnetic moment carried by a nanoparticle rotates inside it while the nanoparticle stays fixed. The relaxation follows the faster mechanism. The characteristic time depends on the size of the nanoparticles. Néel mechanism dominates in smaller nanoparticles, said magnetically weak. Brownian mechanism dominates in larger nanoparticles, said magnetically hard. The critical diameter is close to 20 nm for magnetite [12, pp. 20-22]. Rosensweig [10, pp. 61-62] mentions a relaxation time between 10^{-8} and 10^{-5} s for a kerosene / magnetite ferrofluid.

2.2.2 Governing equations

Ferrofluids are often considered Newtonian and incompressible. We present here a complete set of governing equations, based on these assumptions, inspired by Neuringer and Rosensweig [33]. The ferrofluid magnetization is assumed collinear to the magnetic field and has the same direction. Other authors take into account the relaxation by including an additional equation for the magnetization (concept of *internal rotations* of the magnetic nanoparticles) [34, 35], but we do not consider this aspect owing to the short relaxation time.

Magnetic field equations

The ferrofluid is electrically non-conductive and the displacement currents are neglected. The magnetic field is governed by the law of Maxwell-Ampère

$$\nabla \times \mathbf{H} = 0 \quad (2.28)$$

and the divergence free condition

$$\nabla \cdot \mathbf{B} = 0, \quad (2.29)$$

where \mathbf{H} is the magnetic field and \mathbf{B} is the induction field. The induction field is related to the magnetic field through

$$\mathbf{B} = \mu_0(\mathbf{H} + \mathbf{M}), \quad (2.30)$$

where μ_0 is the magnetic permeability of vacuum and \mathbf{M} is the ferrofluid magnetization.

Equations of fluid dynamics

The incompressible Navier-Stokes equations are used. The momentum equation and the continuity equation are

$$\rho \partial_t \mathbf{u} + \rho(\mathbf{u} \cdot \nabla) \mathbf{u} + \nabla p - \eta \nabla^2 \mathbf{u} = \rho \mathbf{g} + \mathbf{f}_m, \quad (2.31)$$

$$\nabla \cdot \mathbf{u} = 0, \quad (2.32)$$

where \mathbf{u} is the velocity, p is the pressure, η is the dynamic viscosity, \mathbf{g} is the gravity and \mathbf{f}_m is the magnetic body force, i.e., the force per unit volume generated by a magnetic field on the ferrofluid.

The magnetic body force is an unclear aspect of ferrofluid modeling since many different forms are used in the literature on the subject. At the microscopic scale, there are two models for the force acting on a magnetic dipole of moment \mathbf{m} :

$$\mathbf{F}_1 = \mu_0 \nabla(\mathbf{m} \cdot \mathbf{H}), \quad \mathbf{F}_2 = \mu_0(\mathbf{m} \cdot \nabla) \mathbf{H}, \quad (2.33)$$

depending on the model of the magnetic dipole (current loop for the first, magnetic charge for the second) [36]. These two models lead to two macroscopic body forces called the Maxwell body force and the Kelvin body force [37]:

$$\mathbf{f}_M = \mu_0 \nabla_{\mathbf{M}}(\mathbf{M} \cdot \mathbf{H}), \quad \mathbf{f}_K = \mu_0(\mathbf{M} \cdot \nabla) \mathbf{H}, \quad (2.34)$$

where $\nabla_{\mathbf{M}}$ means that \mathbf{M} is fixed, i.e., $\forall i, \{\nabla_{\mathbf{M}}(\mathbf{M} \cdot \mathbf{H})\}_i = M_j \partial_i H_j$. Nevertheless, these two body forces are equal in a ferrofluid owing to the vector equality

$$\nabla_{\mathbf{M}}(\mathbf{M} \cdot \mathbf{H}) - \mathbf{M} \cdot \nabla \mathbf{H} = \mathbf{M} \times (\nabla \times \mathbf{H})$$

and (2.28).

The Kelvin body force is the most popular model in the literature on ferrofluids. As indicated in [38, p. 3.8], this model does not take into account the magnetic dipole interactions, which are negligible in ferrofluids. Here, the Kelvin body force can be simplified because the ferrofluid magnetization is assumed collinear to the magnetic field. Owing to this assumption, we can write

$$\mu_0(\mathbf{M} \cdot \nabla) \mathbf{H} = \mu_0 \frac{M}{H} (\mathbf{H} \cdot \nabla) \mathbf{H}.$$

The vector equality

$$(\mathbf{H} \cdot \nabla) \mathbf{H} = H \nabla H - \mathbf{H} \times (\nabla \times \mathbf{H})$$

combined with (2.28) leads to $\mathbf{f}_K = \mathbf{f}_K^\parallel$ with

$$\mathbf{f}_K^\parallel = \mu_0 M \nabla H. \quad (2.35)$$

The Kelvin body force can be simplified further by using the assumption of linear magnetic material for the ferrofluid ($M = \chi H$, with χ the magnetic susceptibility). We have then $\mathbf{f}_K^\parallel = \mathbf{f}_K^{\parallel,l}$ with

$$\mathbf{f}_K^{\parallel,l} = \mu_0 \chi \nabla \left(\frac{H^2}{2} \right). \quad (2.36)$$

Macroscopic body force expressions can be directly obtained by energetic considerations. Under the assumptions of incompressibility, of collinearity of the ferrofluid magnetization and the magnetic field and of linear magnetic material, another body force, that we call the Helmholtz body force, can be used:

$$\mathbf{f}_H = -\frac{H^2}{2} \nabla \mu, \quad (2.37)$$

where $\mu = \mu_0(1 + \chi)$ is the magnetic permeability of the ferrofluid [38, p. 3.15]. The Helmholtz body force can be obtained by using the method of the virtual power principle [39]. One interest of this expression for ferrofluids is that it can be expressed with the temperature gradient (see [28, eq. (16)]), which is a necessary ingredient for thermomagnetic convection. By using the relation between μ and χ , the Helmholtz body force can be re-written as

$$\mathbf{f}_H = -\mu_0 \frac{H^2}{2} \nabla \chi. \quad (2.38)$$

Owing to the relation

$$\mu_0 \chi \nabla \left(\frac{H^2}{2} \right) = -\mu_0 \frac{H^2}{2} \nabla \chi + \nabla \left(\mu_0 \chi \frac{H^2}{2} \right),$$

the Kelvin body force in (2.36) and the Helmholtz body force in (2.38) are equal up to a gradient:

$$\mathbf{f}_K^{\parallel,l} = \mathbf{f}_H + \nabla \Phi, \quad \Phi = \mu_0 \chi \frac{H^2}{2}. \quad (2.39)$$

It is possible to have a tensor vision of the body forces. Owing to (2.28), (2.29) and (2.30), the Kelvin body force can be re-written as $\mathbf{f}_K = \nabla \cdot [\sigma_0]$, with

$$[\sigma_0] = \mathbf{H} \otimes \mathbf{B} - \frac{1}{2} \mu_0 H^2 [I], \quad (2.40)$$

where $[I]$ is the identity tensor [40]. We have thus

$$\mathbf{f}_K = \nabla \cdot (\mathbf{H} \otimes \mathbf{B}) - \frac{1}{2} \mu_0 \nabla (H^2). \quad (2.41)$$

The tensor $[\sigma_0]$ is close to the classical Maxwell stress tensor, given in [41],

$$[\sigma_M] = \mathbf{H} \otimes \mathbf{B} - \frac{1}{2} \mu H^2 [I]. \quad (2.42)$$

As a matter of fact, the only difference is that μ_0 in (2.40) is replaced with μ in (2.42). As explained in [41], the divergence of $[\sigma_M]$ is equal to the Helmholtz body force when (2.28) is true (non-conductive medium). Applying the divergence to $[\sigma_M]$ yields

$$\nabla \cdot [\sigma_M] = \nabla \cdot (\mathbf{H} \otimes \mathbf{B}) - \frac{1}{2} \nabla (\mu H^2). \quad (2.43)$$

Notice that this body force is therefore also equal to the Kelvin body force in (2.41) up to a gradient.

Temperature equation

Considerations of thermodynamics on magnetic materials lead to the temperature equation

$$\rho c \partial_t T + \rho \mathbf{c} \mathbf{u} \cdot \nabla T - \mu_0 K T (\partial_t H + (\mathbf{u} \cdot \nabla) H) - \nabla \cdot (\lambda \nabla T) = 2\eta \nabla^s \mathbf{u} : \nabla \mathbf{u}, \quad (2.44)$$

where T is the temperature, c is the specific heat, K is the pyromagnetic coefficient defined by

$$K = -\frac{\partial M}{\partial T} \quad (2.45)$$

and $\nabla^s \mathbf{u}$ is the strain rate tensor defined by

$$\nabla^s \mathbf{u} = \frac{1}{2} (\nabla \mathbf{u} + (\nabla \mathbf{u})^T). \quad (2.46)$$

2.2.3 Thermophysical properties

The density, specific heat, thermal expansion coefficient, thermal conductivity and viscosity of a ferrofluid are different from that of the base fluid. As a matter of fact, the magnetic nanoparticles are made of metallic material and modify these properties, even in the absence of an applied magnetic field.

Density, heat capacity and thermal expansion coefficient

The density, specific heat and thermal expansion coefficient of a ferrofluid can be obtained by basic calculations [42]. Let us consider a volume V_{ff} of ferrofluid, containing a volume V_{bf} of base fluid and a volume V_{p} of magnetic nanoparticles (we assimilate the surfactant to the base fluid). The volumes are related through

$$V_{\text{bf}} = (1 - \phi)V_{\text{ff}}, \quad V_{\text{p}} = \phi V_{\text{ff}}, \quad (2.47)$$

where ϕ is the volume fraction of magnetic nanoparticles. The mass of the ferrofluid, the base fluid and the magnetic nanoparticles are denoted by M_{ff} , M_{bf} and M_{p} , respectively.

We denote by ρ_{ff} , ρ_{bf} and ρ_{p} the density of the ferrofluid, the base fluid and the magnetic nanoparticles, respectively. We can write

$$\rho_{\text{ff}} = \frac{M_{\text{ff}}}{V_{\text{ff}}} = \frac{M_{\text{bf}} + M_{\text{p}}}{V_{\text{ff}}} = \frac{\rho_{\text{bf}} V_{\text{bf}} + \rho_{\text{p}} V_{\text{p}}}{V_{\text{ff}}} = \rho_{\text{bf}} \frac{V_{\text{bf}}}{V_{\text{ff}}} + \rho_{\text{p}} \frac{V_{\text{p}}}{V_{\text{ff}}},$$

By using (2.47), we obtain the law for the density of the ferrofluid:

$$\rho_{\text{ff}} = (1 - \phi)\rho_{\text{bf}} + \phi\rho_{\text{p}}, \quad (2.48)$$

We denote by c_{ff} , c_{bf} and c_{p} the specific heat of the ferrofluid, the base fluid and the magnetic nanoparticles, respectively. We can write

$$\rho_{\text{ff}} c_{\text{ff}} V_{\text{ff}} = \rho_{\text{bf}} c_{\text{bf}} V_{\text{bf}} + \rho_{\text{p}} c_{\text{p}} V_{\text{p}},$$

By dividing by V_{ff} and by using (2.47), we obtain the law for the specific heat of the ferrofluid:

$$\rho_{\text{ff}} c_{\text{ff}} = (1 - \phi)\rho_{\text{bf}} c_{\text{bf}} + \phi\rho_{\text{p}} c_{\text{p}}. \quad (2.49)$$

We denote by α_{ff} , α_{bf} and α_{p} the thermal expansion coefficient of the ferrofluid, the base fluid and the magnetic nanoparticles, respectively. We can write

$$\alpha_{\text{ff}} = -\frac{1}{V_{\text{ff}}} \frac{\partial V_{\text{ff}}}{\partial T} = -\frac{1}{V_{\text{ff}}} \frac{\partial (V_{\text{bf}} + V_{\text{p}})}{\partial T} = -\frac{1}{V_{\text{ff}}} \frac{\partial V_{\text{bf}}}{\partial T} - \frac{1}{V_{\text{ff}}} \frac{\partial V_{\text{p}}}{\partial T}.$$

By using (2.47), we have

$$\frac{1}{V_{\text{ff}}} = \frac{1 - \phi}{V_{\text{bf}}} = \frac{\phi}{V_{\text{p}}}.$$

The law for the thermal expansion coefficient of the ferrofluid is thus:

$$\alpha_{\text{ff}} = (1 - \phi)\alpha_{\text{bf}} + \phi\alpha_{\text{p}}. \quad (2.50)$$

Thermal conductivity

The thermal conductivity of a material characterizes its ability to transfer heat by conduction (heat transfer from most energetic atoms or molecules to their less energetic neighbours). The magnetic nanoparticles being metallic, they present a higher thermal conductivity than the base fluid. It is well established that the thermal conductivity of metallic nanofluids and ferrofluids increases with the volume fraction of nanoparticles, see the experimental studies [43, 44, 45] (nanofluids) and [46, 47, 48] (ferrofluids) for instance. There are many models for the thermal conductivity of nanofluids, e.g., [42, 49]. The most popular model is that of Maxwell, developed for electromagnetism and valid for spherical particles:

$$\lambda_{\text{ff}} = \left(1 + \frac{3\phi(\lambda_{\text{p}} - \lambda_{\text{bf}})}{3\lambda_{\text{bf}} + (1 - \phi)(\lambda_{\text{p}} - \lambda_{\text{bf}})} \right) \lambda_{\text{bf}}, \quad (2.51)$$

where λ_{ff} is the thermal conductivity of the ferrofluid, λ_{bf} is that of the base fluid and λ_{p} is that of the nanoparticles [49]. This model is used as a reference for the study of nanofluids and gives reasonable predictions, see Figure 2.8.

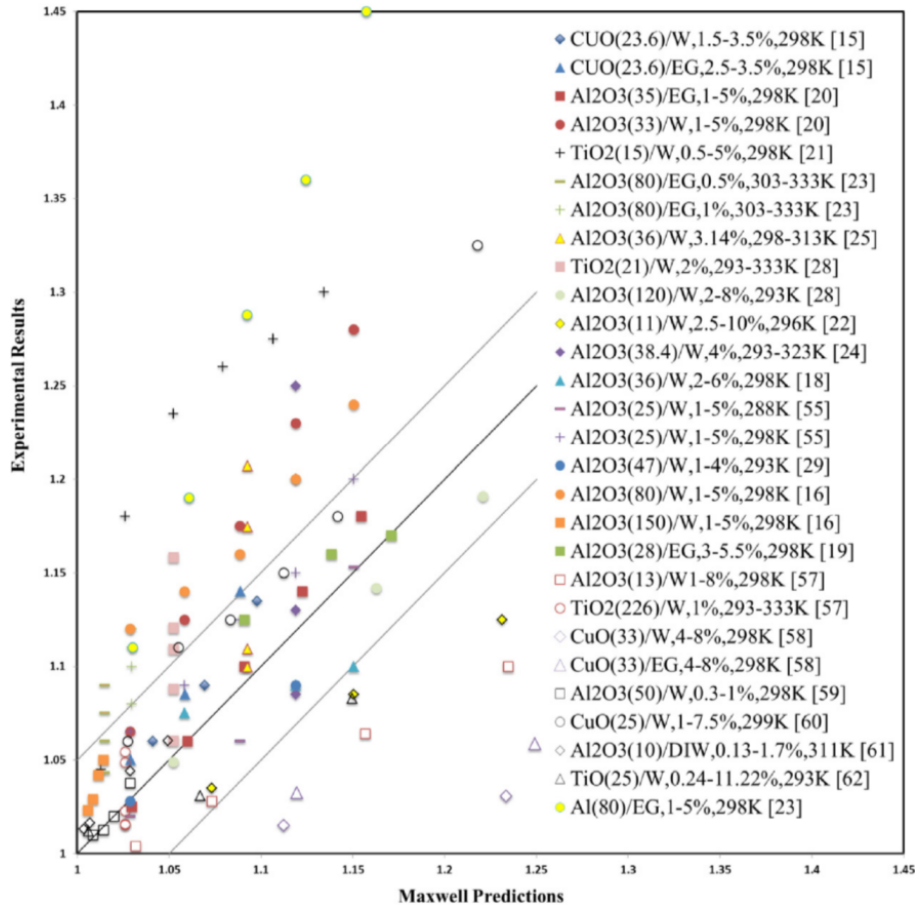


Figure 2.8: Experimental versus predicted values of the thermal conductivity ratio $\lambda_{\text{ff}}/\lambda_{\text{bf}}$ for various nanofluids. From [50].

The particularity of ferrofluids, compared to regular nanofluids, is that an applied magnetic field can enhance the thermal conductivity. This phenomenon was observed by Philip et al. [51] for instance, and explained by the formation of chainlike structures of magnetic nanoparticles. There does not exist a model though, and the chainlike structures are likely to collapse once convection is generated.

Viscosity

The viscosity of a fluid characterizes the diffusion of the momentum inside it. In the theoretical model of a perfect fluid, i.e., presenting a zero viscosity, two close fluid veins can move independently without interacting. In an actual fluid, thermal agitation of the fluid molecules, which creates collisions, diffuses the momentum from one fluid vein to the other [52]. It is well established that the viscosity of nanofluids and ferrofluids increases with the volume fraction of nanoparticles, see the experimental studies [43, 53, 45] (nanofluids) and [54, 55, 56] (ferrofluids) for instance. In the case of ferrofluids, the layer of surfactant must be taken into account, which increases further the viscosity. The volume fraction of nanoparticles and surfactant $\tilde{\phi}$ is given by

$$\tilde{\phi} = \left(\frac{d + 2s}{d} \right)^3 \phi, \quad (2.52)$$

where d is the nanoparticle diameter, s is the surfactant thickness and ϕ is the volume fraction of nanoparticles without surfactant. The most famous model for the viscosity of suspensions is that of Einstein [57, 58], theoretically developed for highly diluted spherical particles:

$$\eta_{\text{ff}} = \left(1 + \frac{5}{2} \tilde{\phi} \right) \eta_{\text{bf}}, \quad (2.53)$$

where η_{ff} is the dynamic viscosity of the ferrofluid and η_{bf} is that of the base fluid. Numerous theoretical and empirical models have been developed since then, e.g., [42, 59]. Some of the theoretical models are extensions of Einstein's model for different ranges of volume fraction or different particle shapes. For ferrofluids of typical concentrations, the following model was proposed by Rosensweig:

$$\eta_{\text{ff}} = \left(1 - \frac{5}{2} \tilde{\phi} + \frac{5}{2} \frac{\tilde{\phi}_c - 1}{\tilde{\phi}_c^2} \tilde{\phi}^2 \right)^{-1} \eta_{\text{bf}}, \quad (2.54)$$

where $\tilde{\phi}_c = 0.74$ is the volume fraction of nanoparticles with surfactant corresponding to a close packing of spheres [10, pp. 63-65]. This model is built such that:

- it tends to that of Einstein when $\tilde{\phi} \rightarrow 0$;
- it tends to infinity (solid behaviour) when $\tilde{\phi} \rightarrow \tilde{\phi}_c$.

In Figure 2.9, the models of Einstein and Rosensweig are compared to measurements on kerosene / magnetite ferrofluid samples containing a volume fraction $\tilde{\phi} \leq 30\%$. The mean diameter of the nanoparticles is 10 nm and the surfactant thickness is 2 nm. Einstein's model is valid for $\tilde{\phi} \leq 5\%$ but underestimates the viscosity of the ferrofluid for $\tilde{\phi} \geq 5\%$. Rosensweig's model perfectly matches the measurements over the whole range of $\tilde{\phi}$. Note that both models are consistent for low concentrations, as expected.

As the thermal conductivity, the viscosity of ferrofluids may be increased by an applied magnetic field. This phenomenon, called magnetoviscous effect, was shown experimentally by McTague [60] and explained by the hindrance of the nanoparticle rotations, the magnetic moments of the nanoparticles being aligned with the magnetic field [61]. Shliomis [62] developed a theoretical model for highly diluted suspensions:

$$\frac{\eta_H - \eta_0}{\eta_0} = \frac{3}{2} \tilde{\phi} \frac{\xi - \tanh(\xi)}{\xi + \tanh(\xi)} \sin^2(\alpha), \quad (2.55)$$

where η_H is the dynamic viscosity in the presence of an applied magnetic field \mathbf{H} , η_0 is the dynamic viscosity when $\mathbf{H} = \mathbf{0}$, ξ is the parameter in (2.20) and α is the angle between \mathbf{H} and the vorticity $\nabla \times \mathbf{u}$. Nevertheless, Odenbach [63] proved experimentally that only magnetically hard nanoparticles (the magnetization relaxation is due to the rotation of the nanoparticle) contribute to the magnetoviscous effect. Thus, in ferrofluids with a small amount of large nanoparticles, the magnetoviscous effect is negligible.

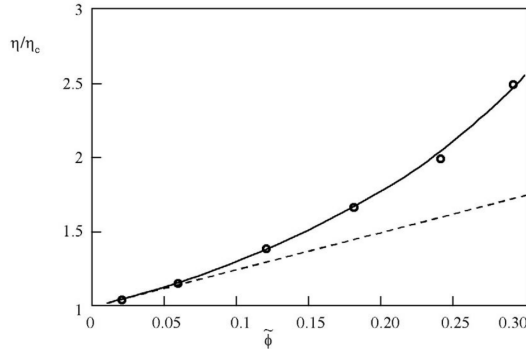


Figure 2.9: Comparison of the Einstein (dashed line) and Rosensweig (solid line) viscosity models with measurements on kerosene / magnetite ferrofluid samples ($\eta = \eta_{ff}$, $\eta_c = \eta_{bf}$). From [12].

2.3 Thermomagnetic convection

Thermomagnetic convection is a phenomenon which arises when ferrofluids are in the presence of a temperature gradient and a magnetic field. The ferrofluid magnetization being a function of the temperature, variations of the magnetic body force can develop and lead to a convective flow. Several analytical, experimental or numerical studies have highlighted this phenomenon and investigated its benefit for heat transfer.

2.3.1 Thermomagnetic instability

Thermomagnetic convection is due to the variations of the magnetic body force between hot and cold regions. The Kelvin body force in (2.35) is proportional to the magnetization intensity and oriented toward the magnetic field source. The magnetization intensity being a decreasing function of the temperature, see Section 2.2.1, the magnetic body force is more intense in a cold region than in a hot one. If the magnetic field source is near the heat source, a convective flow appears: the cold more attracted fluid flows toward the heat source and forces away the hot less attracted one.

This phenomenon can be compared to the natural convection driven by the buoyancy effect. If the heat source is at the bottom, because the hot fluid is less dense than the cold one above, the gravity action is less intense and the hot fluid is replaced by the cold one. Magnetization intensity for thermomagnetic convection is similar to density for thermogravitational convection.

The theoretical analysis of the mechanism of thermomagnetic convection by Odenbach [17] is presented here. We consider a ferrofluid comprised between hot (top) and cold (bottom) plates, in the presence of a magnetic field. The magnetic field intensity gradient is toward the top plate and uniform, as illustrated in Figure 2.10. Let us study a fluid particle located at height z , with volume V , temperature T , density ρ and magnetization intensity M . The system is at equilibrium initially. We suppose that the fluid particle slightly moves up to $z + \Delta z$. Assuming no conduction heat transfer during the displacement, its temperature, magnetization intensity and density stay unchanged. The resulting force \mathbf{F}_{res} acting on it after its displacement is composed of the gravity, the magnetic force and the pressure force:

$$\mathbf{F}_{res} = -\rho V g \mathbf{e}_z + \mu_0 M \frac{dH}{dz} V \mathbf{e}_z + \mathbf{F}_p. \quad (2.56)$$

Conventionally, \mathbf{e}_z is the unit vector pointing upwards. The pressure force is the same as the one which was acting on the volume of replaced fluid. The surrounding fluid is at

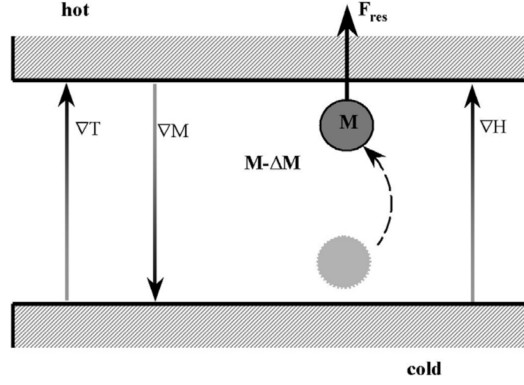


Figure 2.10: Configuration of thermomagnetic convection. A ferrofluid layer is comprised between two plates at different temperature and in the presence of a magnetic field intensity gradient. From [12].

temperature $T + \Delta T$, with density $\rho - \Delta\rho$ and magnetization intensity $M - \Delta M$ ($\Delta\rho > 0$ and $\Delta M > 0$). By using the fundamental law of dynamics applied to the replaced fluid volume, we can write

$$\mathbf{F}_p = (\rho - \Delta\rho)Vg\mathbf{e}_z - \mu_0(M - \Delta M)\frac{dH}{dz}V\mathbf{e}_z. \quad (2.57)$$

By replacing \mathbf{F}_p in (2.56) with (2.57), the resulting force on the fluid particle after its displacement can be written

$$\mathbf{F}_{res} = \left(-\Delta\rho g + \mu_0\Delta M\frac{dH}{dz}\right)V\mathbf{e}_z. \quad (2.58)$$

If the difference of magnetization intensity ΔM and the magnetic field intensity derivative $\frac{dH}{dz}$ are sufficient, i.e., they satisfy

$$\mu_0\Delta M\frac{dH}{dz} > \Delta\rho g, \quad (2.59)$$

the resulting force is oriented toward the top plate ($\mathbf{F}_{res} \cdot \mathbf{e}_z > 0$) and it pushes the fluid particle further in its upward displacement. The same conclusion is obtained in the case of a downward displacement of the fluid particle: the resulting force pushes the fluid particle further in its downward displacement. Thus, if the condition in (2.59) is satisfied, the situation is unstable and thermomagnetic convection can arise.

This example shows the importance of the direction of the magnetic field intensity gradient. If this gradient is downward ($\frac{dH}{dz} < 0$), the condition (2.59) cannot be satisfied, no matter what is the value of ΔM . The magnetic field intensity gradient must have the same direction as the temperature gradient. This example also shows the importance of the magnetic field intensity. The destabilizing effect is proportional to ΔM in (2.59). In the linear regime, the ferrofluid magnetization intensity is proportional to the magnetic field intensity. Thus, the higher H , the higher ΔM . This example finally shows the importance of the ferrofluid magnetic properties. The magnetization needs to be sensitive to the temperature for ΔM to be large and the destabilizing effect to increase. In other words, the pyromagnetic coefficient K in (2.45) needs to be high.

Notice that, in this example, the buoyancy force has a stabilizing effect while the magnetic force has a destabilizing effect. It is the opposite if the hot and the cold plates are inverted. Thus, the magnetic force does not always have a positive influence on heat transfer.

Thermal conduction and viscous friction have both stabilizing effects. Thermal conduction leads to heat transfer between the fluid particle and the surrounding fluid while viscous friction slows the fluid particle down. The temperature difference between the fluid particle and the surrounding fluid is thus reduced due to these two phenomena. Even if the stabilizing effect of the gravity is not considered, thermomagnetic convection might not arise. The variation of the magnetization intensity and the magnetic field intensity gradient must be strong enough to overcome thermal conduction and viscous friction. Thermomagnetic convection is characterized by a dimensionless number, called magnetic Rayleigh number, taking into account all of these factors and defined by

$$R_{a,m} = \frac{\mu_0 K \|\nabla H\| \Delta T L^3}{\kappa \eta}, \quad (2.60)$$

where K is the pyromagnetic coefficient, ∇H is the magnetic field intensity gradient, ΔT is the temperature difference between the walls, L is the distance between them, κ is the thermal diffusivity and η is the dynamic viscosity. The magnetic Rayleigh number indicates the relative importance of the destabilizing factors, the variation of the magnetization intensity and the magnetic field intensity gradient, and the stabilizing factors, thermal conduction and viscous friction. The Rayleigh number for thermogravitational convection is

$$R_a = \frac{g \alpha \Delta T L^3}{\kappa \nu}, \quad (2.61)$$

where g is the gravity, α is the thermal expansion coefficient and ν is the kinematic viscosity.

Recall that the heat transfer enhancement due to convection is characterized by the Nusselt number. In the literature, it is usually defined by

$$N_u = \frac{qL}{\lambda \Delta T}, \quad (2.62)$$

where q is the heat transfer rate and λ is the thermal conductivity. It represents the ratio of the heat transfer rate with motion and the heat transfer rate by conduction. As long as convection is not operative, q is the heat transfer rate by conduction only, and the Nusselt number is thus equal to 1. The Nusselt number gets greater than 1 once convection is operative.

2.3.2 Literature review

Finlayson [64] was one of the first researchers to study the natural convection of ferrofluids in 1970, analysing the stability of a ferrofluid layer in the presence of a uniform vertical magnetic field. Examples of the numerous works which have investigated this phenomenon after Finlayson are presented here.

Experimental studies

Schwab et al. [65] conducted an experiment on a hydrocarbon-based ferrofluid layer heated from below and under a uniform vertical magnetic field generated by a Helmholtz coil arrangement. They observed an influence of the magnetic field on the critical Rayleigh number of onset of convection, in good agreement with [64].

Odenbach [66] studied thermomagnetic convection in a hollow cylinder cavity under microgravity (sounding rocket experiments) to remove thermogravitational convection. The inner cylinder was heated while the outer one was cooled and the fluid layer was subjected to an azimuthal magnetic field. Except for the curvature, the temperature gradient and the magnetic field intensity gradient were in the same configuration as in Figure 2.10.

The measured temperature exhibited oscillations which matched former numerical predictions of the flow due to thermomagnetic convection: counter-rotating axial vortices were formed, see Figure 2.11.

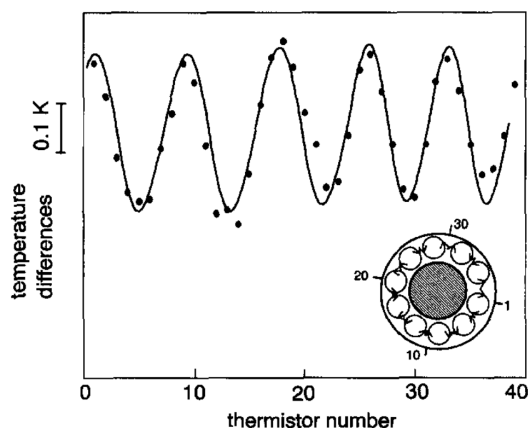


Figure 2.11: Thermomagnetic convection in a hollow cylinder under microgravity [66]. Measured temperature at the outer cylinder boundary and corresponding flow.

Bozhko and Putin [67] studied the natural convection of a kerosene-based ferrofluid layer heated from below or from above in the presence of a uniform transversal magnetic field generated by a Helmholtz coil arrangement. They measured the heat transfer rate and calculated the associated Nusselt number in various configurations. The thermomagnetic convection effect was confirmed, the Nusselt number increasing with the magnetic field intensity, see Figure 2.12. Notice that the Nusselt number is multiplied by 2-3 approximately between curves 1 (zero magnetic field) and 4 ($H = 70$ kA/m).

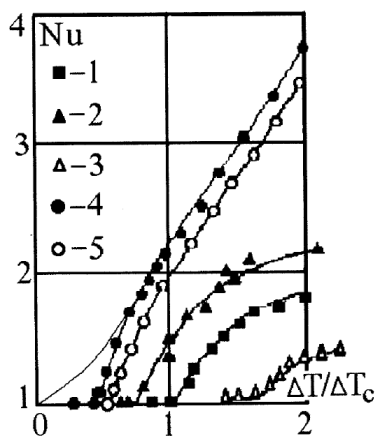


Figure 2.12: Natural convection in a ferrofluid layer under a transversal uniform magnetic field [67]. Nusselt number with respect to the temperature difference across the layer (normalized by the critical temperature difference of onset of convection at zero magnetic field). 1, 2, 4: heated from below and $H = 0, 10, 70$ kA/m. 3, 5: heated from above and $H = 10, 70$ kA/m.

Krauzina et al. [68] studied the natural convection of a transformer oil-based ferrofluid in a spherical cavity with a uniform vertical temperature difference and under a uniform vertical magnetic field generated by electromagnets. They calculated the Nusselt number in various configurations of magnetic field intensity and temperature gradient. When the sphere was heated from above (no thermogravitational convection), the Nusselt number

increased with the magnetic field intensity. When the sphere was heated from below (operative thermogravitational convection), the Nusselt number decreased. In the later case and for a strong magnetic field intensity, the heat transfer rate was even found lower than for pure transformer oil, showing that using ferrofluid is not always advantageous.

Numerical studies

Krakov and Nikiforov [69] simulated by finite element method the natural convection of a ferrofluid in a square cavity heated from the bottom, with side walls thermally insulated, in the presence of a uniform magnetic field. The angle between the temperature gradient and the magnetic field was found to influence the convective structure and the heat transfer rate.

Snyder et al. [70] studied the situation of a water-based ferrofluid in a cubic cavity with two side walls at different temperatures and all the others adiabatic, also using the finite element method. Two orientations of the applied uniform magnetic field intensity gradient, aligned with or opposite to the gravity, and different values of the magnetic field intensity were tested. The computed Nusselt numbers and the temperature profiles were compared to former experiments on the same configuration and a relatively good agreement was found.

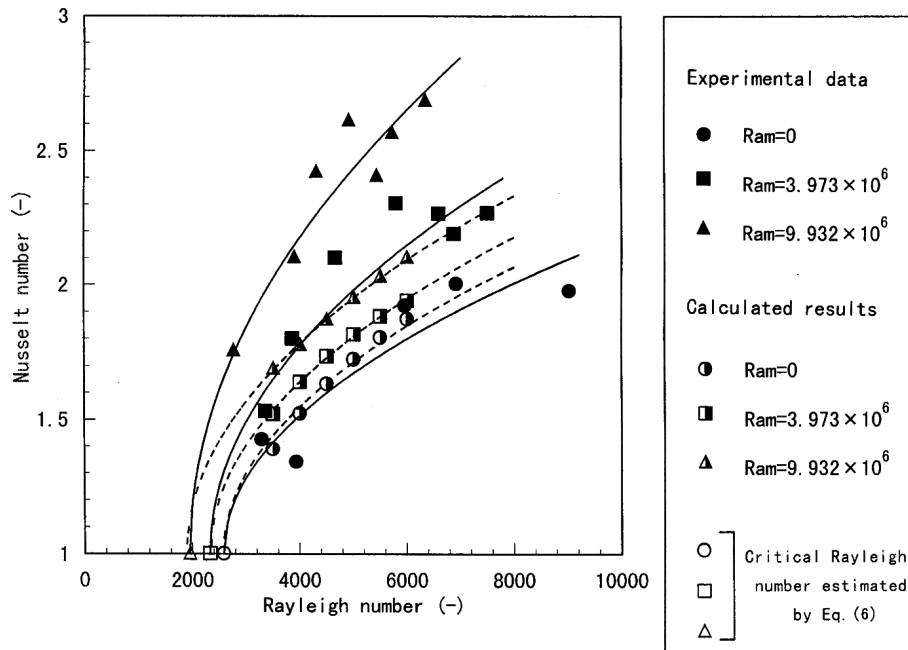
Ashouri and Shafii [71] simulated the natural convection of an oil-based ferrofluid in a square cavity containing a permanent magnet. The side walls were maintained at different temperatures while the top and bottom ones were adiabatic. The numerical study (still finite element method) showed that the size of the magnet had positive and negative influences on the heat transfer enhancement. While a larger magnet creates a stronger magnetic field and generates stronger thermomagnetic convection, it also reduces the fluid volume. For each tested magnetic Rayleigh number, an optimal magnet size was found to get the maximum Nusselt number.

Combined experimental and numerical studies

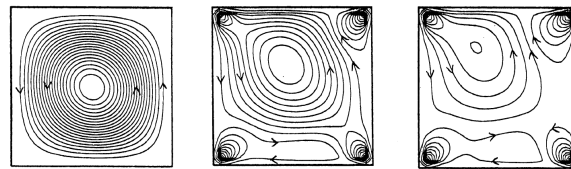
Yamaguchi et al. [72] studied thermomagnetic convection in a two-dimensional square cavity heated from below, cooled from the top, with adiabatic side walls and under a vertical magnetic field generated by electromagnets. They used Mn-Zn ferrite nanoparticles, which make the ferrofluid temperature-sensitive: the pyromagnetic coefficient is high, i.e., the magnetization intensity exhibits strong variations with the temperature. This kind of ferrofluid is more sensitive to thermomagnetic instability than regular ferrofluids. The experiment and the numerical simulations (finite difference method) showed the same trend: the Nusselt number increases when the magnetic field is applied, and increases further when the magnetic field intensity is increased, see Figure 2.13a. The numerical simulations showed that the unique convection cell at zero magnetic field is perturbed by local vortices at the corners of the cavity when the magnetic field is applied, see Figure 2.13b.

Yamaguchi et al. [73] extended this work by considering a cubic cavity in the presence of a uniform magnetic field (still Mn-Zn ferrite nanoparticles). The cavity was heated from below and cooled from the top while the side walls were adiabatic. Again, the experiment and the numerical simulations (lattice Boltzmann method) showed an increase of the Nusselt number when the magnetic field intensity was increased.

Zablotsky et al. [74] studied thermomagnetic convection in a flat rectangular cell. The cell was vertically oriented and a non-uniform magnetic field was generated by permanent magnets at each flat side. The bottom and top ends were maintained at different temperatures while the other walls were adiabatic. The ferrofluid contained Mn-Zn ferrite nanoparticles. The numerical results (ANSYS software) and the experimental results were



(a) Nusselt number with respect to the Rayleigh number

(a) $Ram=0.0$ (b) $Ram=3.973 \times 10^6$ (c) $Ram=9.932 \times 10^6$

(b) Convection patterns for a Rayleigh number of 4000

Figure 2.13: Simulation of the natural convection of a ferrofluid in a two-dimensional cavity heated from below and under the influence of a vertical magnetic field [72].

qualitatively in good agreement. The thermomagnetic convection effect was optimal when the magnets were shifted toward the heat source.

Yamaguchi et al. [75] completed the work published in [73] by studying the configuration of a cubic cavity containing a heating stick inside, in the presence of a uniform magnetic field. The ferrofluid was still temperature-sensitive but with Mg-Zn ferrite nanoparticles. As in [73], the experiment and the numerical simulations (lattice Boltzmann method) both showed an increase of the Nusselt number when the magnetic field intensity was increased. The size of the object was shown to affect heat transfer as well. The Nusselt number was lower with the largest stick because the fluid volume was reduced.

2.3.3 Conclusive remarks

Thermomagnetic convection has been experimentally and numerically studied in various configurations and with different ferrofluids. Most of the popular computational methods have been used. Successful comparisons between experiments and numerical simulations were carried out. The literature on ferrofluids confirms the theoretical analysis reported in Section 2.3.1 regarding the influence factors of thermomagnetic convection: the magnetic field intensity and direction, the temperature gradient and the ferrofluid magnetic properties.

To maximize the thermomagnetic convection effect, scientists work with temperature-sensitive ferrofluids, i.e., ferrofluids whose magnetization is strongly affected by the tem-

perature (high pyromagnetic coefficient). In these ferrofluids, the magnetic nanoparticles are made of a material with a weak Curie temperature. As a matter of fact, the slope of the saturation magnetization of a ferromagnetic material is large in the neighbourhood of the Curie temperature but negligible far from it. Figure 2.14 shows the saturation magnetization curve of nickel for instance. Iron, cobalt, nickel and magnetite have a Curie temperature of 1044 K, 1388 K, 628 K and 856 K, respectively [76, p. 9]. But some materials, such as Mn-Zn ferrites, have a much lower Curie temperature, in the range 100–200°C [77].

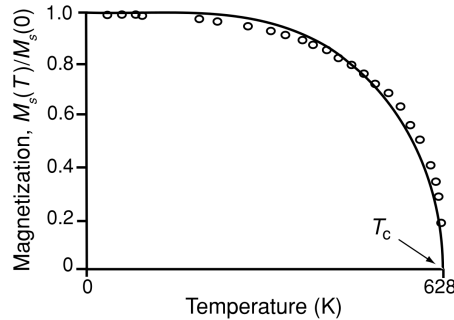


Figure 2.14: Saturation magnetization of nickel with respect to temperature. From [76].

Some of the mentioned studies consider a uniform applied magnetic field while thermomagnetic convection requires a gradient of magnetic field intensity (see Section 2.3.1). Note that (2.29) and (2.30) imply

$$\nabla \cdot \mathbf{H} = -\nabla \cdot \mathbf{M}. \quad (2.63)$$

Thus, spatial variations of the magnetization may lead to spatial variations of the magnetic field. Since the magnetization intensity of a ferrofluid is a function of the temperature, a temperature gradient can therefore induce a gradient of magnetic field intensity. Following Shliomis and Smorodin [78], let us consider a ferrofluid layer subjected to a vertical magnetic field $H\mathbf{e}_z$ generating a non-zero magnetization $M\mathbf{e}_z$ inside. Owing to (2.63), if an axial gradient of temperature $\frac{dT}{dz}\mathbf{e}_z$ is enforced, we have

$$\frac{dH}{dz} = -\frac{dM}{dz} = -\frac{\partial M}{\partial T} \frac{dT}{dz} - \frac{\partial M}{\partial H} \frac{dH}{dz} = K \frac{dT}{dz} - \chi \frac{dH}{dz},$$

where K is the pyromagnetic coefficient and χ is the magnetic susceptibility. It follows that

$$\frac{dH}{dz} = \frac{K}{1 + \chi} \frac{dT}{dz}. \quad (2.64)$$

We see in this example how a gradient of temperature can produce a gradient of magnetic field intensity. To conclude, it does not matter whether the applied magnetic field is uniform or not to generate thermomagnetic convection. Spatial variations of the temperature will naturally induce a gradient of magnetic field intensity.

Numerous studies have shown that heat transfer in ferrofluids can be enhanced in the presence of an applied magnetic field, due to thermomagnetic convection. This phenomenon makes ferrofluids promising cooling solutions. Nevertheless, as detailed in Section 2.2.3, the thermophysical properties of a ferrofluid are different from that of the liquid carrier. The thermal conductivity is stronger but the viscosity too. The first point is an advantage while the second is not. It is not clear whether the change of thermophysical properties can improve or reduce heat transfer. The studies usually do not compare the heat transfer in the ferrofluid and that in the liquid carrier. This should be done to truly assess the cooling performance of ferrofluids compared to regular fluids.

2.4 Transformer cooling

Several studies have shown the benefit of ferrofluids for transformer cooling by exploiting experimental or numerical results. In the meantime, other studies have focused on the suitability of transformer oil mixed with magnetic nanoparticles, in particular regarding electrical insulation.

2.4.1 Cooling performance

The idea of transformer cooling by using ferrofluids is not recent. Raj and Moskowitz [77] patented the principle of electromagnetic system cooling by using ferrofluid in 1995. The patent is based on the fact that, in an electromagnetic system such as a transformer, the source of magnetic field is the same as the source of heat. The magnetic field intensity gradient and the temperature gradient are parallel. Thus, the configuration is basically that of Figure 2.10 and thermomagnetic convection can arise. The use of temperature-sensitive ferrofluids is already mentioned in the patent. The authors specify that the magnetic material of the nanoparticles should have a Curie temperature slightly above the operating temperature. If the Curie temperature is too much above the operating temperature, thermomagnetic convection will not develop. If it is lower than the operating temperature, the ferrofluid will lose its magnetization before it arrives at the hot spot. Several magnetic materials are cited, including the Mn-Zn ferrites.

Since this patent, several research teams have studied by experiments and / or numerical approaches the benefit of transformer oil-based ferrofluid for transformer cooling. Segal and Raj [1] experimented the use of ferrofluid for power transformer cooling on two small distribution transformers (10 and 50 kVA). Various transformer oil-based ferrofluids with different saturation magnetization were tested. Passive or active cooling systems were used. The temperatures in the system for transformer oil-based ferrofluid and pure transformer oil were compared, showing a contrasted influence of the magnetic nanoparticles. At most, a temperature decrease of approximately 10°C was observed in the windings using ferrofluid, see Figure 2.15. Other measurements in this work showed a negative influence of the magnetic nanoparticles though.

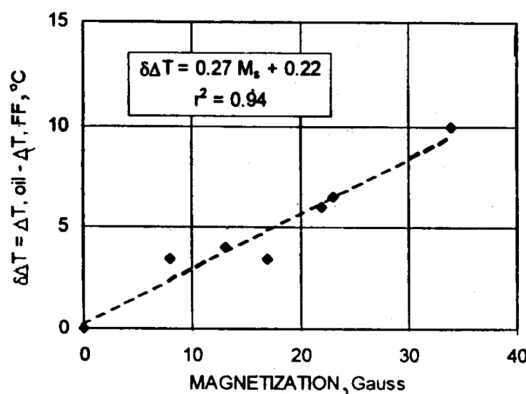


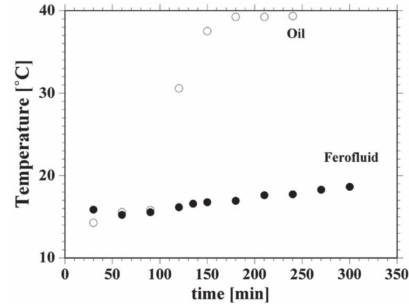
Figure 2.15: Experiment on a 50 kVA transformer prototype [1]. Difference of the temperature rise ΔT in the windings with pure transformer oil and with ferrofluid versus ferrofluid saturation magnetization.

Pîslaru-Danescu et al. [2] studied the cooling of a transformer by ferrofluid with numerical simulations (finite element method with COMSOL software) and experiments on a transformer prototype (36 kV / 40 kVA), see Figure 2.16a. The ferrofluid contained a volume fraction $\phi = 1.2\%$ of magnetite nanoparticles. In their model, the magnetization intensity was not temperature-dependant (only magnetic field intensity-dependant),

while thermomagnetic convection is due to the variation of the magnetization intensity with respect to the temperature. In the prototype, they measured a temperature up to 20°C lower with ferrofluid than with pure transformer oil, see Figure 2.16b. The authors claimed that the prototype had a smaller size than a regular transformer of same voltage and power owing to the heat transfer enhancement.



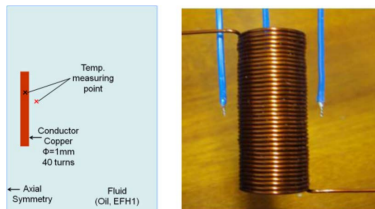
(a) Transformer prototype



(b) Temperature rise in the active part

Figure 2.16: Experiment on a 40 kVA transformer prototype [2].

Jeong et al. [3] studied the cooling of a coil in a cylindrical container filled by either transformer oil or ferrofluid. An experiment was set up and simulated by using the finite element method (COMSOL software). A volume fraction of magnetic nanoparticles up to 7% was used in the ferrofluid. They do not mention whether the liquid carrier is transformer oil or not. In the experiment, the temperature rise in the coil was reduced by 5°C at most when using the ferrofluid with $\phi = 7\%$, see Figure 2.17. The numerical simulations brought results in good agreement with the experimental ones.



(a) Coil and thermal sensors

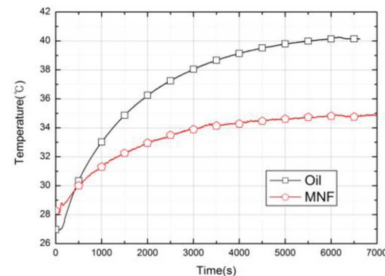
(b) Temperature rise at the coil (Oil: transformer oil, MNF: ferrofluid with $\phi = 7\%$)

Figure 2.17: Experiment on an immersed coil [3].

Patel et al. [4, 30] carried out experiments on a 3 kVA transformer prototype cooled by a transformer oil-based ferrofluid ($\phi = 1.27\%$). Mn-Zn ferrite magnetic nanoparticles were used, as suggested in [77], because their Curie temperature was close to the operating temperature. Various electrical loadings were tested (under loading, normal loading, overloading). As in [1, 2], the measurements showed a positive influence of the ferrofluid, see Figure 2.18. The winding temperature was up to 20°C lower with the ferrofluid. They estimated that the transformer life could be multiplied by 2 to 9 times owing to the temperature decrease with ferrofluid.

To conclude, experiments on transformer prototypes (or similar system) have already shown that it is possible to reduce the temperature inside the system by using transformer oil-based ferrofluid, illustrating the benefit claimed in the patent [77]. A negative influence of the magnetic nanoparticles has also been experimentally observed, and numerical results are rare and questionable.

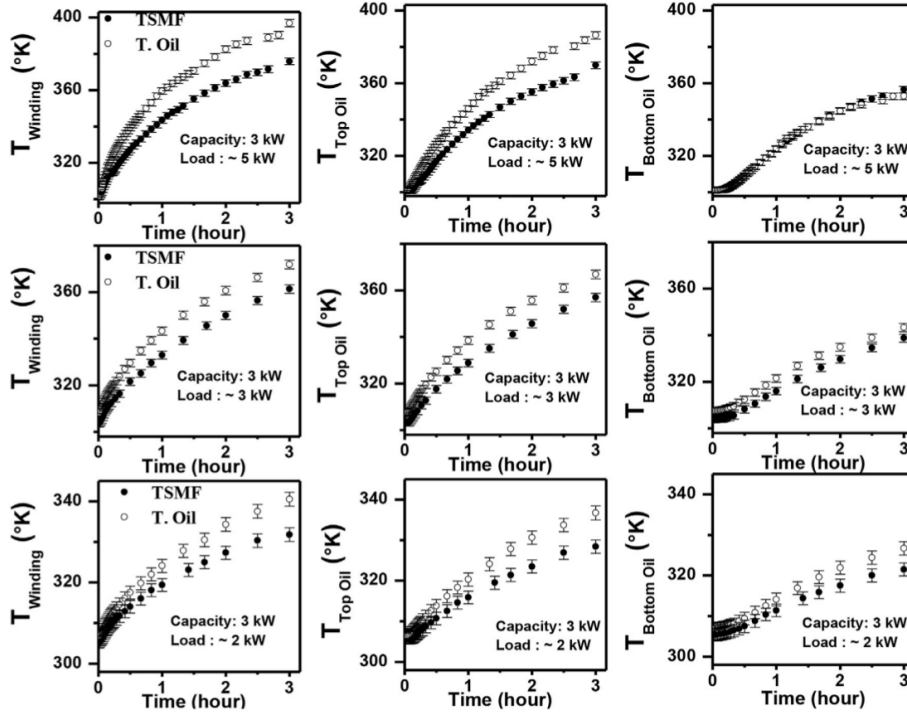


Figure 2.18: Experiment on a 3 kVA transformer prototype [30]. Temperature rise for different loadings and at various locations (TSMF: ferrofluid, T. Oil: transformer oil).

2.4.2 Suitability as insulating liquid

Transformer oil is an insulating medium as much as a cooling fluid. The dielectric properties of transformer oil-based ferrofluids have been measured to assess the suitability of such a mixture for transformer cooling [1, 79, 80, 81, 82, 83, 84, 85, 86, 87]. Main studies use ferrofluids with a low volume fraction of magnetic nanoparticles ($\phi \leq 1\%$). The magnetic nanoparticles are often made of magnetite. The measured properties are the breakdown voltage, the voltage above which an insulating medium becomes electrically conductive, and the electrical resistivity. Surprisingly, ferrofluids show a breakdown voltage of the same order of magnitude, and even higher sometimes, than pure transformer oil. Figure 2.19 shows the results of Lee and Kim [85] for instance. As pointed out by Segal et al. [79], transformer oil is usually purified from any particle to obtain optimal dielectric properties, while a ferrofluid naturally contains nanoparticles (even though the nanoparticles are two or three orders of magnitude smaller than the particles usually found in transformer oil). Moreover, the nanoparticles in a ferrofluid are made of metallic materials, which have much higher electrical conductivity than transformer oil. To explain the increase of the breakdown voltage, several authors mention the role of *electron scavenger* of the magnetic nanoparticles. As a matter of fact, Hang et al. [88] have proposed a theoretical explanation based on the trapping of the free electrons by the magnetic nanoparticles; the nanoparticles being much slower than the free electrons, it results in the reduction of the streamer velocity and a higher breakdown voltage. Kudelcik et al. [83] measured the breakdown voltage of transformer oil-based ferrofluids with a volume fraction of magnetic nanoparticles up to 2%. For $\phi = 2\%$, they measured a lower breakdown voltage than that of pure transformer oil. Apparently, 1% is the maximum volume fraction leading to an enhancement of the breakdown voltage. Regarding the electrical resistivity, the measurements show that the magnetic nanoparticles strongly reduce the electrical resistivity of the transformer oil (division by 10 to 100). The question is whether the electrical resistivity of the ferrofluid still respects the transformer norms. Note that Segal [89] patented the

use of ferrofluid in transformers, for its enhanced insulating as well as cooling properties, for the transformer manufacturer ABB in 1999.

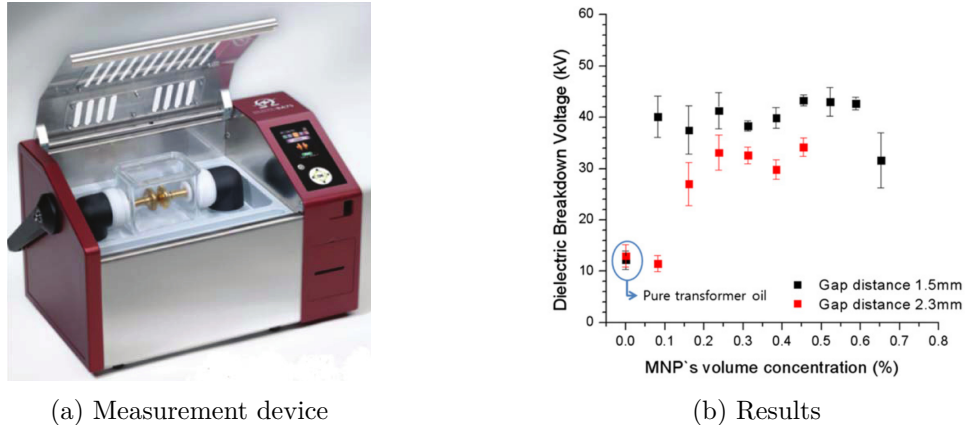


Figure 2.19: Breakdown voltage measurement of a transformer oil-based ferrofluid [85]. Notice the electrodes of the measurement device.

A transformer is supposed to last many years at high temperature. Thermal ageing experiments have also been carried out [90, 91, 92]. The stability of the ferrofluid, the dielectric properties, the magnetic properties and the interactions of the magnetic nanoparticles with the solid insulator over time were investigated, with optimistic conclusions or not. Chaudhari et al. [92] warned about the possible risk of electrical breakdown of the solid insulator due to the magnetic nanoparticles.

Note that ferrofluids can be very costly. Table 2.1 shows the price of ferrofluids from Ferrotec containing a nanoparticle volume fraction of approximately 5%. A litre of ferrofluid would cost \$1600-1700, while some transformers contain several tens of thousands of litres of insulating liquid.

Name	M_s (G)	η (cP)	Carrier	Price (\$/cm ³)
APG O47n	150	65	Ester oil	1.60
APG 312	150	75	Hydrocarbon oil	1.60
APG S15n	150	75	Ester oil	1.60
APG J12	200	40	Ester oil	1.70

Table 2.1: Ferrofluids from Ferrotec company. A volume fraction of 5% (10%) corresponds to a saturation magnetization of approximately 150 G (300 G). The measurements are made at 25 – 27°C (1 G = 10⁻⁴ T, 1 cP = 10⁻³ Pa · s).

2.5 Conclusion of the chapter

Ferrofluids are suspensions of magnetic nanoparticles in a liquid carrier, which react as a magnetic single phase fluid in the presence of an applied magnetic field. The stability of ferrofluids is guaranteed by the addition of a surfactant and the control of the nanoparticle size. Ferrofluids are used in various applications such as audio speakers or liquid seals.

These specific fluids show super-paramagnetic behavior, which is modeled by Langevin's law for paramagnetism. They are generally considered as continuum media with homogeneous properties. The velocity and the pressure are commonly governed by the incompressible Navier-Stokes equations, with an additional magnetic body force to take into account the action of an applied magnetic field. Several models of magnetic force in magnetic materials exist. The Kelvin body force, continuous version of the force generated

on a magnetic dipole in the presence of a magnetic field, is the most popular in the literature on ferrofluids. The addition of the magnetic nanoparticles do not just modify the magnetic properties of the base fluid, it also impacts its thermophysical properties. The thermal conductivity and the viscosity of ferrofluids can be modeled by classical laws for nanofluids taking into account the volume fraction of magnetic nanoparticles.

Owing to their magnetic properties, ferrofluids exhibit a specific convective instability called thermomagnetic convection. Numerous experimental and numerical studies have proved the existence of this phenomenon and its positive influence on heat transfer in ferrofluids. According to the literature, thermomagnetic convection mainly depends on the magnetic field intensity and direction, the temperature gradient and the ferrofluid magnetic properties. Temperature-sensitive ferrofluids, which nanoparticles are made of magnetic materials with a low Curie temperature, are particularly sensitive to this phenomenon.

The use of ferrofluid has been investigated to enhance heat transfer in electrical transformers, which present the good configuration for thermomagnetic convection to develop. Two patents have been registered in the nineties. Several works have since then obtained optimistic results on transformer prototypes, where the temperature was lowered by using transformer oil-based ferrofluid instead of pure transformer oil. Numerical results are nevertheless rare. Measurements have also showed that the breakdown voltage of such a mixture can be higher than that of pure transformer oil, but doubts on the suitability of ferrofluids as insulating liquid remain.

Chapter 3

New developments in SFEMaNS: ferrohydrodynamics applications

The SFEMaNS code has been being developed in LIMSI and TAMU since 2001. The code was originally designed to study magnetohydrodynamics, i.e., the interactions between an electrically conductive fluid (such as liquid metal) and a magnetic field, in axisymmetric geometries. Numerous developments have since then been brought so that SFEMaNS can deal with a wide range of problems involving the Navier-Stokes, Maxwell and energy conservation equations, see the PhDs [93, 94, 95, 96, 97]. The numerical method combines finite element and spectral approaches. Based on the cylindrical coordinates, the code uses a spectral decomposition in the azimuthal direction and finite element approximations in the meridian plane. During this PhD, a new class of applications has been created to study heat transfer in ferrofluids: ferrohydrodynamics applications. While this class is mostly based on the existing numerical schemes, some adaptations have been carried out. This chapter presents these developments and the associated validations. The first section describes the typical ferrofluid problem (geometry and governing equations) that can be addressed by SFEMaNS. The second section details the numerical method of SFEMaNS, highlighting the new terms in the numerical schemes. The third section reports the convergence tests on manufactured solutions used to validate the new developments.

3.1 Physical setting

3.1.1 Geometry

The equations of ferrohydrodynamics are solved in an axisymmetric domain $\Omega \subset \mathbb{R}^3$. Ω is partitioned into a fluid region Ω_f and a solid region Ω_s , as follows:

$$\overline{\Omega} = \overline{\Omega_f} \cup \overline{\Omega_s}, \quad \Omega_f \cap \Omega_s = \emptyset. \quad (3.1)$$

The velocity and the pressure are computed in Ω_f . The magnetic field is computed in Ω . The temperature was originally computed in Ω_f only. With the new developments, the temperature can also be computed in Ω_s , or part of it. We denote by Ω_T the temperature subdomain. The temperature is always computed in the fluid domain, for the thermo-hydrodynamical coupling. We have

$$\Omega_f \subset \Omega_T \subset \Omega. \quad (3.2)$$

The boundary of every subdomain (including the whole domain) is denoted by the subdomain symbol with the symbol ∂ in front, e.g., $\partial\Omega$ for the boundary of Ω . Dirichlet and Neumann boundary conditions can be enforced on the magnetic field. The parts of $\partial\Omega$

where these boundary conditions are enforced are denoted by $\partial\Omega_d$ and $\partial\Omega_n$, respectively. The new developments include the implementation of Robin boundary conditions on the temperature. Dirichlet, homogeneous Neumann and Robin boundary conditions can now be enforced on the temperature. The parts of $\partial\Omega_T$ where these boundary conditions are enforced are denoted by $\partial\Omega_{T,d}$, $\partial\Omega_{T,n}$ and $\partial\Omega_{T,r}$, respectively. Dirichlet conditions are enforced on the velocity over the whole fluid region boundary, $\partial\Omega_f$.

The domain Ω is also partitioned into N subsets Ω_i , $i \in \{1, \dots, N\}$, such that

$$\overline{\Omega} = \cup_{i \in \{1, \dots, N\}} \overline{\Omega}_i, \Omega_i \cap \Omega_j = \emptyset, \forall (i, j) \in \{1, \dots, N\}^2. \quad (3.3)$$

These subsets represent different components of the physical setup. The magnetic permeability and the thermophysical properties (density, specific heat, thermal conductivity) are constant in each subset, i.e., the fields of these properties are piecewise constant over the domain where they are defined. The interface between the subsets Ω_i , $i \in \overline{1, N}$, is denoted by

$$\Sigma_\mu = \cup_{(i,j) \in \{1, \dots, N\}^2} \overline{\Omega}_i \cap \overline{\Omega}_j, \quad (3.4)$$

due to the possible jump of magnetic permeability. A typical example of computational domain is presented in Figure 3.1.

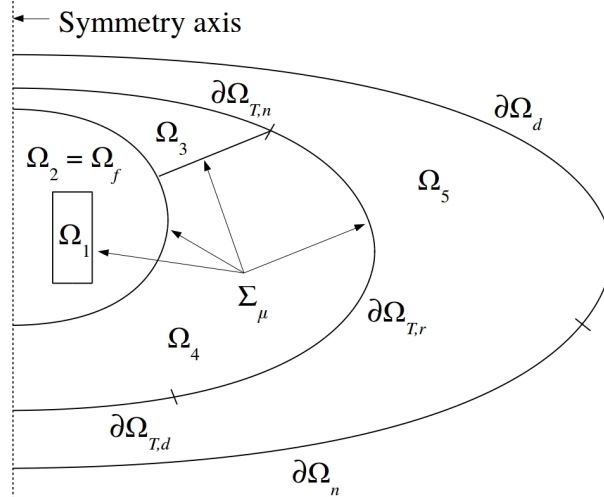


Figure 3.1: Typical example of a computational domain Ω . View of a meridian section; the full domain is obtained by a 360° angle rotation around the symmetry axis. The temperature domain is composed of subdomain 1 to 4. The thermophysical properties may vary in subdomains 1 to 4. The magnetic permeability may vary in subdomains 1 to 5.

3.1.2 Equations

The velocity is denoted by \mathbf{u} , the pressure is denoted by p , the temperature is denoted by T and the magnetic field is denoted by \mathbf{H} . For every vector field \mathbf{a} , we use the notation $a = \|\mathbf{a}\|$. In the boundary conditions, \mathbf{n} represents the outer unit normal vector.

Ferrofluid modeling

The equations rely on several assumptions on the ferrofluid:

- the ferrofluid is a continuum with homogeneous properties;
- the ferrofluid has Newtonian behavior;

- the magnetization of the ferrofluid is collinear to the magnetic field (the relaxation time is zero);
- the collinearity coefficient between the ferrofluid magnetization and the magnetic field depends on the temperature but not on the magnetic field.

The last assumption implies that the ferrofluid is considered as a linear magnetic material, as discussed in Section 2.2.1. Due to the last two assumptions, the ferrofluid magnetization and the magnetic field are related by

$$\mathbf{M} = \chi(T)\mathbf{H}, \quad (3.5)$$

where χ is the magnetic susceptibility of the ferrofluid.

Temperature equations

As said, the temperature can be computed in a domain with fluid and solid regions. In the fluid region, the temperature is governed by the temperature equation of incompressible Newtonian fluids (A.24). The viscous dissipation term is neglected and removed from the equation, as usually done. In the solid region, the temperature is governed by the standard temperature equation of solids. The new developments include the implementation of a magnetic coupling term in the ferrofluid and of the Robin boundary conditions. The magnetic coupling term comes from the magnetic work in the first principle of thermodynamics, according to the work of [33]. The magnetic coupling term is called the pyromagnetic coefficient term in the following.

We introduce the velocity extension

$$\tilde{\mathbf{u}} = \begin{cases} \mathbf{u} & \text{in } \Omega_f \times \mathbb{R}_+, \\ \mathbf{u}_{\text{ext}} & \text{in } (\Omega_T \setminus \Omega_f) \times \mathbb{R}_+, \end{cases} \quad (3.6)$$

where \mathbf{u}_{ext} is the velocity in the solid. The equations are

$$\left\{ \begin{array}{ll} \rho c \partial_t T + \rho c \tilde{\mathbf{u}} \cdot \nabla T - \nabla \cdot (\lambda \nabla T) & \\ + \mu_0 T \frac{\partial \chi}{\partial T}(T) \left(\partial_t \left(\frac{H^2}{2} \right) + \mathbf{u} \cdot \nabla \left(\frac{H^2}{2} \right) \right) = f_T & \text{in } \Omega_f \times \mathbb{R}_+^* \\ \rho c \partial_t T + \rho c \tilde{\mathbf{u}} \cdot \nabla T - \nabla \cdot (\lambda \nabla T) = f_T & \text{in } (\Omega_T \setminus \Omega_f) \times \mathbb{R}_+^* \\ T = T_d & \text{on } \partial\Omega_{T,d} \times \mathbb{R}_+^*, \\ \partial_{\mathbf{n}} T = 0 & \text{on } \partial\Omega_{T,n} \times \mathbb{R}_+^*, \\ -\lambda \nabla T \cdot \mathbf{n} = h_c (T - T_r) & \text{on } \partial\Omega_{T,r} \times \mathbb{R}_+^*, \\ T|_{t=0} = T_0 & \text{in } \Omega_T, \end{array} \right. \quad (3.7)$$

where ρ is the density, c is the specific heat, λ is the thermal conductivity, μ_0 is the magnetic permeability of vacuum, f_T is the heat source, T_d is the temperature at the Dirichlet boundary, h_c is the convection heat transfer coefficient, T_r is the exterior temperature at the Robin boundary and T_0 is the initial temperature. We use the notation $\partial_{\mathbf{n}} T = \nabla T \cdot \mathbf{n}$.

The pyromagnetic coefficient term in (2.44) is re-formulated by using (3.5). Note that h_c and T_r are constants. The Robin boundaries can be split and different values of h_c and T_r can be affected to each part.

Equations of fluid dynamics

The ferrofluid flow is governed by the continuity equation and the momentum equation for Newtonian fluids with the Boussinesq approximation, see (A.20) and (A.27). A Dirichlet

boundary condition is enforced on the boundary. The new developments include the implementation of two models of magnetic body force (Kelvin and Helmholtz) and of a viscosity function of the temperature.

The equations are

$$\left\{ \begin{array}{l} \partial_t \mathbf{u} + (\nabla \times \mathbf{u}) \times \mathbf{u} + \nabla \left(\frac{p}{\rho_f} \right) \\ -\nabla \cdot (2\nu_f(T) \nabla^s \mathbf{u}) = \alpha_f (T - T_*) g \mathbf{e}_z + \frac{\mu_0}{\rho_f} \chi(T) \nabla \left(\frac{H^2}{2} \right) + \frac{\mathbf{f}}{\rho_f} \quad \text{in } \Omega_f \times \mathbb{R}_+^*, \\ \nabla \cdot \mathbf{u} = 0 \quad \text{in } \Omega_f \times \mathbb{R}_+^*, \\ \mathbf{u} = \mathbf{u}_d \quad \text{on } \partial\Omega_f \times \mathbb{R}_+^*, \\ \mathbf{u}|_{t=0} = \mathbf{u}_0 \quad \text{in } \Omega_f, \end{array} \right. \quad (3.8)$$

where T_* is the temperature of the Boussinesq approximation, ρ_f is the density of the fluid at T_* , ν_f is the kinematic viscosity, α_f is the thermal expansion coefficient, \mathbf{f} represents the body forces except the gravitational and the magnetic ones, \mathbf{u}_d is the velocity at the boundary and \mathbf{u}_0 is the initial velocity (satisfying $\nabla \cdot \mathbf{u}_0 = 0$). We use the notation

$$\nabla^s \mathbf{u} = \frac{1}{2} (\nabla \mathbf{u} + (\nabla \mathbf{u})^T) \quad (3.9)$$

for the strain rate tensor.

Notice that the momentum equation is under the rotational form. The nonlinear term $(\mathbf{u} \cdot \nabla) \mathbf{u}$ in (A.27) is replaced by using the equality

$$(\mathbf{u} \cdot \nabla) \mathbf{u} = (\nabla \times \mathbf{u}) \times \mathbf{u} + \nabla \left(\frac{u^2}{2} \right).$$

This variation induces the change of variable $p \leftarrow p + \rho u^2/2$, compared to (A.27). Two models of magnetic body force were implemented: the Kelvin body force¹, used in (3.8),

$$\mathbf{f}_K = \mu_0 \chi(T) \nabla \left(\frac{H^2}{2} \right), \quad (3.10)$$

and the Helmholtz body force

$$\mathbf{f}_H = -\mu_0 \frac{H^2}{2} \nabla \chi(T). \quad (3.11)$$

While their expressions are totally different, the two magnetic body forces give the same velocity field, as shown in the next chapter.

Magnetic field equations

The equations of electromagnetism are considered under the quasi-static assumption, i.e., the displacement currents are neglected [98, pp. 5-6]. The ferrofluid magnetic permeability is considered temperature-independent. We need to introduce additional notations for the interface conditions. Let $i \neq j \in \{1, \dots, N\}$ such that $\overline{\Omega}_i \cap \overline{\Omega}_j \neq \emptyset$. Assume that $i < j$. Then, $\forall \mathbf{x} \in \overline{\Omega}_i \cap \overline{\Omega}_j$, we define

$$\mathbf{H}_1(\mathbf{x}) = \lim_{\mathbf{y} \in \Omega_i \rightarrow \mathbf{x}} \mathbf{H}(\mathbf{y}) \quad \text{and} \quad \mathbf{H}_2(\mathbf{x}) = \lim_{\mathbf{y} \in \Omega_j \rightarrow \mathbf{x}} \mathbf{H}(\mathbf{y}). \quad (3.12)$$

We also define:

¹The subscript of $\mathbf{f}_K^{||,l}$ in (2.36) is removed for simplicity.

- \mathbf{n}_1 and \mathbf{n}_2 the outer unit normal vectors of Ω_i and Ω_j , respectively;
- μ_1 and μ_2 the magnetic permeability in Ω_i and Ω_j , respectively.

Subscripts 1 and 2 are reversed if $j > i$.

The equations are

$$\begin{cases} \nabla \times \mathbf{H} = \mathbf{j} & \text{in } \Omega \times \mathbb{R}_+^*, \\ \nabla \cdot (\mu \mathbf{H}) = 0 & \text{in } \Omega \times \mathbb{R}_+^*, \\ \mathbf{H} \times \mathbf{n} = \mathbf{H}_d \times \mathbf{n} & \text{on } \partial\Omega_d \times \mathbb{R}_+^*, \\ \mu \mathbf{H} \cdot \mathbf{n} = \mu \mathbf{H}_n \cdot \mathbf{n} & \text{on } \partial\Omega_n \times \mathbb{R}_+^*, \end{cases} \quad (3.13)$$

where \mathbf{j} is the user-defined current density, μ is the magnetic permeability, \mathbf{H}_d is the magnetic field at the Dirichlet boundary and \mathbf{H}_n is the magnetic field at the Neumann boundary. The interface conditions

$$\begin{cases} \mathbf{H}_1 \times \mathbf{n}_1 + \mathbf{H}_2 \times \mathbf{n}_2 = \mathbf{0} & \text{on } \Sigma_\mu \times \mathbb{R}_+^*, \\ \mu_1 \mathbf{H}_1 \cdot \mathbf{n}_1 + \mu_2 \mathbf{H}_2 \cdot \mathbf{n}_2 = 0 & \text{on } \Sigma_\mu \times \mathbb{R}_+^*, \end{cases} \quad (3.14)$$

are enforced in the weak formulation by using a penalty method [99].

Couplings

The global set of equations presents:

- a strong coupling velocity \leftrightarrow temperature through the convective term in the temperature equation and the body forces in the momentum equation;
- a weak coupling magnetic field \rightarrow temperature through the pyromagnetic coefficient term in the temperature equation;
- a weak coupling magnetic field \rightarrow velocity through the magnetic body force in the momentum equation;
- no coupling temperature \rightarrow magnetic field.

The magnetic field is not affected by the evolution of the other variables. If the current density is constant (DC current), the magnetic field is constant as well.

3.2 Numerical method

The numerical method implemented in SFEMaNS combines finite element and spectral methods. The particularity of the method is the Fourier representation of the approximate variables. The components of the Fourier decomposition are approximated in finite element spaces. The time-marching algorithm is based on the method of lines [100, p. 286]. The problem is approximated in time by the finite difference method.

3.2.1 Fourier representation

The code is based on the cylindrical coordinates. The fields are represented by partial Fourier sums in the azimuthal direction. The approximation f_h of any scalar field f is under the form

$$f_h(r, \theta, z, t) = \sum_{m=-m_{\max}}^{m_{\max}} f_h^m(r, z, t) e^{im\theta}, \quad (3.15)$$

where $(r, \theta, z) \in \mathbb{R}_+ \times [0, 2\pi) \times \mathbb{R}$ are the cylindrical coordinates, $t \in \mathbb{R}_+$ is the time, $m_{\max} \in \mathbb{N}$ is the maximum considered mode and f_h^m , $m \in \{-m_{\max}, \dots, m_{\max}\}$, are complex

functions. The code only deals with real fields. The complex components of the partial Fourier sum (3.15) thus satisfy

$$\forall m \in \{0, \dots, m_{\max}\}, \overline{f_h^m} = f_h^{-m}. \quad (3.16)$$

Under this condition, the partial sum can be expressed as

$$f_h(r, \theta, z, t) = \sum_{m=0}^{m_{\max}} f_h^{m, \cos}(r, z, t) \cos(m\theta) + \sum_{m=1}^{m_{\max}} f_h^{m, \sin}(r, z, t) \sin(m\theta), \quad (3.17)$$

where

$$\begin{cases} f_h^{0, \cos} = f_h^0, \\ f_h^{m, \cos} = 2\operatorname{Re}(f_h^m), \forall m \in \{1, \dots, m_{\max}\}, \\ f_h^{m, \sin} = -2\operatorname{Im}(f_h^m), \forall m \in \{1, \dots, m_{\max}\}, \end{cases} \quad (3.18)$$

Re and Im being the real part and the imaginary part, respectively. A vector field is approximated similarly, component by component. The components of the partial Fourier sums live in the finite element spaces defined next.

3.2.2 Finite element approximation spaces

To present the approximation spaces, we introduce Ω^{2D} , Ω_T^{2D} , Ω_f^{2D} and Ω_i^{2D} , $\forall i \in \{1, \dots, N\}$, the meridian sections, say at $\theta = 0$, of Ω , Ω_T , Ω_f and Ω_i , $\forall i \in \{1, \dots, N\}$, respectively. Figure 3.2 shows an example of cylindrical domain of computation and the associated meridian section, for illustration.

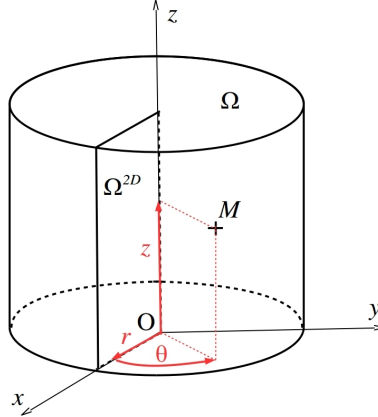


Figure 3.2: Example of cylindrical domain of computation Ω and the associated meridian section Ω^{2D} . A point $M \in \Omega$ is located by its cylindrical coordinates (r, θ, z) , with $(r, z) \in \Omega^{2D}$ and $\theta \in [0, 2\pi)$.

We denote by $\{\mathcal{T}_h\}_{h>0}$, $\{\mathcal{T}_h^T\}_{h>0}$ and $\{\mathcal{T}_h^f\}_{h>0}$ the families of non-overlapping quadratic triangular meshes of the meridian sections Ω^{2D} , Ω_T^{2D} and Ω_f^{2D} , respectively. h denotes the maximum mesh size.

The approximation spaces are defined for given meshes \mathcal{T}_h , \mathcal{T}_h^T and \mathcal{T}_h^f . Given two spaces A and B , we denote by $\mathcal{C}^0(A; B)$ the space of the continuous functions from A to B . The space of the functions from A to B is denoted by $\mathcal{F}(A; B)$. \mathbb{P}_1 and \mathbb{P}_2 are the spaces of real-valued bivariate polynomials of total degree at most 1 and 2, respectively. For the temperature, the components of the partial Fourier sum are approximated by using Lagrange, \mathbb{P}_2 , finite elements. We define the meridian finite element space for the temperature

$$S_h^{2D} = \left\{ s_h \in \mathcal{C}^0(\overline{\Omega_T^{2D}}; \mathbb{C}); s_h|_K \in \mathbb{P}_2^2, \forall K \in \mathcal{T}_h^T \right\}. \quad (3.19)$$

The temperature is approximated in

$$S_h = \left\{ s_h = \sum_{k=-m_{\max}}^{m_{\max}} s_h^k(r, z) e^{ik\theta}; s_h^k \in S_h^{2D}, \overline{s_h^k} = s_h^{-k}, \forall k \in \{-m_{\max}, \dots, m_{\max}\} \right\}. \quad (3.20)$$

We also define the space of the temperature test functions

$$S_h^0 = \{s_h \in S_h; s_h = 0 \text{ on } \partial\Omega_{T,d}\}. \quad (3.21)$$

For the velocity and the pressure, the components of the partial Fourier sums are approximated by Taylor-Hood, $\mathbb{P}_2/\mathbb{P}_1$, finite elements. We define the meridian finite element spaces for the velocity and the pressure

$$\mathbf{V}_h^{2D} = \left\{ \mathbf{v}_h \in \mathcal{C}^0(\overline{\Omega_f^{2D}}; \mathbb{C})^3; \mathbf{v}_h|_K \in \mathbb{P}_2^6, \forall K \in \mathcal{T}_h^f \right\}, \quad (3.22)$$

and

$$M_h^{2D} = \left\{ q_h \in \mathcal{C}^0(\overline{\Omega_f^{2D}}; \mathbb{C}); q_h|_K \in \mathbb{P}_1^2, \forall K \in \mathcal{T}_h^f \right\}. \quad (3.23)$$

The velocity and the pressure are approximated in

$$\mathbf{V}_h = \left\{ \mathbf{v}_h = \sum_{k=-m_{\max}}^{m_{\max}} \mathbf{v}_h^k(r, z) e^{ik\theta}; \mathbf{v}_h^k \in \mathbf{V}_h^{2D}, \overline{\mathbf{v}_h^k} = \mathbf{v}_h^{-k}, \forall k \in \{-m_{\max}, \dots, m_{\max}\} \right\}, \quad (3.24)$$

and

$$M_h = \left\{ q_h = \sum_{k=-m_{\max}}^{m_{\max}} q_h^k(r, z) e^{ik\theta}; q_h^k \in M_h^{2D}, \overline{q_h^k} = q_h^{-k}, \forall k \in \{-m_{\max}, \dots, m_{\max}\} \right\}, \quad (3.25)$$

respectively. We also define the space of the velocity test functions

$$\mathbf{V}_h^0 = \{\mathbf{v}_h \in \mathbf{V}_h; \mathbf{v}_h = 0 \text{ on } \partial\Omega_f\}. \quad (3.26)$$

For the magnetic field, the components of the partial Fourier sums are approximated by Lagrange, \mathbb{P}_2 finite elements. We define the meridian finite element space for the magnetic field

$$\mathbf{X}_h^{2D} = \left\{ \mathbf{b}_h \in \mathcal{F}(\Omega; \mathbb{C})^3; \mathbf{b}_h|_{\Omega_i} \in \mathcal{C}^0(\overline{\Omega_i}; \mathbb{C})^3, \forall i \in \{1, \dots, N\}, \mathbf{b}_h|_K \in \mathbb{P}_2^6, \forall K \in \mathcal{T}_h \right\}. \quad (3.27)$$

The magnetic field is approximated in

$$\mathbf{X}_h = \left\{ \mathbf{b}_h = \sum_{k=-m_{\max}}^{m_{\max}} \mathbf{b}_h^k(r, z) e^{ik\theta}; \mathbf{b}_h^k \in \mathbf{X}_h^{2D}, \overline{\mathbf{b}_h^k} = \mathbf{b}_h^{-k}, \forall k \in \{-m_{\max}, \dots, m_{\max}\} \right\}. \quad (3.28)$$

Details on the Lagrange and Taylor-Hood finite elements are given in [100, pp. 4-13 and 192-195].

3.2.3 Time-marching algorithm

General principle

We denote by τ the time step and by n_{\max} the total number of iterations. One iteration of the solver corresponds to one increment τ of the physical time t . For every

$n \in \{0, \dots, n_{\max}\}$, $t_n = n\tau$ denotes the time at the n^{th} iteration. We also introduce $t_{-1} = -\tau$ for the initialization. The approximations of the temperature, the velocity, the pressure and the magnetic field at time t_n are denoted by T_h^n , \mathbf{u}_h^n , p_h^n and \mathbf{H}_h^n , $\forall n \in \{-1, \dots, n_{\max}\}$, respectively.

The variables are initialized at t_{-1} and t_0 by using the initial conditions. In the following, we assume that T_0 , \mathbf{u}_0 and \mathbf{H}_0 (the initial magnetic field) are in the corresponding approximation spaces. At every iteration following the initialization, all fields are updated in the following order: 1) temperature, 2) velocity and pressure. The magnetic field is solved only at the first iteration, after the other fields, because there is no retro-action of the temperature or the velocity on it. For every following iteration, the magnetic field is propagated, as is, from time n to time $n+1$. If the current density is sinusoidal, the magnetic field is simply modified in the coupling terms by using the linearity of the magnetostatics equations (3.13). The time derivatives are approximated by the second-order Backward Difference Formula (BDF2)

$$\partial_t T_h(t_{n+1}) = \frac{3T_h^{n+1} - 4T_h^n + T_h^{n-1}}{2\tau} + O(\tau^2), \forall n \geq 0, \quad (3.29)$$

and

$$\partial_t \mathbf{u}_h(t_{n+1}) = \frac{3\mathbf{u}_h^{n+1} - 4\mathbf{u}_h^n + \mathbf{u}_h^{n-1}}{2\tau} + O(\tau^2), \forall n \geq 0. \quad (3.30)$$

See Appendix B for the derivation of the BDF2. The nonlinear terms are made explicit and treated as source terms. The unknown variables on the right-hand side are extrapolated by using second-order approximations:

- $T_h^{n+1} = T_h^{*,n+1} + O(\tau^2)$, with $T_h^{*,n+1} = 2T_h^n - T_h^{n-1}$, $\forall n \geq 0$;
- $\mathbf{u}_h^{n+1} = \mathbf{u}_h^{*,n+1} + O(\tau^2)$, with $\mathbf{u}_h^{*,n+1} = 2\mathbf{u}_h^n - \mathbf{u}_h^{n-1}$, $\forall n \geq 0$;
- $\mathbf{H}_h^{n+1} = \mathbf{H}_h^{*,n+1} + O(\tau^2)$, with $\mathbf{H}_h^{*,n+1} = 2\mathbf{H}_h^n - \mathbf{H}_h^{n-1}$, $\forall n \geq 0$.

See Appendix B for the derivation of these extrapolations. The nonlinear terms are then computed in the physical space. The Fast Fourier Transform method is used to transform the fields in the Fourier space into the fields in the physical space, and reversely. For every $n \in \{0, \dots, n_{\max} - 1\}$, the computation of T_h^{n+1} , \mathbf{u}_h^{n+1} and \mathbf{H}_h^{n+1} consist in solving $2m_{\max} + 1$, $3(2m_{\max} + 1)$ and $3(2m_{\max} + 1)$ linear systems, respectively. As a matter of fact, each component of the partial Fourier sum (3.17) is solution of one linear system (and a vector field is represented by three scalar fields). Because these problems are $2D$, SFEMaNS is still more efficient than a classical $3D$ code (for a reasonable n_{\max}). Because the nonlinear terms are made explicit, the algebra of the solver is time-independent: the matrices that need to be reversed are computed only once. The solver presents two levels of parallelization: mode-by-mode resolution and domain decomposition in the meridian plane.

Note that, the fields being carried by different meshes, a transmission step of the coupling variables is necessary before solving the temperature and the velocity. Before solving the temperature, the velocity and the magnetic field are transmitted on the temperature mesh (extension and restriction of the coupling field, respectively). Before solving the velocity, the temperature and the magnetic field are transmitted on the velocity mesh (restriction for both coupling fields). The magnetic problem is not coupled to the velocity or the temperature so no projection is needed.

Figure 3.3 shows the flowchart of the algorithm. The numerical schemes corresponding to each problem (temperature, velocity/pressure, magnetic field) are detailed next.

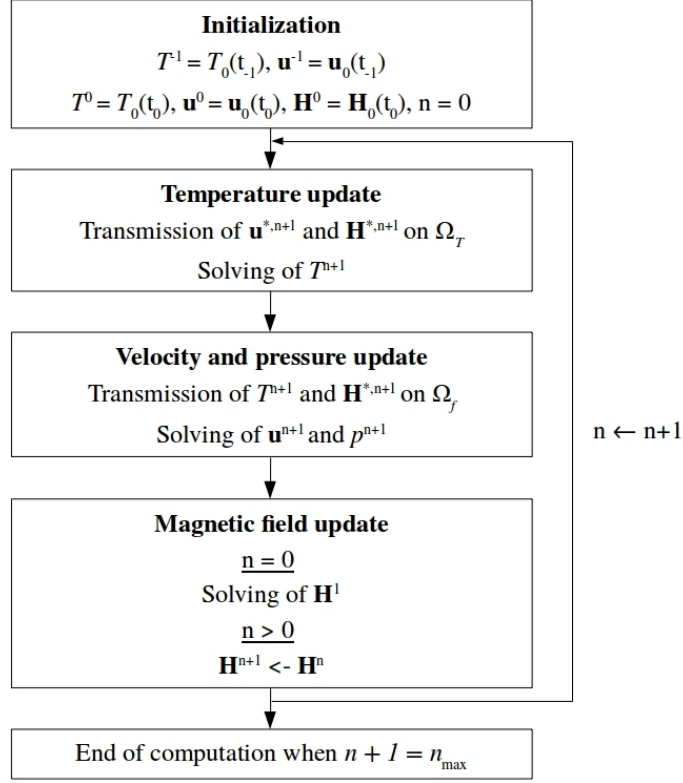


Figure 3.3: Time-marching algorithm of SFEMaNS code for the applications of ferrohydrodynamics.

Temperature scheme

The space and time approximation of the heat equation by the finite element method is treated in [100, pp. 279-300] for instance. The treatment of the boundary conditions follows the associated weak formulations for scalar elliptic PDEs, see [100, pp. 112-115] for details. The approximating sequence $\{T_h^n\}_{n \in \{0, \dots, n_{\max}\}}$ is constructed as follows:

1. Initialization: $T_h^{-1} = T_0(t_{-1})$, $T_h^0 = T_0(t_0)$
2. Computation of T_h^{n+1} , $\forall n \in \{0, \dots, n_{\max} - 1\}$, by solving:
Seek $T_h^{n+1} \in S_h$, such that $T_h^{n+1} = T_d(t_{n+1})$ on $\partial\Omega_{T,d}$ and

$$\begin{aligned}
 & \int_{\Omega_T} \rho c \frac{3T_h^{n+1}}{2\tau} s_h dV + \int_{\Omega_T} \lambda \nabla T_h^{n+1} \cdot \nabla s_h dV + \int_{\partial\Omega_{T,r}} h_c T_h^{n+1} s_h dS = \\
 & \int_{\Omega_T} \left(\rho c \frac{4T_h^n - T_h^{n-1}}{2\tau} - \rho c \nabla \cdot (T_h^{*,n+1} \tilde{\mathbf{u}}_h^{*,n+1}) + f_T(x, t^{n+1}) \right) s_h dV \\
 & - \int_{\Omega_f} \mu_0 T_h^{*,n+1} \frac{\partial \chi}{\partial T}(T_h^{*,n+1}) \left(\mathbf{H}_h^{*,n+1} \cdot \frac{\mathbf{H}_h^n - \mathbf{H}_h^{n-1}}{\tau} + \frac{1}{2} \mathbf{u}_h^{*,n+1} \cdot \nabla ((H_h^{*,n+1})^2) \right) s_h dV \\
 & + \int_{\partial\Omega_{T,r}} h_c T_r s_h dS, \forall s_h \in S_h^0.
 \end{aligned} \tag{3.31}$$

Notice that the nonlinear term $\rho c \tilde{\mathbf{u}} \cdot \nabla T$ in (3.7) is implemented in the form $\nabla \cdot (T \tilde{\mathbf{u}})$ in the scheme. These forms are equivalent due to the equality

$$\nabla \cdot (T \tilde{\mathbf{u}}) = \tilde{\mathbf{u}} \cdot \nabla T + T \nabla \cdot \tilde{\mathbf{u}}$$

and the fact that $\nabla \cdot \tilde{\mathbf{u}} = 0$. Notice that the partial derivative of $(H_h)^2/2$ in the pyromagnetic coefficient term is approximated by the first-order formula

$$\partial_t \left(\frac{(H_h)^2}{2} \right) (t_{n+1}) = \mathbf{H}_h^{*,n+1} \cdot \frac{\mathbf{H}_h^n - \mathbf{H}_h^{n-1}}{\tau} + O(\tau). \quad (3.32)$$

See Appendix B for the derivation of this extrapolation. When this term is active, i.e., when the current is alternating, the time-convergence of the solver is first-order. The approximate time derivative $(\mathbf{H}_h^n - \mathbf{H}_h^{n-1})/\tau$ is projected on Ω_T like $\mathbf{H}^{*,n+1}$ and $\mathbf{u}^{*,n+1}$.

The terms implemented in (3.31) during the thesis are:

- the terms for the Robin boundary conditions on the left-hand side and the right-hand side;
- the term for the magnetic work on the right-hand side.

Velocity and pressure scheme

The nonlinear terms being treated as source terms, the equations of fluid dynamics can be solved as the Stokes equations. The space and time approximation of the Stokes equations by the finite element method is treated in [100, pp. 300-312] for instance. The time approximation follows the rotational form of a projection method, with elimination of the projected velocity. Details on these methods can be found in [100, pp. 306-312] or [101, 102]. The approximating sequence $\{(\mathbf{u}_h^n, p_h^n)\}_{n \in \{0, \dots, n_{\max}\}}$ is constructed as follows:

1. Initialization: $\mathbf{u}_h^{-1} = \mathbf{u}_0(t_{-1})$, $\mathbf{u}_h^0 = \mathbf{u}_0(t_0)$, $p_h^0 = p_0(t_0)$
2. Computation of \mathbf{u}_h^{n+1} and p_h^{n+1} , $\forall n \in \{0, \dots, n_{\max} - 1\}$, by solving:

- (a) Seek $\mathbf{u}_h^{n+1} \in \mathbf{V}_h$ such that $\mathbf{u}_h^{n+1} = \mathbf{u}_d$ on $\partial\Omega_f$ and

$$\begin{aligned} & \int_{\Omega_f} \frac{3\mathbf{u}_h^{n+1}}{2\tau} \cdot \mathbf{v}_h dV + \int_{\Omega_f} 2\bar{\nu}_f \nabla^s \mathbf{u}_h^{n+1} : \nabla \mathbf{v}_h dV + \int_{\Omega_f} c_{\text{div}} \bar{\nu}_f \nabla \cdot \mathbf{u}_h^{n+1} \nabla \cdot \mathbf{v}_h dV = \\ & \int_{\Omega_f} \left(\frac{4\mathbf{u}_h^n - \mathbf{u}_h^{n-1}}{2\tau} - (\nabla \times \mathbf{u}_h^{*,n+1}) \times \mathbf{u}_h^{*,n+1} + \frac{\mathbf{f}(t_{n+1})}{\rho_f} \right) \cdot \mathbf{v}_h dV \\ & - \int_{\Omega_f} \nabla \left(\frac{p^n}{\rho_f} + \frac{4\psi^n - \psi^{n-1}}{3} \right) \cdot \mathbf{v}_h dV - \int_{\Omega_f} 2\tilde{\nu}_f(T^{n+1}) \nabla^s \mathbf{u}_h^{*,n+1} : \nabla \mathbf{v}_h dV \\ & + \int_{\Omega_f} \left(\alpha_f(T_h^{n+1} - T_*) g \mathbf{e}_z + \frac{\mu_0}{\rho_f} \chi(T^{n+1}) \frac{1}{2} \nabla \cdot ((H^{*,n+1})^2) \right) \cdot \mathbf{v}_h dV, \forall \mathbf{v}_h \in \mathbf{V}_h^0. \end{aligned} \quad (3.33)$$

- (b) Seek $\psi_h^{n+1} \in M_h$ such that

$$\int_{\Omega_f} \nabla \psi_h^{n+1} \cdot \nabla q_h dV = \frac{3}{2\tau} \int_{\Omega_f} \mathbf{u}_h^{n+1} \cdot \nabla q_h dV, \forall q_h \in M_h. \quad (3.34)$$

- (c) Seek $\delta_h^{n+1} \in M_h$ such that

$$\int_{\Omega_f} q_h \delta_h^{n+1} dV = \int_{\Omega_f} q_h \nabla \cdot \mathbf{u}_h^{n+1} dV, \forall q_h \in M_h. \quad (3.35)$$

(d) Update p_h^{n+1} by

$$\frac{p_h^{n+1}}{\rho_f} = \frac{p_h^n}{\rho_f} + \psi_h^{n+1} - 2\bar{\nu}\delta_h^{n+1} - c_{\text{div}}\bar{\nu}\delta_h^{n+1}, \quad (3.36)$$

$$\frac{p_h^{n+1}}{\rho_f} \leftarrow \frac{p_h^{n+1}}{\rho_f} - \frac{1}{V_f} \int_{\Omega_f} \frac{p_h^{n+1}}{\rho_f} dV, \quad (3.37)$$

where V_f is the volume of Ω_f .

The variables $\bar{\nu}$ and $\tilde{\nu}$ are defined as the maximum kinematic viscosity over the whole temperature range

$$\bar{\nu} = \max_{T \in [T_{\min}, T_{\max}]} \{\nu(T)\} \quad (3.38)$$

and the variable part of the kinematic viscosity

$$\tilde{\nu}(T) = \nu(T) - \bar{\nu}. \quad (3.39)$$

The parameter c_{div} is defined by the user to control the divergence. ψ_h is the scalar field involved in the Helmholtz decomposition of the velocity. δ_h is the approximation of the divergence of the velocity. We refer to [96] for more details on this algorithm.

The terms implemented in (3.33) during the thesis are:

- the term for the temperature-dependent viscosity on the right-hand side;
- the term for the Kelvin body force on the right-hand side;
- the term for the Helmholtz body force

$$- \int_{\Omega_f} \frac{\mu_0}{2\rho_0} (H^{*,n+1})^2 \nabla \chi(T^{n+1}) \cdot \mathbf{v}_h dV$$

that replaces the term for the Kelvin body force on the right-hand side, if needed.

Magnetic field scheme

The magnetic field scheme has not been modified to study ferrohydrodynamics during the thesis. The space and time approximations of the Maxwell equations in SFEMaNS are discussed in [103, 104, 99].

3.3 Validation

In this section, we present the convergence tests done to validate the developments in the code. In the tests, the equations are solved in the nondimensionalized form. Owing to the degree of polynomial approximation in the finite element spaces, the code is third-order in space for the temperature, the velocity and the magnetic field, and second-order in space for the pressure, with the L^2 - or \mathbf{L}^2 -norm². Owing to the time approximations, the code is second-order in time for all fields, with the L^2 - or \mathbf{L}^2 -norm. The L^2 -norm of a scalar field a defined in Ω is

$$\|a\|_{L^2(\Omega)} = \left(\int_{\Omega} a^2 dV \right)^{\frac{1}{2}}. \quad (3.40)$$

The \mathbf{L}^2 -norm of a vector field \mathbf{a} defined in Ω is

$$\|\mathbf{a}\|_{\mathbf{L}^2(\Omega)} = \left(\int_{\Omega} \mathbf{a} \cdot \mathbf{a} dV \right)^{\frac{1}{2}}. \quad (3.41)$$

We refer to [100, pp. 477-479] for details on Lebesgue spaces and associated norms.

²We define $\mathbf{L}^2(\Omega) = L^2(\Omega)^3$.

3.3.1 Nondimensionalized equations

The nondimensionalization does not depend on the system of coordinates. The Cartesian coordinates are used for simplicity.

Dimensionless spaces and fields

We give ourselves the following reference scales:

- L_{ref} for the size of the system and τ_{ref} for the evolution time;
- $T_{\text{ref}}, U_{\text{ref}}, P_{\text{ref}}$ and H_{ref} for the temperature, the velocity, the pressure and the magnetic field;
- $f_{T,\text{ref}}, f_{\text{ref}}$ and J_{ref} for the heat source, the body force and the current density;
- $\rho_{\text{ref}}, c_{\text{ref}}$ and λ_{ref} for the density, the heat capacity and the thermal conductivity;
- $h_{c,\text{ref}}$ for the heat transfer coefficient.

The reference magnetic permeability is the magnetic permeability of vacuum μ_0 .

The dimensionless coordinates in space and time are defined by

$$\hat{x} = \frac{x}{L_{\text{ref}}}, \hat{y} = \frac{y}{L_{\text{ref}}}, \hat{z} = \frac{z}{L_{\text{ref}}}, \hat{t} = \frac{t}{\tau_{\text{ref}}}. \quad (3.42)$$

The dimensionless computational domain $\hat{\Omega}$ and its boundary $\partial\hat{\Omega}$ are defined by

$$\begin{aligned} \hat{\Omega} &= \left\{ (\hat{x}, \hat{y}, \hat{z}) \in \mathbb{R}^3; (L_{\text{ref}}\hat{x}, L_{\text{ref}}\hat{y}, L_{\text{ref}}\hat{z}) \in \Omega \right\}, \\ \partial\hat{\Omega} &= \left\{ (\hat{x}, \hat{y}, \hat{z}) \in \mathbb{R}^3; (L_{\text{ref}}\hat{x}, L_{\text{ref}}\hat{y}, L_{\text{ref}}\hat{z}) \in \partial\Omega \right\}. \end{aligned} \quad (3.43)$$

The dimensionless spaces corresponding to all the subdomains and their boundaries are defined similarly. Let ϕ be the function connecting the physical coordinates and the dimensionless coordinates:

$$\begin{aligned} \phi: \quad \Omega \times \mathbb{R}_+ &\rightarrow \hat{\Omega} \times \mathbb{R}_+ \\ (x, y, z, t) &\mapsto (\hat{x}, \hat{y}, \hat{z}, \hat{t}). \end{aligned} \quad (3.44)$$

The dimensionless unknown fields live in the dimensionless space and time domain. They are defined by

$$\begin{aligned} T(x, y, z, t) &= T_{\text{ref}}\hat{T} \circ \phi(x, y, z, t) = T_{\text{ref}}\hat{T}(\hat{x}, \hat{y}, \hat{z}, \hat{t}), \\ \mathbf{u}(x, y, z, t) &= U_{\text{ref}}\hat{\mathbf{u}} \circ \phi(x, y, z, t) = U_{\text{ref}}\hat{\mathbf{u}}(\hat{x}, \hat{y}, \hat{z}, \hat{t}), \\ p(x, y, z, t) &= P_{\text{ref}}\hat{p} \circ \phi(x, y, z, t) = P_{\text{ref}}\hat{p}(\hat{x}, \hat{y}, \hat{z}, \hat{t}), \\ \mathbf{H}(x, y, z, t) &= H_{\text{ref}}\hat{\mathbf{H}} \circ \phi(x, y, z, t) = H_{\text{ref}}\hat{\mathbf{H}}(\hat{x}, \hat{y}, \hat{z}, \hat{t}). \end{aligned} \quad (3.45)$$

Note that the partial derivatives of the fields and the partial derivatives of the dimensionless fields are related by (example of the temperature):

$$\begin{aligned} \partial_x T(x, y, z, t) &= T_{\text{ref}}\partial_x \phi(x, y, z, t)\partial_{\hat{x}}\hat{T} \circ \phi(x, y, z, t) = \frac{T_{\text{ref}}}{L_{\text{ref}}}\partial_{\hat{x}}\hat{T}(\hat{x}, \hat{y}, \hat{z}, \hat{t}), \\ \partial_y T(x, y, z, t) &= T_{\text{ref}}\partial_y \phi(x, y, z, t)\partial_{\hat{y}}\hat{T} \circ \phi(x, y, z, t) = \frac{T_{\text{ref}}}{L_{\text{ref}}}\partial_{\hat{y}}\hat{T}(\hat{x}, \hat{y}, \hat{z}, \hat{t}), \\ \partial_z T(x, y, z, t) &= T_{\text{ref}}\partial_z \phi(x, y, z, t)\partial_{\hat{z}}\hat{T} \circ \phi(x, y, z, t) = \frac{T_{\text{ref}}}{L_{\text{ref}}}\partial_{\hat{z}}\hat{T}(\hat{x}, \hat{y}, \hat{z}, \hat{t}), \\ \partial_t T(x, y, z, t) &= T_{\text{ref}}\partial_t \phi(x, y, z, t)\partial_{\hat{t}}\hat{T} \circ \phi(x, y, z, t) = \frac{T_{\text{ref}}}{\tau_{\text{ref}}}\partial_{\hat{t}}\hat{T}(\hat{x}, \hat{y}, \hat{z}, \hat{t}). \end{aligned} \quad (3.46)$$

The dimensionless fields of the sources are defined by

$$\begin{aligned}\mathbf{f}(x, y, z, t) &= f_{\text{ref}}\hat{\mathbf{f}} \circ \phi(x, y, z, t) = f_{\text{ref}}\hat{\mathbf{f}}(\hat{x}, \hat{y}, \hat{z}, \hat{t}), \\ f_T(x, y, z, t) &= f_{T,\text{ref}}\hat{f}_T \circ \phi(x, y, z, t) = f_{T,\text{ref}}\hat{f}_T(\hat{x}, \hat{y}, \hat{z}, \hat{t}), \\ \mathbf{j}(x, y, z, t) &= J_{\text{ref}}\hat{\mathbf{j}} \circ \phi(x, y, z, t) = J_{\text{ref}}\hat{\mathbf{j}}(\hat{x}, \hat{y}, \hat{z}, \hat{t}).\end{aligned}\quad (3.47)$$

The dimensionless thermophysical and magnetic properties are defined by

$$\hat{\rho} = \frac{\rho}{\rho_{\text{ref}}}, \hat{c} = \frac{c}{c_{\text{ref}}}, \hat{\lambda} = \frac{\lambda}{\lambda_{\text{ref}}}, \hat{\mu} = \frac{\mu}{\mu_0}.\quad (3.48)$$

The dimensionless heat transfer coefficient is defined by

$$\hat{h}_c = \frac{h_c}{h_{c,\text{ref}}}.\quad (3.49)$$

The various other fields or constants (boundary conditions, initial conditions, etc.) are nondimensionalized following the same method.

In the following, only the dimensionless quantities are presented. We remove the hat from the symbols for simplicity.

Temperature equations

We replace the physical fields and properties in the temperature equation of ferrofluids in (3.7) by the dimensionless quantities. We obtain

$$\begin{aligned}\frac{\rho_{\text{ref}}c_{\text{ref}}T_{\text{ref}}}{\tau_{\text{ref}}}\rho c\partial_t T + \frac{\rho_{\text{ref}}c_{\text{ref}}U_{\text{ref}}T_{\text{ref}}}{L_{\text{ref}}}\rho c\tilde{\mathbf{u}} \cdot \nabla T - \frac{\lambda_{\text{ref}}T_{\text{ref}}}{(L_{\text{ref}})^2}\nabla \cdot (\lambda \nabla T) \\ + \frac{\mu_0 T_{\text{ref}}(H_{\text{ref}})^2}{T_{\text{ref}}\tau_{\text{ref}}}T \frac{\partial \chi}{\partial T}(T) \left(\partial_t \left(\frac{H^2}{2} \right) + \mathbf{u} \cdot \nabla \left(\frac{H^2}{2} \right) \right) = f_{T,\text{ref}}f_T.\end{aligned}$$

We divide the equation by $\rho_{\text{ref}}c_{\text{ref}}T_{\text{ref}}/\tau_{\text{ref}}$. We have then

$$\begin{aligned}\rho c\partial_t T + \frac{\tau_{\text{ref}}U_{\text{ref}}}{L_{\text{ref}}}\rho c\tilde{\mathbf{u}} \cdot \nabla T - \frac{\tau_{\text{ref}}\lambda_{\text{ref}}}{\rho_{\text{ref}}c_{\text{ref}}(L_{\text{ref}})^2}\nabla \cdot (\lambda \nabla T) \\ + \frac{\mu_0(H_{\text{ref}})^2}{\rho_{\text{ref}}c_{\text{ref}}T_{\text{ref}}}T \frac{\partial \chi}{\partial T}(T) \left(\partial_t \left(\frac{H^2}{2} \right) + \mathbf{u} \cdot \nabla \left(\frac{H^2}{2} \right) \right) = \frac{\tau_{\text{ref}}f_{T,\text{ref}}}{\rho_{\text{ref}}c_{\text{ref}}T_{\text{ref}}}f_T.\end{aligned}$$

We choose

$$\tau_{\text{ref}} = \frac{L_{\text{ref}}}{U_{\text{ref}}}, \lambda_{\text{ref}} = \frac{\rho_{\text{ref}}c_{\text{ref}}(L_{\text{ref}})^2}{\tau_{\text{ref}}}, f_{T,\text{ref}} = \frac{\rho_{\text{ref}}c_{\text{ref}}T_{\text{ref}}}{\tau_{\text{ref}}}.\quad (3.50)$$

We replace the physical quantities in the Robin boundary condition in (3.7) by the dimensionless quantities. We obtain

$$-\frac{\lambda_{\text{ref}}}{L_{\text{ref}}}\lambda \nabla T = h_{c,\text{ref}}T_{\text{ref}}h_c(T - T_r).$$

We choose

$$h_{c,\text{ref}} = \frac{\lambda_{\text{ref}}}{L_{\text{ref}}}.\quad (3.51)$$

The nondimensionalization of the other equations of (3.7) is obvious. The nondimensionalized equations of the temperature are

$$\left\{ \begin{array}{ll} \rho c \partial_t T + \rho c \tilde{\mathbf{u}} \cdot \nabla T - \nabla \cdot (\lambda \nabla T) \\ + C_p T \frac{\partial \chi}{\partial T}(T) \left(\partial_t \left(\frac{H^2}{2} \right) + \mathbf{u} \cdot \nabla \left(\frac{H^2}{2} \right) \right) = f_T & \text{in } \Omega_f \times \mathbb{R}_+^* \\ \rho c \partial_t T + \rho c \tilde{\mathbf{u}} \cdot \nabla T - \nabla \cdot (\lambda \nabla T) = f_T & \text{in } (\Omega_T \setminus \Omega_f) \times \mathbb{R}_+^* \\ T = T_d & \text{on } \partial\Omega_{T,d} \times \mathbb{R}_+^*, \\ \partial_{\mathbf{n}} T = 0 & \text{on } \partial\Omega_{T,n} \times \mathbb{R}_+^*, \\ -\lambda \nabla T \cdot \mathbf{n} = h_c(T - T_r) & \text{on } \partial\Omega_{T,r} \times \mathbb{R}_+^*, \\ T|_{t=0} = T_0 & \text{in } \Omega_T, \end{array} \right. \quad (3.52)$$

where

$$C_p = \frac{\mu_0(H_{\text{ref}})^2}{\rho_{\text{ref}} c_{\text{ref}} T_{\text{ref}}}. \quad (3.53)$$

Equations of fluid dynamics

We replace the physical fields in the momentum equation of ferrofluids in (3.8) by the dimensionless quantities. We obtain

$$\frac{U_{\text{ref}}}{\tau_{\text{ref}}} \partial_t \mathbf{u} + \frac{(U_{\text{ref}})^2}{L_{\text{ref}}} (\nabla \times \mathbf{u}) \times \mathbf{u} + \frac{P_{\text{ref}}}{\rho_f L_{\text{ref}}} \nabla p - \nabla \cdot \left(2 \frac{U_{\text{ref}} \nu_f(T)}{(L_{\text{ref}})^2} \nabla^s \mathbf{u} \right) = \\ \alpha_f g T_{\text{ref}} (T - T_*) \mathbf{e}_z + \frac{\mu_0 (H_{\text{ref}})^2}{\rho_f L_{\text{ref}}} \chi(T) \nabla \left(\frac{H^2}{2} \right) + \frac{f_{\text{ref}}}{\rho_f} \mathbf{f}.$$

We divide the equation by $U_{\text{ref}}/\tau_{\text{ref}}$. We obtain

$$\partial_t \mathbf{u} + \frac{\tau_{\text{ref}} U_{\text{ref}}}{L_{\text{ref}}} (\nabla \times \mathbf{u}) \times \mathbf{u} + \frac{\tau_{\text{ref}} P_{\text{ref}}}{\rho_f U_{\text{ref}} L_{\text{ref}}} \nabla p - \nabla \cdot \left(2 \frac{\tau_{\text{ref}} \nu_f(T)}{(L_{\text{ref}})^2} \nabla^s \mathbf{u} \right) = \\ \frac{\alpha_f g \tau_{\text{ref}} T_{\text{ref}}}{U_{\text{ref}}} (T - T_*) \mathbf{e}_z + \frac{\mu_0 \tau_{\text{ref}} (H_{\text{ref}})^2}{\rho_f U_{\text{ref}} L_{\text{ref}}} \chi(T) \nabla \left(\frac{H^2}{2} \right) + \frac{\tau_{\text{ref}} f_{\text{ref}}}{\rho_f U_{\text{ref}}} \mathbf{f}.$$

Owing to the relations between the reference scales, this equation can be written

$$\partial_t \mathbf{u} + (\nabla \times \mathbf{u}) \times \mathbf{u} + \frac{P_{\text{ref}}}{\rho_f (U_{\text{ref}})^2} \nabla p - \nabla \cdot \left(2 \frac{\nu_f(T)}{U_{\text{ref}} L_{\text{ref}}} \nabla^s \mathbf{u} \right) = \\ \frac{\alpha_f g \tau_{\text{ref}} T_{\text{ref}}}{U_{\text{ref}}} (T - T_*) \mathbf{e}_z + \frac{\mu_0 (H_{\text{ref}})^2}{\rho_f (U_{\text{ref}})^2} \chi(T) \nabla \left(\frac{H^2}{2} \right) + \frac{\tau_{\text{ref}} f_{\text{ref}}}{\rho_f U_{\text{ref}}} \mathbf{f}.$$

We choose

$$P_{\text{ref}} = \rho_f (U_{\text{ref}})^2, \quad f_{\text{ref}} = \frac{\rho_f U_{\text{ref}}}{\tau_{\text{ref}}}. \quad (3.54)$$

The nondimensionalization of the other equations of (3.8) is obvious. The nondimensionalized equations of fluid dynamics are

$$\left\{ \begin{array}{ll} \partial_t \mathbf{u} + (\nabla \times \mathbf{u}) \times \mathbf{u} + \nabla p \\ - \nabla \cdot \left(\frac{2}{R_e(T)} \nabla^s \mathbf{u} \right) = C_g (T - T_*) \mathbf{e}_z + C_m \chi(T) \nabla \left(\frac{H^2}{2} \right) + \mathbf{f} & \text{in } \Omega_f \times \mathbb{R}_+^*, \\ \nabla \cdot \mathbf{u} = 0 & \text{in } \Omega_f \times \mathbb{R}_+^*, \\ \mathbf{u} = \mathbf{u}_d & \text{on } \partial\Omega_f \times \mathbb{R}_+^*, \\ \mathbf{u}|_{t=0} = \mathbf{u}_0 & \text{in } \Omega_f, \end{array} \right. \quad (3.55)$$

where

$$Re(T) = \frac{U_{\text{ref}} L_{\text{ref}}}{\nu_f(T)}, C_g = \frac{\alpha_f g \tau_{\text{ref}} T_{\text{ref}}}{U_{\text{ref}}}, C_m = \frac{\mu_0 (H_{\text{ref}})^2}{\rho_f (U_{\text{ref}})^2}. \quad (3.56)$$

Note that the Reynolds number is temperature-dependent because the viscosity can be temperature-dependent. If the Helmholtz body force is used, the magnetic body force in (3.55) must be replaced by

$$-C_m \frac{H^2}{2} \nabla \chi(T).$$

Magnetic field equations

We replace the physical fields in the Maxwell-Ampère equation in (3.13) by the dimensionless quantities. We obtain

$$\frac{H_{\text{ref}}}{L_{\text{ref}}} \nabla \times \mathbf{H} = J_{\text{ref}} \mathbf{j}.$$

We choose

$$J_{\text{ref}} = \frac{H_{\text{ref}}}{L_{\text{ref}}}. \quad (3.57)$$

The nondimensionalization of the other equations of (3.13) is obvious. The nondimensionalized magnetic field equations are

$$\begin{cases} \nabla \times \mathbf{H} = \mathbf{j} & \text{in } \Omega \times \mathbb{R}_+^*, \\ \nabla \cdot (\mu \mathbf{H}) = 0 & \text{in } \Omega \times \mathbb{R}_+^*, \\ \mathbf{H} \times \mathbf{n} = \mathbf{H}_d \times \mathbf{n} & \text{on } \partial\Omega_d \times \mathbb{R}_+^*, \\ \mu \mathbf{H} \cdot \mathbf{n} = \mu \mathbf{H}_n \cdot \mathbf{n} & \text{on } \partial\Omega_n \times \mathbb{R}_+^*. \end{cases} \quad (3.58)$$

3.3.2 Magnetostatics

These tests show that the code is able to solve a magnetostatic problem with a \mathbf{H} -formulation in the whole domain, including insulating regions.

Uniform magnetic permeability

The problem is solved in a cylinder of square meridian section

$$\Omega = \left\{ (r, \theta, z) \in \mathbb{R}^3; 0 \leq r < 1, 0 \leq \theta < 2\pi, 0 < z < 1 \right\}.$$

We solve the magnetic field equations (3.58) in Ω . A Dirichlet condition is imposed on the whole boundary: $\partial\Omega_d = \partial\Omega$ and $\partial\Omega_n = \emptyset$. The magnetic permeability is taken equal to 1 in the whole domain.

The solution is

$$\mathbf{H}(r, \theta, z) = r \sin(\pi r) \sin(\pi z) \mathbf{e}_r + \left(\frac{2}{\pi} \sin(\pi r) + r \cos(\pi r) \right) \cos(\pi z) \mathbf{e}_z \text{ in } \Omega. \quad (3.59)$$

The imposed current density is

$$\mathbf{j}(r, \theta, z) = (2\pi r \sin(\pi r) - 3 \cos(\pi r)) \cos(\pi z) \mathbf{e}_\theta \text{ in } \Omega. \quad (3.60)$$

\mathbf{H}_d is set to match the solution. Note that the case of a θ -dependent and time-dependent magnetic field is treated next.

The problem is approximated with

$$h \in \left\{ \frac{1}{2}, \frac{1}{4}, \frac{1}{8}, \frac{1}{16}, \frac{1}{32}, \frac{1}{64}, \frac{1}{128} \right\}.$$

The mesh of the meridian section with $h = 1/8$ is shown in Figure 3.4. The problem is solved on mode 0. Four processors are used in the meridian plane and one processor is used in the Fourier space.

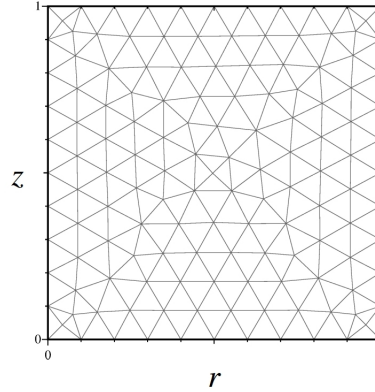


Figure 3.4: Mesh of the meridian section with $h = 1/8$.

The relative errors on \mathbf{H} and $\nabla \times \mathbf{H}$ in \mathbf{L}^2 -norm, respectively

$$\frac{\|\mathbf{H}_h - \mathbf{H}\|_{\mathbf{L}^2(\Omega)}}{\|\mathbf{H}\|_{\mathbf{L}^2(\Omega)}} \quad \text{and} \quad \frac{\|\nabla \times \mathbf{H}_h - \nabla \times \mathbf{H}\|_{\mathbf{L}^2(\Omega)}}{\|\nabla \times \mathbf{H}\|_{\mathbf{L}^2(\Omega)}}, \quad (3.61)$$

for the different mesh sizes are presented in Table 3.1. Say that the mesh sizes are denoted by $h_i, i \in \{1, \dots, i_{\max}\}$, where i_{\max} is the number of meshes, such that $h_1 > h_2 > \dots > h_{i_{\max}}$. The computed order of convergence (COC) for mesh size $i \geq 2$ is computed as follows:

$$\text{COC}_i = \frac{\ln(e_{i-1}/e_i)}{\ln(h_{i-1}/h_i)}, \quad (3.62)$$

where $e_i, i \in \{1, \dots, i_{\max}\}$ is the relative error obtained for mesh size i . The decrease of the relative error on the magnetic field when the mesh size is reduced is satisfying regarding the theoretical third-order convergence rate. The decrease of the relative error on the curl of the magnetic field when the mesh size is reduced follows the theoretical second-order convergence rate.

h	Rel. error	COC	Curl rel. error	COC
0.5	4.1600E-1	-	7.2231E-2	-
0.25	3.8498E-2	3.43	1.3566E-2	2.41
0.125	4.6177E-3	3.06	2.8863E-3	2.23
0.0625	5.7894E-4	3.00	6.6694E-4	2.11
0.03125	7.4904E-5	2.95	1.3658E-4	2.29
0.015625	1.0152E-5	2.88	2.8975E-5	2.24
0.0078125	1.4335E-6	2.82	6.1089E-6	2.25

Table 3.1: Relative errors on \mathbf{H} and $\nabla \times \mathbf{H}$ in \mathbf{L}^2 -norm, and associated computed order of convergence.

Non-uniform magnetic permeability (composite sphere)

The test is based on the following problem: a sphere composed of an inner sphere, with magnetic permeability μ_1 and radius r_1 , and an outer sphere, with magnetic permeability μ_2 and radius $r_2 > r_1$, is surrounded by vacuum of magnetic permeability μ_0 . A magnetic field is generated by some device far from the sphere. The magnetic field is assumed to be

uniform and one-directional, say along \mathbf{e}_z , when the sphere is absent. We want to know how the composite sphere changes the magnetic field of the device. Mathematically, the problem consists in seeking \mathbf{H} such that

$$\begin{cases} \nabla \times \mathbf{H} = 0, \\ \nabla \cdot (\mu \mathbf{H}) = 0, \\ \lim_{\|\mathbf{x}\| \rightarrow \infty} \mathbf{H}(\mathbf{x}) = H_0 \mathbf{e}_z, \end{cases} \quad (3.63)$$

where $H_0 \in \mathbb{R}$ is the amplitude of the exterior magnetic field. The analytical solution is presented in [99]. There exists a scalar potential ψ such that the magnetic field is in the form $\mathbf{H} = \nabla \psi$. Using the spherical coordinates $(\varrho, \varsigma, \theta)$, where ϱ is the distance to the center of the composite sphere, $\varsigma \in [0, \pi]$ is the colatitude and $\theta \in [0, 2\pi)$ is the azimuth, ψ is defined by

$$\psi(\varrho, \varsigma, \theta) = \begin{cases} -A\varrho \cos(\varsigma) & \text{if } 0 \leq \varrho \leq r_1, \\ -\left(B\varrho + C\frac{r_1^3}{\varrho^2}\right) \cos(\varsigma) & \text{if } r_1 \leq \varrho \leq r_2, \\ -\left(D\frac{r_1^3}{\varrho^2} - H_0\varrho\right) \cos(\varsigma) & \text{if } r_2 \leq \varrho, \end{cases} \quad (3.64)$$

where A, B, C and D are constants. Assuming that $\mu_1 = \mu_0$ and using the notation $\bar{\mu} = \mu_2/\mu_0$, these constants are defined by

$$\begin{aligned} A &= -\frac{9\bar{\mu}H_0}{(2\bar{\mu}+1)(\bar{\mu}+2) - 2(\bar{\mu}-1)^2 \left(\frac{r_1}{r_2}\right)^3}, \\ B &= \frac{1}{3} \left(2 + \frac{1}{\bar{\mu}}\right) A, \\ C &= \frac{1}{3} \left(1 - \frac{1}{\bar{\mu}}\right) A, \\ D &= \frac{(2\bar{\mu}+1)(\bar{\mu}-1) \left(\left(\frac{r_2}{r_1}\right)^3 - 1\right) H_0}{(2\bar{\mu}+1)(\bar{\mu}+2) - 2(\bar{\mu}-1)^2 \left(\frac{r_1}{r_2}\right)^3}. \end{aligned} \quad (3.65)$$

Using the cylindrical coordinates, ψ is defined by

$$\psi(r, \theta, z) = \begin{cases} -Az & \text{if } 0 \leq \sqrt{r^2 + z^2} \leq r_1, \\ -\left(B\sqrt{r^2 + z^2} + C\frac{r_1^3}{r^2 + z^2}\right) \frac{z}{\sqrt{r^2 + z^2}} & \text{if } r_1 \leq \sqrt{r^2 + z^2} \leq r_2, \\ -\left(D\frac{r_1^3}{r^2 + z^2} - H_0\sqrt{r^2 + z^2}\right) \frac{z}{\sqrt{r^2 + z^2}} & \text{if } r_2 \leq \sqrt{r^2 + z^2}. \end{cases} \quad (3.66)$$

The magnetic field is

$$\mathbf{H}(r, \theta, z) = \begin{cases} -A\mathbf{e}_z & \text{if } 0 < \sqrt{r^2 + z^2} < r_1, \\ \frac{3Cr_1^3rz}{(r^2 + z^2)^{\frac{5}{2}}}\mathbf{e}_r - \left(B + \frac{Cr_1^3(r^2 - 2z^2)}{(r^2 + z^2)^{\frac{5}{2}}}\right)\mathbf{e}_z & \text{if } r_1 < \sqrt{r^2 + z^2} < r_2, \\ \frac{3Dr_1^3rz}{(r^2 + z^2)^{\frac{5}{2}}}\mathbf{e}_r + \left(H_0 - \frac{Dr_1^3(r^2 - 2z^2)}{(r^2 + z^2)^{\frac{5}{2}}}\right)\mathbf{e}_z & \text{if } r_2 < \sqrt{r^2 + z^2}. \end{cases} \quad (3.67)$$

For the test, we set $r_1 = 0.5$ and $r_2 = 1$. The problem is solved in a cylindrical domain of rectangular meridian section

$$\Omega = \left\{ (r, \theta, z) \in \mathbb{R}^3; 0 \leq r < 2, 0 \leq \theta < 2\pi, -2 < z < 2 \right\}.$$

We define the inner sphere subdomain

$$\Omega_1 = \left\{ (r, \theta, z) \in \Omega; \sqrt{r^2 + z^2} < 0.5 \right\},$$

the outer sphere subdomain

$$\Omega_2 = \left\{ (r, \theta, z) \in \Omega; 0.5 < \sqrt{r^2 + z^2} < 1 \right\}$$

and the vacuum subdomain

$$\Omega_3 = \left\{ (r, \theta, z) \in \Omega; \sqrt{r^2 + z^2} > 1 \right\}.$$

We solve the magnetic field equations (3.58) in Ω . A Dirichlet condition is imposed on the whole boundary: $\partial\Omega_d = \partial\Omega$ and $\partial\Omega_n = \emptyset$. The interface between the subdomains of different magnetic permeabilities is $\Sigma_\mu = \partial\Omega_2$. We set $H_0 = 1$, $\mu_1 = \mu_0 = 1$ and $\mu_2 = 10$.

The solution is the magnetic field previously defined. The imposed current density is $\mathbf{j} = \mathbf{0}$. \mathbf{H}_d is set to match the solution.

The problem is approximated with

$$h \in \left\{ \frac{1}{10}, \frac{1}{20}, \frac{1}{40}, \frac{1}{80}, \frac{1}{160} \right\}.$$

The mesh of the meridian section with $h = 1/10$ is shown in Figure 3.5. The problem is solved on modes 0, 1, 2 and 3. We want to verify that modes ≥ 1 are equal to zero. Eight processors are used in the meridian plane and four processors are used in the Fourier space.

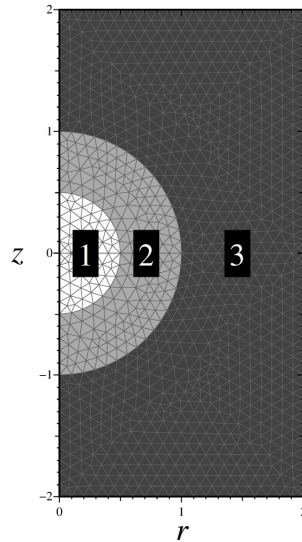


Figure 3.5: Mesh of the meridian section with $h = 1/10$. 1: inner sphere, 2: outer sphere, 3: vacuum.

The relative error on \mathbf{H} and the error on $\nabla \times \mathbf{H}$ in \mathbf{L}^2 -norm for the different mesh sizes are presented in Table 3.2. The error on $\nabla \times \mathbf{H}$ in \mathbf{L}^2 -norm is $\|\nabla \times \mathbf{H}_h - \nabla \times \mathbf{H}\|_{\mathbf{L}^2(\Omega)}$. The error instead of the relative error on the curl of the magnetic field is presented since

$\nabla \times \mathbf{H} = 0$. The decrease of the relative error on the magnetic field when the mesh size is reduced is satisfying regarding the theoretical third-order convergence rate. The decrease of the error on the curl of the magnetic field when the mesh size is reduced follows the theoretical second-order convergence rate. A similar test is reported in [99, Tab. 5].

h	Rel. error	COC	Curl error	COC
0.1	2.7077E-4	-	1.3507E-2	-
0.05	3.5930E-5	2.91	3.0051E-3	2.17
0.025	5.6888E-6	2.66	6.5850E-4	2.19
0.0125	8.8783E-7	2.68	1.5020E-4	2.13
0.00625	1.4181E-7	2.65	3.4021E-5	2.14

Table 3.2: Relative error on \mathbf{H} and error on $\nabla \times \mathbf{H}$ in \mathbf{L}^2 -norm, and associated computed order of convergence.

3.3.3 Temperature computation in solid regions

The problem is solved in a cylinder of square meridian section

$$\Omega = \{(r, \theta, z) \in \mathbb{R}^3; 0 \leq r < 1, 0 \leq \theta < 2\pi, 0 < z < 1\}.$$

The computational domain is composed of a solid region

$$\Omega_s = \{(r, \theta, z) \in \Omega; 0 \leq r < 0.5\}$$

and a fluid region

$$\Omega_f = \{(r, \theta, z) \in \Omega; 0.5 < r < 1\}.$$

We solve the temperature equations (3.52) in Ω and the equations of fluid dynamics (3.55) in Ω_f . The fluid is not a ferrofluid. The magnetic body force and the pyromagnetic coefficient term are absent from the momentum equation and the temperature equation, respectively ($C_p = C_m = 0$). We enforce only Dirichlet conditions on the temperature: $\partial\Omega_{T,d} = \partial\Omega_T$, $\partial\Omega_{T,n} = \partial\Omega_{T,r} = \emptyset$. The temperature of the Boussinesq approximation is not relevant: $T_* = 0$. The viscosity is constant. The values of the dimensionless coefficients are given in Table 3.3.

Coefficient	Domain	
	Solid	Fluid
ρc	1	2
λ	10	1
R_e	-	1
C_g	-	1

Table 3.3: Dimensionless coefficients.

The solution is

$$\begin{aligned}
 T(r, \theta, z, t) &= \frac{1}{\lambda} r^2 (r - r_0) \sin(z) (1 + \cos(\theta)) \cos(t) && \text{in } \Omega, \\
 u_r(r, \theta, z, t) &= -(r - r_0)^2 \cos(z) (1 + \cos(\theta)) \cos(t) && \text{in } \Omega_f, \\
 u_\theta(r, \theta, z, t) &= (r - r_0)^2 \cos(z) (1 + \cos(\theta)) \cos(t) && \text{in } \Omega_f, \\
 u_z(r, \theta, z, t) &= \frac{r - r_0}{r} \sin(z) (3r - r_0 + (3r - r_0) \cos(\theta) + (r - r_0) \sin(\theta)) \cos(t) && \text{in } \Omega_f, \\
 p(r, \theta, z, t) &= r^3 \sin(z) \cos(\theta) \cos(t) && \text{in } \Omega_f,
 \end{aligned} \tag{3.68}$$

where $r_0 = 0.5$ is the limit between the solid and fluid parts. Note that the heat flux is continuous at the interface solid / fluid. The velocity is defined by $\mathbf{u} = \nabla \times \mathbf{v}$, with

$$\mathbf{v}(r, \theta, z, t) = (r - r_0)^2 \cos(z)(1 + \cos(\theta)) \cos(t)(\mathbf{e}_r + \mathbf{e}_\theta) \text{ in } \Omega_f.$$

The continuity equation $\nabla \cdot \mathbf{u} = 0$ is thus satisfied. Note that the extension of the velocity $\tilde{\mathbf{u}}$ is zero in the solid and that it is consistent with the velocity solution at the interface. The source terms are defined by

$$\begin{aligned} f_T &= \rho c \partial_t T + \rho c \tilde{\mathbf{u}} \cdot \nabla T - \nabla \cdot (\lambda \nabla T) && \text{in } \Omega, \\ \mathbf{f} &= \partial_t \mathbf{u} + (\nabla \times \mathbf{u}) \times \mathbf{u} + \nabla p - \frac{1}{Re} \Delta \mathbf{u} - C_g T \mathbf{e}_z && \text{in } \Omega_f. \end{aligned} \quad (3.69)$$

The initial conditions, \mathbf{u}_0 and T_0 , and the boundary conditions, \mathbf{u}_d and T_d , are set to match the solution.

The problem is approximated with

$$h \in \left\{ \frac{1}{10}, \frac{1}{20}, \frac{1}{40}, \frac{1}{80}, \frac{1}{160} \right\}, \quad \tau \in \left\{ \frac{1}{50}, \frac{1}{100}, \frac{1}{200}, \frac{1}{400}, \frac{1}{800} \right\}.$$

The mesh of the meridian section with $h = 1/10$ is shown in Figure 3.6. The problem is solved on modes 0, 1 and 2 due to the nonlinear terms in the source terms. Two processors are used in the meridian plane and three processors are used in the Fourier space.

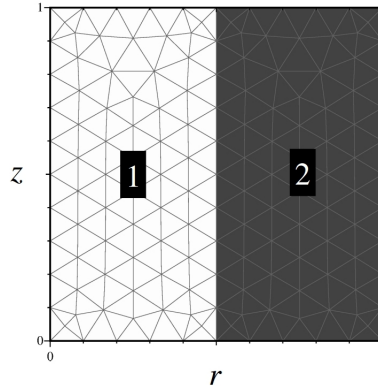


Figure 3.6: Mesh of the meridian section with $h = 1/10$. 1: solid, 2: fluid.

We study the relative errors on the temperature, the velocity and the pressure in L^2 -norm or \mathbf{L}^2 -norm, defined by

$$\frac{\|T_h - T\|_{L^2(\Omega)}}{\|T\|_{L^2(\Omega)}}, \quad \frac{\|\mathbf{u}_h - \mathbf{u}\|_{\mathbf{L}^2(\Omega_f)}}{\|\mathbf{u}\|_{\mathbf{L}^2(\Omega_f)}} \quad \text{and} \quad \frac{\|p_h - p\|_{L^2(\Omega_f)}}{\|p\|_{L^2(\Omega_f)}}, \quad (3.70)$$

respectively. The evolution with the mesh size of these relative errors, at a given time and for a fixed time step, is presented in Figure 3.7. The time step is sufficiently small for the time discretization error to be negligible. The decrease of the relative error on the temperature follows the theoretical third-order convergence rate. Same comment for the velocity. The decrease of the relative error on the pressure follows the theoretical second-order convergence rate.

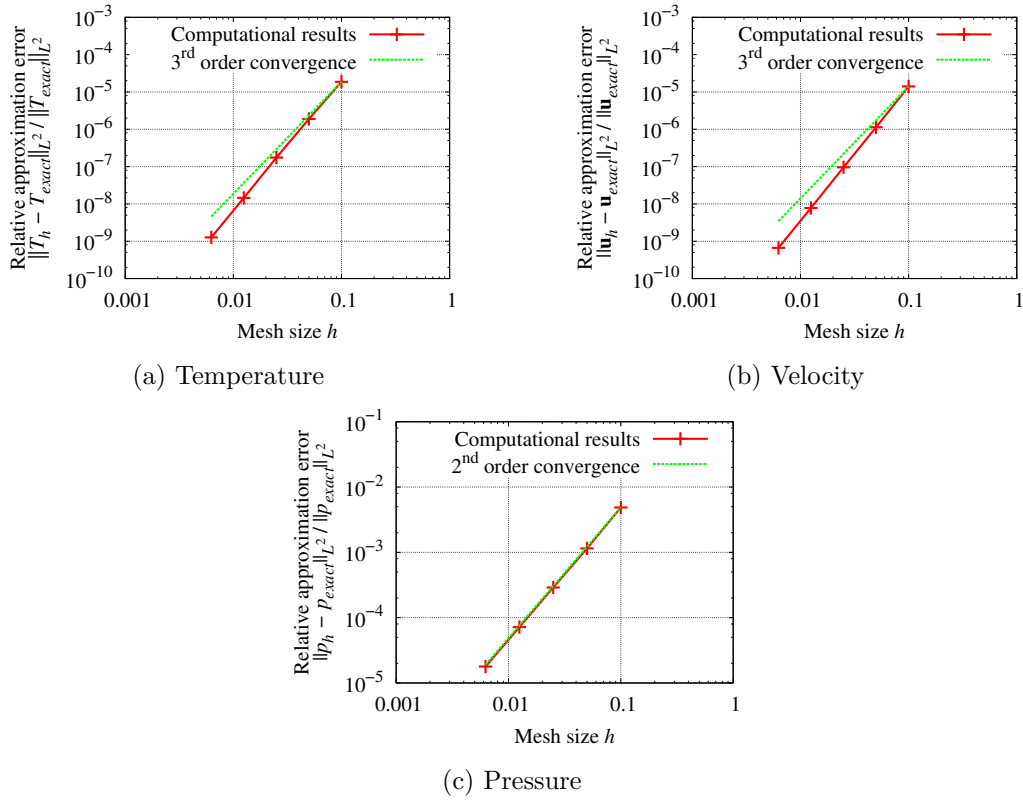


Figure 3.7: Relative error in L^2 -norm or \mathbf{L}^2 -norm at $t = 0.01$ with respect to mesh size, and for a fixed time step $\tau = 10^{-4}$; comparison with the theoretical convergence.

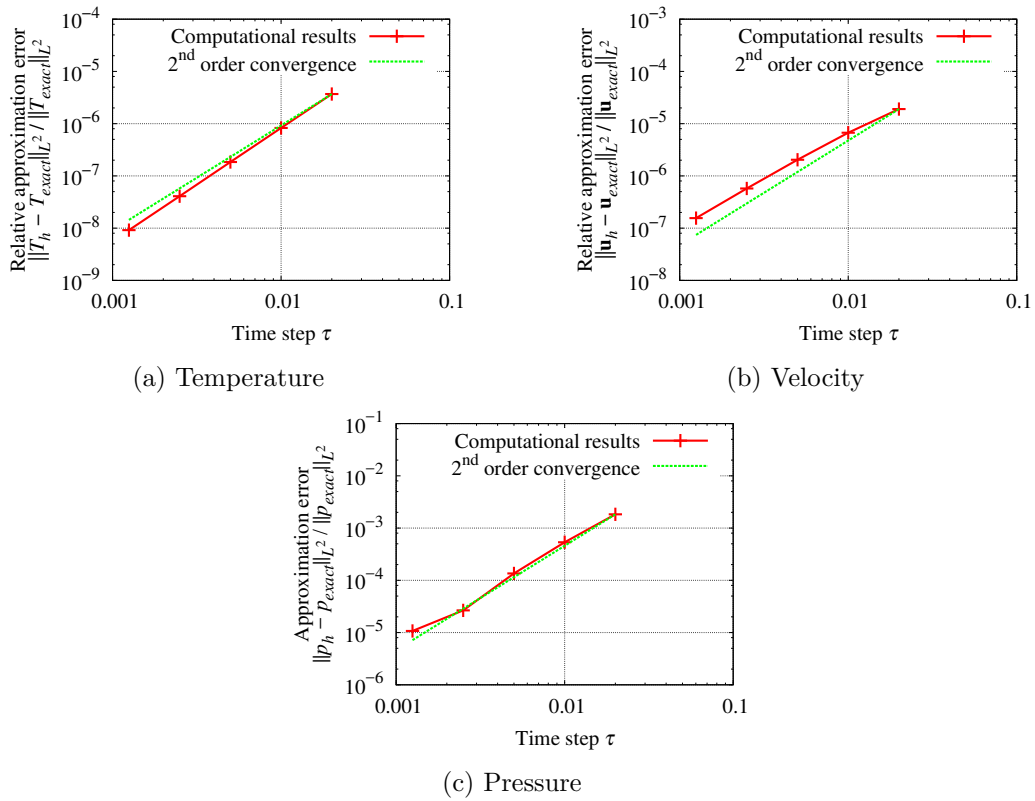


Figure 3.8: Relative error in L^2 -norm or \mathbf{L}^2 -norm at $t = 0.1$ with respect to time step, on the mesh $h = 1/160$; comparison with the theoretical convergence.

The evolution with the time step of the relative errors on T , \mathbf{u} and p in L^2 -norm or \mathbf{L}^2 -norm, at a given time and for a fixed mesh size, is presented in Figure 3.8. The mesh size is sufficiently small for the space discretization error to be negligible. The decrease of the relative error on all fields follows the theoretical second-order convergence rate.

The evolution with the mesh size at fixed C_{CFL} of the relative errors on T , \mathbf{u} and p in L^2 -norm or \mathbf{L}^2 -norm, at a given time, is presented in Figure 3.8. C_{CFL} is the constant of Courant–Friedrichs–Lewy (CFL) condition, defined for a given mesh size h and a given time step τ by

$$C_{\text{CFL}} = \frac{u_{\max}\tau}{h}, \quad (3.71)$$

where u_{\max} is the maximum velocity amplitude. The decrease of the relative error on the velocity is between the second-order (time step) and third-order (mesh size) convergence rates. The decrease of the relative error on the temperature follows the third-order (mesh size) convergence rate because the error is apparently mesh-dominated. The decrease of the relative error on the pressure follows the theoretical second-order convergence rate (time step and mesh size).

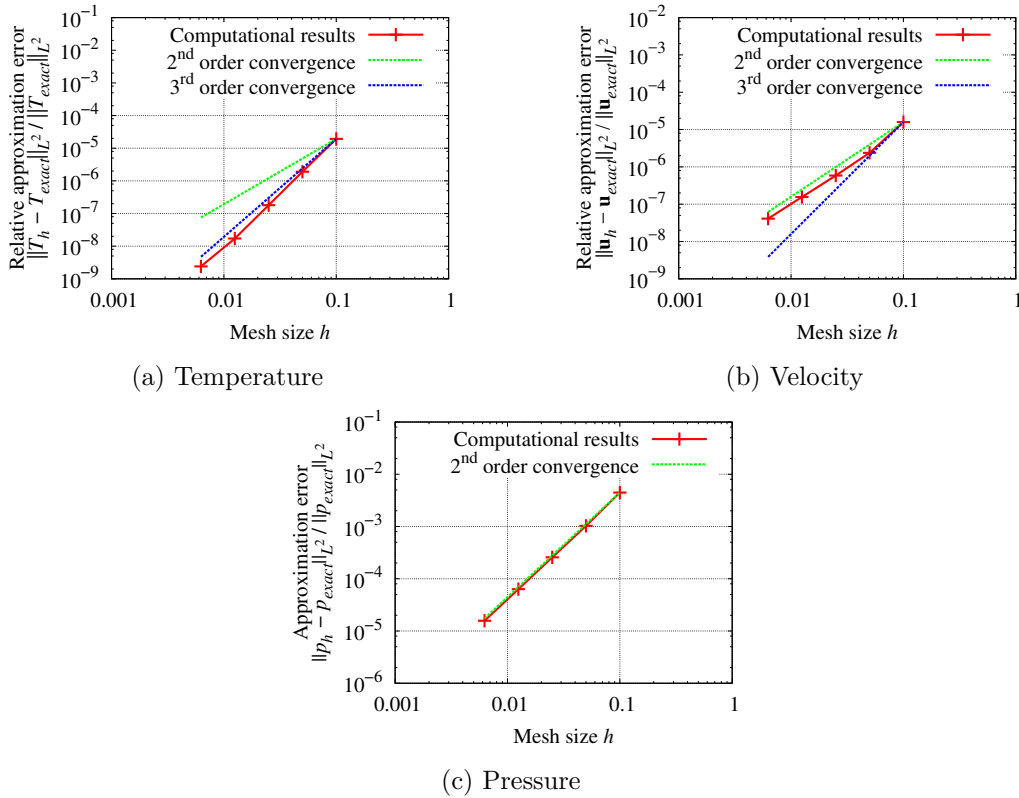


Figure 3.9: Relative error in L^2 -norm or \mathbf{L}^2 -norm at $t = 0.1$ with respect to mesh size, for a constant ratio $\tau/h = 0.1$; comparison with the theoretical spatial and time convergences.

3.3.4 Kelvin magnetic body force

The problem is solved in a cylinder of square meridian section

$$\Omega = \{(r, \theta, z) \in \mathbb{R}^3; 0 \leq r < 1, 0 \leq \theta < 2\pi, 0 < z < 1\}.$$

The computational domain is composed of a solid region

$$\Omega_s = \{(r, \theta, z) \in \Omega; 0 \leq r < 0.5\}$$

and a fluid region

$$\Omega_f = \{(r, \theta, z) \in \Omega; 0.5 < r < 1\}.$$

We solve the temperature equations (3.52) in Ω , the equations of fluid dynamics (3.55) in Ω_f and the magnetic field equations (3.58) in Ω . We have $\Omega_T = \Omega$. The pyromagnetic coefficient term in the temperature equation is not considered ($C_p = 0$). We enforce only Dirichlet conditions on the temperature: $\partial\Omega_{T,d} = \partial\Omega_T = \partial\Omega$, $\partial\Omega_{T,n} = \partial\Omega_{T,r} = \emptyset$. We enforce only Dirichlet conditions on the magnetic field: $\partial\Omega_d = \partial\Omega$, $\partial\Omega_n = \emptyset$. The temperature of the Boussinesq approximation is not relevant: $T_* = 0$. The viscosity is constant. The magnetic permeability is taken equal to 1 in the whole domain. The values of the dimensionless coefficients are given in Table 3.4.

Coefficient	Domain	
	Solid	Fluid
ρc	1	2
λ	10	1
Re	-	1
C_g	-	1
C_m	-	1
μ	1	1

Table 3.4: Dimensionless coefficients.

The law of the magnetic susceptibility is

$$\chi(T) = T^2. \quad (3.72)$$

The solution is

$$\begin{aligned}
T(r, \theta, z, t) &= r^2(r - r_0)^2 \sin(z)(1 + \cos(\theta)) \cos(t) && \text{in } \Omega, \\
u_r(r, \theta, z, t) &= -(r - r_0)^2 \cos(z)(1 + \cos(\theta)) \cos(t) && \text{in } \Omega_f, \\
u_\theta(r, \theta, z, t) &= (r - r_0)^2 \cos(z)(1 + \cos(\theta)) \cos(t) && \text{in } \Omega_f, \\
u_z(r, \theta, z, t) &= \frac{r - r_0}{r} \sin(z)((3r - r_0)(1 + \cos(\theta)) + (r - r_0) \sin(\theta)) \cos(t) && \text{in } \Omega_f, \\
p(r, \theta, z, t) &= 0 && \text{in } \Omega_f, \\
H_r(r, \theta, z, t) &= -r^3 \exp(z)(1 + \sin(\theta) \cos(t)) && \text{in } \Omega, \\
H_\theta(r, \theta, z, t) &= r^3 \exp(z)(1 + \sin(\theta)) \cos(t) && \text{in } \Omega, \\
H_z(r, \theta, z, t) &= r^2 \exp(z)(4 - \cos(\theta) + 4 \sin(\theta)) \cos(t) && \text{in } \Omega,
\end{aligned} \quad (3.73)$$

where $r_0 = 0.5$ is the limit between the solid and fluid parts. Note that the heat flux is continuous at the interface solid / fluid. See details on the velocity solution in Section 3.3.3. The magnetic field is defined by $\mathbf{H} = \nabla \times \mathbf{K}$, with

$$\mathbf{K}(r, \theta, z, t) = r^3 \exp(z)(1 + \sin(\theta)) \cos(t)(\mathbf{e}_r + \mathbf{e}_\theta) \text{ in } \Omega.$$

The equation $\nabla \cdot (\mu \mathbf{H}) = 0$ is thus satisfied. The source terms are defined by

$$\begin{aligned}
f_T &= \rho c \partial_t T + \rho c \tilde{\mathbf{u}} \cdot \nabla T - \nabla \cdot (\lambda \nabla T) && \text{in } \Omega, \\
\mathbf{f} &= \partial_t \mathbf{u} + (\nabla \times \mathbf{u}) \times \mathbf{u} + \nabla p - \frac{1}{Re} \Delta \mathbf{u} - C_g T \mathbf{e}_z - C_m \chi(T) \nabla \left(\frac{H^2}{2} \right) && \text{in } \Omega_f, \\
\mathbf{j} &= \nabla \times \mathbf{H} && \text{in } \Omega.
\end{aligned} \quad (3.74)$$

The initial conditions, \mathbf{u}_0 and T_0 , and the boundary conditions, \mathbf{u}_d , T_d and \mathbf{H}_d , are set to match the solution.

The problem is approximated with

$$h \in \left\{ \frac{1}{10}, \frac{1}{20}, \frac{1}{40}, \frac{1}{80}, \frac{1}{160} \right\}, \tau \in \left\{ \frac{1}{100}, \frac{1}{200}, \frac{1}{400}, \frac{1}{800}, \frac{1}{1600} \right\}.$$

The mesh of the meridian section with $h = 1/10$ is shown in Figure 3.6. The problem is solved on modes 0, 1, 2, 3 and 4. Eight processors are used in the meridian plane and five processors are used in the Fourier space.

We study the relative errors on the temperature, the velocity, the pressure and the magnetic field in L^2 -norm or \mathbf{L}^2 -norm, defined in (3.61) and (3.70). These relative errors, at a given time, for the various mesh sizes and time steps are presented in Tables 3.5, 3.6, 3.7, 3.8 and 3.9, respectively. For the temperature, the velocity and the magnetic field, at fixed (small) time step, the relative error is divided by about 8 when the mesh size is divided by 2, as long as the error due to the time discretization is negligible. The third-order convergence rate in space is thus respected. For the pressure and the curl of the magnetic field, at fixed (small) time step, the relative error is divided by about 4 when the mesh size is divided by 2, as long as the error due to the time discretization is negligible. The second-order convergence rate in space is thus respected. For all fields except the magnetic field and the curl of the magnetic field, at fixed (small) mesh size, the relative error is divided by about 4 when the time step is divided by 2, as long as the error due to the space discretization is negligible. The second-order convergence rate in time is thus respected. The relative errors on the magnetic field and the curl of the magnetic field do not change with the time step since there is no time derivative in the equations. For all fields, at fixed C_{CFL} (in the diagonal), the relative error is divided by at least 4 when the mesh size and the time step are divided by 2. The second-order / third-order convergence rates are thus respected.

$h \backslash \tau$	0.01	0.005	0.0025	0.00125	0.000625
0.1	7.6075E-5	7.6287E-5	7.6342E-5	7.6356E-5	7.6359E-5
0.05	6.5647E-6	6.5375E-6	6.5546E-6	6.5604E-6	6.5619E-6
0.025	1.4295E-6	6.7993E-7	6.1753E-7	6.1695E-7	6.1780E-7
0.0125	1.3341E-6	3.3418E-7	9.4713E-8	5.3162E-8	5.0080E-8
0.00625	1.3358E-6	3.3307E-7	8.3162E-8	2.1073E-8	6.6354E-9

Table 3.5: Relative L^2 -norm error on the temperature at $t = 1$.

$h \backslash \tau$	0.01	0.005	0.0025	0.00125	0.000625
0.1	1.4187E-5	1.4021E-5	1.3965E-5	1.3943E-5	1.3934E-5
0.05	1.3385E-6	1.1418E-6	1.1165E-6	1.1113E-6	1.1099E-6
0.025	6.2502E-7	1.8398E-7	1.0255E-7	9.3252E-8	9.2120E-8
0.0125	6.0969E-7	1.5156E-7	3.8851E-8	1.2418E-8	8.0050E-9
0.00625	6.0911E-7	1.5087E-7	3.7628E-8	9.4397E-9	2.4601E-9

Table 3.6: Relative \mathbf{L}^2 -norm error on the velocity at $t = 1$.

$h \backslash \tau$	0.01	0.005	0.0025	0.00125	0.000625
0.1	3.8560E-4	3.7620E-4	3.7333E-4	3.7229E-4	3.7190E-4
0.05	6.4072E-5	5.4122E-5	5.2710E-5	5.2382E-5	5.2277E-5
0.025	3.0670E-5	1.0466E-5	7.3977E-6	7.0761E-6	7.0293E-6
0.0125	2.9332E-5	7.2844E-6	2.0379E-6	1.0349E-6	9.2822E-7
0.00625	2.9286E-5	7.1958E-6	1.7918E-6	4.6273E-7	1.6413E-7

Table 3.7: L^2 -norm error on the pressure at $t = 1$.

$h \backslash \tau$	0.01	0.005	0.0025	0.00125	0.000625
0.1	8.6058E-5	8.6058E-5	8.6058E-5	8.6058E-5	8.6058E-5
0.05	1.1657E-5	1.1657E-5	1.1657E-5	1.1657E-5	1.1657E-5
0.025	1.6635E-6	1.6635E-6	1.6635E-6	1.6635E-6	1.6635E-6
0.0125	2.5123E-7	2.5123E-7	2.5123E-7	2.5123E-7	2.5123E-7
0.00625	4.0002E-8	4.0002E-8	4.0002E-8	4.0002E-8	4.0002E-8

Table 3.8: Relative L^2 -norm error on the magnetic field at $t = 1$.

$h \backslash \tau$	0.01	0.005	0.0025	0.00125	0.000625
0.1	3.1978E-4	3.1978E-4	3.1978E-4	3.1978E-4	3.1978E-4
0.05	6.9037E-5	6.9037E-5	6.9037E-5	6.9037E-5	6.9037E-5
0.025	1.4949E-5	1.4949E-5	1.4949E-5	1.4949E-5	1.4949E-5
0.0125	3.0428E-6	3.0428E-6	3.0428E-6	3.0428E-6	3.0428E-6
0.00625	6.5083E-7	6.5083E-7	6.5083E-7	6.5083E-7	6.5083E-7

Table 3.9: Relative L^2 -norm error on the curl of the magnetic field at $t = 1$.

3.3.5 Robin boundary conditions

The problem is solved in a hollow cylinder of rectangular meridian section

$$\Omega = \left\{ (r, \theta, z) \in \mathbb{R}^3; 0.5 \leq r < 1, 0 \leq \theta < 2\pi, 0 < z < 1 \right\}.$$

We solve the temperature equations (3.52) and the equations of fluid dynamics (3.55) in Ω . We have $\Omega_f = \Omega_T = \Omega$. The fluid is not a ferrofluid. The magnetic body force and the pyromagnetic coefficient term are absent from the momentum equation and the temperature equation, respectively ($C_p = C_m = 0$). We enforce Dirichlet conditions on the temperature on the bottom and interior sides: $\partial\Omega_{T,d} = \partial\Omega_{\text{bot}} \cup \partial\Omega_{\text{int}}$. We enforce Robin boundary conditions on the temperature on the top and exterior sides: $\partial\Omega_{T,n} = \partial\Omega_{\text{top}} \cup \partial\Omega_{\text{ext}}$. The convection coefficient on the exterior side is $h_{c,1} = 5$. The convection coefficient on the top side is $h_{c,2} = 2$. The exterior temperatures on both sides are $T_{r,1} = T_{r,2} = 3$. The Boussinesq force is not considered. The viscosity is constant. The values of the dimensionless coefficients are given in Table 3.10.

Coefficient	Value
ρc	2
λ	10
R_e	1
C_g	0

Table 3.10: Dimensionless coefficients.

The solution is

$$\begin{aligned}
T(r, \theta, z, t) &= \left(e^{-\frac{h_{c,1}r+h_{c,2}z}{\lambda}} + (r-1)^2(z-1)^2 \right) (1 + \cos(\theta)) \cos(t) + T_{r,1} && \text{in } \Omega, \\
u_r(r, \theta, z, t) &= 0 && \text{in } \Omega, \\
u_\theta(r, \theta, z, t) &= 0 && \text{in } \Omega, \\
u_z(r, \theta, z, t) &= 0 && \text{in } \Omega, \\
p(r, \theta, z, t) &= 0 && \text{in } \Omega.
\end{aligned} \tag{3.75}$$

The velocity is equal to zero: we basically solve the temperature in a solid. We have

$$\begin{aligned}
-\lambda \partial_r T(r=1, \theta, z, t) &= \left(h_{c,1} e^{-\frac{h_{c,1}+h_{c,2}z}{\lambda}} \right) (1 + \cos(\theta)) \cos(t) = h_{c,1}(T(r=1, \theta, z, t) - T_{r,1}), \\
-\lambda \partial_z T(r, \theta, z=1, t) &= \left(h_{c,2} e^{-\frac{h_{c,1}r+h_{c,2}}{\lambda}} \right) (1 + \cos(\theta)) \cos(t) = h_{c,2}(T(r, \theta, z=1, t) - T_{r,2}).
\end{aligned}$$

The Robin boundary conditions are thus satisfied (on the boundaries only due to the term $(r-1)(z-1)^2$). The source terms are defined by

$$\begin{aligned}
f_T &= \rho c \partial_t T + \rho c \tilde{\mathbf{u}} \cdot \nabla T - \nabla \cdot (\lambda \nabla T) && \text{in } \Omega, \\
\mathbf{f} &= \partial_t \mathbf{u} + (\nabla \times \mathbf{u}) \times \mathbf{u} + \nabla p - \frac{1}{R_e} \Delta \mathbf{u} && \text{in } \Omega_f.
\end{aligned} \tag{3.76}$$

The initial conditions, \mathbf{u}_0 and T_0 , and the boundary conditions, \mathbf{u}_d and T_d , are set to match the solution.

The problem is approximated with

$$h \in \left\{ \frac{1}{10}, \frac{1}{20}, \frac{1}{40}, \frac{1}{80}, \frac{1}{160} \right\}, \quad \tau \in \left\{ \frac{1}{100}, \frac{1}{200}, \frac{1}{400}, \frac{1}{800}, \frac{1}{1600} \right\}.$$

The mesh of the meridian section with $h = 1/10$ is shown in Figure 3.6. Only the fluid part of the mesh is used for the computation. The problem is solved on modes 0 and 1. Two processors are used in the meridian plane and two processors are used in the Fourier space.

The errors on the temperature in L^2 -norm $\|T_h - T\|_{L^2(\Omega)}$, at a given time, for the various mesh sizes and a fixed time step, are shown in Table 3.11. The time step is sufficiently small for the error due to the time discretization to be negligible. The computed order of convergence (see (3.62)) is satisfying regarding the theoretical third-order convergence.

h	Error	COC
0.1	2.9773E-06	-
0.05	3.6670E-07	3.02
0.025	3.1301E-08	3.55
0.0125	2.6415E-09	3.57
0.00625	2.3087E-10	3.52

Table 3.11: Errors on the temperature in L^2 -norm at time $t = 0.1$ for a fixed time step $\tau = 10^{-4}$, and associated computed order of convergence.

The errors on the temperature in L^2 -norm, at a given time, for various time steps and a fixed mesh size, are shown in Table 3.12. The mesh size is sufficiently small for the error due to the time discretization to be negligible. Say that the time steps are denoted by τ_i , $i \in \{1, \dots, i_{\max}\}$, where i_{\max} is the number of time steps, such that $\tau_1 > \tau_2 > \dots > \tau_{i_{\max}}$. The computed order of convergence for time step $i \geq 2$ is computed as follows:

$$\text{COC}_i = \frac{\ln(e_{i-1}/e_i)}{\ln(\tau_{i-1}/\tau_i)}, \quad (3.77)$$

where e_i , $i \in \{1, \dots, i_{\max}\}$ is the relative error obtained for time step i . The evolution of the error follows the theoretical second-order convergence.

τ	Error	COC
0.01	4.1436E-7	-
0.005	1.0384E-7	2.00
0.0025	2.5987E-8	2.00
0.00125	6.4950E-9	2.00
0.000625	1.6219E-9	2.00

Table 3.12: Errors on the temperature in L^2 -norm at $t = 1$ for a fixed mesh size $h = 6.25 \times 10^{-3}$, and associated computed order of convergence.

3.3.6 Temperature-dependent viscosity

The problem is solved in a cylinder of square meridian section

$$\Omega = \{(r, \theta, z) \in \mathbb{R}^3; 0 \leq r < 1, 0 \leq \theta < 2\pi, 0 < z < 1\}.$$

The computational domain is composed of a solid region

$$\Omega_s = \{(r, \theta, z) \in \Omega; 0 \leq r < 0.5\}$$

and a fluid region

$$\Omega_f = \{(r, \theta, z) \in \Omega; 0.5 < r < 1\}.$$

We solve the temperature equations (3.52) in Ω and the equations of fluid dynamics (3.55) in Ω_f . We have $\Omega_T = \Omega$. The fluid is not a ferrofluid. The magnetic body force and the pyromagnetic coefficient term are absent from the momentum equation and the temperature equation, respectively ($C_p = C_m = 0$). We enforce only Dirichlet conditions on the temperature: $\partial\Omega_{T,d} = \partial\Omega_T = \partial\Omega$, $\partial\Omega_{T,n} = \partial\Omega_{T,r} = \emptyset$. The temperature of the Boussinesq approximation is not relevant: $T_* = 0$. The variable Reynolds number is defined by

$$\frac{1}{R_e(T)} = \frac{1}{\overline{R_e}} \left(1 - \frac{T^2}{2}\right), \quad (3.78)$$

where $\overline{R_e}$ is the minimum Reynolds number. The values of the dimensionless coefficients are given in Table 3.13.

Coefficient	Domain	
	Solid	Fluid
ρc	1	2
λ	10	1
$\overline{R_e}$	-	1
C_g	-	1

Table 3.13: Dimensionless coefficients.

The solution is

$$\begin{aligned}
T(r, \theta, z, t) &= \frac{1}{\lambda} r^2 (r - r_0) \sin(z) (1 + \cos(\theta)) \cos(t) && \text{in } \Omega, \\
u_r(r, \theta, z, t) &= -(r - r_0)^2 \cos(z) (1 + \cos(\theta)) \cos(t) && \text{in } \Omega_f, \\
u_\theta(r, \theta, z, t) &= (r - r_0)^2 \cos(z) (1 + \cos(\theta)) \cos(t) && \text{in } \Omega_f, \\
u_z(r, \theta, z, t) &= \frac{r - r_0}{r} \sin(z) (3r - r_0 + (3r - r_0) \cos(\theta) + (r - r_0) \sin(\theta)) \cos(t) && \text{in } \Omega_f, \\
p(r, \theta, z, t) &= r \sin(z) \cos(\theta) && \text{in } \Omega_f,
\end{aligned} \tag{3.79}$$

where $r_0 = 0.5$ is the limit between the solid and fluid parts. See details on the temperature and velocity solutions in Section 3.3.3. The source terms are defined by

$$\begin{aligned}
f_T &= \rho c \partial_t T + \rho c \tilde{\mathbf{u}} \cdot \nabla T - \nabla \cdot (\lambda \nabla T) && \text{in } \Omega, \\
\mathbf{f} &= \partial_t \mathbf{u} + (\nabla \times \mathbf{u}) \times \mathbf{u} + \nabla p - \nabla \cdot \left(\frac{2}{Re(T)} \nabla^s \mathbf{u} \right) - C_g T \mathbf{e}_z && \text{in } \Omega_f.
\end{aligned} \tag{3.80}$$

The initial conditions, \mathbf{u}_0 and T_0 , and the boundary conditions, \mathbf{u}_d and T_d , are set to match the solution.

The problem is approximated with

$$h \in \left\{ \frac{1}{10}, \frac{1}{20}, \frac{1}{40}, \frac{1}{80}, \frac{1}{160} \right\}, \quad \tau \in \left\{ \frac{1}{100}, \frac{1}{200}, \frac{1}{400}, \frac{1}{800}, \frac{1}{1600} \right\}.$$

The mesh of the meridian section with $h = 1/10$ is shown in Figure 3.6. The problem is solved on modes 0, 1, 2 and 3. Four processors are used in the meridian plane and two processors are used in the Fourier space.

The relative errors in L^2 norm or \mathbf{L}^2 -norm with respect to the mesh size, at a given time and for a fixed time step, are presented in Figure 3.10. The errors on the temperature and the velocity follow the theoretical third-order convergence rate. The errors on the pressure follow the theoretical second-order convergence rate.

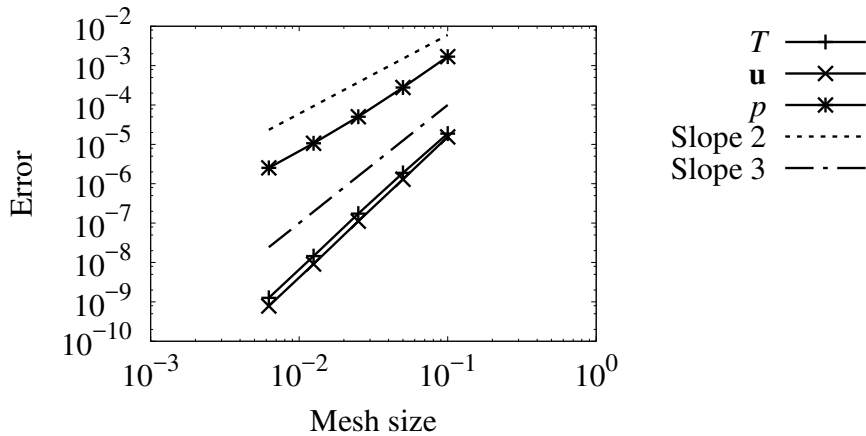


Figure 3.10: Relative errors in L^2 -norm or \mathbf{L}^2 -norm computed at $t = 10^{-2}$ with respect to the mesh size. Fixed time step of $\tau = 10^{-4}$.

The relative errors in L^2 norm or \mathbf{L}^2 -norm with respect to the time step, at a given time and for a fixed mesh size, are presented in Figure 3.11. The errors on the temperature, the velocity and the pressure follow the theoretical second-order convergence rate.

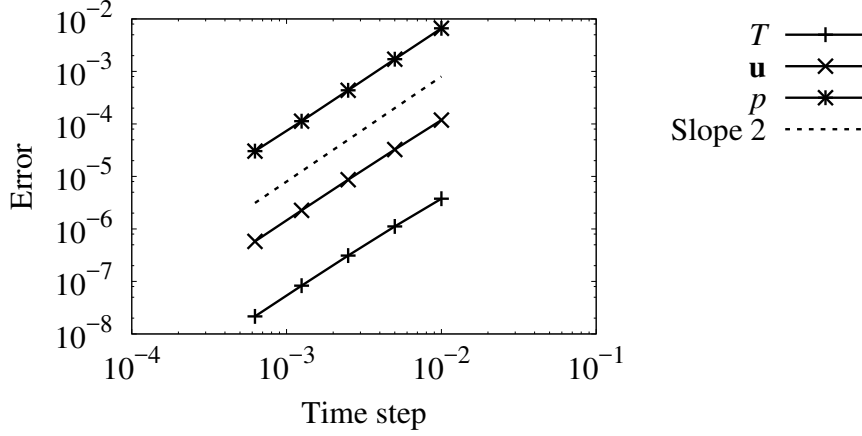


Figure 3.11: Relative errors in L^2 -norm or \mathbf{L}^2 -norm computed at $t = 1$ with respect to the time step. Fixed mesh size of $h = 6.25 \times 10^{-3}$.

3.3.7 Helmholtz magnetic body force

The problem is solved in a cylinder of square meridian section

$$\Omega = \{(r, \theta, z) \in \mathbb{R}^3; 0 \leq r < 1, 0 \leq \theta < 2\pi, 0 < z < 1\}.$$

The computational domain is composed of a solid region

$$\Omega_s = \{(r, \theta, z) \in \Omega; 0 \leq r < 0.5\}$$

and a fluid region

$$\Omega_f = \{(r, \theta, z) \in \Omega; 0.5 < r < 1\}.$$

We solve the temperature equations (3.52) in Ω , the equations of fluid dynamics (3.55) with the Helmholtz body force in Ω_f and the magnetic field equations (3.58) in Ω . We have $\Omega_T = \Omega$. The pyromagnetic coefficient term in the temperature equation is not considered ($C_p = 0$). We enforce only Dirichlet conditions on the temperature: $\partial\Omega_{T,d} = \partial\Omega_T = \partial\Omega$, $\partial\Omega_{T,n} = \partial\Omega_{T,r} = \emptyset$. We enforce only Dirichlet conditions on the magnetic field: $\partial\Omega_d = \partial\Omega$, $\partial\Omega_n = \emptyset$. The temperature of the Boussinesq approximation is not relevant: $T_* = 0$. The viscosity is constant. The magnetic permeability is taken equal to 1 in the whole domain. The values of the dimensionless coefficients are given in Table 3.14.

Coefficient	Domain	
	Solid	Fluid
ρc	1	2
λ	10	1
R_e	-	1
C_g	-	1
C_m	-	1
μ	1	1

Table 3.14: Dimensionless coefficients.

The law of the magnetic susceptibility is

$$\chi(T) = -T^2. \quad (3.81)$$

The solution is

$$\begin{aligned}
T(r, \theta, z, t) &= \frac{1}{\lambda} r^2 (r - r_0) \sin(2\pi z) (1 + \cos(\theta)) \cos(t) && \text{in } \Omega, \\
u_r(r, \theta, z, t) &= -2\pi (r - r_0)^2 \cos(2\pi z) (1 + \cos(\theta)) \cos(t) && \text{in } \Omega_f, \\
u_\theta(r, \theta, z, t) &= 2\pi (r - r_0)^2 \cos(2\pi z) (1 + \cos(\theta)) \cos(t) && \text{in } \Omega_f, \\
u_z(r, \theta, z, t) &= \frac{r - r_0}{r} \sin(2\pi z) (3r - r_0 + (3r - r_0) \cos(\theta) + (r - r_0) \sin(\theta)) \cos(t) && \text{in } \Omega_f, \\
p(r, \theta, z, t) &= r^3 \sin(2\pi z) \cos(\theta) \cos(t) && \text{in } \Omega_f \\
H_r(r, \theta, z, t) &= 2\pi r^3 \sin(2\pi z) (1 + \sin(\theta)) \cos(t) && \text{in } \Omega, \\
H_\theta(r, \theta, z, t) &= -2\pi r^3 \sin(2\pi z) (1 + \sin(\theta)) \cos(t) && \text{in } \Omega, \\
H_z(r, \theta, z, t) &= -r^2 \cos(2\pi z) (4 - \cos(\theta) + 4 \sin(\theta)) \cos(t) && \text{in } \Omega,
\end{aligned} \tag{3.82}$$

where $r_0 = 0.5$ is the limit between the solid and fluid parts. Note that the heat flux is continuous at the interface solid / fluid. The velocity is defined by $\mathbf{u} = \nabla \times \mathbf{v}$, with

$$\mathbf{v}(r, \theta, z, t) = (r - r_0)^2 \cos(2\pi z) (1 + \cos(\theta)) \cos(t) (\mathbf{e}_r + \mathbf{e}_\theta) \text{ in } \Omega_f.$$

The continuity equation $\nabla \cdot \mathbf{u} = 0$ is thus satisfied. Note that the extension of the velocity $\tilde{\mathbf{u}}$ is zero in the solid and that it is consistent with the velocity solution at the interface. The magnetic field is defined by $\mathbf{H} = \nabla \times \mathbf{K}$, with

$$\mathbf{K}(r, \theta, z, t) = r^3 \cos(2\pi z) (1 + \sin(\theta)) \cos(t) (\mathbf{e}_r + \mathbf{e}_\theta) \text{ in } \Omega.$$

The equation $\nabla \cdot (\mu \mathbf{H}) = 0$ is thus satisfied. The source terms are defined by

$$\begin{aligned}
f_T &= \rho c \partial_t T + \rho c \tilde{\mathbf{u}} \cdot \nabla T - \nabla \cdot (\lambda \nabla T) && \text{in } \Omega, \\
\mathbf{f} &= \partial_t \mathbf{u} + (\nabla \times \mathbf{u}) \times \mathbf{u} + \nabla p - \frac{1}{Re} \Delta \mathbf{u} - C_g T \mathbf{e}_z + C_m \frac{H^2}{2} \nabla \chi(T) && \text{in } \Omega_f, \\
\mathbf{j} &= \nabla \times \mathbf{H} && \text{in } \Omega.
\end{aligned} \tag{3.83}$$

The initial conditions, \mathbf{u}_0 and T_0 , and the boundary conditions, \mathbf{u}_d , T_d and \mathbf{H}_d , are set to match the solution.

The problem is approximated with

$$h \in \left\{ \frac{1}{10}, \frac{1}{20}, \frac{1}{40}, \frac{1}{80}, \frac{1}{160} \right\}, \quad \tau \in \left\{ \frac{1}{50}, \frac{1}{100}, \frac{1}{200}, \frac{1}{400}, \frac{1}{800} \right\}.$$

The mesh of the meridian section with $h = 1/10$ is shown in Figure 3.6. The problem is solved on modes 0, 1, 2 and 3. Two processors are used in the meridian plane and four processors are used in the Fourier space.

The evolution of the relative errors on T , \mathbf{u} , p , \mathbf{H} and $\nabla \times \mathbf{H}$ in L^2 -norm or \mathbf{L}^2 -norm with the mesh size at fixed time step is presented in Figure 3.12. The decrease of the error on the temperature, the velocity and the magnetic field follows the theoretical third-order convergence rate. The decrease of the error on the pressure and the curl of the magnetic field follows the theoretical second-order convergence rate.

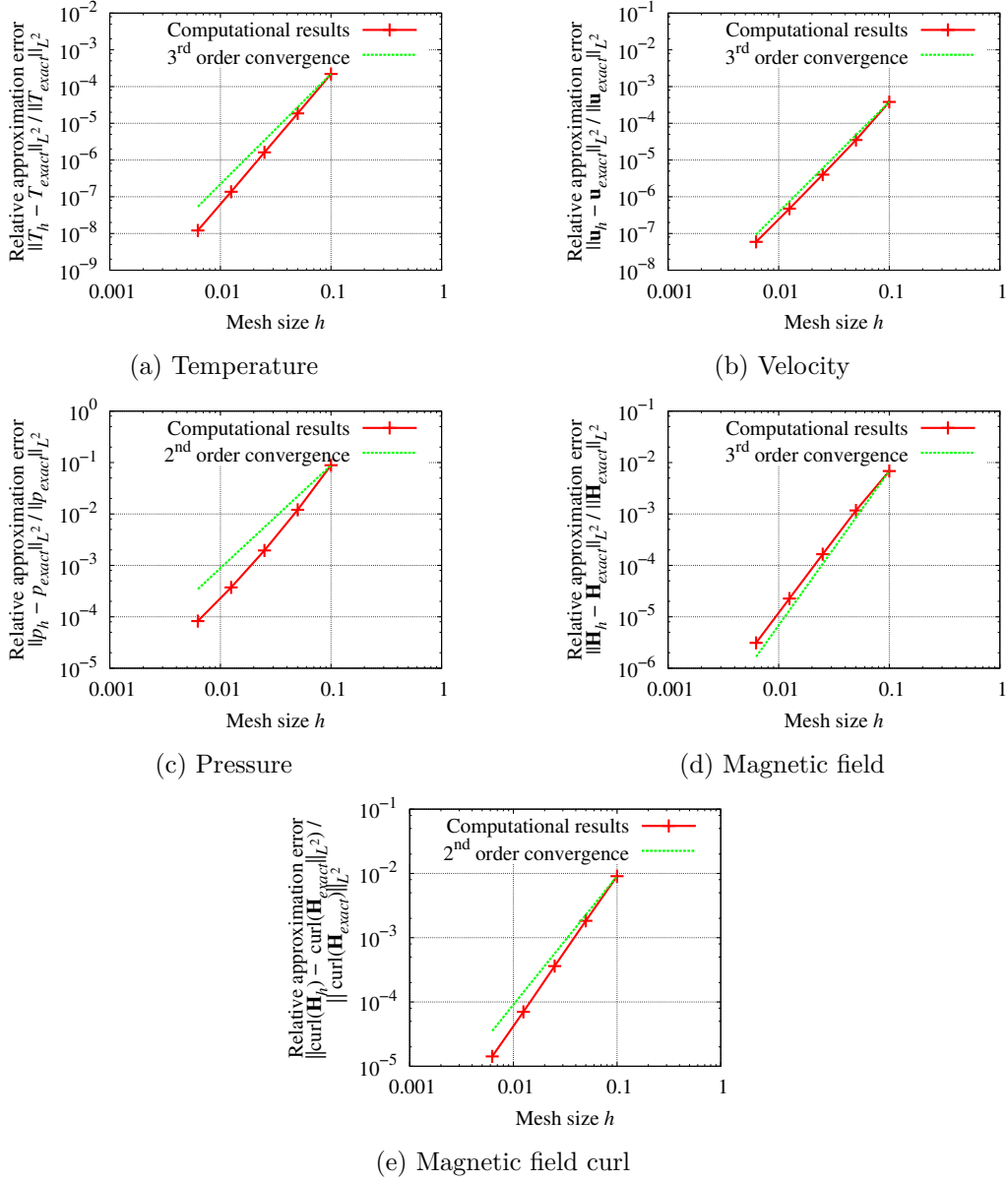


Figure 3.12: Relative error in L^2 -norm or \mathbf{L}^2 -norm at $t = 0.01$, for a fixed time step $\tau = 10^{-4}$; comparison with the theoretical convergence.

The evolution of the relative errors on T , \mathbf{u} and p in L^2 -norm or \mathbf{L}^2 -norm with the time step at fixed mesh size is presented in Figure 3.13. The decrease of the error on all fields follows the theoretical second-order convergence rate.

The evolution of the relative errors on T , \mathbf{u} and p in L^2 -norm or \mathbf{L}^2 -norm with the mesh size at fixed C_{CFL} is presented in Figure 3.13. The decrease of the error on the temperature and the velocity is between the second-order (time step) and third-order (mesh) convergence rates.

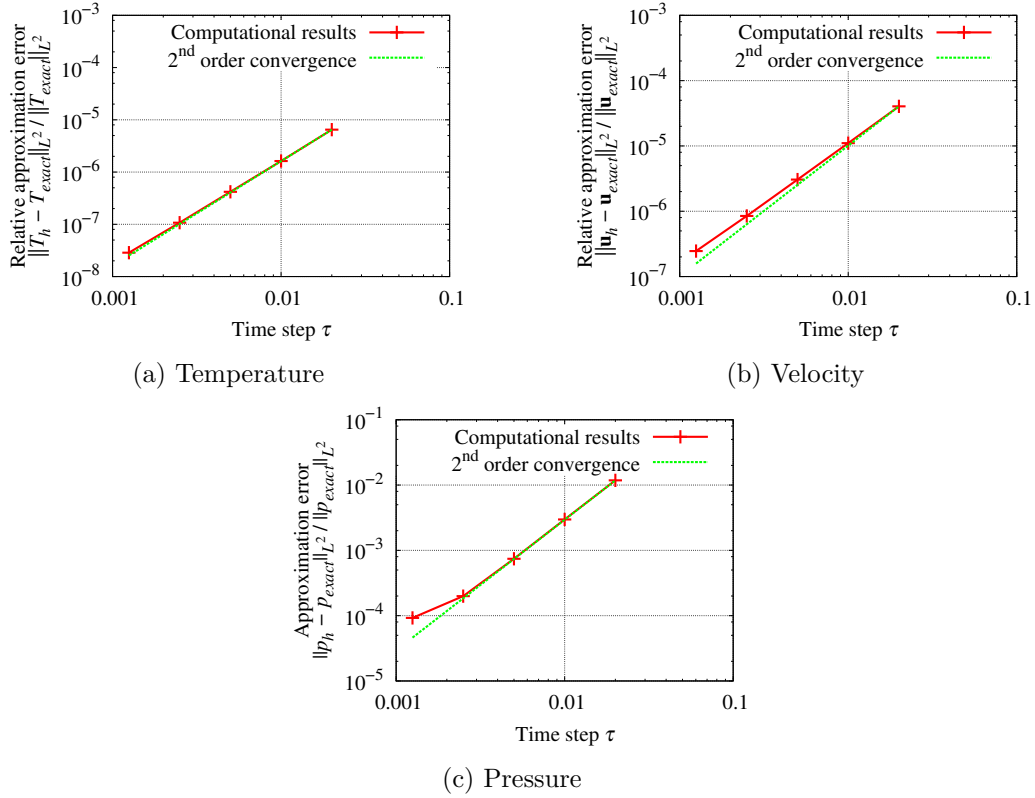


Figure 3.13: Error in L^2 -norm or \mathbf{L}^2 -norm at $t = 0.1$ with respect to time step, on the mesh with $h = 6.25 \times 10^{-3}$; comparison with the theoretical convergence.

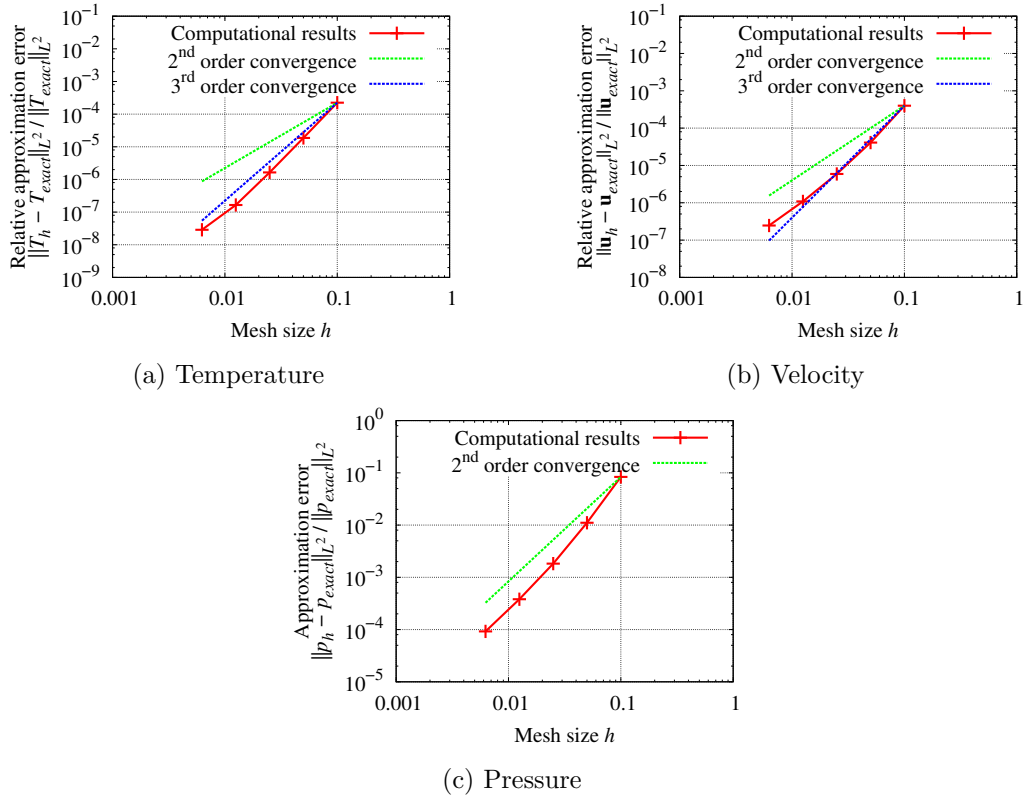


Figure 3.14: Error in L^2 -norm or \mathbf{L}^2 -norm at $t = 0.1$ with respect to mesh size, for a constant ratio $\tau/h = 0.2$; comparison with the theoretical spatial and time convergences.

3.3.8 Pyromagnetic coefficient term in the temperature equation

The problem is solved in a cylinder of square meridian section

$$\Omega = \{(r, \theta, z) \in \mathbb{R}^3; 0 \leq r < 1, 0 \leq \theta < 2\pi, 0 < z < 1\}.$$

The computational domain is composed of a solid region

$$\Omega_s = \{(r, \theta, z) \in \Omega; 0 \leq r < 0.5\}$$

and a fluid region

$$\Omega_f = \{(r, \theta, z) \in \Omega; 0.5 < r < 1\}.$$

We solve the temperature equations (3.52) in Ω , the fluid dynamics equations (3.55) in Ω_f and the magnetic field equations (3.58) in Ω . We have $\Omega_T = \Omega$. We enforce only Dirichlet conditions on the temperature: $\partial\Omega_{T,d} = \partial\Omega_T = \partial\Omega$, $\partial\Omega_{T,n} = \partial\Omega_{T,r} = \emptyset$. We enforce only Dirichlet conditions on the magnetic field: $\partial\Omega_d = \partial\Omega$, $\partial\Omega_n = \emptyset$. The temperature of the Boussinesq approximation is not relevant: $T_* = 0$. The viscosity is constant. The magnetic permeability is taken equal to 1 in the whole domain. The values of the dimensionless coefficients are given in Table 3.15.

Domain Coefficient	Solid	Fluid
ρc	1	2
λ	10	1
C_p	-	-1
R_e	-	1
C_g	-	1
C_m	-	-1
μ	1	1

Table 3.15: Dimensionless coefficients.

The law of the magnetic susceptibility is

$$\chi(T) = -T^2 \tag{3.84}$$

The solution is

$$\begin{aligned} T(r, \theta, z, t) &= \frac{1}{\lambda} r^2 (r - r_0) \sin(2\pi z) (1 + \cos(\theta)) \cos(t) && \text{in } \Omega, \\ u_r(r, \theta, z, t) &= -2\pi (r - r_0)^2 \cos(2\pi z) (1 + \cos(\theta)) \cos(t) && \text{in } \Omega_f, \\ u_\theta(r, \theta, z, t) &= 2\pi (r - r_0)^2 \cos(2\pi z) (1 + \cos(\theta)) \cos(t) && \text{in } \Omega_f, \\ u_z(r, \theta, z, t) &= \frac{r - r_0}{r} \sin(2\pi z) (3r - r_0 + (3r - r_0) \cos(\theta) + (r - r_0) \sin(\theta)) \cos(t) && \text{in } \Omega_f, \\ p(r, \theta, z, t) &= r^3 \sin(2\pi z) \cos(\theta) \cos(t) && \text{in } \Omega_f, \\ H_r(r, \theta, z, t) &= 2\pi r^3 \sin(2\pi z) (1 + \sin(\theta)) \cos(t) && \text{in } \Omega, \\ H_\theta(r, \theta, z, t) &= -2\pi r^3 \sin(2\pi z) (1 + \sin(\theta)) \cos(t) && \text{in } \Omega, \\ H_z(r, \theta, z, t) &= -r^2 \cos(2\pi z) (4 - \cos(\theta) + 4 \sin(\theta)) \cos(t) && \text{in } \Omega, \end{aligned} \tag{3.85}$$

where $r_0 = 0.5$ is the limit between the solid and fluid parts. See details on the solution in Section 3.3.7. The source terms are defined by

$$\begin{aligned}
 f_T &= \rho c \partial_t T + \rho c \tilde{\mathbf{u}} \cdot \nabla T - \nabla \cdot (\lambda \nabla T) + C_p T \frac{\partial \chi}{\partial T}(T) \left(\partial_t \left(\frac{H^2}{2} \right) + \mathbf{u} \cdot \nabla \left(\frac{H^2}{2} \right) \right) && \text{in } \Omega, \\
 \mathbf{f} &= \partial_t \mathbf{u} + (\nabla \times \mathbf{u}) \times \mathbf{u} + \nabla p - \frac{1}{Re} \Delta \mathbf{u} - C_g T \mathbf{e}_z - C_m \chi(T) \nabla \left(\frac{H^2}{2} \right) && \text{in } \Omega_f, \\
 \mathbf{j} &= \nabla \times \mathbf{H} && \text{in } \Omega.
 \end{aligned} \tag{3.86}$$

The initial conditions, \mathbf{u}_0 and T_0 , and the boundary conditions, \mathbf{u}_d , T_d and \mathbf{H}_d , are set to match the solution.

The problem is approximated with

$$h \in \left\{ \frac{1}{10}, \frac{1}{20}, \frac{1}{40}, \frac{1}{80}, \frac{1}{160} \right\}, \tau \in \left\{ \frac{1}{200}, \frac{1}{400}, \frac{1}{800}, \frac{1}{1600}, \frac{1}{3200}, \frac{1}{6400}, \frac{1}{12800} \right\}.$$

The mesh of the meridian section with $h = 1/10$ is shown in Figure 3.6. The problem is solved on modes 0, 1, 2, 3, 4 and 5. Four processors are used in the meridian plane and three processors are used in the Fourier space.

The evolution of the relative errors on T , \mathbf{u} , p and \mathbf{H} in L^2 -norm or \mathbf{L}^2 -norm with the mesh size at fixed time step is presented in Figure 3.15. The decrease of the error on the temperature, the velocity and the magnetic field follows the theoretical third-order convergence rate. The decrease of the error on the pressure follows a greater rate than the theoretical second-order convergence rate.

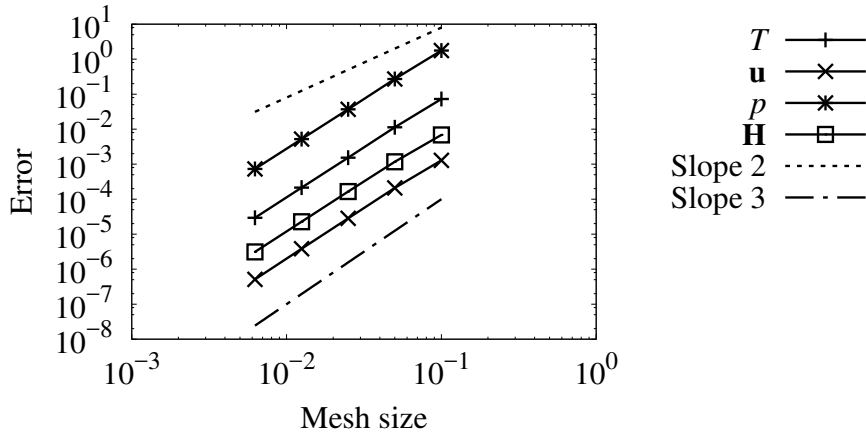


Figure 3.15: Relative error in L^2 -norm or \mathbf{L}^2 -norm at $t = 10^{-3}$ with respect to mesh size, for a fixed time step $\tau = 10^{-5}$; comparison with the theoretical convergence.

The evolution of the relative errors on T , \mathbf{u} and p in L^2 -norm or \mathbf{L}^2 -norm with the time step at fixed mesh size is presented in Figure 3.16. The decrease of the error on all fields follows the theoretical first-order convergence rate (in spite of a superconvergence with the larger time steps for the pressure).

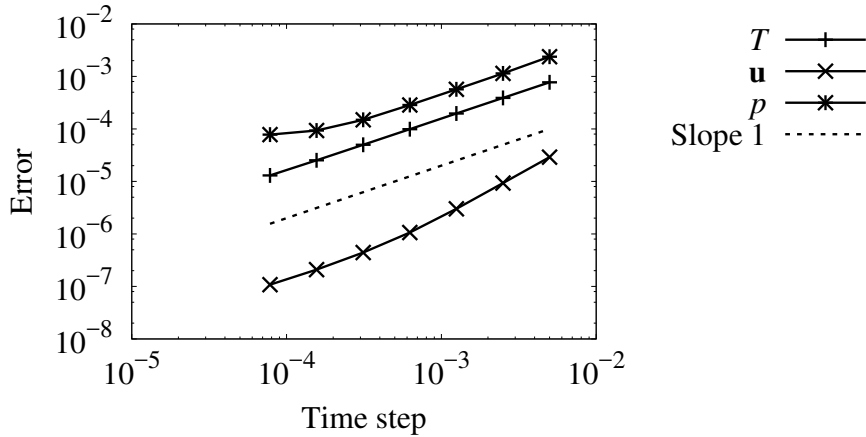


Figure 3.16: Relative error in L^2 -norm or \mathbf{L}^2 -norm at $t = 1$ with respect to time step, on the mesh with $h = 6.25 \times 10^{-3}$; comparison with the theoretical convergence.

3.4 Conclusion of the chapter

A new class of applications is implemented in SFEMaNS to study ferrohydrodynamics. The ferrofluid is considered as a continuum with Newtonian behavior. The governing equations are composed of the temperature equations, the Navier-Stokes equations under the Boussinesq approximation and the magnetostatics equations. Two models of magnetic body force, Kelvin and Helmholtz, are implemented to take into account the action of the magnetic field on the ferrofluid. An additional term containing the pyromagnetic coefficient is implemented in the temperature equation. Other developments also valid for a regular fluid are completed: computation of the temperature in mixed solid and fluid domains, Robin boundary conditions for the temperature and a temperature-dependent viscosity. Convergence tests are performed to validate every new functionality. All of these developments lead to a complete numerical scheme to solve convection problems in complex geometries, possibly with ferrofluid. In the next chapters, the new developments in SFEMaNS are exploited to study realistic problems of convection involving regular or magnetic fluids.

Chapter 4

Thermomagnetic convection in an oil bath heated by a solenoid

In this chapter, we study the influence of thermomagnetic convection on heat transfer in a simple electromagnetic system. The simulations are based on the first experimental setup: a solenoid is immersed in transformer oil and the temperature rise is monitored by two sensors. The solenoid represents the windings of an actual transformer, which generate heat by the Joule effect and a magnetic field. In this chapter, the thermophysical properties of the ferrofluid are those of the transformer oil to highlight the effect of the magnetic body force (Kelvin force model). The first section presents a series of results published in IEEE Transaction on Magnetics. The experiment using pure transformer oil is used to validate the thermo-hydrodynamical model (no experiment has eventually been performed with ferrofluid on this particular setup). One simulation is performed with the transformer oil as coolant and one simulation is performed with a transformer oil-based ferrofluid¹ as coolant. The velocity and temperature fields in the permanent regime are compared to assess the influence of the magnetic body force on the heat transfer in the system. The second section details the model, briefly described in the article, and some results such as the time evolution of the physical quantities in the transitory regime. The third section presents complementary numerical results on the experimental setup. The magnetic body force is visualized to understand how it modifies the flow. A posteriori 3D computations are performed to verify the axisymmetry assumption of the first simulations. The viscosity being strongly temperature-dependent, the model is adapted to take into account this dependence and the new results are reported. The Kelvin and Helmholtz force models are compared theoretically and numerically. In this chapter, we do not consider the pyromagnetic coefficient term in the temperature equation.

¹In the whole thesis, *regular oil* refers to transformer oil without magnetic nanoparticles and *magnetic oil* refers to transformer oil with magnetic nanoparticles, i.e., to transformer oil-based ferrofluid.

Study of Magnetoconvection Impact on a Coil Cooling by Ferrofluid with a Spectral / Finite Element Method

Raphaël Zanella^{1,2,3}, Caroline Nore¹, Frédéric Bouillault², Loïc Cappanera³, Ignacio Tomas³, Xavier Mininger², and Jean-Luc Guermond³

¹LIMSI, CNRS, Univ. Paris-Sud, Université Paris-Saclay, F-91405 Orsay, France

²GeePs, UMR 8507 CNRS / CentraleSupélec - Universités UPMC et UPSud, 91192 Gif sur Yvette cedex, France

³Department of Mathematics, Texas A&M University, College Station, TX 77843 USA

The benefit of magnetoconvection for transformer cooling by ferrofluid is numerically studied. A code combining spectral and finite element methods is applied on a solenoid system. Magnetostatic, Navier-Stokes and energy equations are solved simultaneously. A vegetable oil seeded with magnetite nanoparticles at a volume fraction of 10 % is considered. The magnetization of the ferrofluid is a function of temperature through an approximation of the classical Langevin's law. Magnetic and temperature fields are used to update the magnetic action, modeled by the Kelvin force, on the ferrofluid momentum at each time step. Numerical results for regular oil are consistent with experimental temperature data obtained for pure vegetable oil cooling. Numerical results for ferrofluid show that the magnetoconvection modifies the flow convection pattern and speed. The temperature increase in the coil is consequently reduced by about 9.4 % with ferrofluid cooling.

Index Terms—coupled problem, finite element, magnetoconvection, spectral method, transformer cooling.

I. INTRODUCTION

A FERROFLUID is a stable suspension of magnetic nanoparticles in a non magnetic liquid carrier. A magnetic field transfers momentum to the ferrofluid through the nanoparticles. Literature often mentions the Kelvin force model (in N/m^3) to consider this effect [1],

$$\mathbf{F} = \mu_0(\mathbf{M} \cdot \nabla)\mathbf{H}, \quad (1)$$

where \mathbf{M} is the magnetization and \mathbf{H} the magnetic field.

The dependence of the magnetization with respect to temperature can lead to magnetoconvection when magnetic field and temperature gradients are combined, as it is the case in immersed transformers [2]. If the heat transfer rate is increased because of the nanoparticles, the volume of cooling fluid could be reduced, or mechanical cooling systems avoided. Moreover, instead of conventional mineral oil, the liquid carrier could be substituted by vegetable oil, with higher viscosity but biodegradable and non toxic.

Heat transfer enhancement when using ferrofluid instead of regular oil was pointed out in the work on an immersed coil [3]. Encouraging results on a transformer were obtained in [4] but the ferrofluid magnetization model was temperature independent. The experimental work based on a transformer prototype [5] also showed the benefit of ferrofluid as coolant. In this work, a setup close to that of [3] is simulated with the SFEMaNS code [6], based on spectral and finite element methods. The ferrofluid magnetization follows an approximation of the Langevin's law [7] to include the effects of temperature dependence. Dynamics and symmetry features of the solutions, with or without nanoparticles, are presented

Manuscript received April 1, 2015; revised May 15, 2015 and June 1, 2015; accepted July 1, 2015. Date of publication July 10, 2015; date of current version July 31, 2015. Corresponding author: R. Zanella (e-mail: zanella@limsi.fr).

Color versions of one or more of the figures in this paper are available online at <http://ieeexplore.ieee.org>.

Digital Object Identifier (inserted by IEEE).

and the decrease of the coil temperature with ferrofluid cooling is explained by studying the flow pattern.

In a first step, a simulation without Kelvin force is ran to validate the model against an experiment with pure vegetable oil. In a second step, the Kelvin force is added and the numerical results for regular oil and ferrofluid are compared.

II. EXPERIMENTAL SETUP AND MODELING

A. Experimental Setup

The experiment [8] is based on an electromagnetic system constituted of a triple copper coil crossed by a DC current and immersed in vegetable oil, as presented in Fig. 1. The fluid is a sample of oil produced by the Midel company for transformer cooling. The temperature increase is locally measured at the boundary of the coil and in the fluid until a steady state is reached (typically 10000 s time).

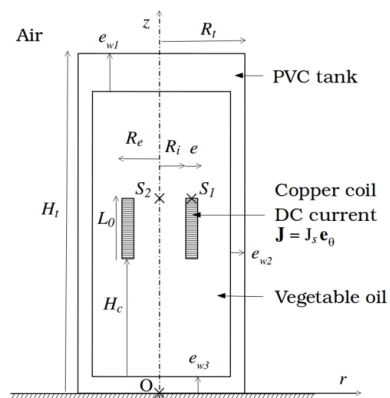


Fig. 1. Experimental setup model. S_1 and S_2 represent the thermal sensors.

The dimensions are: $H_t = 12.5$ cm, $R_t = 2.5$ cm, $R_i = 0.8$ cm, $R_e = 1.175$ cm, $e = 0.375$ cm, $L_0 = 2.1$ cm, $H_c = 3.9$ cm, $e_{w1} = 2$ cm, $e_{w2} = 0.45$ cm, and $e_{w3} = 1$ cm.

The current in each spire, about 8 A, is controlled with a dSPACE setup so that the power dissipated in the coil keeps its initial value of 3.0 W over the period of measurement. The coil electrical resistance decrease due to the heating by Joule effect is thus counterbalanced.

B. Modeling

Regular oil and ferrofluid cases use the same equations, except for the body forces in the momentum equation, as presented hereafter. Quasi-steady regime approximation for electromagnetism is used. Like the regular oil, the ferrofluid is a continuum medium with Newtonian fluid behavior [1]. Boussinesq approximation is used and viscous dissipation is neglected. Regarding the ferrofluid, its magnetization is assumed to be instantaneously aligned with the magnetic field.

The magnetostatic equations are

$$\nabla \times \mathbf{H} = \mathbf{J}, \quad (2)$$

$$\nabla \cdot (\mu \mathbf{H}) = 0, \quad (3)$$

where \mathbf{J} is the current density (enforced current density $J_s \mathbf{e}_\theta$ in the coil, null elsewhere) and μ the magnetic permeability. The fluid equations, based on Navier-Stokes equations, are

$$\rho \partial_t \mathbf{u} + \rho (\mathbf{u} \cdot \nabla) \mathbf{u} + \nabla p - \eta \Delta \mathbf{u} \quad (4)$$

$$= \alpha (T - T_0) \rho g \mathbf{e}_z + \mu_0 M \nabla H, \quad (5)$$

where ρ is the density, \mathbf{u} the velocity, p the pressure, η the dynamic viscosity, α the thermal expansion coefficient, T the temperature, T_0 the exterior temperature and g the gravity. The first term of the right hand side is the Boussinesq force and the second represents the simplified expression of the Kelvin force in (1) considering that \mathbf{M} and \mathbf{H} are collinear [1]. The conservation of energy is written as

$$\rho c \partial_t T + \rho c (\mathbf{u} \cdot \nabla) T - \nabla \cdot (\lambda \nabla T) = f_T, \quad (6)$$

where c is the heat capacity, λ the thermal conductivity and f_T the heat source, equal to the Joule effect J_s^2 / σ_{cl} in the coil and null elsewhere (σ_{cl} is the coil electrical conductivity). The magnetic field impacts the velocity with no retroaction. Velocity and temperature are strongly coupled and are thus solved simultaneously.

The boundary condition $\mathbf{H} \times \mathbf{n} = 0$ is applied on the tank's exterior border. The non-slip boundary condition $\mathbf{u} = 0$ is enforced on the border of the fluid domain. The air convection at the top and the lateral boundaries of the tank is modeled by a Robin boundary condition on temperature:

$$-\lambda \nabla T \cdot \mathbf{n} = h(T - T_0), \quad (7)$$

where h is the convection coefficient and \mathbf{n} the outer normal vector. The Dirichlet condition $T = T_0$ is enforced on the bottom of the tank, which is in contact with the setup table. Initially, $\mathbf{u} = 0$, $T = T_0$, and $\mathbf{H} = 0$.

The magnetization intensity of the ferrofluid is proportional to the magnetic field intensity:

$$\mathbf{M} = \chi(T) \mathbf{H}, \quad (8)$$

with χ the susceptibility given by an approximation of the Langevin's law [7]:

$$\chi(T) = \frac{\varphi \mu_0 \pi d^3 M_0^2}{18 k_B (T + 273.15)}, \quad (9)$$

where φ is the volume fraction of magnetic material, d the particle diameter, M_0 the particle magnetization and k_B the Boltzmann constant.

The thermo-physical properties used in each subdomain (coil, fluid, tank) are presented in Table 1.

TABLE I
THERMO-PHYSICAL PROPERTIES

Property	Coil	Fluid	Tank
Density (kg/m ³)	3888	922	1400
Dynamic viscosity (Pa·s)	-	2.9e-2	-
Thermal expansion coefficient (/K)	-	7.4e-4	-
Heat capacity (J/K·kg)	622	1970	1000
Thermal conductivity (W/m·K)	0.361	0.166	0.16

The viscosity is set to the value taken at 40 °C, the temperature approximately reached at the end of the experiment. The other fluid properties present reduced variations over the temperature range and are taken at 20 °C.

In the model, the coil represents the copper coil itself and the oil stuck by viscosity between the spires. The properties are homogeneous properties between copper and Midel oil properties, the volume fraction of copper being approximately 37 %. The density and the heat capacity are obtained by using a mix law. The thermal conductivity is given by the analytical law developed by [9].

The temperature in the lab is measured at $T_0 = 18$ °C. The tank / air convection coefficient is chosen in the range given by the literature: $h = 17$ W/m²·K. The Joule effect and the current density in the coil are calculated to be consistent with the enforced current in the experiment.

A ferrofluid containing magnetite nanoparticles with classical characteristics is considered: $\varphi = 0.1$, $d = 10$ nm and $M_0 = 446$ kA/m. In the magnetostatic equation (3), the magnetic permeability μ is piecewise constant: $\mu_0(1 + \chi(T_0))$ in the ferrofluid and μ_0 elsewhere.

III. THE SFEMANS CODE

A. Numerical Method

We use our own magneto-hydrodynamics code called SFEMaNS, see [6], using a hybrid spatial discretization mixing Fourier expansions and finite elements. The method is based on cylindrical coordinates and every field f is solved as a partial Fourier sum relative to the azimuthal direction:

$$f(r, \theta, z) = f_0^c(r, z) + \sum_{m=1}^{m_{max}} f_m^c(r, z) \cos(m\theta) \quad (10)$$

$$+ \sum_{m=1}^{m_{max}} f_m^s(r, z) \sin(m\theta),$$

where m_{max} is the maximum considered mode. The problem can be approximated independently (modulo the computations of nonlinear terms) for each Fourier mode in the meridian plane with Lagrange finite elements. Thanks to the Fourier decomposition, SFEMaNS can be less computationally expensive than a classical 3D finite element code on axisymmetric geometries. Second order elements are used for the temperature and the velocity while first order elements are used for the pressure for computational efficiency. For the magnetic part, the algorithm solves the problem using the magnetic field \mathbf{H} in the conducting region (after standard elimination of the electric field) and a scalar magnetic potential ($\mathbf{H} = \nabla \phi$) in the insulating exterior if needed. The

fields in each region are approximated by using H^1 -conforming Lagrange elements, with a technique to enforce $\nabla \cdot (\mu \mathbf{H}) = 0$ based on a penalty method. The coupling across the axisymmetric interfaces of discontinuous electric conductivity or magnetic permeability is enforced by an interior penalty method. The equations are solved separately at each time step, allowing strong couplings.

SFEMaNS has been thoroughly validated on numerous analytical solutions and against other magneto-hydrodynamics codes [6,10,11,12].

B. Validation on a Rayleigh-Bénard Convection Test Case

We study a classical Rayleigh-Bénard convection problem in a cylindrical cavity heated from below and insulated laterally following [13]. Using non-slip boundary conditions on the lateral wall, the motionless conducting state of a cylinder of radius to height aspect ratio of $R/H = 0.75$ becomes unstable above a critical Rayleigh number

$$Ra = \frac{\alpha \Delta T g H^3}{\kappa \nu} = 2590, \quad (11)$$

where ΔT is the characteristic temperature difference, κ the thermal diffusivity and ν the kinematic viscosity, in excellent agreement with [13]. The stationary convection forms a roll corresponding to a $m = 1$ mode which breaks the axisymmetry of the base state (see Fig. 2).

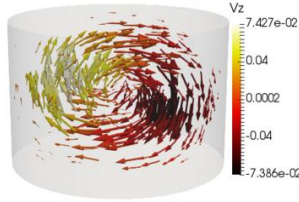


Fig. 2. Rayleigh-Bénard convection roll [13] simulated by SFEMaNS.

IV. RESULTS

A. Comparison with the Experiment on Pure Vegetable Oil

The flow and temperature fields are simulated in the experiment case of pure vegetable oil. In (4), the only force is the Boussinesq one and (2) and (3) are not solved.

Computations show that, for the chosen parameters, the steady solution is carried by the mode 0 only, i.e. is axisymmetric. Even initially populated, the other modes vanish and $m_{max} = 0$ in (10) is chosen. The mesh contains 3031 nodes and a time step of 0.02 s is used over 5×10^5 iterations (about 11 wall-clock hours using 8 processors on the cluster IBM x3750-M4 from GENCI-IDRIS).

The numerical solution reaches a steady regime in about 10000 s, a time consistent with the experimental observation. Fig. 3 presents the time evolution of the kinetic energy:

$$E_k(t) = \int_{\Omega_f} \frac{1}{2} \rho u^2(\mathbf{x}, t) d\mathbf{x}, \quad (12)$$

where Ω_f is the fluid domain, and the spatial quadratic mean of the temperature increment:

$$\overline{T - T_0}(t) = \sqrt{\frac{1}{V} \int_{\Omega} (T - T_0)^2(\mathbf{x}, t) d\mathbf{x}}, \quad (13)$$

where Ω is the whole domain and V its volume. These global quantities show that velocity and temperature fields eventually reach a stationary state.

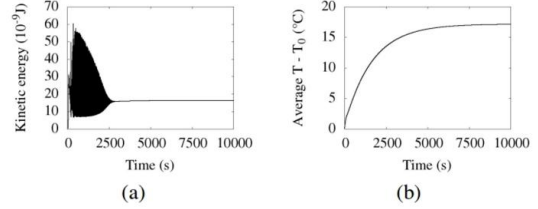


Fig. 3. Time evolution of the kinetic energy (a) and the spatial quadratic mean of the temperature increment $T - T_0$ (b) in the regular oil case.

The numerical results for temperature are in good agreement with the experimental data, as shown in Fig. 4.

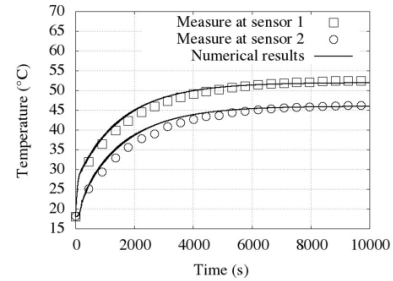


Fig. 4. Comparison of the temperature increase obtained experimentally and numerically in the pure vegetable oil case. Experimental data from [8].

B. Numerical Results on Magnetoconvection

The code is here used to assess the effect of the magnetoconvection when the vegetable oil is replaced by ferrofluid. Both Boussinesq and Kelvin forces create momentum in (4). In these simulations, the regular oil and the ferrofluid have the same thermo-physical properties to highlight the Kelvin force effect.

The final solution is axisymmetric and $m_{max} = 0$ is taken. The same numerical setup (mesh, time step, processors) leads to a completed computation in about 16 wall-clock hours.

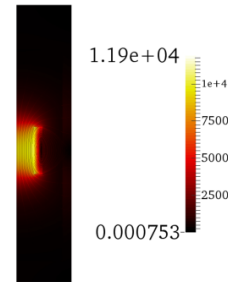


Fig. 5. Magnetic field intensity H (A/m) and field lines in a meridian plane (symmetry axis on the left) in the ferrofluid case.

The Kelvin force, generated by the magnetic field of Fig. 5, impacts the system dynamics. In this case, the velocity field does not reach a static state, as shown in Fig. 6a. The kinetic energy, after an initial transitory regime, reaches a plateau and then switches (between 8000 and 9000 s) to an oscillating

state. Further computations show that the oscillations of the kinetic energy survive after $t = 10000$ s. The temperature field reaches an almost static state, oscillations due to the changes in the velocity field being very small, in the time needed for vegetable oil (Fig. 6b). The cooling performance of ferrofluid can be assessed since the coil temperature is stable.

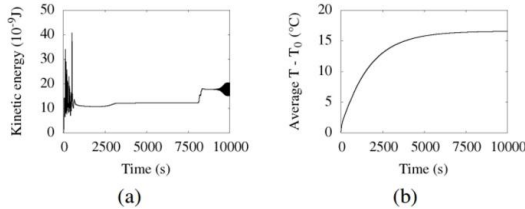


Fig. 6. Time evolution of the kinetic energy (a) and the spatial quadratic mean of the temperature increment $T - T_0$ (b) in the ferrofluid case.

The flow pattern is transformed because of the Kelvin force. In the pure vegetable oil case (Fig. 7a), a natural convection cell appears at the top of the coil. The fluid flows up along the coil while heating and then down along the tank while cooling. In the ferrofluid case (Fig. 7b), a strong upward flow appears at the symmetry axis and leads to an additional convection cell that cools down the coil.

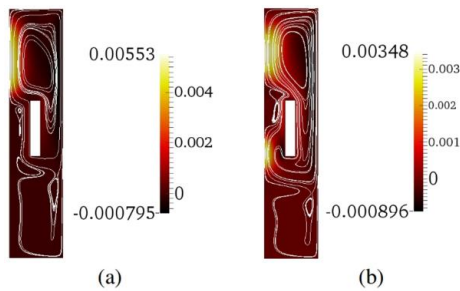


Fig. 7. Axial velocity u_z (m/s) and streamlines in a meridian plane (symmetry axis on the left) at $t = 10000$ s for regular oil (a) and ferrofluid (b).

The magnetoconvection improves the heat removal in the ferrofluid system. The temperature increment $T - T_0$ in the coil goes from 37.3 °C with regular oil to 33.8 °C with ferrofluid, see Fig. 8. Thanks to the nanoparticles, the increase of temperature in the coil is reduced by about 9.4 %.

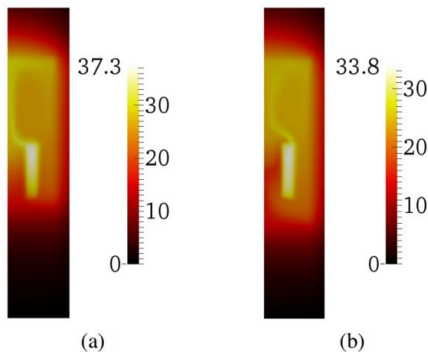


Fig. 8. Temperature increment $T - T_0$ (°C) in a meridian plane (symmetry axis on the left) at $t = 10000$ s for regular oil (a) and ferrofluid (b).

V. CONCLUSION

A mathematical model has been developed to study transformer cooling with ferrofluid on an immersed coil case. The action of the magnetic field on the fluid is modeled by the Kelvin force while the magnetization of the ferrofluid follows the Langevin's law for paramagnetism.

Numerical simulations based on an experimental setup are consistent with the temperature measured in the case of regular oil cooling. Numerical experiments show an improvement of the heat removal when regular oil is replaced by ferrofluid, the temperature rise in the coil being reduced by 9.4 % due to magnetoconvection.

Further developments will include a model taking into account the modification of the fluid properties with nanoparticles and the comparison with ferrofluid experimental results.

ACKNOWLEDGEMENT

This work is supported by the Labex LaSIPS (Nano-in-Oil Grant). Code's development and simulations were performed with HPC resources from GENCI-IDRIS (Grant 2016-0254) and TAMU.

REFERENCES

- [1] J. L. Neuringer, and R. E. Rosensweig, "Ferrohydrodynamics," *The Physics of Fluids*, vol. 7, no. 12, pp. 1927-1937, Dec. 1964.
- [2] S. Odenbach, "Magnetoviscous Effects in Ferrofluids," *Lecture Notes in Physics Monographs*, vol. 71, Springer, 2002.
- [3] G.-Y. Jeong, S. P. Jang, H.-Y. Lee, J.-C. Lee, S. Choi, and S.-H. Lee, "Magnetic-Thermal-Fluidic Analysis for Cooling Performance of Magnetic Nanofluids Comparing With Transformer Oil and Air by Using Fully Coupled Finite Element Method," *IEEE Trans. Magn.*, vol. 49, no. 5, pp. 1865-1868, May 2013.
- [4] L. Pislaru-Dănescu, A. M. Morega, G. Telipan, M. Morega, J. B. Dumitru, and V. Marinescu, "Magnetic Nanofluid Applications in Electrical Engineering," *IEEE Trans. Magn.*, vol. 49, no. 11, pp. 5489-5497, Nov. 2013.
- [5] J. Patel, K. Parekh, R. V. Upahyay, "Prevention of hot spot temperature in a distribution transformer using magnetic fluid as a coolant," *International Journal of Thermal Sciences*, vol. 103, pp. 35-40, 2016.
- [6] J.-L. Guermond, R. Laguerre, J. Léorat, C. Nore, "Nonlinear magneto-hydrodynamics in axisymmetric heterogeneous domains using a Fourier/finite element technique and an interior penalty method," *Journal of Computational Physics*, vol. 228, pp. 2739-2757, 2009.
- [7] R. E. Rosensweig, "Magnetic Fluids," *Annual Review of Fluid Mechanics*, vol. 19, pp. 437-63, 1987.
- [8] N. Puigmal, A. Nait Djoudi, E. Berthelot, R. Zanella, X. Mininger, "Etudes numériques et expérimentales du refroidissement par bain d'huile d'un système électromagnétique," submitted to NUMELEC 2017 conference.
- [9] W. T. Perrins, D. R. McKenzie, R. C. McPhedran, "Transport properties of regular arrays of cylinders," *Proc. R. Soc. Lond. A*, vol. 369, pp. 207-225, 1979.
- [10] A. Bonito, J.-L. Guermond, F. Luddens, "Regularity of the Maxwell equations in heterogeneous media and Lipschitz domains," *Journal of Math. Analysis and Applications*, vol. 408, no. 2, pp. 498-512, 2013.
- [11] C. Nore, H. Zaidi, F. Bouillault, A. Bossavit, J.-L. Guermond, "Approximation of the time-dependant induction equation with advection using Whitney elements: Application to dynamo action," *COMPEL*, vol. 35, no. 1, pp. 326-338, 2016.
- [12] A. Giesecke, C. Nore, F. Stefani, G. Gerbeth, J. Léorat, W. Herreman, F. Luddens, J.-L. Guermond, "Influence of high-permeability discs in an axisymmetric model of the Cadarache dynamo experiment," *New Journal of Physics*, vol. 14, no. 5, pp. 053005, 2012.
- [13] M. Wanschura, H. C. Kuhlmann, H. J. Rath, "Three-dimensional instability of axisymmetric buoyant convection in cylinders heated from below," *J. Fluid Mech.*, vol. 326, pp. 399-415, 1996.

4.2 Additional comments

In this section, we detail the model and some results presented in the article. In particular, we discuss the time evolution of the physical quantities in the transitory regime.

4.2.1 Experimental setup

The experimental setup is shown in Figure 4.1. More details are reported in [105]. The experimental setup has been designed following preparatory simulations presented in Appendix D.

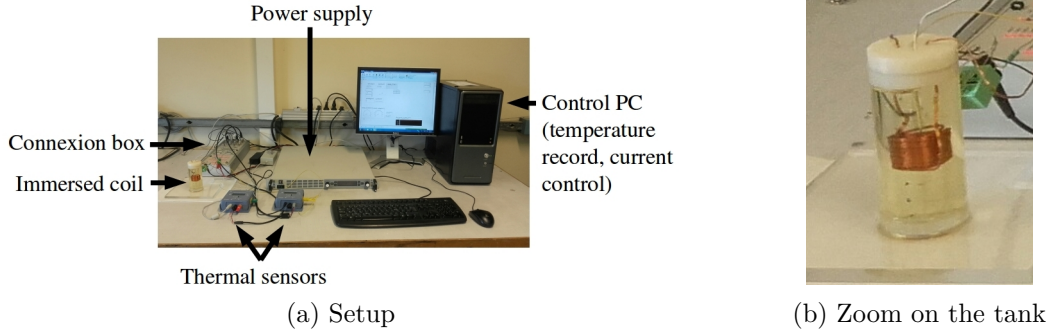


Figure 4.1: First experimental setup (PVC tank).

4.2.2 Governing equations

We now detail some elements of the article. The current density in the coil domain of the magnetostatics equations (equation (2) of the article) is defined by

$$J_s = \frac{NI}{S_{cl}}, \quad (4.1)$$

where $N = 33$ is the number of turns, $I = 8$ A is the current in the coil and $S_{cl} = (R_e - R_i)L_0$ is the section of the coil body. We have $J_s \simeq 3.4 \times 10^6$ A/m². The source term in the coil domain of temperature equation (equation (6) of the article) is defined by

$$f_T = \frac{R_{es}I^2}{V_{cl}}, \quad (4.2)$$

where $R_{es} = 47 \times 10^{-3}$ Ω is the electrical resistance of the coil and $V_{cl} = \pi(R_e^2 - R_i^2)L_0$ is the volume of the coil body. We have $f_T \simeq 6.2 \times 10^5$ W/m³ in the coil domain. The magnetic body force in the momentum equation (equation (4) of the article) is implemented using the form

$$\mathbf{f}_m = \mu_0 \Delta \chi(T) \nabla \left(\frac{H^2}{2} \right), \quad (4.3)$$

where $\Delta \chi(T) = \chi(T) - \chi(T_0)$ is the difference of ferrofluid magnetic susceptibility between the local temperature $T(\mathbf{x}, t)$ and the exterior temperature T_0 . The magnetic body force is split for numerical stability, and the gradient part is included in the gradient of the pressure. We use the change of variable $p \leftarrow p - \mu_0 \chi(T_0) H^2 / 2$.

4.2.3 Physical properties

Based on the dimensions of the coil body, the wire and the number of windings, we estimate that the copper represents $\phi_{Cu} = 37\%$ of the volume of the coil body. To account for the

presence of oil within the coil body, the properties of the coil are homogenized in the numerical simulations. The density and the heat capacity are given by the expressions:

$$\rho_{\text{coil}} = \phi_{\text{Cu}}\rho_{\text{Cu}} + (1 - \phi_{\text{Cu}})\rho_f, \quad (4.4)$$

$$\rho_{\text{coil}}c_{\text{coil}} = \phi_{\text{Cu}}\rho_{\text{Cu}}c_{\text{Cu}} + (1 - \phi_{\text{Cu}})\rho_fc_f. \quad (4.5)$$

The subscripts Cu and f refer to copper and fluid (eN 1215 from Midel). The thermal conductivity is given by the analytical law developed in [106, eq. (12)-(13)]:

$$\frac{\lambda_{\text{coil}}}{\lambda_f} = 1 - 2\phi_{\text{Cu}} \left(\Lambda + \phi_{\text{Cu}} - \frac{0.075422 \phi_{\text{Cu}}^6 \Lambda}{\Lambda^2 - 1.060283 \phi_{\text{Cu}}^{12}} - \frac{0.000076 \phi_{\text{Cu}}^{12}}{\Lambda} \right)^{-1}, \quad (4.6)$$

$$\Lambda = \left(1 + \frac{\lambda_{\text{Cu}}}{\lambda_f} \right) \left(1 - \frac{\lambda_{\text{Cu}}}{\lambda_f} \right)^{-1}. \quad (4.7)$$

The properties are from various sources. Copper properties are from [107, p. 983]. Oil properties are from the manufacturer (Midel). PVC properties are from [108, p. 68].

As said in the article, we take into account the fact that the permeability of the ferrofluid is different from that of vacuum to solve the magnetic problem (equation (3) of the article). Nevertheless, the magnetic permeability of the ferrofluid is considered constant equal to $\mu_0(1 + \chi(T_0))$, where the law of $\chi(T)$ is given by equation (9) of the article and $T_0 = 18^\circ\text{C}$ is the initial temperature. Thus, the relative magnetic permeability of the ferrofluid is $1 + \chi(T_0) \simeq 2.09$ in this work. The maximum temperature increment with ferrofluid cooling is $\Delta T = 33.8^\circ\text{C}$, see Figure 8b. At $T_1 = T_0 + \Delta T = 51.8^\circ\text{C}$, the relative magnetic permeability of the ferrofluid is $1 + \chi(T_1) \simeq 1.97$. The relative difference is less than 6%. It is thus valid to consider that the magnetic permeability of the ferrofluid is constant in the magnetic problem.

4.2.4 Mesh choice

The mesh of the meridian section is shown in Figure 4.2. The mesh size is chosen considering the thickness of the boundary layers for the velocity and the temperature at the coil, denoted by δ and δ_T , respectively. Since oils have high Prandtl numbers, $\delta \gg \delta_T$ [107, p. 407]. The thermal diffusivity of our oil at 20°C is $\kappa_f = \lambda_f/(\rho_fc_f) \simeq 9.13 \times 10^{-8} \text{ m}^2/\text{s}$ and its Prandtl number is $P_r = \nu_f/\kappa_f \simeq 733$ (we use the subscript f to identify the properties of the fluid²). Based on the dimensions of the coil and the dissipated heat ($P = 3.0 \text{ W}$), we can estimate that the heat flux across the coil walls is

$$q_S = \frac{P}{2\pi(L_0(R_i + R_e) + R_e^2 - R_i^2)} \simeq 977 \text{ W/m}^2. \quad (4.8)$$

The Rayleigh number (case of an enforced flux q_S) is

$$R_a = \frac{g\alpha_f q_S L_0^4}{\kappa_f \nu_f \lambda_f} \simeq 1.4 \times 10^7. \quad (4.9)$$

Following the correlations for a vertical plate and an enforced heat flux reported in [109, p. 18], the thickness of the thermal boundary layer is estimated by

$$\delta_T = L_0(P_r R_a)^{-\frac{1}{5}} \simeq 3.3 \times 10^{-4} \text{ m}. \quad (4.10)$$

The mesh size in the coil being at most $8 \times 10^{-4} \text{ m}$, it is sufficient to observe the variations of the temperature along δ_T (considering that we use quadratic elements). Consequently, it is also sufficient to observe the variations of the velocity along δ , which is much greater than δ_T .

²At 20°C , the dynamic viscosity of the oil is $\nu_f = 6.7 \times 10^{-5} \text{ Pa} \cdot \text{s}$. The other properties are reported in the article.

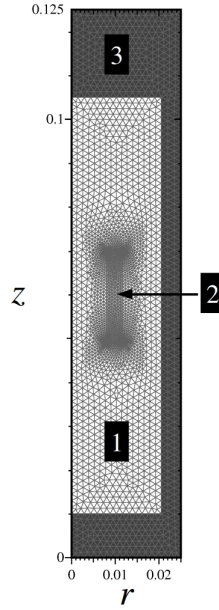


Figure 4.2: Mesh of the meridian section (symmetry axis on the left). Axes in meters. 1: fluid, 2: coil, 3: tank. The mesh size goes from 8×10^{-4} to 2×10^{-4} m in the coil (the mesh is refined in the corners of the coil due to singularities). The mesh size is 1.5×10^{-3} m in the tank.

4.2.5 Comparison with another experiment

Another experiment has been performed with a lower intensity of approximately 6 A in the coil. In the model, the source term in the temperature equation, given by (4.2), is adapted by using $I = 6$ A. The comparison of the measured temperature and the computed temperature at each sensor is presented in Figure 4.3. Note that a convection coefficient of $15 \text{ W/m}^2 \cdot \text{K}$ is used to fit the experimental data obtained with a lower current. As with the former current, the numerical results are in good agreement with the experimental data. The thermo-hydrodynamical model is confirmed by this second experiment.

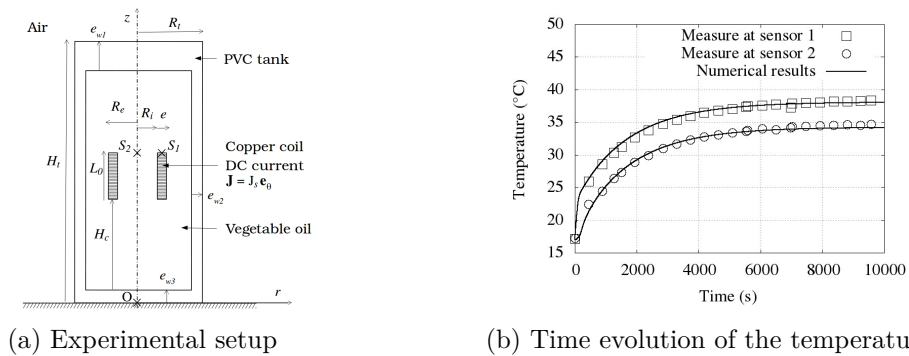


Figure 4.3: Second experiment with a lower intensity of approximately 6 A in the coil. Temperature measured at the thermal sensors versus computed temperature.

4.2.6 Interface conditions on the magnetic field

The relative magnetic permeability of the ferrofluid is close to 2 while the relative magnetic permeability of the coil and the tank is 1. The interface conditions in (3.14) must therefore be enforced on the borders of the fluid domain. In order to verify that they are

respected, we study the profiles of the magnetic field components along a radial axis and a vertical axis. Both axes cross all the interfaces of magnetic permeability jump. The profiles of the magnetic field components along the radial axis $z = 6.5$ cm are presented in Figure 4.4. The axis crosses the interior coil boundary, the exterior coil boundary and the tank boundary. The radial component is normal to every interface. At every interface, it is discontinuous and its value is twice weaker in the ferrofluid. The azimuthal component is zero by symmetry. The axial component is parallel to every interface. At every interface, it is continuous. The interface conditions are respected.

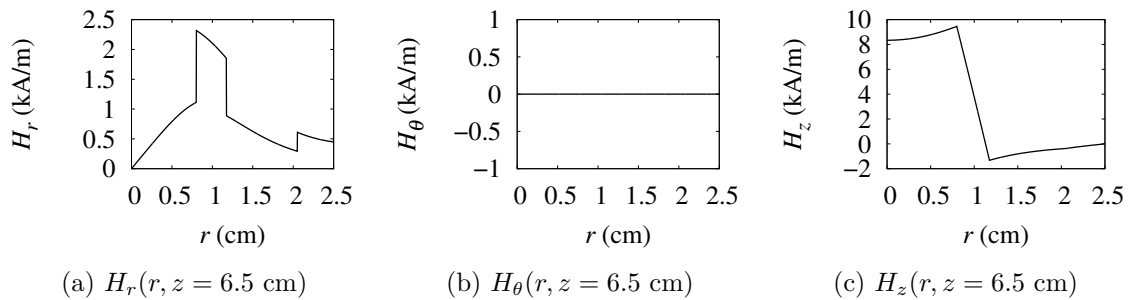


Figure 4.4: Profile of the magnetic field components at $z = 6.5$ cm.

The profiles of the magnetic field components along the vertical axis $r = 1$ cm are presented in Figure 4.5. The axis crosses the bottom tank boundary, the bottom coil boundary, the top coil boundary and the top tank boundary. The radial component is parallel to every interface. At every interface, it is continuous. The azimuthal component is zero by symmetry. The axial component is normal to every interface. At every interface, it is discontinuous and its value is twice weaker in the ferrofluid. The interface conditions are respected. We can conclude that the interface conditions are correctly dealt with by the code.

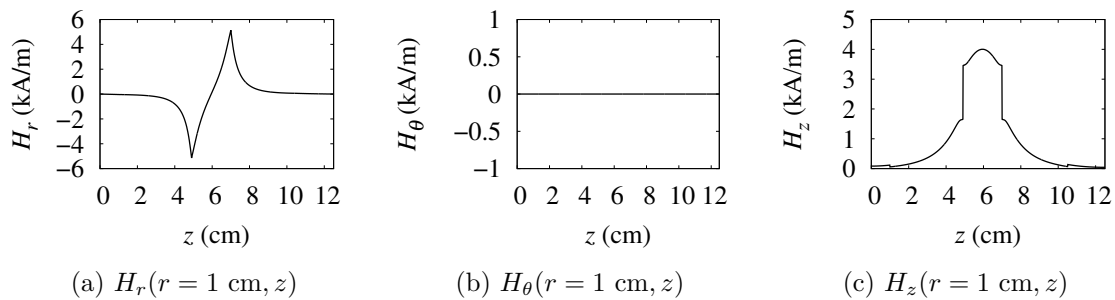


Figure 4.5: Profile of the magnetic field components at $r = 1$ cm.

4.2.7 Focus on the convective flow

The velocity components obtained with the regular oil and the magnetic oil are presented in Figures 4.6 and 4.7, respectively. The simulation time is $t = 10000$ s, i.e., the fields are presented in the permanent regime. The visualization of all components offers a better understanding of the convective flow than the visualization of the axial component only, presented in the article. Note that the azimuthal component is zero (for the regular oil and the magnetic oil), and is therefore not displayed. The flow does not grow in the azimuthal direction, it is contained in the meridian section. We first study the case of the regular oil, see Figure 4.6. The radial component is strongly negative right above the coil and strongly positive right under the top wall of the tank. The axial component is strongly

positive on the symmetry axis, above the coil, and strongly negative along the lateral wall of the tank. These fields are consistent. The hot fluid close to the coil is first brought toward the symmetry axis, then brought toward the top wall of the tank, then brought toward the lateral wall of the tank and finally brought toward the bottom of the tank. The hot fluid loses its thermal energy along the top and lateral walls of the tank. On the way to the bottom, it is heated again by the coil and starts a new circular movement.

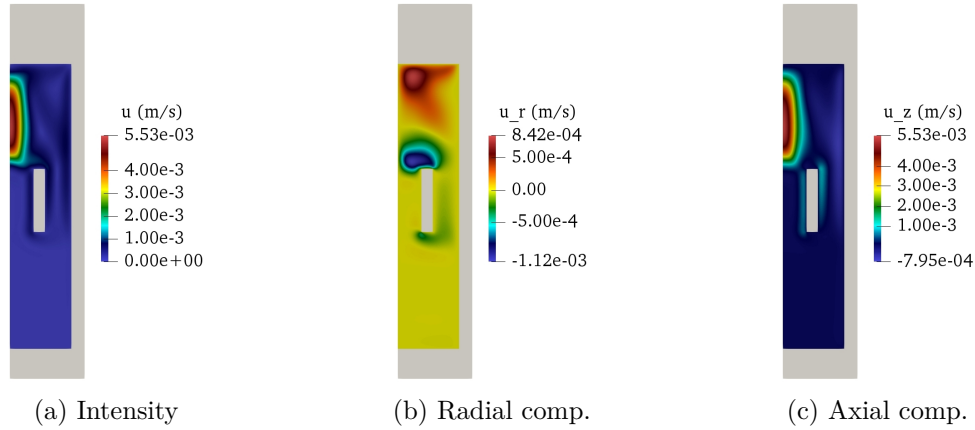


Figure 4.6: Regular oil simulation. Velocity intensity and components in a meridian section (symmetry axis on the left) at $t = 10000$ s.

We secondly study the case of the magnetic oil, see Figure 4.7. The areas of positive or negative radial and axial components, seen in the case of regular oil, are present in this case too. The same convective flow exists but other areas of interest are present. The radial component is positive at the bottom of the coil and negative right under. The axial component is positive on the symmetry axis, in front of the bottom of the coil, and negative along the interior boundary of the coil, at the bottom of it. These observations show that the hot fluid close to the coil is put into motion following another circular movement, localized at the bottom of the coil. The magnetic body force does not destroy the convection cell due to the Boussinesq force; it rather generates a supplementary convection cell that cools down the coil. Figure 8 of the article shows that the coil temperature is lowered by a few degrees when using magnetic oil. Even though velocity intensity is weaker in the magnetic oil, see Figures 4.6a and 4.7a, the supplementary convection cell makes the cooling by magnetic oil more efficient.

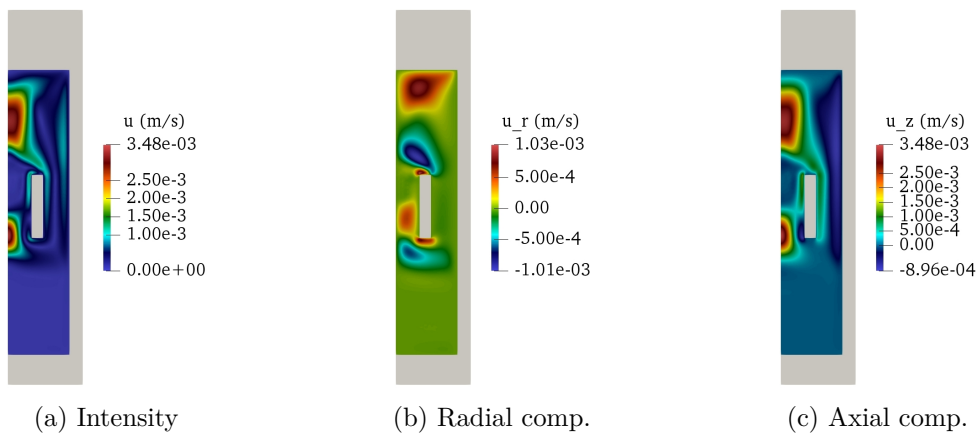
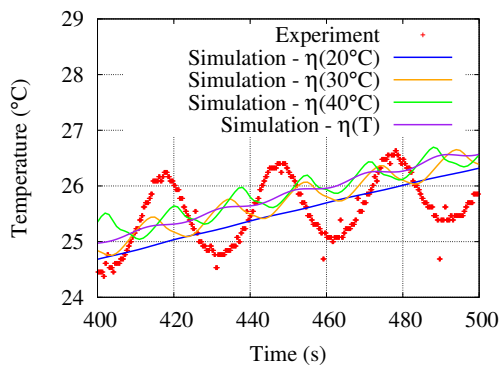


Figure 4.7: Magnetic oil simulation. Velocity intensity and components in a meridian section (symmetry axis on the left) at $t = 10000$ s.

4.2.8 Presence of oscillations in the regular oil case

Figure 4.8 shows the time evolution of the temperature at the sensor in the fluid (point S_2 in Figure 1 of the article) obtained experimentally and numerically between 400 and 500 s. The simulations are performed with different values of the dynamic viscosity, and with a temperature-dependent dynamic viscosity (see Section 4.3.3). The dynamic viscosity is indeed a key parameter for this problem. Like the experimental data, the numerical data present oscillations, for some values of the dynamic viscosity. It is the case for the dynamic viscosity at 40°C used in the article for instance. The oscillation periods for all cases are reported in Table 4.1. In the simulations, the oscillation period decreases when the dynamic viscosity is reduced (the viscosity decreases with temperature). The oscillation periods are not consistent between the experiment and the simulations, no matter what is the value of the dynamic viscosity used in the simulation. Note that the amplitude and the lifetime of the oscillations are not consistent as well. The oscillations observed in the simulations are smaller in amplitude and last longer. The model seems to capture an oscillation phenomenon. Nevertheless, we cannot be sure that it is the one observed in the experiment.



Case	Period (s)
Experiment	33
Simulation - $\eta(20^\circ\text{C})$	-
Simulation - $\eta(30^\circ\text{C})$	20
Simulation - $\eta(40^\circ\text{C})$	17
Simulation - $\eta(T)$	20

Table 4.1: Period of the oscillations in Figure 4.8.

Figure 4.8: Temperature at the fluid sensor (point S_2 in Figure 1 of the article).

Figure 3a of the article shows the time evolution of the kinetic energy. Until $t = 3000$ s, the kinetic energy strongly oscillates. The period and the lifetime of the oscillations are consistent with that of the temperature at the fluid sensor (in the simulation). The oscillations of the velocity and the temperature are apparently related. Figure 4.9 presents the time evolution of the temperature field during an entire period of oscillation (around 17 s). During this period, a mass of hot fluid closed to the coil is convected toward the top of the tank. In the meantime, another mass of hot fluid gets ready to follow the same path. The convective flow is irregular. This phenomenon stops after the permanent regime starts. Further visualizations show that the convective flow is regular in the permanent regime. We can conclude that the oscillations shown in Figure 4.8 are due to the irregular plume of hot fluid during the transient regime. The velocity should be measured in the experiment to confirm this convection feature.

4.2.9 Time evolution of the velocity field in the magnetic oil case

As shown in Figure 6a of the article, the time evolution of the kinetic energy of the magnetic oil is not regular: around $t = 8000$ s, the kinetic energy suddenly changes. In order to understand this feature, we look into the time evolution of the axial velocity between 8000 and 8300 s, see Figure 4.10. The convection cell above the coil at $t = 10000$ s, see Figure 4.7c, is not present at $t = 8000$ s, see Figure 4.10a. At $t = 8000$ s, the hot fluid coming from the coil does not flow toward the symmetry axis; it flows directly toward

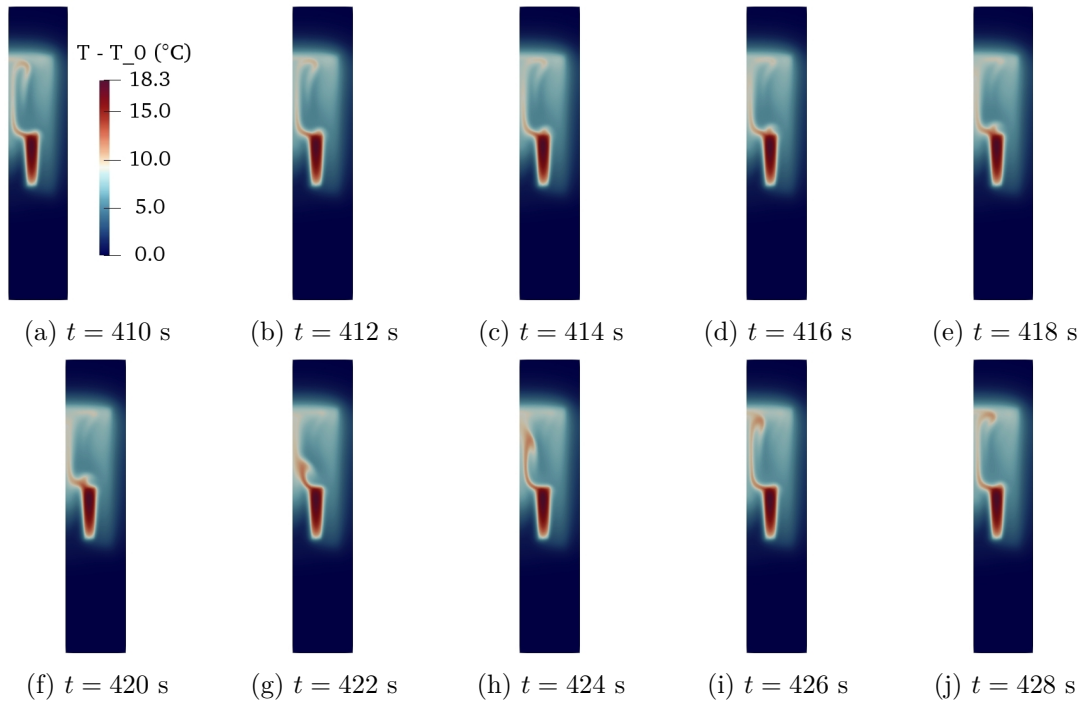


Figure 4.9: Time evolution of the temperature in a meridian section (symmetry axis on the left) during the oscillatory regime.

the top wall of the tank. Once cooled down, it flows downward along the symmetry axis and the lateral wall of the tank. The flow is actually modified during the next 300 s, see Figures 4.10b, 4.10c and 4.10d. The circulation of the hot fluid is brought toward the symmetry axis and the convection cell of the permanent regime is formed. Thus, the sudden change of kinetic energy is not due to a numerical issue, but to the transition of the convection pattern to the final convection pattern.

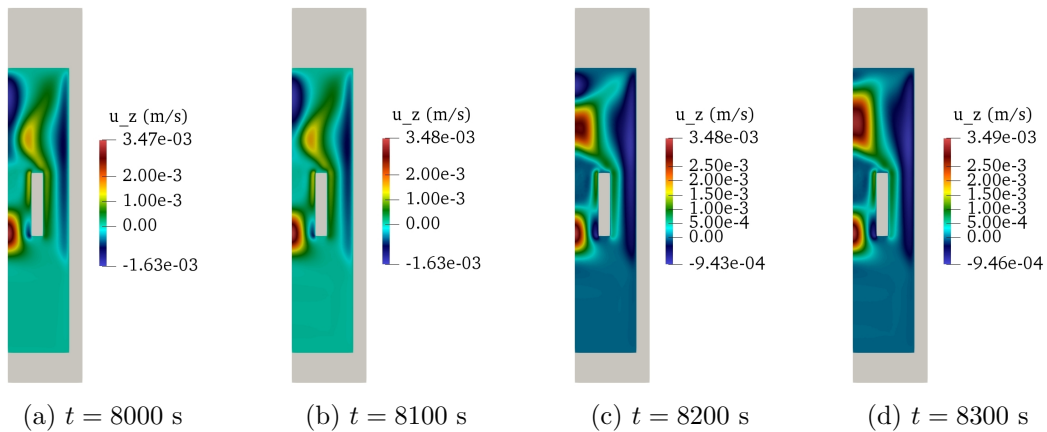


Figure 4.10: Time evolution of the axial velocity during the modification of the flow in a meridian section (symmetry axis on the left).

We can see in Figure 6a of the article that the kinetic energy starts to oscillate after this change of convection pattern. Further computations show that the oscillations survive after $t = 10000$ s. Visualizations of the temperature and velocity fields show that these sustained oscillations are due to the oscillations of the plume of hot fluid, similar to that of the regular oil case. This phenomenon does not have a strong impact on the temperature though. As shown in Figure 6b of the article, even if the average temperature increment

actually presents oscillations with a very limited amplitude at $t \geq 8000$ s, it seems to be stationary.

4.3 Complementary discussion

In this section, we present complementary results regarding the simulations of the article. We investigate the influence of the Kelvin body force, the axisymmetry of the solution and the use of an alternative magnetic body force: the Helmholtz body force.

4.3.1 Visualization of the magnetic body force

In order to understand the effect of the magnetic body force, we plot it in a meridian section like the velocity and temperature fields.

Mass matrix inversion

The body forces are plotted by using the subroutines that generate the visualization files for regular fields (temperature, velocity, pressure, magnetic field). In the code, the forcing terms are computed at the Gauss points, while the subroutines that generate the visualization files require fields defined on the nodes. An intermediary step is necessary to compute the body forces defined on the nodes from the body forces defined on the Gauss points. This step actually consists in inverting a mass matrix, as shown in the following.

To present the principle, we consider a scalar body force, denoted by f . Say that the linear system corresponding to the weak formulation of the problem is under the form

$$AU = B, \quad (4.11)$$

where $A \in \mathbb{R}^{n_p} \times \mathbb{R}^{n_p}$ is the matrix that needs to be inverted, $U \in \mathbb{R}^{n_p}$ is the unknown vector and $B \in \mathbb{R}^{n_p}$ is the right-hand side vector (n_p being the number of degrees of freedom). We consider a basis of shape functions $\{\varphi_i\}_{i \in \{1, \dots, n_p\}}$ of the approximation space. The components of the right-hand side vector are defined by

$$\forall i \in \{1, \dots, n_p\}, B_i = \int_{\Omega_f} f \varphi_i dV. \quad (4.12)$$

Say that the body force is in the approximation space. There exists $F \in \mathbb{R}^{n_p}$ such that f is under the form

$$f = \sum_{j=1}^{n_p} F_j \varphi_j. \quad (4.13)$$

Replacing f in (4.12) by using (4.13) yields

$$\forall i \in \{1, \dots, n_p\}, B_i = \sum_{j=1}^{n_p} \left(\int_{\Omega_f} \varphi_j \varphi_i dV \right) F_j. \quad (4.14)$$

It means that F and B are related through

$$MF = B, \quad (4.15)$$

where $M \in \mathbb{R}^{n_p \times n_p}$ is the mass matrix whose components are defined by

$$\forall i, j \in \{1, \dots, n_p\}, M_{ij} = \int_{\Omega_f} \varphi_j \varphi_i dV. \quad (4.16)$$

The code uses Lagrange finite elements. The coefficients F_i , $i \in \{1, \dots, n_p\}$, of the body force in the approximation space are the values of the source term at every node. We can thus obtain the body force at the nodes by inverting the mass matrix:

$$F = M^{-1}B. \quad (4.17)$$

Limit of the straight coil geometry

The geometry of the coil is said straight because the meridian section of the coil is a rectangle with square angles, see Figure 4.2. Figure 4.11a shows the intensity of the Kelvin force variation divided by the fluid density

$$\frac{\mathbf{f}_m}{\rho_f} = \frac{\mu_0}{\rho_f} \Delta \chi(T) \nabla \left(\frac{H^2}{2} \right). \quad (4.18)$$

The division by the fluid density is due to the formulation of the momentum equation in SFEMaNS, see (3.8). We can see that the magnetic force is extremely localized at the interior corners of the coil section. The concentration of the force is due to the concentration of the magnetic field, see Figure 4.11b. The normal vector is not defined at a corner and the mathematical solution for the magnetic field is therefore singular. The geometry needs to be curved in order to have a regular solution.

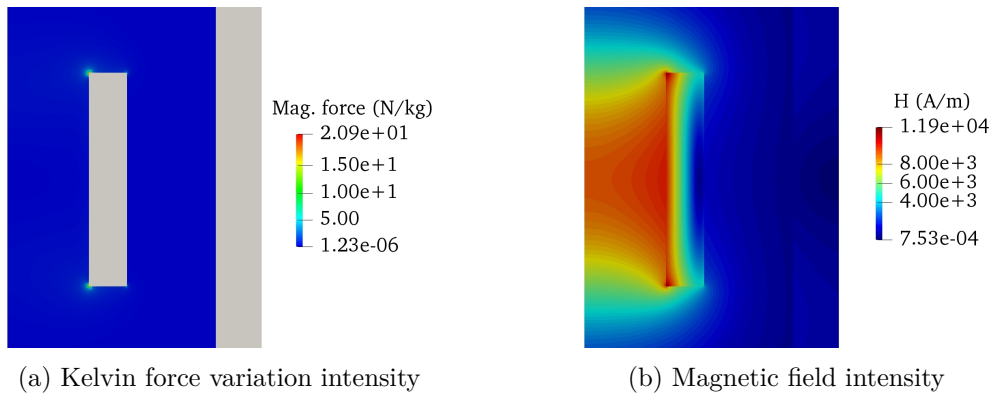


Figure 4.11: Intensity of the Kelvin force variation divided by the fluid density and magnetic field intensity at $t = 10000$ s in a meridian section (symmetry axis on the left).

Use of a curved coil geometry

The geometry of the coil is modified to remove the square angles. The top and bottom boundaries of the coil section are replaced by half circles such that the curved coil is strictly included in the straight coil. The mesh of the meridian section used for the regular oil case is presented in Figure 4.12³. The current density in the magnetostatic equations, given by (4.1), and the source term in the temperature equation, given by (4.2), are adapted to the new geometry. The total current and the total dissipated heat are the same in the two coil geometries.

The two coil geometries give consistent results in term of temperature and velocity. For instance, the maximum temperature increments are close: 37.6°C with a curved coil against 37.3°C with a straight coil for regular oil, 34.1°C with a curved coil against 33.8°C with a straight coil for magnetic oil (temperature fields not displayed). We can suspect that the small difference is due to the smaller exchange surface between the curved coil and the oil.

Figure 4.13 shows the components of the body forces in the magnetic oil: the Kelvin force variation and the Boussinesq force. The azimuthal component of the Kelvin force variation is zero, and is therefore not displayed. The Boussinesq force has an axial component only, and the other components are therefore not displayed. The Kelvin force

³This mesh is used in the case of the regular oil only. Another mesh, locally refined to avoid spurious spatial oscillations, is used in the case of the magnetic oil.

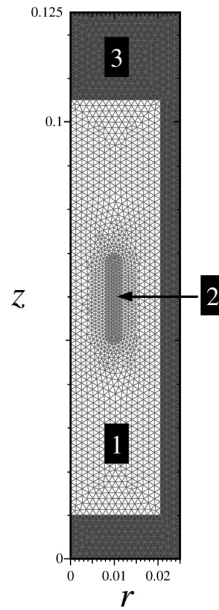


Figure 4.12: Mesh of the meridian section (symmetry axis on the left). Axes in meters. 1: fluid, 2: coil, 3: tank. The mesh size is 8×10^{-4} m in the coil and 1.5×10^{-3} m in the tank.

variation being still localized at the coil boundaries, the view is centred on the coil region. While the Boussinesq force has an axial action only, the Kelvin force variation has both radial and axial actions. At the interior boundary of the coil, the Kelvin force variation pushes the fluid toward the symmetry axis; at the top and bottom boundaries, it pushes the fluid in the other direction (Figure 4.13a). At the top boundary of the coil, the Kelvin force variation pushes the fluid upward; at the bottom boundary of the coil, it pushes the fluid downward (Figure 4.13b). Notice that the Kelvin force variation is almost up-down symmetrical. It indeed depends on the gradient of the magnetic field, which is almost up-down symmetrical as well, see Figure 5 of the article. The Boussinesq force is more diffuse (Figure 4.13c) but, close to the coil, it is clearly weaker in magnitude. The presence of the Kelvin force variation under the coil is consistent with the additional convection cell observed in Figure 4.7. The Kelvin force variation is dominant there and consequently modifies the flow.

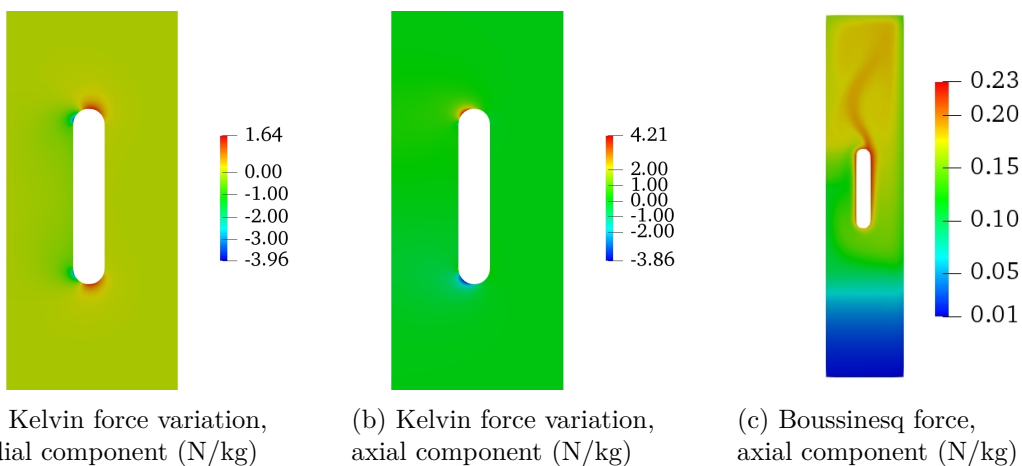


Figure 4.13: Body forces, divided by the fluid density, at $t = 10000$ s in a meridian section (symmetry axis on the left).

4.3.2 Three-dimensional study

In the previous simulations, the solution is assumed axisymmetric and results are obtained with computations on mode 0 only. Here, the computations are performed on 8 modes (mode 0 to mode 7 included) to test this assumption.

3D computations with initial perturbation

The simulations of the article are re-performed on modes 0 to 7 over the whole time range. To test the axisymmetry assumption, modes greater or equal to one of the temperature increment are perturbed at $t = 0$ s. As a matter of fact, these modes are not populated by a source term like the Joule effect carried by mode 0 only. The perturbation can model a possible imperfection in the temperature field, chosen of order 10^{-3}°C and representing 0.01% of the final temperature increment ($30\text{-}40^{\circ}\text{C}$). The magnitude of the perturbation is assumed sufficient for the modes greater or equal to 1 to grow if a breaking of axisymmetry may happen. The modes of the velocity are not perturbed to avoid a non-solenoidal velocity, which would be non-physical. However, the initial temperature perturbation will give rise to velocity perturbations through the Boussinesq force.

We need simple quantities representing, by mode, the fields of velocity and temperature increment in the whole system. We define the modal kinetic energy carried by mode 0:

$$E_k^0 = \int_{\Omega_f} \frac{1}{2} \rho_f [(u_r^{0,\text{cos}})^2 + (u_\theta^{0,\text{cos}})^2 + (u_z^{0,\text{cos}})^2] dV. \quad (4.19)$$

We define the modal kinetic energy carried by mode $m \in \{1, \dots, 7\}$:

$$E_k^m = \int_{\Omega_f} \frac{1}{4} \rho_f [(u_r^{m,\text{cos}})^2 + (u_r^{m,\text{sin}})^2 + (u_\theta^{m,\text{cos}})^2 + (u_\theta^{m,\text{sin}})^2 + (u_z^{m,\text{cos}})^2 + (u_z^{m,\text{sin}})^2] dV. \quad (4.20)$$

Let V be the total volume of the system. We define the modal average temperature increment carried by mode 0:

$$\overline{T - T_0}^0 = \sqrt{\frac{1}{V} \int_{\Omega} ((T - T_0)^{0,\text{cos}})^2 dV}. \quad (4.21)$$

We define the modal average temperature increment carried by mode $m \in \{1, \dots, 7\}$:

$$\overline{T - T_0}^m = \sqrt{\frac{1}{V} \int_{\Omega} \frac{1}{2} [((T - T_0)^{m,\text{cos}})^2 + ((T - T_0)^{m,\text{sin}})^2] dV}. \quad (4.22)$$

E_k^m , $0 \leq m \leq 7$ are homogeneous to Joule and $\overline{T - T_0}^m$, $0 \leq m \leq 7$ are homogeneous to degree Celsius. These quantities are referred to as global quantities in the following.

Figure 4.14 shows the time evolution of E_k^m and $\overline{T - T_0}^m$, for every considered mode m , in the regular oil case. The evolutions of the modes of velocity and temperature increment are similar. Mode 0 is zero initially but it grows until it reaches a permanent value. Modes greater or equal to 1 are not zero initially due to the initial perturbation, they grow until a plateau that lasts until $t = 4000$ s approximately (no change is operated in the model at that time, the own dynamics of the system seems to determine the length of the plateau) and then strongly decrease, finally reaching the numerical zero. Thus, even initially populated, modes greater or equal to 1 decay and do not impact the permanent regime. In the permanent regime, only mode 0 survives, which means that the permanent solution is axisymmetric. Notice that the modes are ordered: mode 0 dominates mode 1, mode 1 dominates mode 2, etc. If the logic is further respected, mode 8 should be dominated by mode 7, mode 9 should be dominated by mode 8, etc. A simulation using

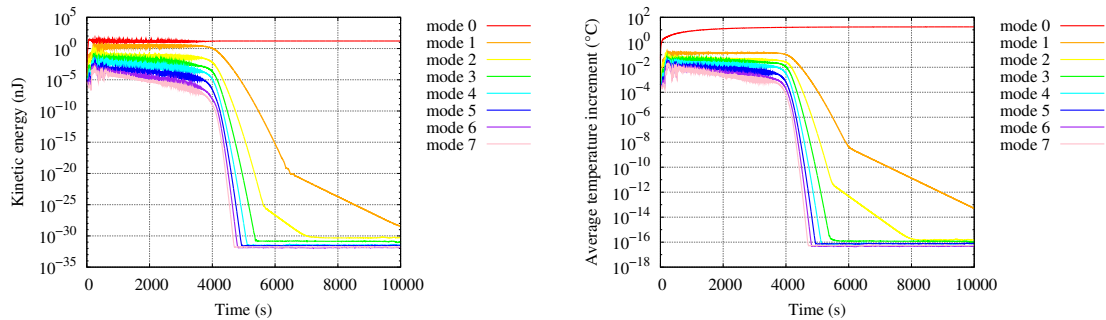
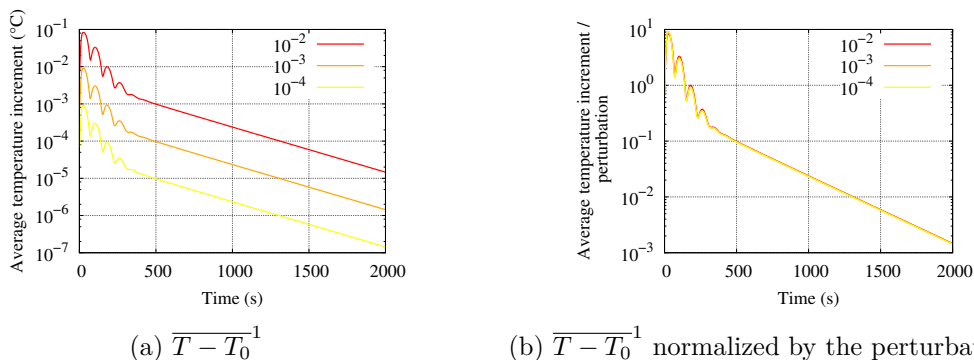


Figure 4.14: Regular oil. Mode-by-mode time evolution of the global quantities.

more modes would not bring another conclusion. Notice also that, even in the transient regime, mode 0 of the temperature increment clearly dominates the other modes. The temperature solution is thus quasi-axisymmetric in the transient regime as well.

Still for the regular oil, Figure 4.15a shows the time evolution of $\overline{T - T_0}^1$ over 2000 s for different values of the initial perturbation. In addition to the first level of perturbation, 10^{-3}°C , the levels of perturbation 10^{-4}°C and 10^{-2}°C are used. The stronger the initial perturbation, the stronger the average temperature increment carried by mode 1. Nevertheless, the evolutions of E_k^1 for all the perturbations follow a similar decrease: even for a stronger level of perturbation, mode 1 decays. Figure 4.15b is the same as Figure 4.15a except that the average temperature increment is normalized by the perturbation. The curves superimpose each other. $\overline{T - T_0}^1$ is thus proportional to the perturbation.



(a) $\overline{T - T_0}^1$

(b) $\overline{T - T_0}^1$ normalized by the perturbation

Figure 4.15: Regular oil. Time evolution of the average temperature increment carried by mode 1 for different levels of perturbation (perturbation in °C).

We now study the magnetic oil case. Figure 4.16 shows the time evolution of E_k^m and $\overline{T - T_0}^m$, for every considered mode m , in this case. The evolutions of the modes of velocity and temperature increment are similar. Mode 0 is zero initially but it grows until it reaches an oscillatory regime around $t = 5000$ s. As in the regular oil case, modes greater or equal to 1 are not zero initially due to the initial perturbation. They all decrease rapidly after initialization but, contrary to the regular oil case, the decrease is not monotonic. Modes greater or equal to 1 increase then decrease twice: around $t = 2000$ s and $t = 4000$ s. At approximately $t = 4000$ s, they definitely decrease to reach the numerical zero. Again, only mode 0 survives in the permanent regime. As in the regular oil case, the permanent solution is axisymmetric. Notice that the modes are still ordered: mode 0 dominates mode 1, mode 1 dominates mode 2, etc. Only mode 5 does not follow this rule during the first 2000 s but it seems to be temporary.

We verify that, in the permanent regime, E_k^0 and $\overline{T - T_0}^0$ are similar to the kinetic energy and the average temperature increment obtained with the axisymmetric computation

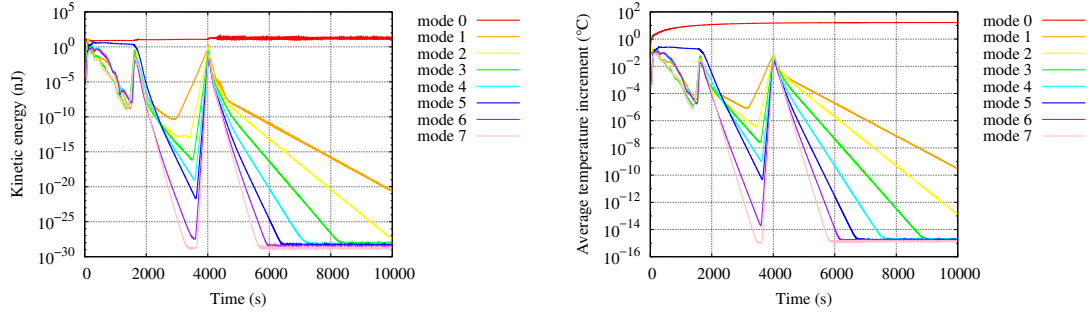


Figure 4.16: Magnetic oil. Mode-by-mode time evolution of the global quantities.

(for the regular oil and the magnetic oil).

3D computations with perturbation in the permanent regime

Previous 3D computations show that the computations on mode 0 are relevant because modes greater or equal to 1 are negligible in the permanent regime. Here, we want to confirm the stability of the axisymmetric solution in the permanent regime. Simulations are performed starting from the axisymmetric solution at $t = 10000$ s with a perturbation on temperature modes greater or equal to 1. The perturbation is again of order 10^{-3}°C . We focus on the regular oil case assuming that results can be extended to the magnetic oil case.

Results lead us to test several coil geometries. As a matter of fact, the coil geometry impacts the symmetry of the solution. The tested coil geometries are: the straight coil of Figure 4.2, the curved coil of Figure 4.12 and the slightly curved coil of Figure 4.17. The latter geometry is between the first two. It adopts the square shape of the coil section but the corners of the coil section are curved.

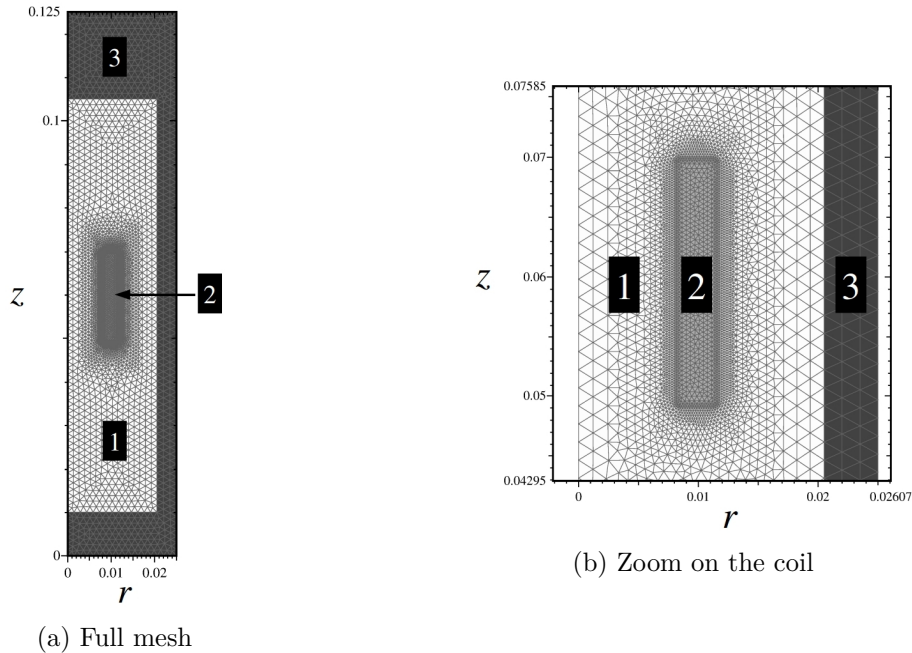


Figure 4.17: Slightly curved coil. Mesh of the meridian section (symmetry axis on the left). Axes in meters. 1: fluid, 2: coil, 3: tank. The mesh size goes from 4×10^{-4} to 2×10^{-4} m in the coil (the mesh is refined at the boundary). The mesh size is 1.5×10^{-3} m in the tank.

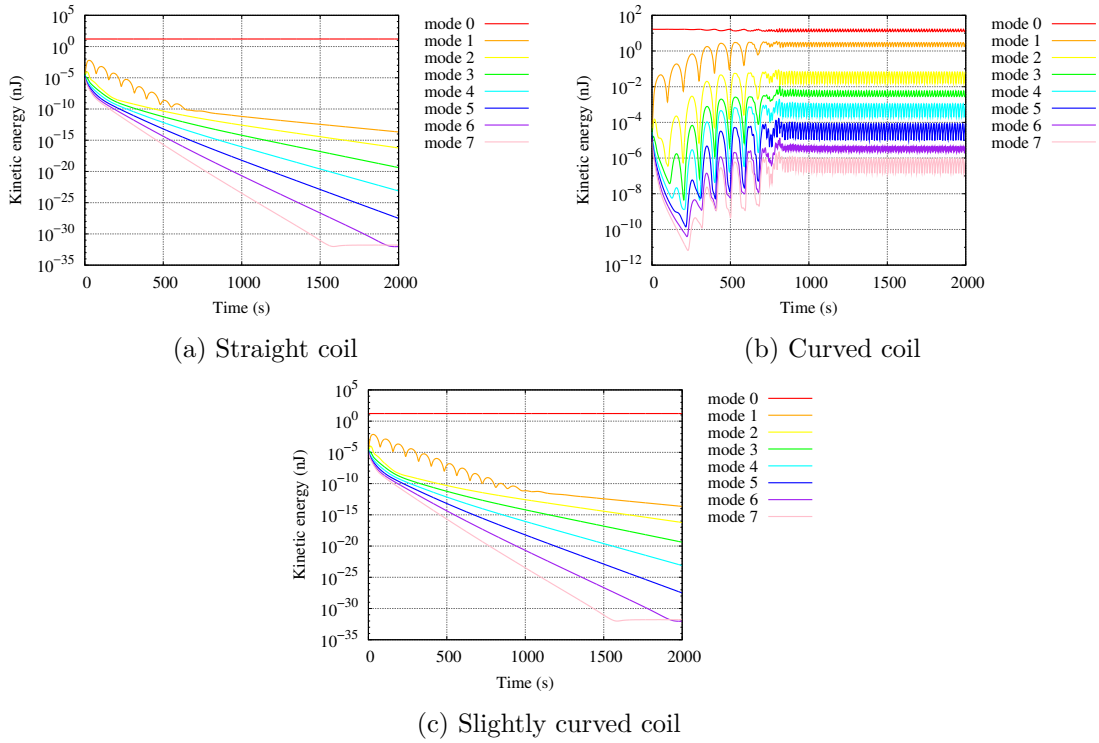


Figure 4.18: Mode-by-mode time evolution of the kinetic energy after restart for the three coil geometries.

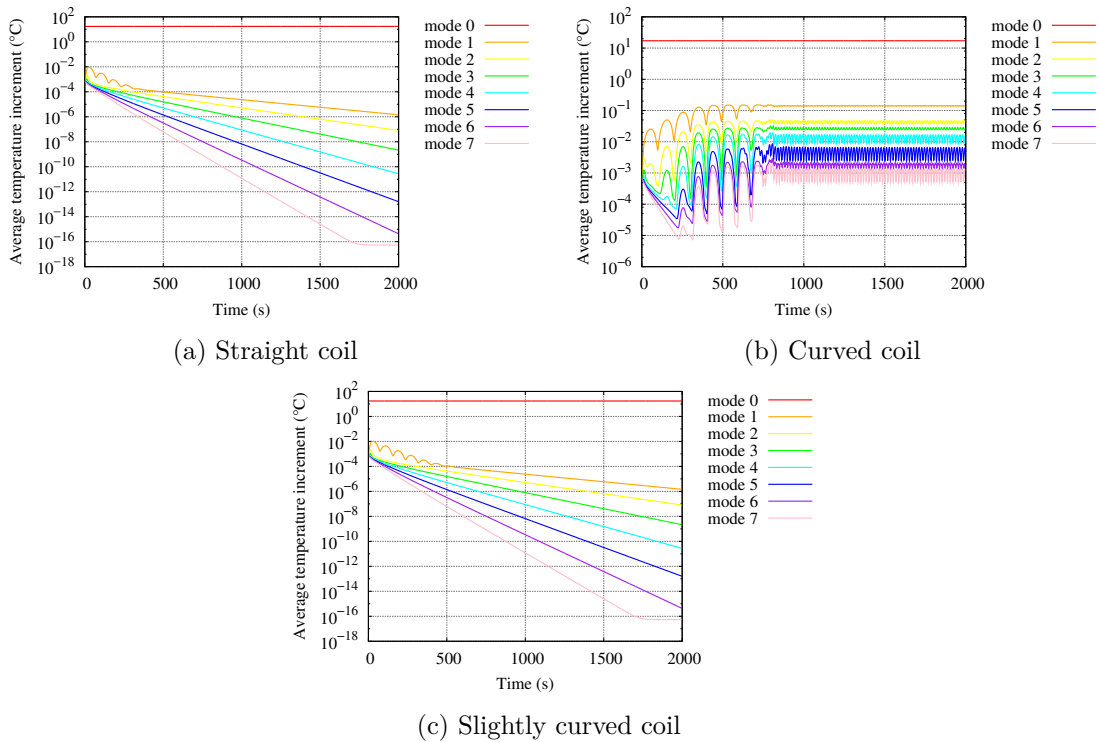


Figure 4.19: Mode-by-mode time evolution of the average temperature increment after restart for the three coil geometries.

Figure 4.18 shows the time evolution of E_k^m , for every considered mode m , after restart. The evolutions of the modal kinetic energies with the straight coil and the slightly curved

coil are similar: mode 0 stays constant; modes greater or equal to 1 are not zero initially, due to the perturbation, and decrease until they reach the numerical zero. For the curved coil, mode 0 stays constant but modes greater or equal to 1 grow until they reach an oscillatory regime around a constant average: modes greater or equal to 1 do not decay as for the two other geometries. The time evolution of $\overline{T - T_0^m}$, for every considered mode m , is very similar, see Figure 4.19. Thus, while the permanent solution is axisymmetric with the straight coil and the slightly curved coil, it is not with the curved coil. Nevertheless, mode 0 of the average temperature increment clearly dominates the other modes (the temperature solution is quasi-axisymmetric).

Visualizations of the temperature increment obtained with the straight coil and the slightly curved coil confirm that the temperature is axisymmetric. Fields are close to that observed in Figure 8a of the article, the circulation of the hot fluid following the symmetry axis. Figure 4.20 shows the temperature increment 2000 s after restart obtained with the curved coil. The lateral view in Figure 4.20a shows that the circulation of the hot fluid deviates from the symmetry axis, which is confirmed by the top view in Figure 4.20b. Visualizations at further times show that the circulation of the hot fluid precesses around the symmetry axis. We can think that the hot fluid close to the coil is not guided upward as well as with the two other geometries. Both the axisymmetry and the stationarity of the solution are broken because modes greater or equal to 1 are populated and present sustained time variations (Figures 4.19b and 4.18b). Note though, that the temperature increment is equivalent to that of in the two other geometries (the geometry does not drastically change the coil temperature).

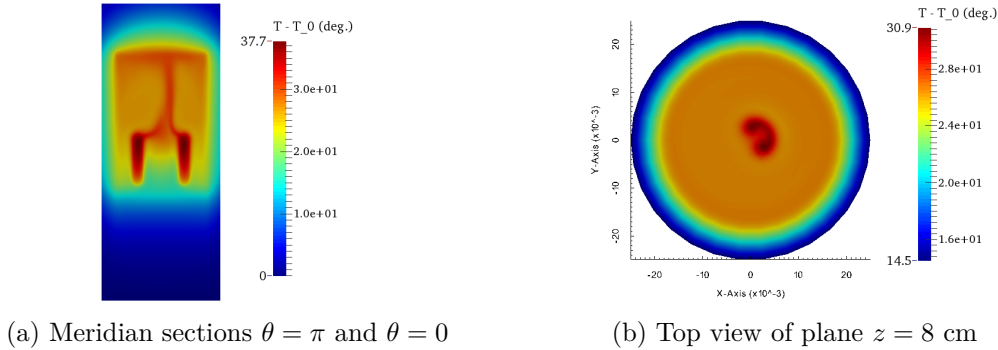


Figure 4.20: Temperature increment 2000 s after restart for the curved coil.

To conclude, the results in the permanent regime obtained with the axisymmetric computations, and their analysis, are valid in 3D.

4.3.3 Use of a temperature-dependent viscosity

Among the thermophysical properties of the oil, the dynamic viscosity is the one that shows the largest variation over the temperature range of the experiment. In this section, we use the law of Andrade [52] to take into account the variation of the dynamic viscosity with temperature. The viscosity of the transformer oil is approximated by

$$\eta(T) = Ae^{\frac{B}{T}}, \quad (4.23)$$

where $A = 9.94 \times 10^{-7}$ Pa \cdot s, $B = 3.23 \times 10^3$ K and T is the temperature in Kelvin. This law is obtained by fitting the manufacturer data with the appropriate function in Python. The comparison between the manufacturer data and the law of approximation is presented in Figure 4.21. The law of approximation is in good agreement with the manufacturer data over the temperature range considered in the experiment.

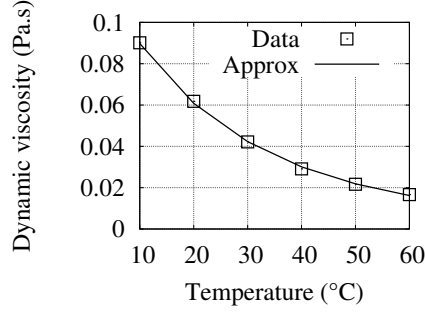
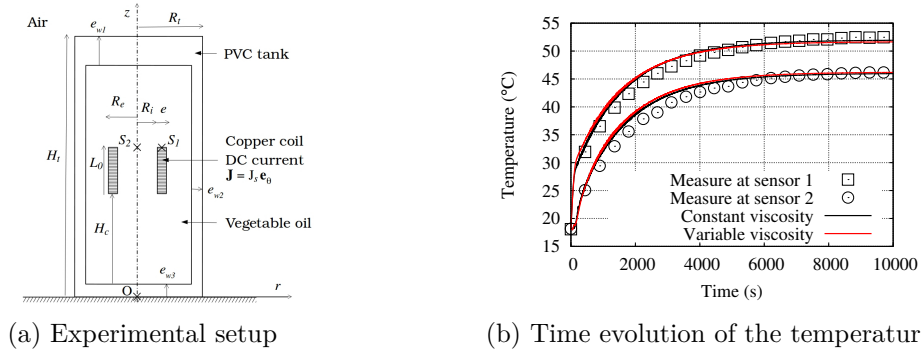


Figure 4.21: Dynamic viscosity of vegetable transformer oil eN 1215 from Midel.

Other simulations show that the viscosity has an impact on the temperature and the velocity. The stronger the viscosity, the lower the velocity and the stronger the temperature. To test the results of the article, the simulation with the regular oil and using a constant dynamic viscosity (that at 40°C) is re-performed by using the approximation given by (4.23). The comparison experiment versus numerics based on the temperature at each sensor is presented in Figure 4.22. The results obtained with the constant dynamic viscosity are also presented. We can see that the results with the variable viscosity and the constant viscosity are very close, and consistent with the experiment. In this case, the use of a temperature dependent-viscosity does not drastically change the temperature. It shows that the use of the dynamic viscosity at 40°C in the article is relevant.



(a) Experimental setup

(b) Time evolution of the temperature

Figure 4.22: Temperature measured at the thermal sensors versus computed temperature when using a constant viscosity and a temperature-dependent viscosity.

Here, the experiment gives the final temperature in the oil (around 40°C) and the viscosity can therefore be chosen appropriately. But, when the temperature of the oil at large times is a priori unknown, it is more accurate to use a temperature-dependent viscosity.

4.3.4 Comparison of the Kelvin and Helmholtz force models

There exist various models to represent the force acting on a magnetic material in a magnetic field [37]. Here, we compare two force models, Kelvin and Helmholtz models, and show that they are equivalent regarding the velocity solution.

Theoretical analysis

We refer to section 2.2.2. Relation (2.39) is important because it means that $\mathbf{f}_K^{\parallel, l}$ and \mathbf{f}_H lead to the same velocity solution for (2.31) and (2.32). As a matter of fact, it follows from (2.39) that if (\mathbf{u}, p) is solution of (2.31) with $\mathbf{f}_m = \mathbf{f}_K^{\parallel, l}$, then $(\mathbf{u}, p - \Phi)$ is solution

of the same equation with $\mathbf{f}_m = \mathbf{f}_H = \mathbf{f}_K - \nabla\Phi$. Only the pressure solution is different. Note that if the velocity is the same, the temperature is the same as well. The velocity is coupled to the temperature but the pressure is not.

In spite of their different expressions, the forces of Kelvin and Helmholtz are equivalent for the velocity solution and the temperature solution, because they are equal up to a gradient. Note that this feature is also used when the gravity is split into a gradient part and a temperature-dependent part under the Boussinesq approximation, see the derivation of (A.27). This feature is also used when the Kelvin body force is split into a gradient part and a temperature-dependent part as well, see the temperature dependent part in (4.3). This equivalence is not ground-breaking. Nevertheless, it partially answers the question of the magnetic body force that needs to be used in the model. Any of these two popular body forces will lead to the same velocity and temperature solutions. Moreover, the reasoning is valid for any magnetic body force. All magnetic body forces will lead to the same velocity and temperature solution as long as they are equal up to a gradient.

Numerical illustration

The previous result is numerically illustrated in the case of the immersed coil. The simulation with magnetic oil is re-performed with the Helmholtz body force instead of the Kelvin body force variation. Recall that the Kelvin body force is split into a gradient part and a temperature-dependent part for numerical instability issues and that only the temperature-dependent part, called variation, is left on the right-hand side. The velocity and temperature fields in the permanent regime obtained by using the two models are compared in Figure 4.23. The fields of velocity and temperature are exactly the same, as expected. Note that the fields are the same all along the simulation time, not just in the permanent regime.

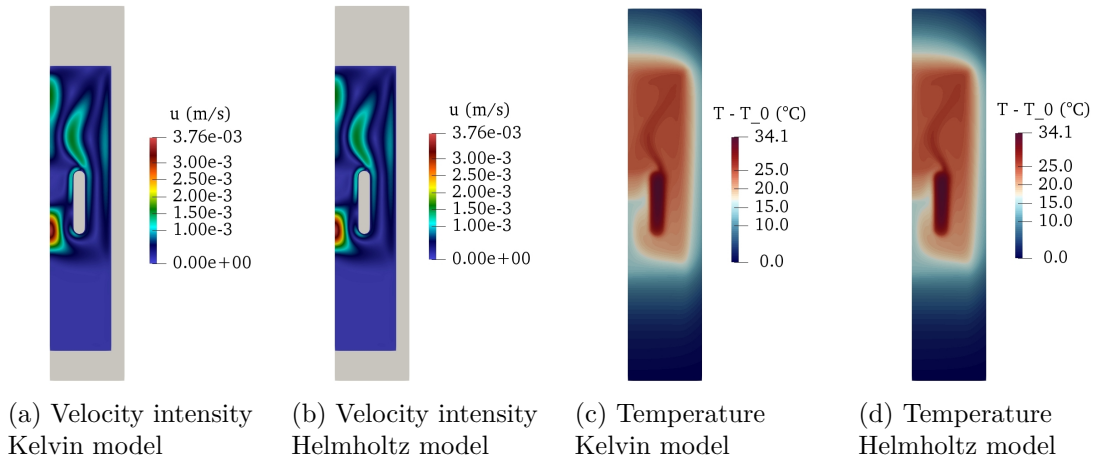


Figure 4.23: Velocity and temperature fields when using Kelvin force model and Helmholtz force model. View in a meridian section (symmetry axis on the left) at $t = 10000$ s.

Figure 4.24 shows the distributions of the magnetic body forces, divided by the fluid density, for both models. The views are centered on the coil region because both forces are mainly localized there. The distributions are totally different. While the Kelvin body force variation is concentrated at the top and bottom boundaries of the coil, the Helmholtz body force is concentrated at the interior boundary of the coil. While the Kelvin body force variation pushes the ferrofluid away from the coil, the Helmholtz body force attracts the ferrofluid toward the coil. The maximum intensity of the forces are nevertheless of the same order: around 4.6 N/kg with the Kelvin model and around 2.1 N/kg with the Helmholtz model.

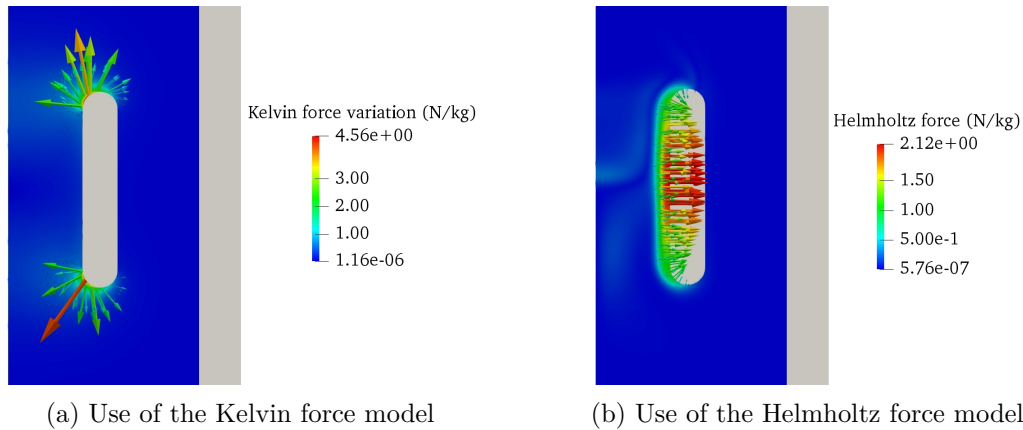


Figure 4.24: Magnetic body force divided by the fluid density in a meridian section (symmetry axis on the left) at $t = 10000$ s. Zoom on the coil region.

The two magnetic force distributions are not the same but they give the same velocity, and thus the same temperature. The theoretical approach is confirmed. The difference lays at the numerical level. The mesh used to compute the solution with the Helmholtz body force is refined at the interior boundary of the coil. It is necessary to refine the mesh where the force is localized to avoid a numerical instability.

4.4 Conclusion of the chapter

A setup representative of a transformer is numerically studied to observe the thermo-magnetic convection effect. The setup consists in a coil immersed in a cylindrical tank. The fluid is either transformer oil or transformer oil-based ferrofluid (volume fraction of nanoparticles $\phi = 10\%$). The thermo-hydrodynamical model for regular oil is validated against experiments. The simulations show that the magnetic oil is more efficient than the regular oil in terms of cooling because the maximum temperature in the coil is reduced by a few degrees. In the model, the thermophysical properties of the magnetic oil are that of the regular oil and this temperature difference is thus only due to the Kelvin body force in the magnetic oil.

An oscillatory phenomenon is observed in the experiment and the simulation using the regular oil: the local temperature measured/computed at the coil, for instance, oscillates in time during the transitory regime. In the simulation, these oscillations are explained by the irregular flow of hot fluid coming from the coil. We can nevertheless not conclude that the same is happening in the experiment due to the lack of consistency between the periods, the amplitudes and the lifetimes of these oscillations in the experimental and numerical data. This phenomenon is negligible in terms of temperature and, while intriguing, does not affect the comparison between the regular oil and the magnetic oil cooling.

Complementary results improve our understanding of the convection happening in this setup, for the regular oil and the magnetic oil. The visualization of the body forces reveals that the Kelvin force dominates the Boussinesq force in terms of intensity and that it is concentrated in the coil area. It modifies the convection pattern by generating an additional convection cell there, leading to enhanced heat transfer. 3D computations using several azimuthal modes show that the velocity and temperature solutions with regular or magnetic oil are axisymmetric in the permanent regime. Thus, axisymmetric computations on mode 0 only appear to be sufficient to simulate this problem. The dynamic viscosity of the oil used in the experiment highly depends on the temperature. Numerical

results obtained with a temperature-dependent viscosity are successfully compared to the experiment, showing that the option of a temperature-dependent viscosity can be further used. The two popular magnetic force models of Kelvin and Helmholtz are theoretically and numerically shown to be equivalent for our problem: they give the same velocity and the same temperature in the magnetic oil. This result is important because it shows that any magnetic body forces of the literature on ferrofluids (which propose many of them) will lead to the same velocity and temperature solutions as long as they are equal up to a gradient.

Chapter 5

Realistic ferrofluid thermophysical properties

In this chapter, we study the benefit of ferrofluids on heat transfer in a setup similar to that of the previous chapter but with two main differences. The simulations are based on the second experimental setup. The particularity of this setup is that the walls of the container are made of aluminium instead of PVC. The model is more realistic: the thermophysical properties of the ferrofluid are different from that of the base fluid due to the addition of the nanoparticles. Classical models are used to obtain the properties of the ferrofluid for every considered volume fraction of nanoparticles. The first section reports a series of results published in the *Journal of Magnetism and Magnetic Material*. The thermo-hydrodynamical model is validated against experimental measurements on pure transformer oil. Simulations are performed with transformer oil-based ferrofluid with various concentrations. The respective effects of the magnetic body force and the modification of the thermophysical properties on the temperature and the flow are discussed. The effect of a ferromagnetic core, like in a transformer, is investigated. The second section presents complementary studies. The most important ones are the 3D analysis, the computation with an alternating current and the comparison with experiments on ferrofluid. The third section details the results obtained with two improvements in the magnetic modeling of the ferrofluid. First, the saturation magnetization of the magnetic nanoparticles is made temperature-dependent; the Curie temperature is introduced. Secondly, the pyromagnetic coefficient term in the temperature equation of ferrofluids is made active and its influence in the immersed coil setup is discussed. As a reading guide, the reader can skip Section 1 of the article in Section 5.1 and go directly to Section 2.

5.1 Article published in Journal of Magnetism and Magnetic Materials

Influence of thermomagnetic convection and ferrofluid thermophysical properties on heat transfers in a cylindrical container heated by a solenoid

Raphaël Zanella^{a,b,c}, Caroline Nore^a, Frédéric Bouillault^b, Jean-Luc Guermond^c, Xavier Mininger^b

^a*LIMSI, CNRS, Univ. Paris-Sud, Université Paris-Saclay, F-91405 Orsay, France*

^b*GeePs, CNRS / CentraleSupélec - UPMC - UPSud, 91192 Gif sur Yvette cedex, France*

^c*Department of Mathematics, Texas A&M University, College Station, TX 77843 USA*

Abstract

The thermal convection in a cylindrical container heated by a solenoid and cooled with an oil-based ferrofluid is numerically studied. The temperature and the velocity fields are compared to those obtained with pure oil to assess the benefits of using ferrofluids for cooling systems like electrical transformers. The influence of the magnetic body force on the flow and the temperature in the system is investigated in various configurations. One original result established in this paper is that the changes in the fluid properties due to the presence of nanoparticles, such as viscosity and thermal conductivity, have a significant impact on the heat transfers. A second result is that the use of a ferromagnetic core enhances the cooling.

Keywords: Ferrofluid, Natural convection, Thermomagnetic convection, Finite element method, Power transformer

1. Introduction

Ferrofluids are suspensions of magnetic nanoparticles in a liquid carrier. Thermal agitation and the addition of a surfactant prevent sedimentation and aggregation of the nanoparticles. If well prepared, the suspension stays stable even under the action of a magnetic field. It is common to use the continuum hypothesis to model ferrofluids. In the presence of a magnetic field, the nanoparticles generate a body force that depends on the gradient of the amplitude of the magnetic field. Among the various models for this effect that are available in the literature, we are going to consider in this paper the so-called Kelvin body force model (N/m^3):

$$\mathbf{F} = \mu_0(\mathbf{M} \cdot \nabla)\mathbf{H}, \quad (1)$$

where μ_0 is the magnetic permeability of vacuum, \mathbf{M} is the ferrofluid magnetization, and \mathbf{H} is the magnetic field. This body force model is dominant in

the literature on ferrofluid modeling, see [1, 2, 3, 4, 5] for instance. Since magnetization decreases with the temperature due to the thermal agitation of the magnetic dipoles of the nanoparticles, temperature gradients generate spatial variations of the magnetic body force. This force is stronger in cold regions than in hot regions. If the magnetic field source is close to the heat source [6], the spatial variations of the magnetic body force lead to a global motion called thermomagnetic convection.

The magnetic nanoparticles, generally composed of metallic material, do not only cause thermomagnetic convection, they also affect the properties of the fluid. The density, the heat capacity, the thermal conductivity, the thermal expansion, and the viscosity of the ferrofluid, seen as an homogeneous medium, are different from that of the base fluid [7, 8]. These changes of properties may have antagonizing effects on the cooling performance of ferrofluids. For example, while the increase of thermal conductivity improves the heat transfer rate, the increase of viscosity slows down the flow and therefore may reduce heat transfers. It is thus unclear whether using ferrofluid for cooling purpose is beneficial or not, [9].

The goal of the present work is to investigate the use of ferrofluids for the cooling of electromagnetic systems, such as power transformers. If the heat transfer rate can be increased in these devices by using ferrofluids, the volume of cooling fluid could be either reduced or mechanical cooling systems could be avoided. Early experiments on small distribution transformers using either a ferrofluid or a pure transformer oil as cooling agent show that the overall temperature is lower in the ferrofluid setup [10]. It is also observed in [11] that heat transfers are enhanced by using ferrofluid instead of regular oil to cool an immersed coil. Encouraging numerical simulations of a transformer prototype are reported in [12]: a strong temperature reduction is observed when using a ferrofluid. Experimental works on a transformer prototype [13, 14] also show the benefit of ferrofluid as coolant: the temperature at hot-spots is significantly lowered. The temperature of an immersed coil is numerically shown to be lower when using ferrofluid in [15], but this result is only theoretical since the impact of the nanoparticles on the physical properties was not taken into account.

The aim of the present paper is to understand the influence on heat transfers of both the thermomagnetic convection and the modifications of the fluid properties due to the presence of magnetic nanoparticles. An immersed coil system, close to that of [11], is simulated with the SFEMaNS code [16]. The thermo-hydrodynamical model is first validated against an experiment on pure transformer oil. The temperature and velocity fields obtained with transformer oil and transformer oil-based ferrofluid are then compared to assess and understand the benefit of using ferrofluids. An iron core is added to observe the effect of a piece of ferromagnetic material representing the magnetic core of an electrical transformer. Classical models for the properties of the ferrofluid taking into account the volume fraction of magnetic nanoparticles are used. The ferrofluid magnetization follows an approximation of Langevin's law, generally considered in the literature to be an appropriate model of the paramagnetic behavior. This model naturally includes the temperature dependence [17].

2. Material and methods

2.1. Problem description

We consider an electromagnetic system constituted of a copper coil immersed in a ferrofluid composed of transformer oil with magnetite nanoparticles in small concentration. The ferrofluid is enclosed in an aluminium container. A magnetic field is produced by a DC current flowing through the coil. The heat source is the Joule effect in the coil. The action of the magnetic field combined with the heat flux generates thermomagnetic convection [6]. This setup is a simplified model of an electrical transformer. In the present paper we present numerical simulations and experimental results on this configuration.

Parameter	H_t	R_t	e_{w1}	e_{w2}	e_{w3}	H_0
Value (cm)	12.5	3.1	1	2	1	3.9
Parameter	L_0	R_i	R_e	R_c	e_{c1}	e_{c2}
Value (cm)	2.1	0.8	1.175	2.6	2	1

Table 1: Dimensions of the experimental setup.

Fig. 1 shows the setup that is used for the experiment and a first series of numerical simulations; the dimensions are reported in Tab. 1. The cap is made of PVC to avoid short circuits. The positions of the thermal sensors are indicated by crosses. Fig. 2 shows two other configurations that are used only for numerical simulations whose purpose is to test the ferrofluid effects. In the first configuration (left panel) there is no ferromagnetic core at the center of the coil, whereas there is one in the second configuration (right panel). In both cases, the dimensions of the coil and the container are the same as those in Fig. 1. The temperature is monitored in the coil in a region where the temperature is close to being maximal; this point is indicated by a cross. The cap of the container is made of aluminium. We have verified numerically that whether the cap is made of PVC or aluminium does not change significantly the temperature distribution. We have chosen to report the numerical results obtained with an aluminium cap since it may better represent an actual transformer.

2.2. Governing equations

In this paper we only consider weakly concentrated ferrofluids (volume fraction of nanoparticles $\phi \leq 7\%$) which, as reported in the abundant literature on the topic, are well described by using the homogeneous fluid hypothesis. The magnetostatic approximation for electromagnetism is used in the solids and in the fluid; the equations are

$$\nabla \times \mathbf{H} = \mathbf{J}, \quad (2)$$

$$\nabla \cdot (\mu \mathbf{H}) = 0, \quad (3)$$

where \mathbf{H} is the magnetic field, \mathbf{J} is the current density, equal to $J_s \mathbf{e}_\theta = \frac{NI}{S} \mathbf{e}_\theta$ in the coil and zero elsewhere (N is the number of windings, I is the enforced

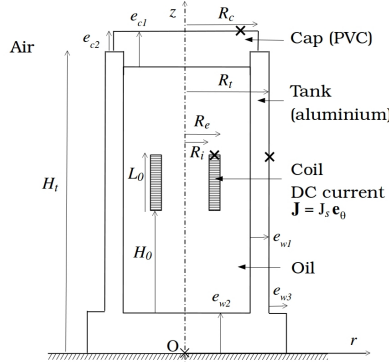


Figure 1: Setup using pure transformer oil (experiment and numerical simulations). The cross marks show the three thermal sensors used to monitor the temperature.

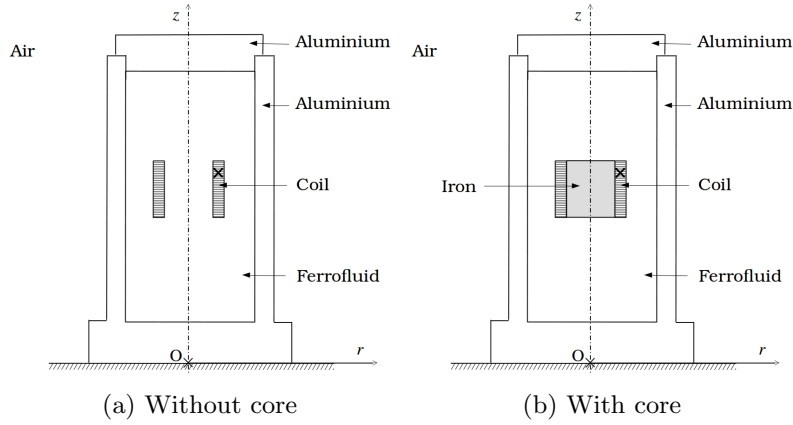


Figure 2: Setups used for numerical simulations with ferrofluid. The cross marks show the points where the temperature is monitored ($r = 1$ cm, $z = 7.5$ cm).

current and S is the section of the coil body), and μ is the magnetic permeability. The motion of the fluid is modeled by the incompressible Navier-Stokes equations:

$$\rho \partial_t \mathbf{u} + \rho (\mathbf{u} \cdot \nabla) \mathbf{u} + \nabla p - \nabla \cdot (\eta(T) \nabla^s \mathbf{u}) = \alpha \rho g (T - T_0) \mathbf{e}_z + \mu_0 M(T) \nabla H, \quad (4)$$

$$\nabla \cdot \mathbf{u} = 0, \quad (5)$$

where \mathbf{u} is the velocity, p is the pressure, T is the temperature, T_0 is the exterior temperature, ρ is the density, η is the dynamic viscosity and α is the thermal expansion. Here we use the notation $\nabla^s \mathbf{u} = \frac{1}{2} (\nabla \mathbf{u} + (\nabla \mathbf{u})^T)$. The buoyancy effects are modeled by using the Boussinesq approximation. The last term on the right-hand side is the simplified expression of the Kelvin body force given in Eq. (1) with the convention $M = \|\mathbf{M}\|$ and $H = \|\mathbf{H}\|$; this expression is obtained by assuming that ferrofluid magnetization \mathbf{M} is instantaneously aligned with the magnetic field \mathbf{H} and $\nabla \times \mathbf{H} = \mathbf{0}$ in the fluid, [1]. The conservation of energy is

modeled as follows:

$$\rho c \partial_t T + \rho c (\mathbf{u} \cdot \nabla) T - \nabla \cdot (\lambda \nabla T) = f_T, \quad (6)$$

where c is the specific heat capacity, λ is the thermal conductivity, and f_T is the heat source, equal to the Joule effect $\frac{RI^2}{V}$ in the coil and zero elsewhere (R is the electrical resistance of the wire and V is the volume of the coil body). The energy production by viscous dissipation is neglected.

The boundary condition for the magnetic problem $\mathbf{H} \times \mathbf{n} = \mathbf{0}$ is enforced at the exterior boundary of the tank and the cap. The non-slip boundary condition $\mathbf{u} = \mathbf{0}$ is applied at the boundary of the fluid domain. The air convection at the top and on the lateral wall of the container is modeled by using a Robin boundary condition on the temperature:

$$-\lambda \nabla T \cdot \mathbf{n} = h(T - T_0), \quad (7)$$

where h is the convection coefficient and \mathbf{n} is the outer unit normal vector. The homogeneous Neumann boundary condition $\partial_z T = 0$ is enforced at the bottom of the tank. The initial conditions are $\mathbf{u} = \mathbf{0}$, $T = T_0$, and $\mathbf{H} = \mathbf{0}$.

2.3. Ferrofluid modeling

We assume that the magnetization intensity is proportional to the magnetic field intensity, and the proportionality constant depends on the temperature:

$$M = \chi(T)H, \quad (8)$$

with χ the susceptibility given by an approximation of Langevin's law [17]:

$$\chi(T) = \frac{\phi \mu_0 \pi d^3 M_0^2}{18 k_B T}, \quad (9)$$

where ϕ is the volume fraction of magnetic material, d is the particle diameter, M_0 is the particle magnetization, and k_B is the Boltzmann constant. Notice that in the present setting, it is essential that χ depends on the temperature for the Kelvin force to be active. If χ is constant, then $\mu_0 M(T) \nabla H = \mu_0 \chi \nabla \frac{1}{2} H^2$, and the Kelvin force in Eq. (4) is just an hydrostatic pressure, which cannot generate any motion. But, when χ depends on T , the gradient of magnetization in the ferrofluid due to the evolution of the temperature leads to a gradient of the magnetic body force in Eq. (4), which generates thermomagnetic convection. In Eq. (3), the magnetic permeability μ is defined to be a piecewise constant. It is equal to $\mu_0(1 + \chi(T_0))$ in the ferrofluid.

The properties of the ferrofluid are obtained from the properties of the transformer oil and the magnetite of the nanoparticles. The density and the specific heat capacity are determined from a mixture law relative to the volume fraction of magnetic material ϕ :

$$\rho_{\text{ff}} = \phi \rho_{\text{p}} + (1 - \phi) \rho_{\text{bf}}, \quad (10)$$

$$\rho_{\text{ff}} c_{\text{ff}} = (1 - \phi) \rho_{\text{bf}} c_{\text{bf}} + \phi \rho_{\text{p}} c_{\text{p}}, \quad (11)$$

where the subscripts “ff”, “bf” and “p” refer to the ferrofluid, the base fluid and the nanoparticles respectively.

The thermal conductivity is described by the classical model of Maxwell for nanofluids [18, 19]:

$$\lambda_{\text{ff}} = \frac{1 + 2\beta\phi}{1 - \beta\phi} \lambda_{\text{bf}}, \quad \beta = \frac{\lambda_{\text{p}} - \lambda_{\text{bf}}}{\lambda_{\text{p}} + 2\lambda_{\text{bf}}}. \quad (12)$$

To avoid sedimentation and aggregation of the nanoparticles, the particles are coated with surfactant. This coating changes some physical properties of the fluid, and this effect is modeled by introducing a second volume fraction, $\tilde{\phi}$, that accounts for the presence of the surfactant. The nanoparticles are supposed to have a diameter $d = 10$ nm and the surfactant thickness is supposed to be $s = 2$ nm. The volume fraction of the nanoparticles free of surfactant and the volume fraction of the nanoparticles when coated with surfactant are related through the following expression:

$$\tilde{\phi} = \left(1 + \frac{2s}{d}\right) \phi. \quad (13)$$

The dynamic viscosity is based on Rosensweig’s model [8]:

$$\eta_{\text{ff}} = \left(1 - \frac{5}{2}\tilde{\phi} + \frac{5}{2}\frac{\tilde{\phi}_c - 1}{\tilde{\phi}_c^2}\tilde{\phi}^2\right)^{-1} \eta_{\text{bf}}. \quad (14)$$

with $\tilde{\phi}_c = 0.74$. The thermal expansion of the magnetic material and the surfactant is neglected and the thermal expansion of the ferrofluid is thus defined by

$$\alpha_{\text{ff}} = (1 - \tilde{\phi})\alpha_{\text{bf}}. \quad (15)$$

2.4. Solid parts modeling

The magnetic permeability μ is equal to μ_0 in the cap, the container walls, and the coil. Based on the dimensions of the coil body, the wire and the number of windings, we estimate that the copper represents $\phi_{\text{Cu}} = 37\%$ of the volume of the coil body. To account for the presence of oil within the coil body, the properties of the coil are homogenized in the numerical simulations by using the expressions:

$$\rho_{\text{coil}} = \phi_{\text{Cu}}\rho_{\text{Cu}} + (1 - \phi_{\text{Cu}})\rho_{\text{xx}}, \quad (16)$$

$$\rho_{\text{coil}}c_{\text{coil}} = \phi_{\text{Cu}}\rho_{\text{Cu}}c_{\text{Cu}} + (1 - \phi_{\text{Cu}})\rho_{\text{xx}}c_{\text{xx}}, \quad (17)$$

where the index xx must be replaced by either bf or ff depending on the configuration considered. The thermal conductivity is given by the analytical law developed in [20, Eq. (12)-(13)]:

$$\frac{\lambda_{\text{coil}}}{\lambda_{\text{xx}}} = 1 - 2\phi_{\text{Cu}} \left(\Lambda + \phi_{\text{Cu}} - \frac{0.075422 \phi_{\text{Cu}}^6 \Lambda}{\Lambda^2 - 1.060283 \phi_{\text{Cu}}^{12}} - \frac{0.000076 \phi_{\text{Cu}}^{12}}{\Lambda} \right)^{-1}, \quad (18)$$

$$\Lambda = \left(1 + \frac{\lambda_{\text{Cu}}}{\lambda_{\text{xx}}}\right) \left(1 - \frac{\lambda_{\text{Cu}}}{\lambda_{\text{xx}}}\right)^{-1}, \quad (19)$$

where λ_{xx} is either λ_{bf} or λ_{ff} depending on the configuration considered. This approach is used in [15] in a similar case.

2.5. Physical properties

The number of windings is $N = 33$. The electrical resistance of the wire is $R = 47 \text{ m}\Omega$. The current flowing in the wire is $I = 12 \text{ A}$.

The transformer oil used in the experiment is the vegetable oil eN 1215. The dynamic viscosity strongly varies with the temperature and is approximated by using the expression:

$$\eta(T) = A \exp\left(\frac{B}{T}\right), \quad (20)$$

with $A \simeq 1.3 \times 10^{-6} \text{ Pa}\cdot\text{s}$, $B \simeq 3.1 \times 10^3 \text{ K}$ and T in K. The comparison between the model (20) and the manufacturer's data is presented in Fig. 3. Since the dependence of the other fluid properties (density, thermal expansion, specific heat capacity, and thermal conductivity) with respect to the temperature is small over the temperature range considered in this work, the said fluid properties are assumed to be constant and are equal to their value at $20 \text{ }^\circ\text{C}$. The properties of the different materials used in this work are presented in Tab. 2.

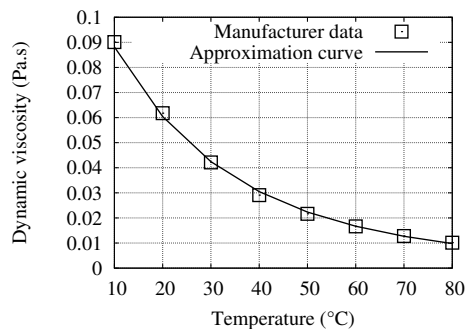


Figure 3: Dynamic viscosity of the vegetable oil eN 1215 with respect to temperature and approximation (20).

Property	Copper	Oil	Aluminum	PVC	Iron	Magnetite
Density (kg/m^3)	8933	922	2.70e3	1.4e3	7870	5.18e3
Thermal expansion (/K)	-	7.4e-4	-	-	-	-
Heat capacity ($\text{J}/\text{K}\cdot\text{kg}$)	385	1970	945	1e3	447	630
Therm. cond. ($\text{W}/\text{m}\cdot\text{K}$)	401	0.166	201	0.16	80.2	6

Table 2: Properties used in the simulations.

The magnetization of the magnetite is $M_0 = 446 \text{ kA}/\text{m}$ and the relative magnetic permeability of the iron core is taken equal to 1000.

3. Computational details

3.1. Numerical method

The numerical simulations are done with the magnetohydrodynamics code called SFEMaNS (see [16]). The approximation in space uses Fourier expansions and finite elements. The method is based on cylindrical coordinates, and every field f is solved as a partial Fourier sum relative to the azimuthal direction

$$f(r, \theta, z) = \sum_{m=0}^{m_{\max}} f_m^c(r, z) \cos(m\theta) + \sum_{m=1}^{m_{\max}} f_m^s(r, z) \sin(m\theta), \quad (21)$$

where m_{\max} is the maximum number of complex Fourier modes. The Fourier coefficients $f_m^c(r, z)$ and $f_m^s(r, z)$ are approximated by using Lagrange finite elements in the meridian section. Once the nonlinear terms are made explicit in Eq. (4)-(6), all the Fourier coefficients can be solved independently in parallel. The nonlinear terms are computed by using a parallelized version of FFT3W. The linear algebra for each Fourier coefficient is done in parallel by using subroutines from the portable extensible toolkit for scientific computation library (PETSc) [21]. In conclusion, the SFEMaNS code is parallelized in the Fourier direction and in each meridian section.

Quadratic, \mathbb{P}_2 , continuous Lagrange elements are used for the temperature and the velocity and linear, \mathbb{P}_1 , continuous Lagrange elements are used for the pressure to ensure the inf-sup condition. The magnetic field is approximated by using quadratic continuous Lagrange elements, with a technique to enforce $\nabla \cdot (\mu \mathbf{H}) = 0$ based on a penalty method. The coupling across the axisymmetric interfaces of discontinuous electric conductivity or magnetic permeability is enforced by an interior penalty method. SFEMaNS has been thoroughly validated on numerous analytical solutions and against other magnetohydrodynamics codes [16, 22, 23, 24].

The equations considered in this paper are solved according to the flowchart shown in Fig. 4. All the computations reported in this paper are done assuming axisymmetry, i.e., $m_{\max} = 0$. We have done various computations with $m_{\max} > 0$ (not reported here) and observed that the solution is axisymmetric in the conditions considered here.

3.2. Finite element meshes

The numerical simulations reported in this paper are done with two different meridian meshes. For the simulations in the configuration without core, the mesh is composed of 3786 \mathbb{P}_1 nodes and 14048 \mathbb{P}_2 nodes. The mesh for the configuration with a core is composed of 4723 \mathbb{P}_1 nodes and 17762 \mathbb{P}_2 nodes. The mesh size goes from 0.04 cm in the coil and close to the core boundary to 0.15 cm at the exterior boundary of the container, see Fig. 5.

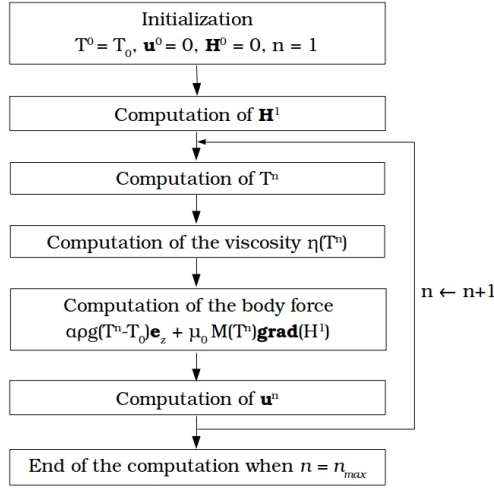


Figure 4: Flowchart of the method; n_{\max} is the maximum number of iterations. Due to the DC current, the magnetic field is computed only once.

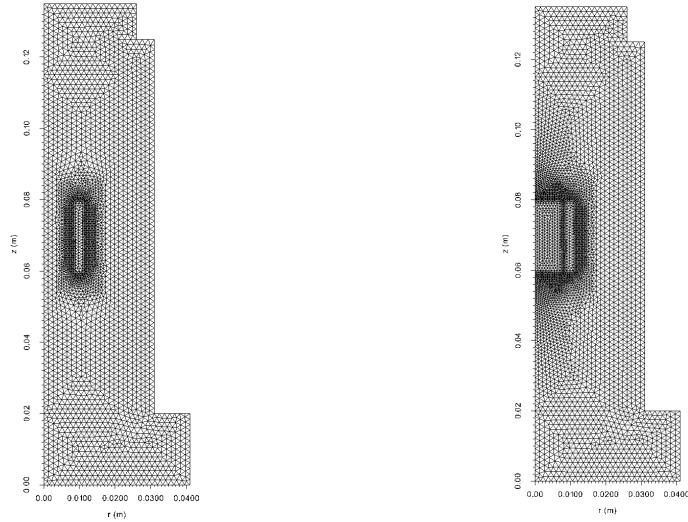


Figure 5: Finite element \mathbb{P}_1 meshes. Left: without core; Right: with core.

In order to test the accuracy of the method we have done computations with various mesh sizes. We show in Fig. 6 two series of computations: one is done on the configuration with pure transformer oil and without the core using the mesh composed of 3786 \mathbb{P}_1 nodes and 14048 \mathbb{P}_2 nodes, the other series is done on the refined mesh obtained from the previous one by dividing each triangle into four new triangles. The global kinetic energy and the L^2 -norm of the temperature are shown as functions of time for the two meshes. We observe that refining the mesh does not bring any significant change to the results, thereby showing that the approximation error is negligible for any practical purpose.

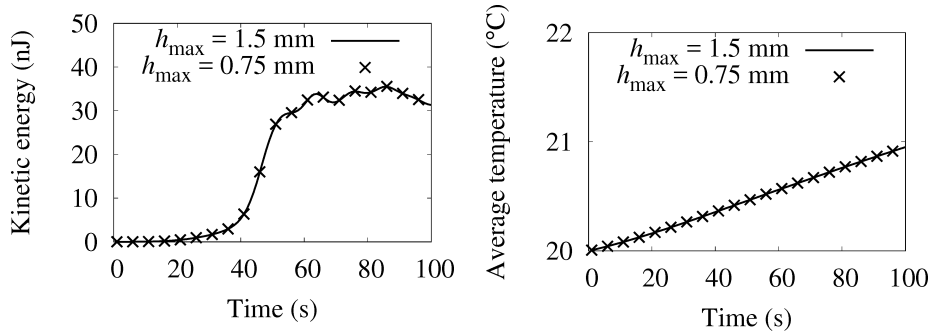


Figure 6: Grid dependence test.

4. Experiment vs. numerics using pure transformer oil

Here, the thermo-hydrodynamical model is validated against experimental data obtained using pure transformer oil. The Kelvin force is zero in this case. We show in Fig. 7 the time evolution of the temperature for the three thermal sensors, see Fig. 1. The convection coefficient $h = 8 \text{ W/m}^2 \cdot \text{K}$ has been optimized to match this experiment and is within the typical range often reported in the literature, [25]. We have observed in the numerical simulations that the oscillations that are visible at the coil sensor are due to an unstable plume of hot fluid flowing up from the coil to the top wall. The period is about 6 s. The numerical results are close to the experimental ones, and the thermo-hydrodynamical model is thus validated.

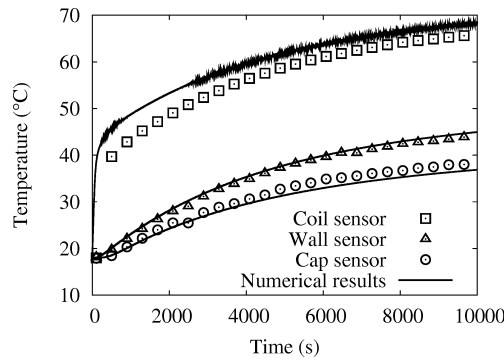


Figure 7: Comparison of the numerical results with the experimental data using pure transformer oil.

5. Numerical simulations with ferrofluid

In this section we report on numerical simulations done with ferrofluids. As previously explained, the properties of the fluid are changed due to the presence of the nanoparticles and an additional (magnetic) body force is present in the

momentum equations. Five volume fractions of nanoparticles ϕ are tested: 0 (pure oil), 1, 3, 5 and 7%.

5.1. Influence of ϕ on the temperature

Fig. 8 shows the time evolution of the temperature at a point in the coil where the temperature is close to being the highest. The results for the volume fractions 0, 1, 3, 5 and 7% are reported. The results in the left panel have been obtained for the configuration without core, and the results in the right panel have been obtained for the configuration with a ferromagnetic core. We observe that, for all the volume fractions considered, the higher the volume fraction, the lower the temperature over the entire time range. In the absence of core, the temperature difference between $\phi = 0$ and $\phi = 7\%$ is approximately $4\text{ }^\circ\text{C}$ at $t = 10000\text{ s}$. In the presence of the ferromagnetic core, this temperature difference is approximately $13\text{ }^\circ\text{C}$. These simulations show that the heat transfer rate is improved when using ferrofluid instead of regular oil. This temperature difference is the highest when there is a ferromagnetic core.

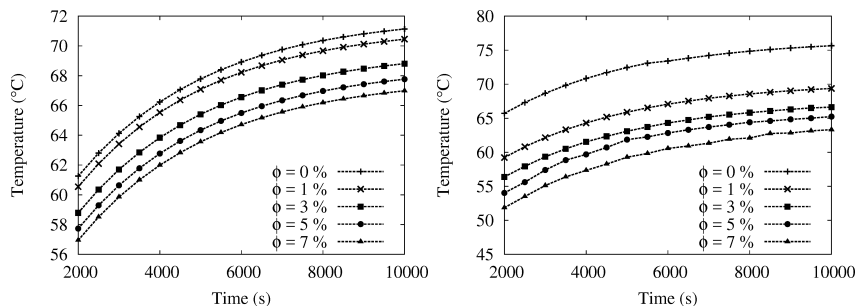


Figure 8: Time evolution of the temperature at the hot spot for various volume fractions of nanoparticles. Left: Without core; Right: With core.

5.2. Compared influence of physical properties and the Kelvin force

In order to compare the effect of the Kelvin force with the changes of physical properties due to the presence of the nanoparticles, we now perform computations with the ferrofluid but with the Kelvin force being switched off. The results are reported in Fig. 9 (no core) and Fig. 10 (core). In each graph, we show again the time evolution obtained with $\phi = 0$ and $\phi \neq 0$ with the Kelvin force being active, and we report also the time evolution obtained with $\phi \neq 0$ and the Kelvin force being switched off. In the absence of core, the effects of the changes in the physical properties are of the same order as that of the Kelvin force. For instance, with $\phi = 7\%$ and at $t = 10000\text{ s}$, the change in physical properties reduces the temperature by $2\text{ }^\circ\text{C}$ approximately and the Kelvin force further reduces the temperature by $2\text{ }^\circ\text{C}$.

When there is a ferromagnetic core, the effects due to the changes in physical properties are small compared to the effects of the Kelvin force. For instance, for $\phi = 7\%$, at $t = 10000\text{ s}$, the changes of the physical properties reduce the

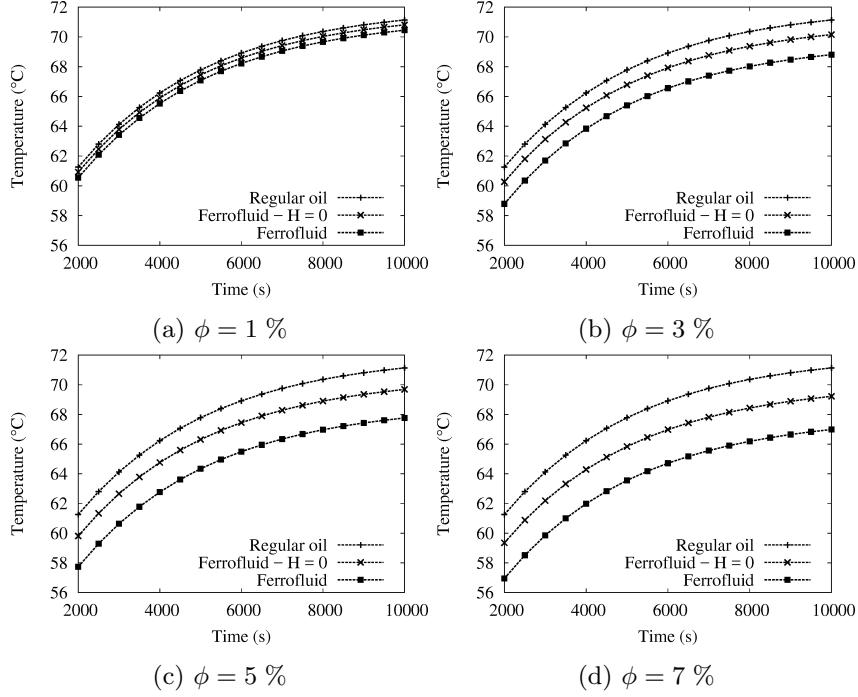


Figure 9: Setup without ferromagnetic core. Time evolution of the temperature at the hot spot with and without the Kelvin force.

temperature by $3\text{ }^{\circ}\text{C}$ approximately, and the Kelvin force further reduces the temperature by $10\text{ }^{\circ}\text{C}$.

In conclusion, the numerical simulations reported in this section show that the changes in physical properties can affect the temperature of the system in a non negligible manner, and in some cases can be of the same order as the effects of the Kelvin force.

5.3. Temperature and velocity fields with and without Kelvin force

In this section we fix $\phi = 7\%$, and we compare the temperature and velocity fields in the meridian section at $t = 10000\text{ s}$ in the same configurations as in §5.2; namely, $\phi = 0$, $\phi = 7\%$ without the Kelvin force, and $\phi = 7\%$ with the Kelvin force.

We show in Fig. 11 and Fig. 12 the temperature and the velocity fields obtained in the configuration without ferromagnetic core. We observe the same behavior on the temperature field as that reported in §5.2 for the hot spot. The temperature decrease induced by the Kelvin force has its origin in the change in the convection pattern. The convection cells in the panels 12a and 12b are similar but are clearly different from that in panel 12c. In this panel, we observe that the Kelvin force generates a second convection cell inside the coil, close to the bottom of the coil. The modifications of the flow induced by the Kelvin force strengthens the heat transfer rate.

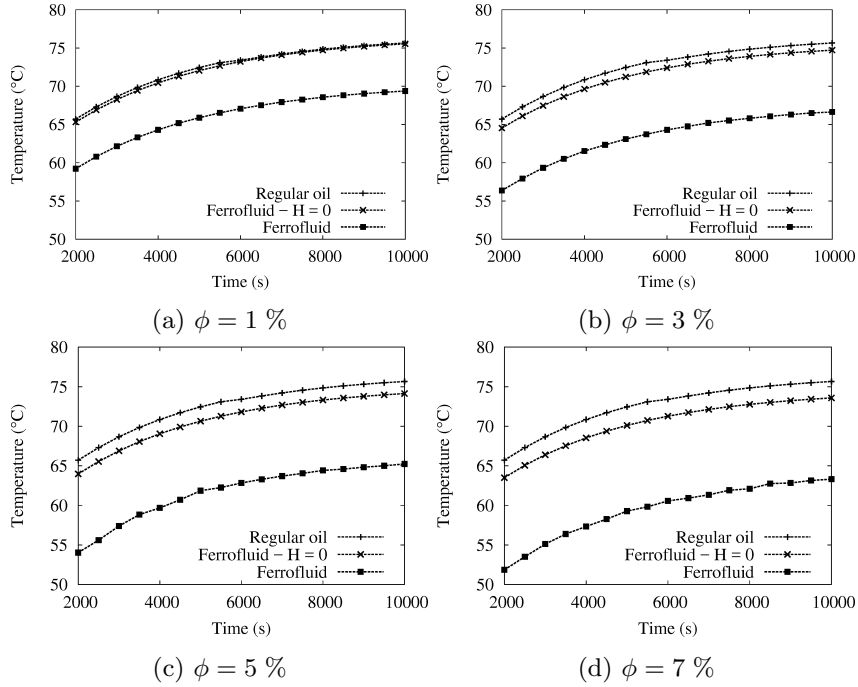


Figure 10: Setup with ferromagnetic core. Time evolution of the temperature at the hot spot with and without the Kelvin force.

The same types of results are presented in Fig. 13 and Fig. 14 for the configuration with the ferromagnetic core. Again, the maximum temperature in the system is reduced when the pure oil is replaced by ferrofluid and with the Kelvin force switched off (from 77.63 °C to 75.3 °C). The action of the Kelvin force makes the convection more vigorous and the cooling is consequently more efficient (from 75.3 °C to 64.4 °C). The temperature drop due to the Kelvin force is more pronounced here (10.9 °C with the core, 2.2 °C without the core). Notice that for pure transformer oil the maximum temperature is larger in the configuration with the ferromagnetic core than in the configuration without the core (71.2 °C without the core, 77.6 °C with the core). This effect is reversed with the ferrofluid ($\phi = 7\%$); the maximum temperature decreases from 67.1 °C without the core to 64.4 °C with the core. The core has thus a negative impact when using pure transformer oil and a positive one when using ferrofluid. The velocity field is strongly modified by the presence of the core; the core blocks the upward flow along the axis, see Fig. 14c. Notice that when the Kelvin force is active there are recirculation cells at the top and at the bottom of the core; the top and bottom spatial distributions of the velocity are almost symmetrical. These two convection cells enhance the cooling effect. Notice finally that the axial velocity is significantly higher when there is a ferromagnetic core.

We show in Fig. 15 the radial temperature profile at $z = 7.5$ cm and $t = 10000$ s. This height is that of the hot spot thermal sensor. One can clearly

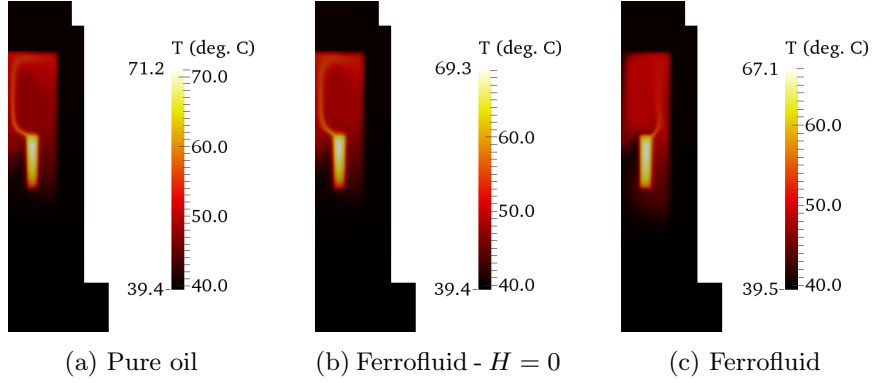


Figure 11: Setup without core ($\phi = 7\%$ for (b) and (c)). Temperature field in the meridian plane at $t = 10000$ s.

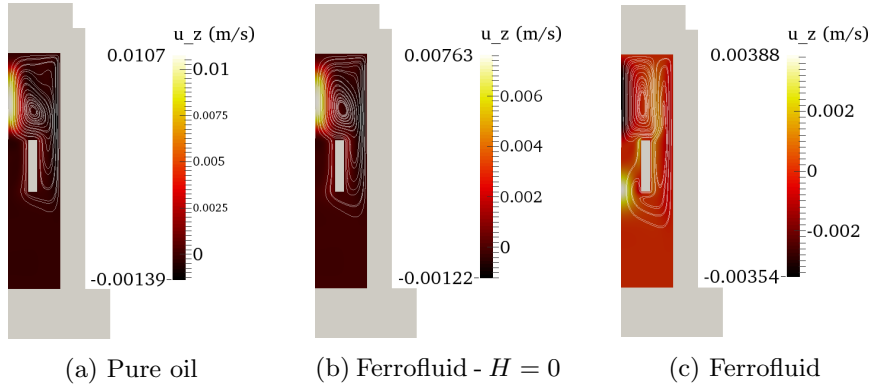


Figure 12: Setup without core ($\phi = 7\%$ for (b) and (c)). Axial velocity field and streamlines in the meridian plane at $t = 10000$ s.

identify the core, coil, fluid and wall regions on the three curves shown in the figure. The plateaus correspond to the core and the wall. The temperature drop observed in the core when the pure oil is replaced by the ferrofluid and the Kelvin force switched off is about 2°C . The temperature drop is about 17°C when the Kelvin force is active in the fluid.

5.4. Maximum temperature and Nusselt number

Fig. 16 shows the maximum temperature in the system at $t = 10000$ s for all the volume fractions considered. The results shown in Fig. 16a correspond to the configuration without the ferromagnetic core, and the results shown in Fig. 16b correspond to the configuration with the core. In each panel we compare the maximum temperature observed when the Kelvin force is active with the temperature observed when the Kelvin force is inactive. For both cases (core or not), the temperature decreases with the volume fraction. Also, for each concentration, the Kelvin force has a positive effect on the cooling. The thermomagnetic effect is stronger when the core is present.

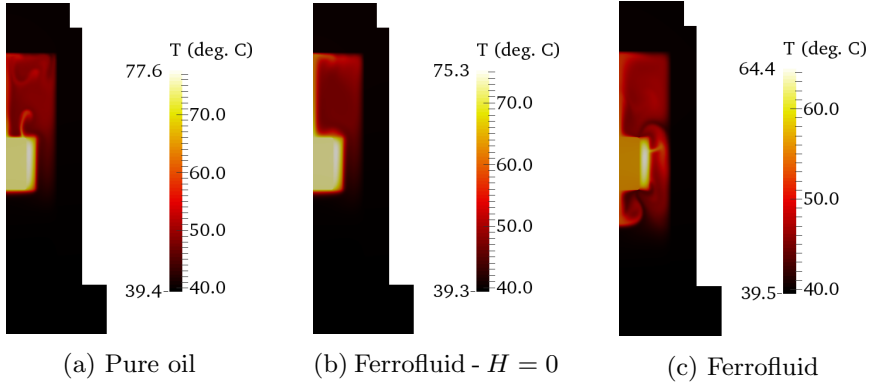


Figure 13: Setup with core ($\phi = 7\%$ for (b) and (c)). Temperature field in a meridian plane at $t = 10000$ s.

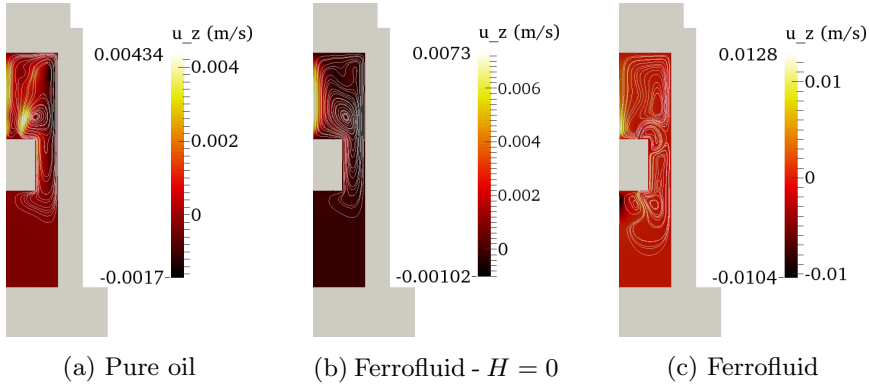


Figure 14: Setup with core ($\phi = 7\%$ for (b) and (c)). Axial velocity field and streamlines in a meridian plane at $t = 10000$ s.

The efficiency of thermal convection is usually characterized in the literature by a Nusselt number, which, in the present case, we define as follows:

$$Nu = \frac{T_{\max}^{\text{cond}} - T_0}{T_{\max}^{\text{conv}} - T_0}, \quad (22)$$

where T_{\max}^{cond} is the maximum temperature in the system when considering only thermal conduction (the velocity is set to zero), and T_{\max}^{conv} is the maximum temperature in the system when the convection is active. Fig. 17 shows the Nusselt number computed at $t = 10000$ s for all the volume fractions considered. The results shown in Fig. 17a correspond to the configuration without the ferromagnetic core; the results shown in Fig. 17b correspond to the configuration with the core. Without the core, the Nusselt number decreases with the volume fraction, whether the Kelvin force is active or not. As expected though, for each concentration, the Nusselt number is larger when the Kelvin force is active. With core, we observe again that the Nusselt number is larger when the Kelvin force is active. The Nusselt number decreases as the volume fraction

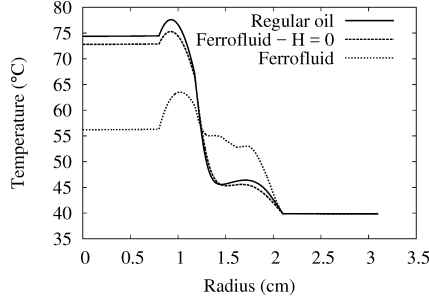


Figure 15: Setup with core (ferrofluid with $\phi = 7\%$). Temperature profile $T(r, z = 7.5 \text{ cm})$ at $t = 10000 \text{ s}$.

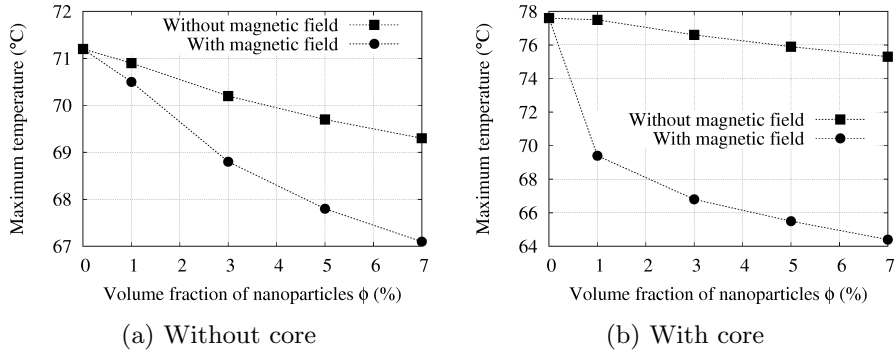


Figure 16: Maximum temperature in the system at $t = 10000 \text{ s}$ as a function of the volume fraction of nanoparticles.

increases when the Kelvin force is switched off. The behavior of the Nusselt number is not monotone when the Kelvin force is active: it first increases until $\phi = 3\%$ and then decreases.

These graphs show again that the thermomagnetic convection improves the cooling of the solenoid by increasing the heat transfer rate. Notice that comparing the Nusselt numbers in the various configurations must be done with care: it may not be appropriate to estimate which configuration is the most efficient for heat transfers. For instance, without core and with the Kelvin force active, the Nusselt number at $\phi = 7\%$ is smaller than that at $\phi = 0\%$ whereas the cooling is more efficient (see Fig. 16a).

5.5. Influence of the ferromagnetic core

The core has two main effects on the heat transfer process: it blocks the upward motion of the flow close to the axis, and its high magnetic permeability ($\mu_r = 1000$) changes the magnetic field, therefore changing the Kelvin force.

To discriminate the influence of these two effects, we set $\phi = 7\%$ and we simulate the configuration with a core whose magnetic permeability is the same as that of the ferrofluid, i.e., $\mu_r \simeq 1.75$. The magnetic field that is generated in this situation is the same as that obtained with ferrofluid in the configuration without core. Hence, this situation only tests the blocking effect of the core.

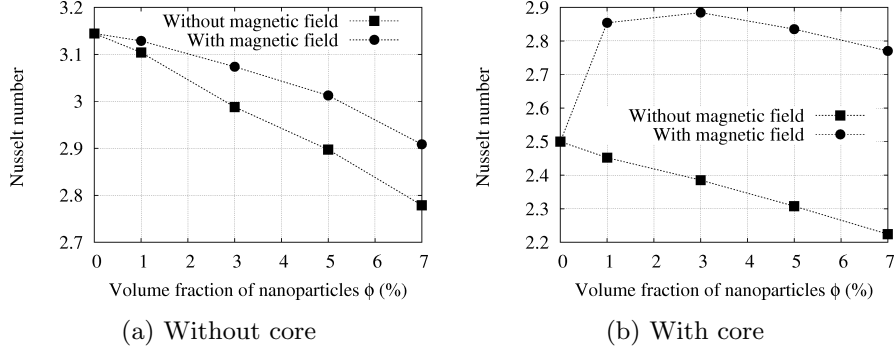


Figure 17: Nusselt number at $t = 10000$ s as a function of the volume fraction of nanoparticles.

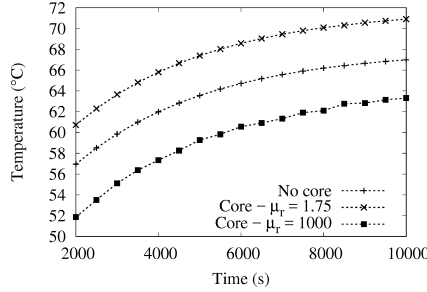


Figure 18: Ferrofluid cooling ($\phi = 7\%$). Effect of the core and its magnetic permeability on the time evolution of the temperature at the hot spot.

Fig. 18 shows the effect of the core and its magnetic permeability on the temperature at the hot spot. The blocking effect of the core has a negative influence on the cooling performance; the temperature is about $4\text{ }^\circ\text{C}$ higher than in the configuration without the core at $t = 10000$ s. This confirms that blocking the flow in the core region reduces the heat transfer rate. When the magnetic permeability is that of iron ($\mu_r = 1000$), the cooling performance is increased: the temperature at the hot spot is about $8\text{ }^\circ\text{C}$ less than that obtained with $\mu_r = 1.75$. The blocking effect of the core is thus more than compensated by increasing the magnetic permeability from $\mu_r = 1.75$ to $\mu_r = 1000$.

Fig. 19 shows the effect of the core and its magnetic permeability on the magnetic field. As expected, the magnetic field in the configuration without core is the same as in the configuration with a core with magnetic permeability $\mu_r = 1.75$. When $\mu_r = 1000$, the magnetic field gets stronger in the fluid region. This increased magnetic field creates the strong convection cells observed in Fig. 14c, which in turn enhances the cooling efficiency.

Figure 20 shows the time evolution of the temperature drop at the hot spot between a case without Kelvin force and a case with the Kelvin force active for three configurations. The curve denoted as 'No core' corresponds to the case without core (see Fig. 11); the 'Core- $\mu_r = 1000$ ' curve corresponds to the case with a core whose magnetic permeability is 1000 (see Fig. 13); the

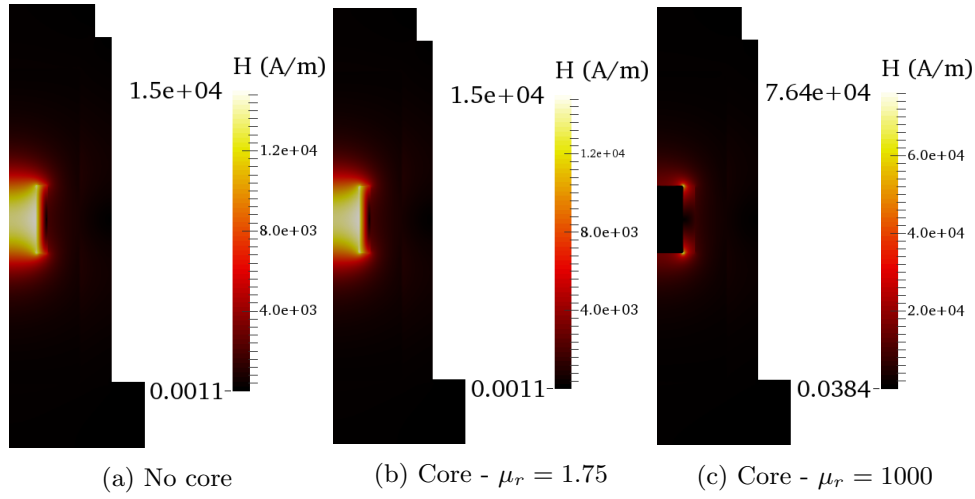


Figure 19: Ferrofluid cooling ($\phi = 7\%$). Effect of the core and its magnetic permeability on the magnetic field intensity.

'Core- $\mu_r = 1.75$ ' curve corresponds to the case with a core whose magnetic permeability is 1.75. The temperature drop goes from about 2 °C without core to 4 °C with the $\mu_r = 1.75$ core and to about 12 °C with the $\mu_r = 1000$ core. Consequently, the change in the magnetic permeability and the associated enhancement of the magnetic field have more impact on the temperature drop than the blocking effect of the core.

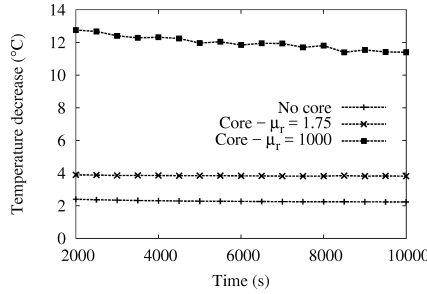


Figure 20: Ferrofluid cooling ($\phi = 7\%$). Effect of the core and its magnetic permeability on the temperature drop at the hot spot due to the Kelvin force.

6. Conclusions

We have numerically simulated the natural convection of a ferrofluid in a cylindrical container heated by a solenoid. The thermo-hydrodynamical model is first validated against an experiment using transformer oil. Simulations with different volume fractions of magnetic nanoparticles are then performed to observe the heat transfer effect of the properties of the ferrofluid and of the ther-

momagnetic convection. In order to make this work more representative of an electrical transformer, we have also studied the influence of a ferromagnetic core.

The ferrofluid appears to be an interesting cooling solution. The maximum temperature decreases as the volume fraction of nanoparticles increases. The heat transfers are increased by the presence of a ferromagnetic core. The Kelvin force significantly modifies the flow pattern whether there is a ferromagnetic core or not. The numerical results also demonstrate that the changes of the physical properties due to the nanoparticles significantly enhance the heat transfers. We have shown that the notion of Nusselt number must be used with care when comparing the cooling efficiency of the various configurations investigated in the present work. Finally, the high magnetic permeability of the core is shown to increase the magnetic field in the fluid region, causing a strengthening of the cooling by thermomagnetic convection.

Acknowledgement

This work was supported by the Labex LaSIPS (Nano-in-Oil Grant). The HPC resources for SFEMaNS were provided by GENCI-IDRIS (grant 2017-0254) in France and by the Texas A&M University Brazos HPC cluster. Support from the National Science Foundation under grants DMS 1620058, DMS 1619892 is acknowledged.

References

- [1] J. L. Neuringer, R. E. Rosensweig, Ferrohydrodynamics, *Physics of Fluids* 7 (12) (1964) 1927–1937.
- [2] H. Yamaguchi, I. Kobori, Y. Uehata, K. Shimada, Natural convection of magnetic fluid in a rectangular box, *Journal of Magnetism and Magnetic Materials* 201 (1999) 264–267.
- [3] S. M. Snyder, T. Cader, B. A. Finlayson, Finite element model of magnetoconvection of a ferrofluid, *Journal of Magnetism and Magnetic Materials* 262 (2003) 269–279.
- [4] H. Yamaguchi, X.-R. Zhang, X.-D. Niu, K. Yoshikawa, Thermomagnetic natural convection of thermo-sensitive magnetic fluids in cubic cavity with heat generating object inside, *Journal of Magnetism and Magnetic Materials* 322 (2010) 698–704.
- [5] P. S. B. Szabo, W.-G. Fürth, The transition from natural convection to thermomagnetic convection of a magnetic fluid in a non-uniform magnetic field, *Journal of Magnetism and Magnetic Materials* 447 (2018) 116–123.
- [6] S. Odenbach, *Magnetoviscous Effect in Ferrofluids*, Springer, 2002.

- [7] V. E. Fertman, L. E. Golovicher, N. P. Matusevich, Thermal Conductivity of Magnetite Magnetic Fluids, *Journal of Magnetism and Magnetic Materials* 65 (1987) 211–214.
- [8] R. E. Rosensweig, *Ferrohydrodynamics*, Cambridge University Press, 1985.
- [9] M. T. Krauzina, A. A. Bozhko, P. V. Krauzin, S. A. Suslov, The use of ferrofluids for heat removal: Advantage or disadvantage?, *Journal of Magnetism and Magnetic Materials* 431 (2017) 241–244.
- [10] V. Segal, K. Raj, An investigation of power transformer cooling with magnetic fluids, *Indian Journal of Engineering & Materials Science* 5 (1998) 416–422.
- [11] G.-Y. Jeong, S. P. Jang, H.-Y. Lee, J.-C. Lee, S. Choi, S.-H. Lee, Magnetic-Thermal-Fluidic Analysis for Cooling Performance of Magnetic Nanofluids Comparing With Transformer Oil and Air by Using Fully Coupled Finite Element Method, *IEEE Transactions on Magnetics* 49 (5) (2013) 1865–1868.
- [12] L. Pîslaru-Danescu, A. M. Morega, M. Morega, V. Stoica, O. M. Marincia, F. Nouras, N. Paduraru, I. Borbàth, T. Borbàth, Prototyping a Ferrofluid-Cooled Transformer, *IEEE Transaction on Industry Application* 49 (3) (2013) 1289–1298.
- [13] J. Patel, K. Parekh, R. V. Upadhyay, Prevention of hot spot temperature in a distribution transformer using magnetic fluid as a coolant, *International Journal of Thermal Sciences* 103 (2016) 35–40.
- [14] J. Patel, K. Parekh, R. V. Upadhyay, Performance of Mn-Zn ferrite magnetic fluid in a prototype distribution transformer under varying loading conditions, *International Journal of Thermal Sciences* 114 (2017) 64–71.
- [15] R. Zanella, C. Nore, F. Bouillault, L. Cappanera, I. Tomas, X. Mininger, J.-L. Guermond, Study of Magnetoconvection Impact on a Coil Cooling by Ferrofluid with a Spectral / Finite Element Method, *IEEE Transaction on Magnetics* 54 (2018) 1–4. doi:10.1109/TMAG.2017.2749539.
- [16] J.-L. Guermond, R. Laguerre, J. Léorat, C. Nore, Nonlinear magnetohydrodynamics in axisymmetric heterogeneous domains using a Fourier/finite element technique and an interior penalty method, *Journal of Computational Physics* 228 (2009) 2739–2757.
- [17] R. E. Rosensweig, *Magnetic Fluids*, *Annual Reviews of Fluid Mechanics* 19 (1987) 437–463.
- [18] J. Eapen, R. Rusconi, R. Piazza, S. Yip, The Classical Nature of Thermal Conduction in Nanofluids, *Journal of Heat Transfer* 132 (102402) (2010) 1–14.

- [19] A. Vatani, P. L. Woodfield, D. V. Dao, A survey of practical equations for prediction of effective thermal conductivity of spherical-particle nanofluids, *Journal of Molecular Liquids* 211 (2015) 712 – 733.
- [20] W. T. Perrins, D. R. McKenzie, R. C. McPhedran, Transport properties of regular arrays of cylinders, *Proceedings of the Royal Society of London. Series A, Mathematical and Physical Sciences* 369 (1737) (1979) 207–225.
- [21] S. Balay, S. Abhyankar, M. F. Adams, J. Brown, P. Brune, K. Buschelman, V. Eijkhout, W. D. Gropp, D. Kaushik, M. G. Knepley, L. C. McInnes, K. Rupp, B. F. Smith, H. Zhang, PETSc users manual, Tech. Rep. ANL-95/11 - Revision 3.5, Argonne National Laboratory (2014).
- [22] A. Bonito, J.-L. Guermond, F. Luddens, Regularity of the Maxwell equations in heterogeneous media and Lipschitz domains, *Journal of Mathematical Analysis and Applications* 408 (2013) 498–512.
- [23] C. Nore, H. Zaidi, F. Bouillault, A. Bossavit, J.-L. Guermond, Approximation of the time-dependent induction equation with advection using Whitney elements, *COMPEL: The International Journal for Computation and Mathematics in Electrical and Electronic Engineering* 35 (1) (2016) 326–338.
- [24] A. Giesecke, C. Nore, F. Stefani, G. Gerbeth, J. Léorat, W. Herreman, F. Luddens, J.-L. Guermond, Influence of high-permeability discs in an axisymmetric model of the Cadarache dynamo experiment, *New Journal of Physics* 14 (053005) (2012) 1–16.
- [25] T. L. Bergman, A. S. Lavine, F. P. Incropera, D. P. Dewitt, *Fundamentals of Heat and Mass Transfer*, John Wiley & Sons, USA, 2011.

5.2 Complementary discussion

In this section, we report results completing those presented in the article. The new results explain some features of the velocity and temperature solutions and show the influence of relevant parameters. Moreover, the comparison of numerical results with an experiment using transformer oil-based ferrofluid is presented.

5.2.1 Experimental setup

The experimental setup is shown in Figure 5.1. More details are reported in [110].

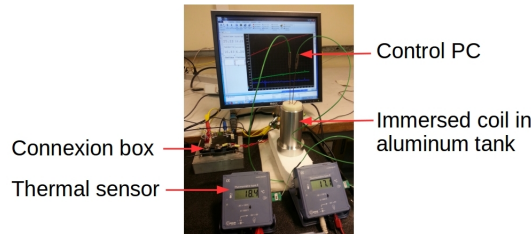


Figure 5.1: Second experiment at GeePs (aluminium tank).

5.2.2 Physical properties

The properties presented in Table 2 of the article are from various sources. Copper and iron properties are from [107, pp. 983-984]. Aluminium properties are from the laboratory (GeePs). Oil properties are from the manufacturer (Midel). PVC properties are from [108]. The density, the heat capacity and the thermal conductivity of magnetite are from [111], [112] and [46], respectively. The NIST Chemical WebBook [112] reports the heat capacity of magnetite in solid phase as a function of temperature. In the temperature range 298-900 K, the molecular heat capacity (J/mol · K) of magnetite in solid phase is given by

$$c_{\text{magnetite,mol}}(\tilde{T}) = A + B\tilde{T} + C\tilde{T}^2 + D\tilde{T}^3 + \frac{E}{\tilde{T}^2}, \quad (5.1)$$

where $A = 104.2096$, $B = 178.5108$, $C = 10.61510$, $D = 1.132534$, $E = -0.994202$, $\tilde{T} = T/1000$, with T the temperature in K. The heat capacity per unit mass is

$$c_{\text{magnetite}} = \frac{c_{\text{magnetite,mol}}}{M_{\text{magnetite}}} \times 1000, \quad (5.2)$$

where $M_{\text{magnetite}} = 251.533$ g/mol is the molecular mass. For $T = 293.15$ K, this formula gives $c_{\text{magnetite}} \simeq 630.20$ J/K · kg, which is the value reported in Table 2 of the article.

5.2.3 Experiment vs. numerics using pure transformer oil

We report complementary results regarding Section 4 of the article. Some features of the velocity and temperature solutions are investigated and three-dimensional results are shown.

Oscillating regime

Notice that the curve of the temperature time evolution computed at the coil sensor in Figure 7 of the article presents oscillations. They first appear between $t = 500$ s and $t = 1000$ s approximately. They reappear around $t = 3000$ s and persist until the end of the simulation. The time evolution of the computed temperature at each sensor is

compared with the experimental data over the last 100 s in Figure 5.2. The numerical oscillations at the coil sensor have an amplitude of approximately 0.5°C and a period around 7 s (Figure 5.2a). The experimental data do not show this feature. The recording presents some variations but, while they have approximately the same amplitude, they do not have the same shape and do not follow a regular frequency. Moreover, they are present at every sensor (Figures 5.2b and 5.2c), while the numerical oscillations are present at the coil sensor only. The variations in the experimental data are most likely due to a parasite signal during the measurement.

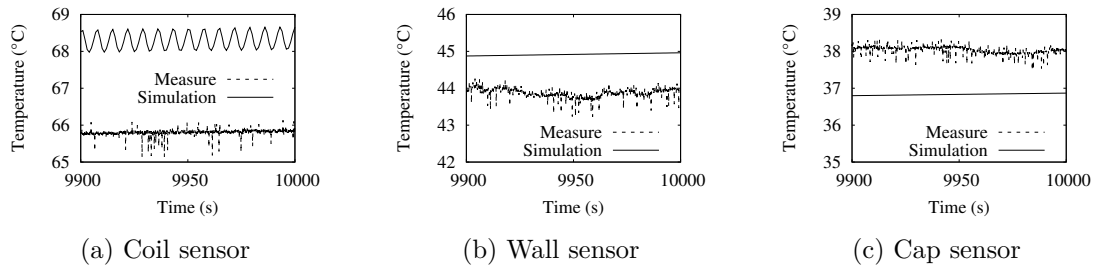


Figure 5.2: Temperature measured and computed at each sensor over the last 100 s.

To understand the numerical oscillations, we study the time evolution of the temperature field in the permanent regime, over 10 s (a little more than the oscillation period) after 10000 s, see Figure 5.3. In this time window, a mass of hot fluid close to the coil flows up toward the cap and another mass of hot fluid gets ready to follow the same path and maintain the oscillations.

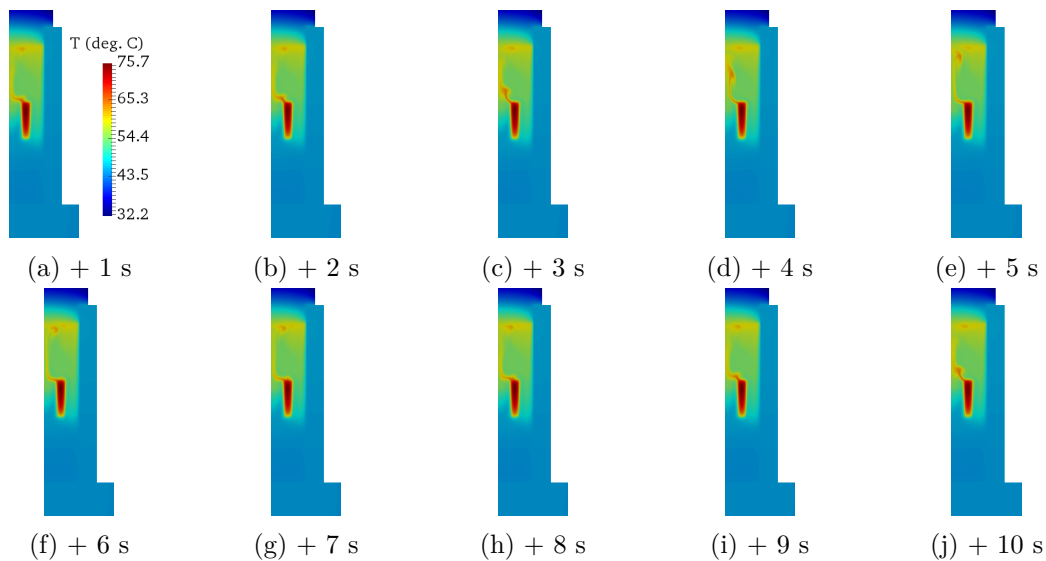


Figure 5.3: Time evolution of the temperature field after $t = 10000$ s

Oscillations with the same period are present on the time evolution of the kinetic energy, see Figure 5.4. By comparing the temperature field time evolution and the kinetic energy time evolution, we notice that the kinetic energy is minimum when the mass of hot fluid is close to the coil (1 s after 10000 s), maximum when it is half way (4 s after 10000 s), minimum again when it hits the cap (6 s after 10000 s).

These observations show that, in the simulation, the heat dissipated in the coil is convected by volutes of hot fluid. This phenomenon causes the oscillations of the temperature at the coil sensor and is the same as that observed in the simulation on the previous setup, see Section 4.2.8.

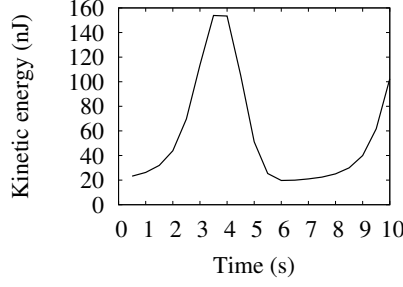


Figure 5.4: Time evolution of the kinetic energy over 10 s after $t = 10000$ s.

The discrepancy between the numerical results and the measurements may be due to the model:

- the geometry and the dimensions of the coil in the model are not accurate;
- the localization of the sensors is approximate;
- the properties of the PVC cap are unknown;
- there might be some variations in the properties furnished by the oil manufacturer (in particular, the viscosity is a key parameter for this problem, see Section 4.2.8);
- the convection coefficient is obtained by comparing with the experiments.

The difference between the numerical results and the measurements may also be due to the experiment itself. If the time needed for the sensor measurement to stabilize is too long, the oscillations cannot be detected.

Meridian flow

As in the simulation on the previous setup, see Section 4.2.7, the azimuthal component of the velocity is zero. The flow is purely meridian. Even though the Boussinesq force is axial, the non linear convective term in the equations of fluid dynamics can theoretically lead to a non-zero azimuthal velocity. The simulation is restarted from the final time $t = 10000$ s with a perturbation on the azimuthal component of the velocity. The perturbation is of order 10^{-3} m/s, which represents approximately one tenth of the maximum velocity magnitude. We study the time evolution of the kinetic energies by component:

$$E_{k,r} = \int_{\Omega_f} \frac{1}{2} \rho_f u_r^2 dV, \quad E_{k,\theta} = \int_{\Omega_f} \frac{1}{2} \rho_f u_\theta^2 dV, \quad E_{k,z} = \int_{\Omega_f} \frac{1}{2} \rho_f u_z^2 dV. \quad (5.3)$$

The numerical results, see Figure 5.5, show that the kinetic energy carried by the azimuthal component of the velocity, initially not null due to the perturbation, exponentially decreases with time, contrary to that carried by the other components. The perturbation is not sustained and tends to the numerical zero. It confirms that the flow cannot grow in the azimuthal direction.

Note that the Reynolds number is small in this problem. At most, the velocity is less than $U_{\text{ref}} = 2 \times 10^{-2}$ m/s. At 20°C , the oil kinematic viscosity is $\nu_f = 6.7 \times 10^{-5}$ m²/s. The height of the system is $L_{\text{ref}} = 10^{-1}$ m approximately. With these values, the Reynolds number is $Re = U_{\text{ref}} L_{\text{ref}} / \nu_f \simeq 30$. The flow regime is laminar, which can explain the meridian flow observed in this particular configuration.

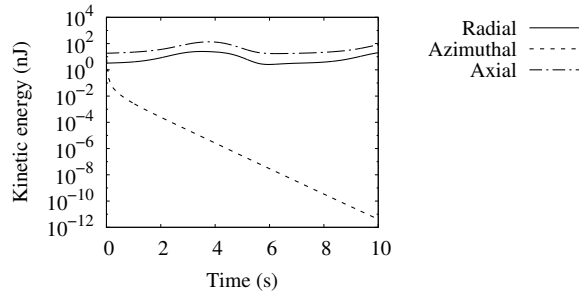


Figure 5.5: Restart from $t = 10000$ s with a perturbation on the azimuthal component of the velocity. Time evolution of the radial, azimuthal and axial kinetic energy over 10 s.

Three-dimensional study

The simulation is re-performed on 8 modes (0 to 7) with an initial perturbation on modes greater or equal to 1 of the temperature. The perturbation is of order 10^{-3} °C, i.e., around 0.01% of the temperature increment. Figure 5.6 shows the time evolution of the modal kinetic energies and the modal average temperatures carried by every considered mode. The modal kinetic energies are defined by (4.19) and (4.20). The modal average temperature carried by mode 0 is defined by

$$\bar{T}^0 = \sqrt{\frac{1}{V} \int_{\Omega} (T^{0,\cos})^2 dV}. \quad (5.4)$$

The modal average temperature carried by mode $m \in \{1, \dots, 7\}$ is defined by

$$\bar{T}^m = \sqrt{\frac{1}{V} \int_{\Omega} \frac{1}{2} [(T^{m,\cos})^2 + (T^{m,\sin})^2] dV}. \quad (5.5)$$

The modes have a similar evolution for the kinetic energy and the average temperature. Mode 0 grows until it reaches an oscillatory permanent regime. Modes greater or equal to 1 first decay (they are not null initially due to the perturbation) and tend to the numerical zero. At $t = 6000$ s, mode 1 starts to increase, followed by the other modes. The increase stops around $t = 8000$ s, when the modes reach an oscillatory permanent regime like mode 0. At $t = 10000$ s, modes greater or equal to 1 are populated, i.e., the velocity and temperature solutions are non-axisymmetric.

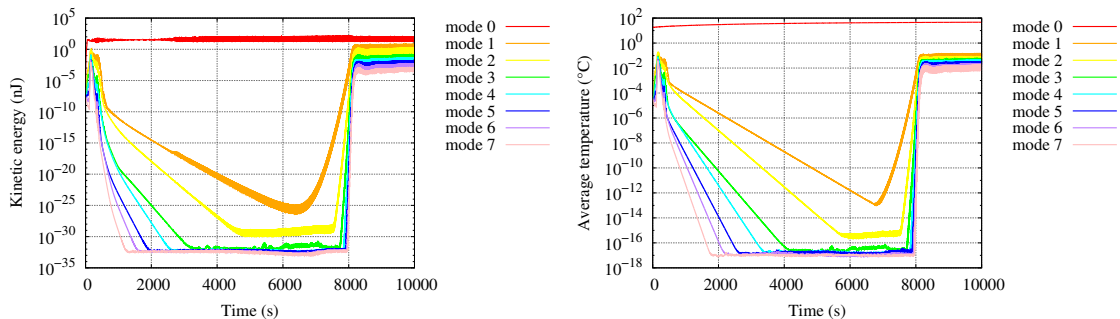


Figure 5.6: Mode-by-mode time evolution of the global quantities.

Notice in Figure 5.6 that the modes are ordered and that mode 0 of the temperature clearly dominates the other temperature modes, meaning that the temperature solution is quasi-axisymmetric. Figure 5.7 compare the temperature fields obtained with the axisymmetric computation and the 3D computation. In the 3D computation, the plume of

hot fluid is non-axisymmetric. Nevertheless, apart from that, the temperature field is very close to that obtained with the axisymmetric computation. There is a 0.1°C difference between the maximum temperatures computed in each case for instance. Therefore, the axisymmetric computation gives a very satisfying approximation of the 3D solution.

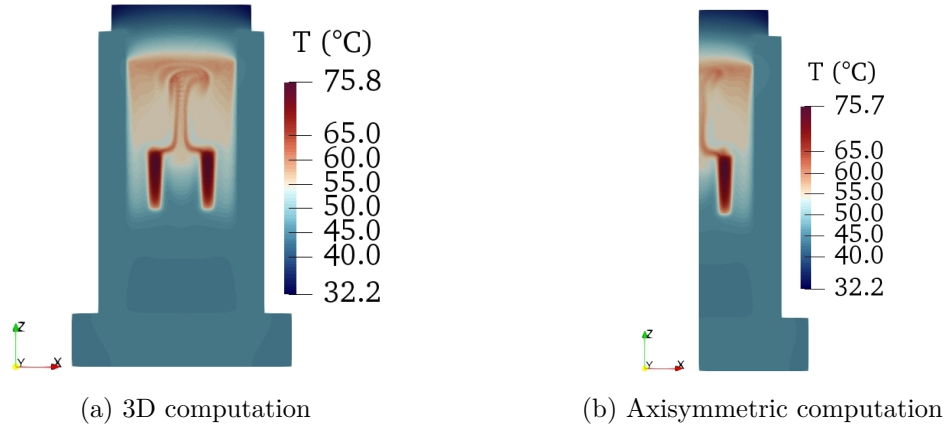


Figure 5.7: Temperature field at $t = 10000$ s obtained with a 3D computation (modes 0 to 7) and an axisymmetric computation (mode 0 only).

5.2.4 Numerical simulations with ferrofluid

We report complementary results regarding Section 5 of the article. The effect of the current intensity and type (AC/DC) is investigated and three-dimensional results are shown.

Influence of the current intensity

The simulations with the regular oil and the magnetic oil with $\phi = 7\%$ are re-performed using different current intensities. The study is based on the setup without core. Figures 5.8a and 5.8b show the time evolution of the temperature at the hot spot in the coil (see Figure 2a of the article) with respect to the current intensity, for regular oil and magnetic oil, respectively. Note that the wire of the coil is made of two sub-wires and that the current indicated in the legend is that flowing in a sub-wire. It must be multiplied by two to obtain the current in the full wire. The simulations discussed in the article correspond to the 6 A case in the legend (total current $I = 2 \times 6 = 12$ A).

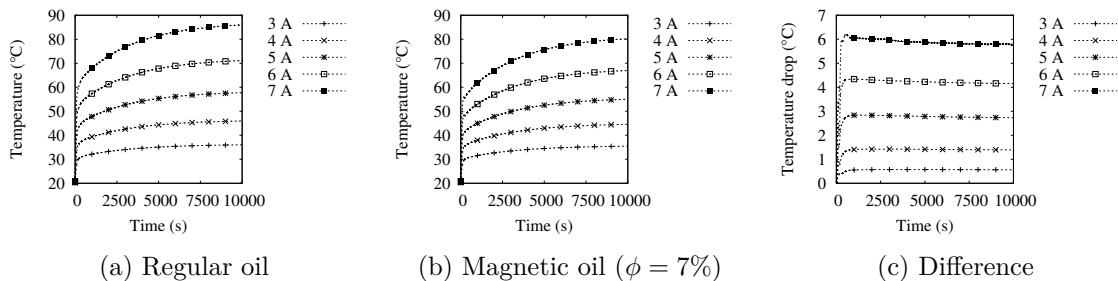


Figure 5.8: Influence of the current on the temperature at the hot spot in the coil.

The stronger the current, the stronger the Joule effect and the higher the temperature in the coil. Figure 5.8c shows the time evolution of the temperature difference between regular and magnetic oil with respect to the current intensity. At $t = 10000$ s, the temperature difference is less than 1°C with 3 A in one sub-wire, around 3°C with 5 A in

one sub-wire and 6°C with 7 A in one sub-wire. The difference of temperature in the coil, when magnetic oil is used instead of regular oil, increases with the current. The stronger the current, the stronger the effect of the ferrofluid on the cooling. Thermomagnetic convection effect is enhanced by increasing the current (and the associated magnetic field). These simulations show that, in the configuration of the experiment, one should increase the current to measure a higher temperature drop with magnetic oil cooling.

Three-dimensional study

We re-perform the simulations on the two setups (without and with core) using 8 modes (0 to 7) and with an initial perturbation on temperature modes greater or equal to 1 (perturbation of order $10^{-3^\circ\text{C}}$). The cases of the regular oil and the magnetic oil with $\phi = 7\%$ only are solved. We assume that the magnetic oils with the other volume fractions behave like the one considered here. The simulations are stopped at $t = 3000$ s, once the evolution of every mode is stable. We first focus on the setup without the ferromagnetic core. The time evolution of E_k^m and $\overline{T} - \overline{T}_0^m$, for every considered mode m , is presented in Figure 5.9 for the regular oil case and in Figure 5.10 for the magnetic oil case. In each case, velocity and temperature modes greater or equal to 1 finally decay and reach the numerical zero, which leads to velocity and temperature solutions totally dominated by mode 0. At $t = 3000$ s, the velocity and temperature solutions are axisymmetric. We cannot be sure that the non-axisymmetric modes will not rise and stabilize around non-zero values at a further time, as in Figure 5.6. Nevertheless, the previous computations show that the temperature is always strongly dominated by mode 0, even if other modes are populated.

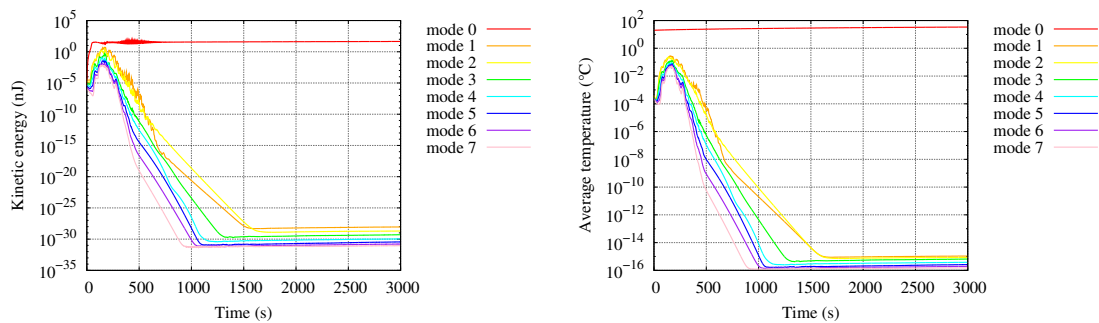


Figure 5.9: Setup without core filled by regular oil. Mode-by-mode time evolution of the global quantities.

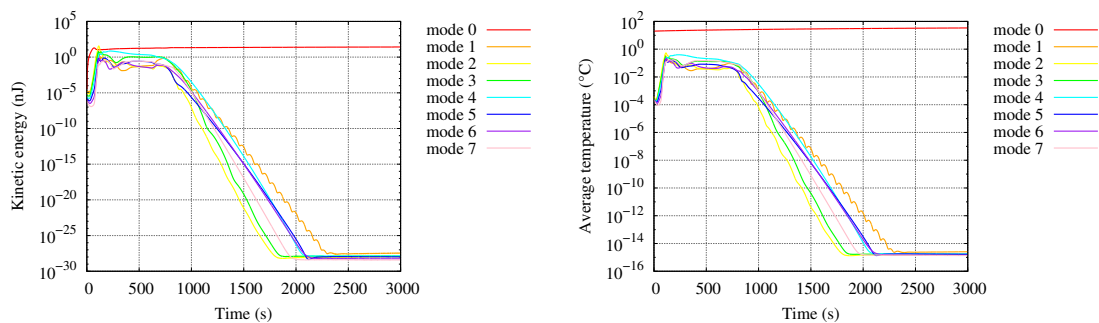


Figure 5.10: Setup without core filled by magnetic oil ($\phi = 7\%$). Mode-by-mode time evolution of the global quantities.

We now focus on the setup with the ferromagnetic core. Here and in the following, the

relative magnetic permeability of the core is $\mu_r = 1000$. The time evolution of E_k^m and $\overline{T} - T_0^m$, for every considered mode m , is presented in Figure 5.11 for the regular oil case and in Figure 5.12 for the magnetic oil case. Here, modes greater or equal to 1 do not decay and present sustained oscillations around values different from the numerical zero, for velocity and temperature. Modes greater or equal to 1 are still dominated by mode 0. For temperature, mode 0 is approximately 100 times stronger than the other modes. Again, the temperature solution is quasi-axisymmetric, even with the core.

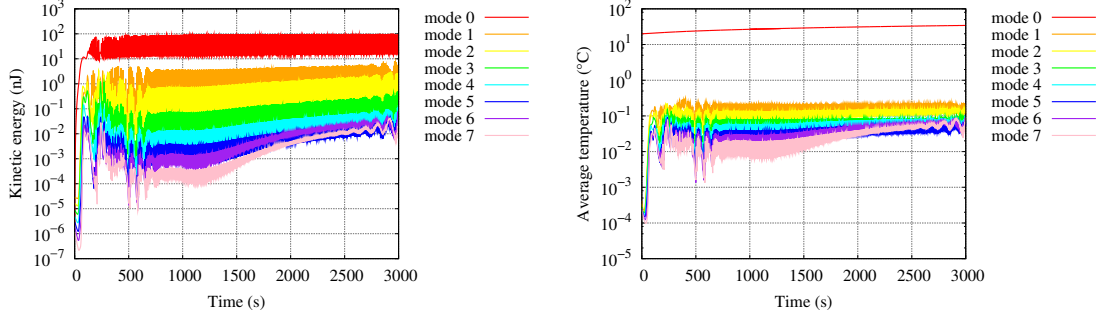


Figure 5.11: Setup with core filled by regular oil. Mode-by-mode time evolution of the global quantities.

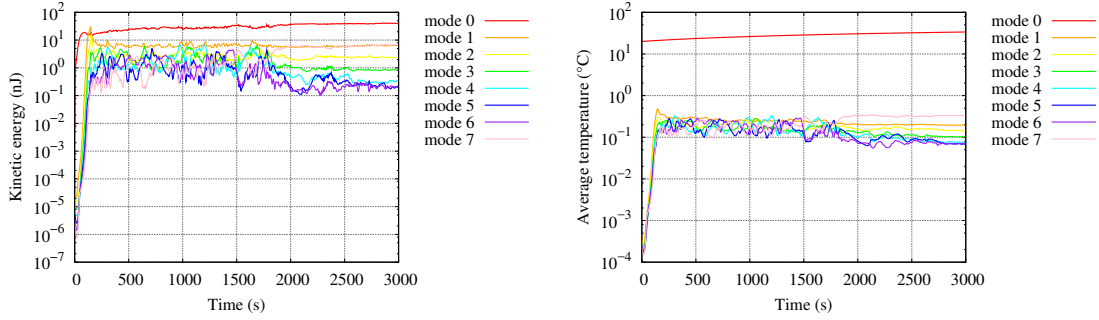


Figure 5.12: Setup with core filled by magnetic oil ($\phi = 7\%$). Mode-by-mode time evolution of the global quantities.

Alternating current

We study the influence of an alternating current in the coil, instead of a continuous one, as in all the other simulations. The study is based on the setup without core. In the article, the current intensity in the coil is

$$J_s = \frac{NI}{S}, \quad (5.6)$$

where N is the number of turns, I is the enforced (DC) current in the experiment and S is the section of the coil body. In the simulations presented here, the current density is

$$J_s(t) = \frac{NI\sqrt{2}\sin(2\pi ft)}{S}, \quad (5.7)$$

where $f = 50$ Hz is the frequency of the signal. The RMS values of both current intensities are the same owing to the constant $\sqrt{2}$ in the definition of the alternating one (5.7). Thus, the time average of the power dissipated by the Joule effect is identical with the DC or the AC current intensity. We first study the influence of the alternating current in the case of regular oil. The only difference with the continuous current case is the time oscillation

of the source term in the temperature equation. Figure 5.13 compares the rise of the temperature at the hot spot in the coil when using the current intensity given by (5.6) or (5.7). The temperature rise is similar in both cases, see the time evolution over 5000 s in Figure 5.13a, even though the temperature rise with the AC current presents oscillations with a small amplitude (less than $2 \times 10^{-3} \text{°C}$), see the zoom over 0.1 s in Figure 5.13b. Note that the oscillations have a frequency of 100 Hz because the power dissipated by the Joule effect is proportional to J_s^2 , which oscillates with a frequency of $2f$. With the frequency considered here, an AC current of same RMS value does not modify the coil temperature.

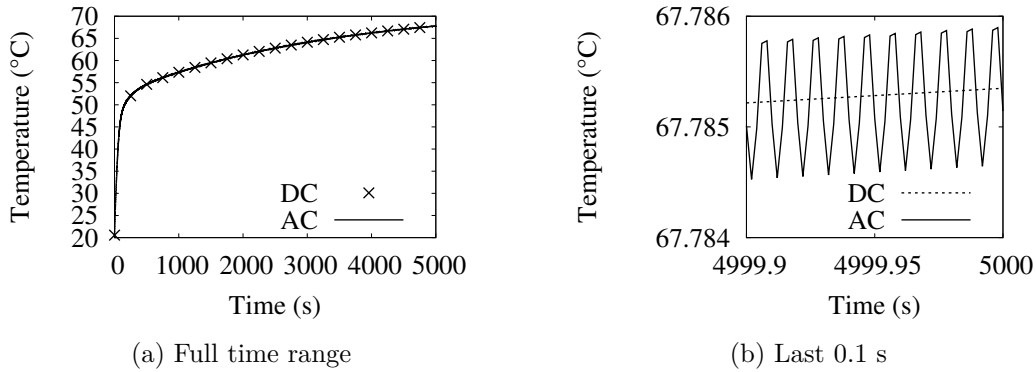


Figure 5.13: Regular oil. Temperature at the hot spot when using DC or AC current.

We then study the influence of the alternating current in the case of magnetic oil. We focus on the magnetic oil with the stronger volume fraction of magnetic nanoparticles ($\phi = 7\%$). The differences with the continuous current case are the time oscillation of the source term in the temperature equation and the time oscillation of the Kelvin force due to the time oscillation of the magnetic field. Figure 5.14 compares the rise of the temperature at the hot spot in the coil when using the current intensity given by (5.6) or (5.7). As for the regular oil, the temperature rise is similar in both cases, see the time evolution over 5000 s in Figure 5.14a. The zoom over 0.1 s in Figure 5.14b only shows a 0.1°C decrease when alternating current is used instead of continuous current. Again, with the frequency considered here, an AC current of same RMS value does not modify the temperature in the coil. The time variations of the magnetic field are too fast to affect the time evolution of the temperature in the system.

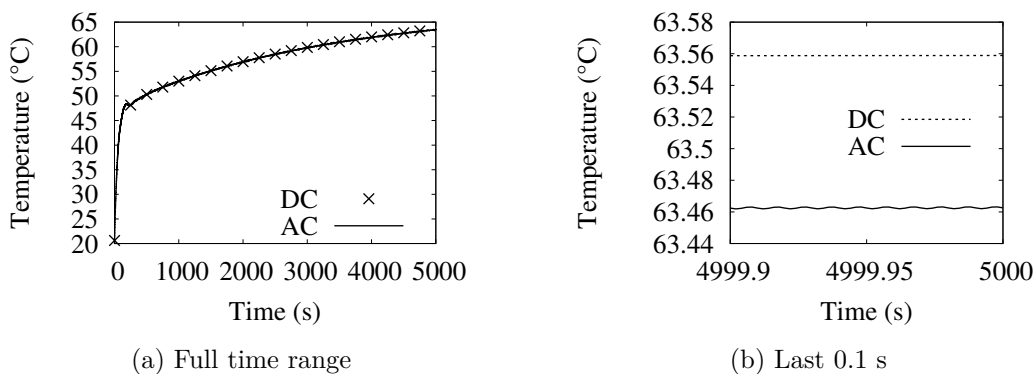


Figure 5.14: Magnetic oil ($\phi = 7\%$). Temperature at the hot spot when using DC or AC current.

5.2.5 Experiment vs. numerics using transformer oil-based ferrofluid

We first report results obtained by the experimental team and then show the numerical simulation performed to match these results.

Experimental details

A transformer oil based ferrofluid is produced by Sophie Neveu at PHENIX lab (Sorbonne University). The vegetable transformer oil eN 1215 of Midel is used as liquid carrier. An experiment is performed with the ferrofluid to highlight the effect of thermomagnetic convection only and discriminate the effect of the change of the thermophysical properties. The wire is double and opposite currents can be enforced in every sub-wire, see Figure 5.15. When the currents in the sub-wires have the same direction, see Figure 5.15a, the magnetic field is the same as that generated by a single wire. Thermomagnetic convection is active. When the currents in the sub-wires have opposite directions, see Figure 5.15b, the magnetic fields generated by each sub-wire compensate each other and the total magnetic field is almost zero. Thermomagnetic convection is not active. By comparing the temperature in both current configurations, we expect to observe the effect of thermomagnetic convection.

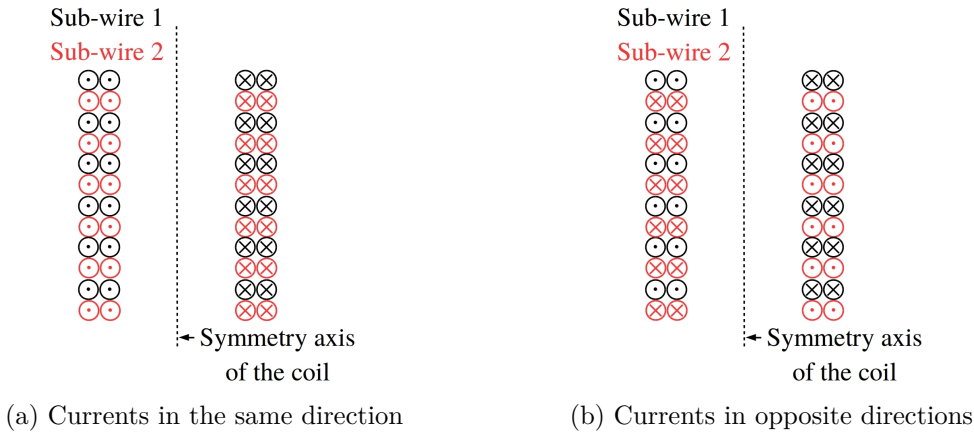


Figure 5.15: Section of the coil for both current configurations in the experiment. A point indicates a current toward the reader, a cross indicates a current in the opposite direction.

Two sensors are used to measure the temperature in the fluid and in the coil, see Figure 5.16. Figure 5.17 shows the evolution of the temperature at each sensor during the experiment. The currents in each sub-wire initially have the same direction. They are then switched from one configuration to the other every 60 minutes. The time evolution of the temperature for both sensors presents abrupt variations of approximately 2°C at every switch. The temperature increases when the currents are switched to the configuration where they have opposite directions (no thermomagnetic convection) and decreases when the currents are switched to the configuration where they have the same direction (active thermomagnetic convection), showing the positive influence of thermomagnetic convection.

Numerical crenelations

We use the setup considered in Figure 5.16. The simulation is performed with the magnetic oil containing a volume fraction $\phi = 7\%$ of nanoparticles instead of the regular oil. The magnetic field is switched off / switched on every 1000 s during the simulation to deactivate / activate the thermomagnetic convection effect. Figure 5.18 shows the time evolution of the temperature at each sensor. Crenelations are indeed reproduced in this simulation. The temperature increases when thermomagnetic convection is switched off

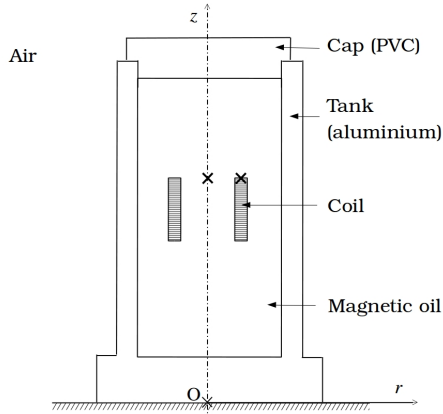


Figure 5.16: Setup using transformer oil-based ferrofluid. Cross: thermal sensor.

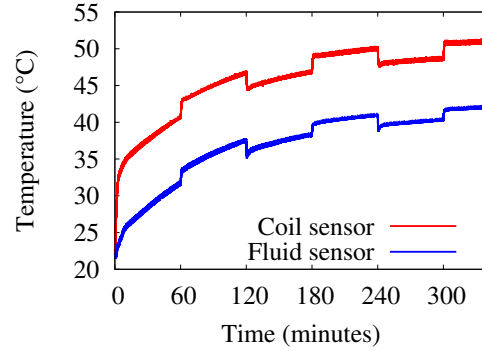


Figure 5.17: Temperature measurements using ferrofluid when changing current configurations every 60 minutes.

and decreases when it is switched on again. The temperature variation at every switch is of approximately 2°C . These temperature crenulations are qualitatively in good agreement with the ones present in the experimental data in Figure 5.17. The consistency of the numerical approach with the experiment confirms the choices made (continuum, Newtonian fluid under Boussinesq approximation, Kelvin magnetic body force) to model the ferrofluid.

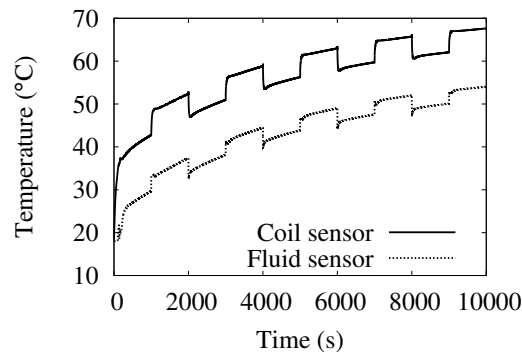


Figure 5.18: Computed temperature at each sensor when deactivating / activating the magnetic field every 1000 s.

5.3 Improvement of the ferrofluid modeling

In this section, we present two independent improvements of the ferrofluid modeling and their consequences on the velocity and the temperature. The simulations are based on those presented in Section 5 of the article.

5.3.1 Temperature-dependent saturation magnetization of the magnetic nanoparticles

In the article, the magnetization of the ferrofluid follows a small field approximation of Langevin's law, see equations (8) and (9) of the article, where the saturation magnetization of the magnetic nanoparticles (denoted by M_0 in the article) is considered constant. Here, we take into account the influence of the temperature on the saturation magnetization of the magnetic nanoparticles. It leads to the introduction of the Curie temperature of the

ferromagnetic material constituting the magnetic nanoparticles, i.e., the temperature over which the ferromagnetic material becomes paramagnetic and loses its strong magnetization. We expect stronger variations of the ferrofluid magnetization and, thus, a stronger thermomagnetic convection effect.

In the new model, the law of the ferrofluid susceptibility given by equation (9) of the article is replaced by

$$\chi(T) = \frac{\phi\mu_0\pi d^3 M_{s,p}(T)^2}{18k_B T}, \quad (5.8)$$

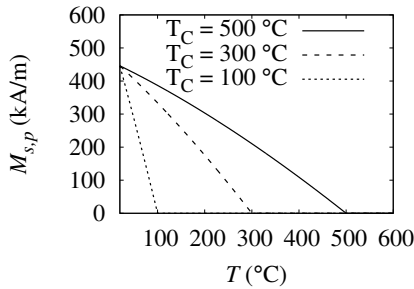
where the saturation magnetization of the magnetic nanoparticles $M_{s,p}$ follows Bloch's law, reported in [113]:

$$M_{s,p}(T) = \begin{cases} M_{s,p}(0) \left(1 - \left(\frac{T}{T_C}\right)^{1.5}\right) & \text{if } T \leq T_C, \\ 0 & \text{if } T \geq T_C, \end{cases} \quad (5.9)$$

where T is the temperature in Kelvin, $M_{s,p}(0)$ is the saturation magnetization of the magnetic nanoparticles at $T = 0$ K and T_C is the Curie temperature (the saturation magnetization is zero for $T \geq T_C$ because the material is then paramagnetic). The saturation magnetization of magnetite at 0 K is not available in the literature. We assume that the saturation magnetization of magnetite given in [114] is measured at room temperature: $M_{s,p}(293.15 \text{ K}) = 4.46 \times 10^5 \text{ A/m}$. Using (5.9), we can replace $M_{s,p}(0)$ using known quantities:

$$M_{s,p}(0) = \frac{M_{s,p}(293.15)}{\left(1 - \left(\frac{293.15}{T_C}\right)^{1.5}\right)}. \quad (5.10)$$

Figure 5.19 shows the evolution of the saturation magnetization following (5.9). The Curie temperature of magnetite is approximately 850 K [111] but there exist materials with lower Curie temperatures. For instance, Mn-Zn oxides have a Curie temperature close to 100°C, see Table 5.1. Various Curie temperatures in the possible range, $T_C = 100, 300$ and 500°C , are used to show the impact of this parameter. The lower the Curie temperature, the higher the rate of the saturation magnetization versus the temperature.



Material	T_C (°C)
$\text{Mn}_{0.5}\text{Zn}_{0.5}\text{OFe}_2\text{O}_3$	150
$\text{Ni}_{0.3}\text{Zn}_{0.7}\text{OFe}_2\text{O}_3$	130
$\text{Ni}_{0.2}\text{Zn}_{0.6}\text{Fe}_{2.2}\text{O}_4$	145
$\text{Zn}_{0.6}\text{Co}_{0.5}\text{Fe}_{1.9}\text{O}_4$	115
$\text{Mg}_{0.5}\text{Zn}_{0.5}\text{OFe}_2\text{O}_3$	120
MnFe_2O_4	300

Figure 5.19: Bloch's law (5.9) for different Curie temperatures.

Table 5.1: Magnetic materials used in ferrofluids and their Curie temperature [77].

Notice that, with this modeling, the ferrofluid magnetization is temperature dependent on two scales:

- ferrofluid scale: the higher the temperature (and the associated thermal agitation), the more disorganized the magnetic dipoles carried by the nanoparticles, the lower the ferrofluid magnetization;
- nanoparticle scale: the higher the temperature, the lower the saturation magnetization of the magnetic nanoparticles, the lower the ferrofluid magnetization.

We want to determine the impact of this more realistic modeling and that of the Curie temperature. The simulations for the magnetic oil with the weaker volume fraction ($\phi = 1\%$) on both setups are re-performed by considering the ferrofluid susceptibility given by (5.8) and (5.9). Different configurations with various Curie temperatures (100, 300 and 500°C) are tested. Figure 5.20 compares the time evolutions of the temperature at the hot spot in the coil (see Figure 2a and 2b of the article) for the different Curie temperatures. The legend « Constant $M_{s,p}$ » refers to the case of the article, where the saturation magnetization of the magnetic nanoparticles is considered constant. It corresponds to the limit $T_C = \infty$ in (5.9). Using Bloch's law with the Curie temperature of magnetite ($T_C = 500^\circ\text{C}$) leads to a slight decrease of the temperature, compared to the case with constant saturation magnetization. When the Curie temperature is reduced ($T_C = 300$ or 100°C), the temperature is again decreased. Without the ferromagnetic core, there is a 2°C decrease between $T_C = \infty$ and $T_C = 100^\circ\text{C}$. With the ferromagnetic core, this decrease reaches 5°C approximately. These results confirm that magnetic materials with low Curie temperatures should be considered for ferrofluid application in transformer cooling, as suggested by [77], because they enhance the thermomagnetic convection effect.

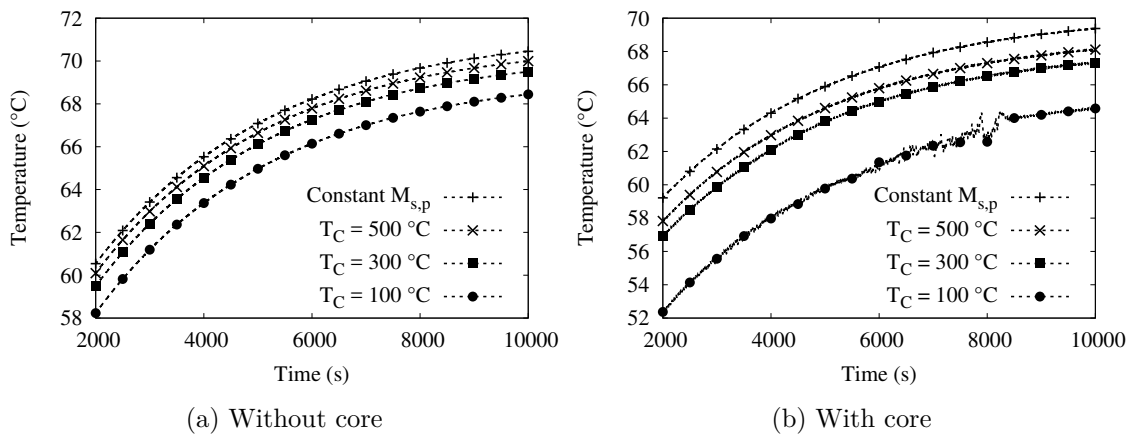


Figure 5.20: Impact of the Curie temperature on the temperature at the hot spot. Volume fraction of magnetic nanoparticles $\phi = 1\%$.

5.3.2 Complete temperature equation of ferrofluids

We improve the ferrofluid modeling by considering the pyromagnetic coefficient term in the temperature equation of ferrofluids in (3.7).

Orders of magnitude

In a Newtonian incompressible fluid, the temperature equation is of the form

$$\rho c \partial_t T + \rho \mathbf{c} \mathbf{u} \cdot \nabla T - \nabla \cdot (\lambda \nabla T) = 2\eta \nabla^s \mathbf{u} : \nabla \mathbf{u}, \quad (5.11)$$

where $\nabla^s \mathbf{u} = \frac{1}{2}(\nabla \mathbf{u} + (\nabla \mathbf{u})^T)$. In [33], the authors obtain an equivalent equation for a ferrofluid, considered as being Newtonian and incompressible, by using thermodynamics. The equation for ferrofluids only differs by an additional term and reads

$$\rho c \partial_t T + \rho \mathbf{c} \mathbf{u} \cdot \nabla T + \mu_0 T \frac{\partial M}{\partial T} (\partial_t H + \mathbf{u} \cdot \nabla H) - \nabla \cdot (\lambda \nabla T) = 2\eta \nabla^s \mathbf{u} : \nabla \mathbf{u}. \quad (5.12)$$

This additional term on the left-hand side is called the pyromagnetic coefficient term due to the presence of the pyromagnetic coefficient $\frac{\partial M}{\partial T}$ of the ferrofluid.

Let us compare the orders of magnitude of the different terms in the temperature equation (5.12). Note that the current being continuous, H is time-independent and we have $\partial_t H = 0$ in the pyromagnetic coefficient term. We first focus on the setup without the ferromagnetic core. We choose the following reference scales:

- $T_{\text{ref}} = 293.15$ K, the room temperature;
- $\Delta T_{\text{ref}} = 50$ K, the typical temperature increment in the simulations;
- $H_{\text{ref}} = 1.5 \times 10^4$ A/m without core, the maximum magnetic field intensity (Figure 19a of the article);
- $\Delta M_{\text{ref}} = |M(T_{\text{ref}} + \Delta T_{\text{ref}}, H_{\text{ref}}) - M(T_{\text{ref}}, H_{\text{ref}})| \simeq 1.4 \times 10^3$ A/m, Langevin's formula (2.19) with $\phi = 7\%$;
- $U_{\text{ref}} = 10^{-3}$ m/s, the average velocity in the simulation;
- $L_{\text{ref}} = 10^{-2}$ m, the distance between the coil and the lateral wall of the tank.

The properties of the ferrofluid are chosen to be that of the base fluid. We use the density, the specific heat, the thermal conductivity and the dynamic viscosity of the transformer oil (Midel, eN 1215) at 20°C, $\rho = 922$ kg/m³, $c = 1970$ J/K · kg, $\lambda = 0.166$ W/m · K and $\eta = 6.2 \times 10^{-2}$ Pa · s, respectively. We get:

$$\left| \mu_0 T \frac{\partial M}{\partial T} \frac{DH}{Dt} \right| \simeq \mu_0 T_{\text{ref}} \frac{\Delta M_{\text{ref}}}{\Delta T_{\text{ref}}} U_{\text{ref}} \frac{H_{\text{ref}}}{L_{\text{ref}}} \simeq 15 \text{ W/m}^3, \quad (5.13)$$

$$|\rho c (\mathbf{u} \cdot \nabla) T| \simeq \frac{\rho c U_{\text{ref}} \Delta T_{\text{ref}}}{L_{\text{ref}}} \simeq 9.1 \times 10^6 \text{ W/m}^3, \quad (5.14)$$

$$|-\nabla \cdot (\lambda \nabla T)| \simeq \frac{\lambda \Delta T_{\text{ref}}}{L_{\text{ref}}^2} \simeq 8.3 \times 10^4 \text{ W/m}^3, \quad (5.15)$$

$$2\eta \nabla^s \mathbf{u} : \nabla \mathbf{u} \simeq 2\eta \left(\frac{U_{\text{ref}}}{L_{\text{ref}}} \right)^2 \simeq 1.2 \times 10^{-3} \text{ W/m}^3. \quad (5.16)$$

The order of magnitude of the pyromagnetic coefficient term is 10 W/m³ while the orders of magnitude of the convective and diffusive terms are 10⁷ W/m³ and 10⁵ W/m³, respectively. The pyromagnetic coefficient term is therefore negligible compared to the convective and diffusive terms. The order of magnitude of the viscous dissipation term is 10⁻³ W/m³. This term is also negligible in the temperature equation.

We then focus on the setup with the ferromagnetic core. The addition of a ferromagnetic core increases the maximum magnetic field intensity. With the ferromagnetic core, we have $H_{\text{ref}} = 7.6 \times 10^4$ A/m (Figure 19c of the article). In this case, we find $\Delta M_{\text{ref}} \simeq 9.6 \times 10^2$ A/m for $\phi = 7\%$. The estimate of the pyromagnetic coefficient term leads to:

$$\left| \mu_0 T \frac{\partial M}{\partial T} \frac{DH}{Dt} \right| \simeq \mu_0 T_{\text{ref}} \frac{\Delta M_{\text{ref}}}{\Delta T_{\text{ref}}} U_{\text{ref}} \frac{H_{\text{ref}}}{L_{\text{ref}}} \simeq 54 \text{ W/m}^3. \quad (5.17)$$

The order of magnitude of the pyromagnetic coefficient term being 10² W/m³, it is still negligible compared to the convective and diffusive terms.

Note that the estimates of the convective and diffusive terms are not of the same order of magnitude, while these estimates should counterbalance. The choice of the reference quantities does not seem relevant. By choosing the reference length to be $L_{\text{ref}} = 10^{-4}$ m (and considering the same other reference scales), these terms have the same order of magnitude. With this reference length, the pyromagnetic coefficient term stays clearly negligible (with or without core) compared to the convection and diffusion terms (10³ – 10⁴ W/m³ against 10⁹ W/m³).

Numerical illustration

The calculus of the orders of magnitude predicts a negligible influence of the pyromagnetic coefficient term in the temperature equation. This section aims at verifying the influence of this term with numerical simulations. The simulations are re-performed after adding the pyromagnetic coefficient term in equation (6) of the article and the results are compared with the previous ones to observe the impact of this term. The situation with the highest proportion of magnetic material, $\phi = 7\%$, is chosen to maximize the pyromagnetic coefficient term. In our case, the current is continuous so the generated magnetic field is time-independent. The ferrofluid is supposed to be a linear material: $M(T) = \chi(T)H$. In the fluid domain, equation (6) of the article is replaced by

$$\rho c \partial_t T + \rho c \mathbf{u} \cdot \nabla T + \mu_0 T \frac{\partial \chi}{\partial T} \mathbf{u} \cdot \nabla H - \nabla \cdot (\lambda \nabla T) = 0, \quad (5.18)$$

where the magnetic susceptibility of the ferrofluid is still described by equation (9) of the article.

We define the kinetic energy of the ferrofluid:

$$E_k = \int_{\Omega_f} \frac{1}{2} \rho u^2 dV. \quad (5.19)$$

Let V be the total volume of the system. We define the average temperature:

$$\overline{T - T_0} = \sqrt{\frac{1}{V} \int_{\Omega} T^2 dV}. \quad (5.20)$$

Figure 5.21 compares the time evolution of the kinetic energy and the average temperature in the setup without the ferromagnetic core for two cases: either the pyromagnetic coefficient term is active, or it is not. The curves perfectly superimpose. The pyromagnetic coefficient term does not affect this problem. Figure 5.22 presents the analogous results obtained on the setup with the ferromagnetic core. The curves also perfectly superimpose, which leads to the same conclusion.

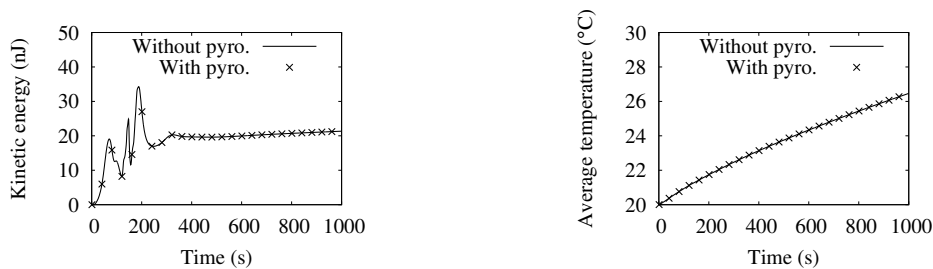


Figure 5.21: Impact of the pyromagnetic coefficient term on the global quantities. Setup without ferromagnetic core, magnetic oil with $\phi = 7\%$.

We now test if any 3D effect may arise when the pyromagnetic coefficient term is active. The solution in the core setup with magnetic oil at $\phi = 7\%$ is computed with and without the pyromagnetic coefficient term on modes 0 to 7 over 1000 s. No difference is observed between the results, as shown in Figure 5.23.

5.3.3 Limit of the linear magnetic material approximation

Figure 5.24 shows the magnetization of the magnetic oil with $\phi = 7\%$ with respect to the magnetic field intensity, according to (2.19) and (2.21). We use the parameters presented in the article ($d = 10$ nm and $M_{s,p} = 4.46 \times 10^5$ W/m²·K) and the room temperature ($T =$

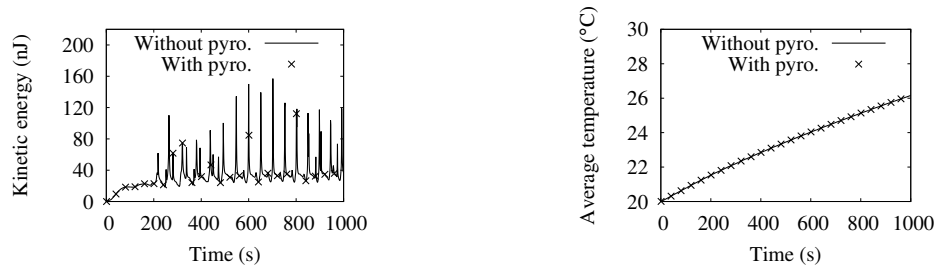


Figure 5.22: Impact of the pyromagnetic coefficient term on the global quantities. Setup with ferromagnetic core, magnetic oil with $\phi = 7\%$.

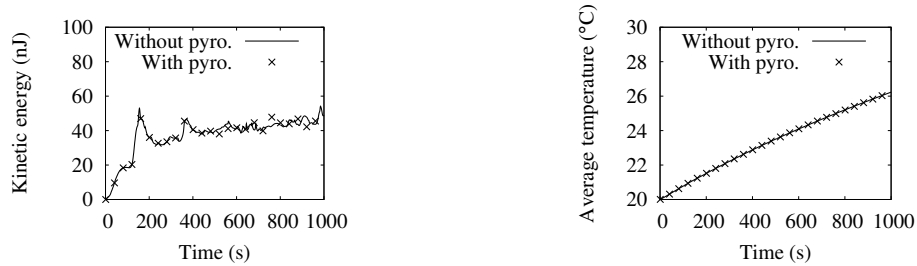


Figure 5.23: Impact of the pyromagnetic coefficient term on the global quantities. Setup with ferromagnetic core, magnetic oil with $\phi = 7\%$. 3D simulations on 8 modes.

293.15 K). The magnetization of the magnetic oil is linear for $H \leq 50$ kA/m approximately and saturates for $H \geq 200$ kA/m approximately. Without the ferromagnetic core, the magnetic field intensity reaches 15 kA/m (Figure 19a of the article), which is in the linear region of the curve. The linear magnetic material approximation is thus valid in this case. With the ferromagnetic core, the magnetic field intensity reaches 76 kA/m (Figure 19c of the article). It is thus questionable to use the linear magnetic material approximation in this case. The simulations on the setup with the ferromagnetic core should be re-performed with not approximated Langevin's law to verify the results.

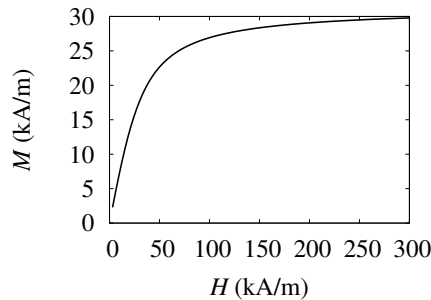


Figure 5.24: Magnetization of the magnetic oil with $\phi = 7\%$ at $T = 20^\circ\text{C}$ with respect to the magnetic field intensity.

5.4 Conclusion of the chapter

The immersed coil setup of Chapter 4 is improved by replacing the PVC walls with aluminium walls, closer to the structure of an actual transformer. The thermo-hydrodynamical model for regular oil is validated against an experiment on pure transformer oil, like in Chapter 4. The ferrofluid modeling is improved by considering the modification of the thermophysical properties with the addition of the magnetic nanoparticles. The density

and the specific heat are modeled by mixture laws; the thermal conductivity is modeled by the classical model of Maxwell for nanofluids; the dynamic viscosity is modeled by the law of Rosensweig for ferrofluids. With the parameters considered in this study, the change of the thermophysical properties is shown to be positive for the cooling of the coil. As a matter of fact, the coil temperature is reduced by up to 2°C when the thermophysical properties of the base fluid are changed into that of the ferrofluid. As in Chapter 4, thermomagnetic convection is shown to have a positive impact on the coil cooling by modifying the convection pattern and reducing the temperature of the coil (by up to 2°C approximately).

The numerical results on the positive influence of thermomagnetic convection are confirmed by an experiment using a transformer oil-based ferrofluid. An alternating current is numerically tested and the results prove that an AC current of 50 Hz and a DC current with the same RMS value give an equivalent temperature rise. As a matter of fact, the time period of the imposed AC current is too short compared to the thermal time to induce any change on the temperature.

The modeling of the ferrofluid is improved by taking into account the temperature dependence of the saturation magnetization of the magnetic nanoparticles. The numerical results confirm the benefit of ferromagnetic materials with low Curie temperatures, because they increase the thermomagnetic convection effect. Finally, the pyromagnetic coefficient term in the temperature equation of ferrofluids is shown to be negligible in our case. The magnetic body force is enough to model the effects of the magnetic oil considered here.

Chapter 6

Thermomagnetic convection in a transformer

In this chapter, we study the benefit of ferrofluid for the cooling of a geometry close to an actual electrical transformer. In a transformer, the magnetic flux passing throughout the ferromagnetic circuit transfers the electrical energy from one coil wound around it to another. In the meantime, the voltage and the current are modified from the first coil to the other due to the different number of turns. We propose to make use of the leakage magnetic flux in the insulating liquid to generate thermomagnetic convection and enhance heat transfer. The magnetic field in the insulating liquid and the Joule effect in the coils can be approximated by an axisymmetric computation. This approach is often used in the electrical engineering community, see [115, 2, 116] for instance. Therefore, the electromagnetic system investigated here is composed of two concentric coils wound around a ferromagnetic core. The voltages and the currents in the coils are that of a 40 kVA (20 kV/400 V) transformer. The first section presents the basic principle of a transformer in order to introduce this electromagnetic system. The second section details the electromagnetic system and the proposed modeling. The third section compares the results obtained with transformer oil cooling and transformer oil-based ferrofluid cooling. Finally, some variations of the model and the associated results are reported in the fourth section.

6.1 Transformer principle

The aim of the present section is to show analytically how a transformer can change the voltage and the current from an electrical circuit, said the primary, to another, said the secondary.

6.1.1 Simplified transformer

The reasoning is based on a simplified transformer, presented in Figure 6.1. We consider a ferromagnetic core, say of iron, of toric shape with a mean radius R and a square section of side a . The core usually has a square shape but the toric shape can fulfill the same function and makes the calculus easier. The primary and the secondary circuits are magnetically connected to the core by two coils, called primary and secondary coils.

6.1.2 Absence of load

In the first step, we consider the system in the absence of load (the electrical load connected to the secondary circuit), see Figure 6.1a. The circuit of the secondary coil is open and

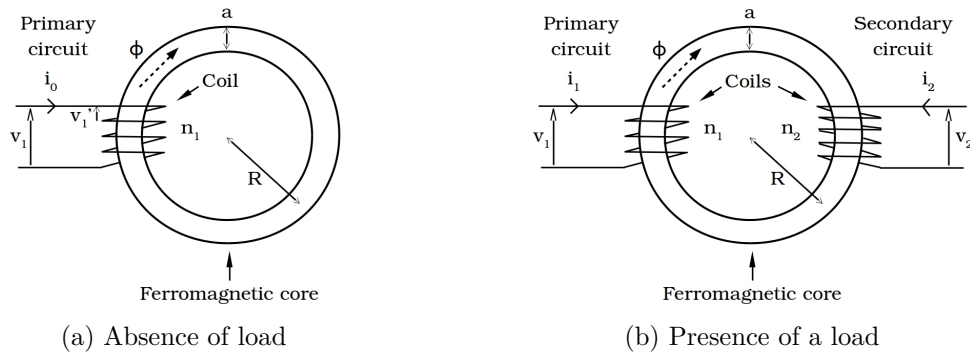


Figure 6.1: Simplified transformer constituted of a toric ferromagnetic core, (b) with and (a) without load. The presence of a load corresponds to the operating configuration. The other case is used for the theoretical calculations. The dashed arrow represents the direction of the induction flux in the core.

is therefore not displayed. The primary coil consists in n_1 wires and is supplied with an alternating voltage $v_1 = V_1\sqrt{2}\sin(\omega t)$, where V_1 is the root mean square value (RMS), defined by

$$V_1 = \left(\frac{\omega}{2\pi} \int_0^{2\pi} v_1(t)^2 dt \right)^{\frac{1}{2}}, \quad (6.1)$$

and ω is the pulsation. The current in the primary coil is named i_0 in this configuration. The alternating voltage creates a flux of induction ϕ in the core. By Faraday's law of induction, we have

$$v_1 = -n_1 \frac{d\phi}{dt}, \quad (6.2)$$

The voltage due to the electrical resistance of the coil, $R_1 i_1$, is neglected. By integrating (6.2), we have

$$\phi = \frac{V_1\sqrt{2}}{n_1\omega} \cos(\omega t). \quad (6.3)$$

The constant coming from the integration is zero since the flux is zero in the absence of current. By calculus, the RMS value Φ of the flux ϕ is

$$\Phi = \frac{V_1}{n_1\omega}. \quad (6.4)$$

(6.2) and (6.4) show that the flux of induction in the core is determined by the voltage and the number of turns in the primary coil.

Due to the high magnetic permeability of the core and the magnetic field interface conditions, the induction in the core can be considered parallel to the core / air interface. Considering that $a \ll R$, we assume that the intensity of the induction in the core is uniform in every section. For simplicity, we assume that it is uniform everywhere in the core. We denote by B_{cr} the intensity of the induction in the core. Under these assumptions, we have

$$\phi = B_{cr} S, \quad (6.5)$$

where $S = a^2$ is the section of the core. The intensity of the magnetic field in the core is thus

$$H_{cr} = \frac{\phi}{\mu_0 \mu_{cr} S}. \quad (6.6)$$

Ampère's theorem applied to the primary coil implies

$$2\pi R H_{cr} = n_1 i_0. \quad (6.7)$$

We replace H_{cr} on the left-hand side by using (6.6). We obtain

$$\mathcal{R}\phi = n_1 i_0, \quad (6.8)$$

where

$$\mathcal{R} = \frac{2\pi R}{\mu_0 \mu_{cr} S} \quad (6.9)$$

is called the magnetic reluctance.

6.1.3 Presence of a load

In the second step, we consider the system in the presence of a load, i.e., in operating configuration. The secondary coil is also wound around the core, see Figure 6.1b. The secondary coil consists in n_2 turns and has a voltage v_2 . The same voltage v_1 is still enforced in the primary coil. In this configuration, the currents in the primary and secondary coils are named i_1 and i_2 , respectively. As in the absence of load, Faraday's law of induction implies (6.2). Similarly, Faraday's law of induction also implies

$$v_2 = -n_2 \frac{d\phi}{dt}. \quad (6.10)$$

It follows from (6.2) and (6.10) that the voltages in the coils are related by

$$\frac{v_2}{v_1} = m, \quad (6.11)$$

where $m = \frac{n_2}{n_1}$ is the ratio of the numbers of turns. By adjusting the number of turns in each coil, the transformer can increase ($n_2 > n_1$) or decrease ($n_2 < n_1$) the voltage. By using the reasoning on the circular circuit throughout the core \mathcal{C}_t of the first case, we have

$$\mathcal{R}\phi = n_1 i_1 + n_2 i_2. \quad (6.12)$$

The right-hand side can be substituted by using (6.8). We then deduce the relation between the currents

$$i_0 - m i_2 = i_1. \quad (6.13)$$

The current i_0 , defined in (6.8), is usually small compared to i_1 because the relative magnetic permeability of the core μ_{cr} is high (several thousands for iron). The change of current between the primary and secondary coils is determined by the inverse ratio of the numbers of turns, as the change of voltage. Notice that the currents are almost opposed in term of sign. Notice also that the current times the number of turns is almost unchanged in absolute value.

This reasoning is valid for an ideal transformer, i.e., the magnetic flux is confined in the ferromagnetic core ($\mu_{cr} \rightarrow \infty$, $\mathcal{R} \rightarrow 0$). In an actual transformer, a small part of the magnetic flux leaks into the insulating liquid. The benefit of thermomagnetic convection and ferrofluids especially relies on the leakage magnetic flux, which is computed in the simulations.

6.1.4 Superimposed coils

The location of the secondary coil on the ferromagnetic core does not impact the analysis (as long as the leakage magnetic field is neglected). The secondary coil can be superimposed to the primary coil for instance, as in an actual transformer. Figure 6.2 shows a sectional view of the system in case of a load and in two configurations of winding: the one used for the theoretical calculations and the one of superimposed coils. To go from the first to the second, the secondary coil is shifted under the primary coil. Notice that

when the coils are superimposed, the current symbols in the primary and secondary coils have the same direction. The theoretical calculations are still valid and the currents are almost opposite in term of sign. In this configuration, the currents in the coils are thus collinear but of opposite direction.

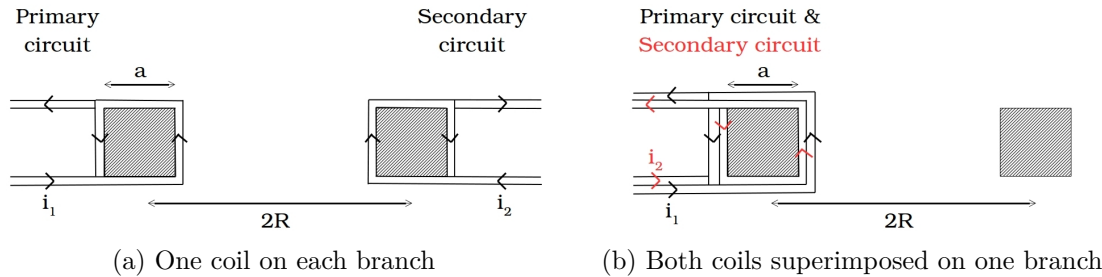


Figure 6.2: Sectional view of the simplified transformer for two winding configurations. The hatched area represents the section of the core.

While the position of the coils does not influence the transformer operation, it influences the magnetic field in the insulating liquid and, therefore, the thermomagnetic convection effect if ferrofluid is used.

6.2 Physical problem and modeling

In this section, we present the electromagnetic system considered to investigate numerically the thermomagnetic convection effect. The basic principle of any transformer, discussed in Section 6.1, is respected in this system.

6.2.1 The considered electromagnetic system

The electromagnetic system is constituted of two concentric coils wound around a ferromagnetic core. These components are immersed in a bath of transformer oil (or transformer oil-based ferrofluid) enclosed by a cylindrical tank. The exterior coil is called the primary coil and the interior coil is called the secondary coil. The core is made of cylindrical shape and it does not form a loop around the coils, i.e., the whole ferromagnetic circuit is not considered. Nevertheless, we assume that this electromagnetic system gives a reasonable approximation of the magnetic field generated in the insulating liquid and of the Joule effect in the coils, and that the thermomagnetic convection and the temperature rise are representative of what would be obtained with a realistic geometry. The simple shapes of the core and the tank in this system allow us to consider that the system is axisymmetric, and thus to perform our simulations with the SFEMaNS code. The system is shown in Figure 6.3 and the dimensions are reported in Table 6.1. Notice that the core and the coils do not touch each other. These components are spaced by gaps filled by oil. The solid isolation parts in an actual transformer are not considered.

Parameter	H_t	R_t	e_w	H_{cr}	H_{cl}	e_{cl}
Value (cm)	46	21.1	1	7	11	4
Parameter	R_{cr}	$R_{cl,1}$	$R_{cl,2}$	L_{cr}	L_{cl}	
Value (cm)	4.5	14.1	9.6	32	24	

Table 6.1: Dimensions of the system.

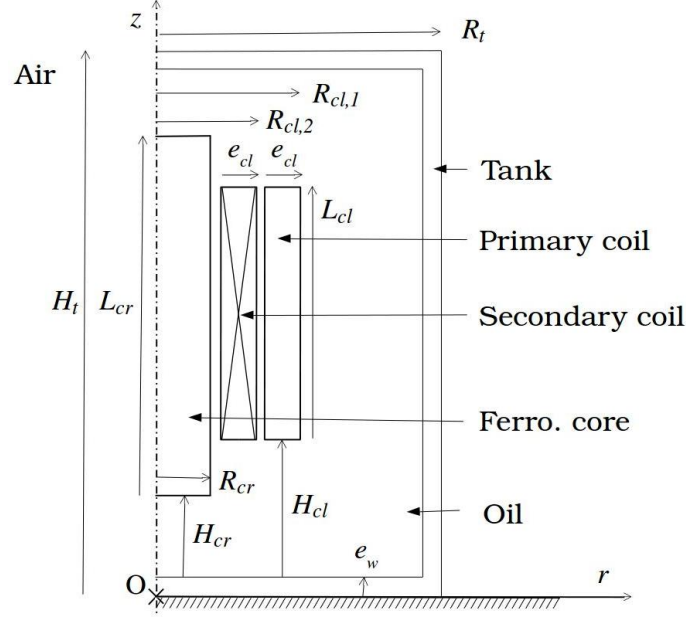


Figure 6.3: Meridian section of the system (symmetry axis = z axis).

Each coil is crossed by an AC current. The present system respects the constraints mentioned in Section 6.1. The current in the secondary coil has the opposite direction compared to the current in the primary coil and the ampere-turns¹ are equal in both coils. In the primary coil, there are $n_1 = 10000$ turns, the RMS voltage is $U_1 = 20$ kV and the RMS current in each turn is $I_1 = 2$ A. In the secondary coil, there are $n_2 = 200$ turns, the RMS voltage is $U_2 = 400$ V and the RMS current in each turn is $I_2 = 100$ A. The RMS voltages satisfy $U_1/U_2 = n_1/n_2$ and are thus consistent with the relation between the voltages (6.11). The RMS currents satisfy $n_1 I_1 = n_2 I_2$ and are thus almost consistent with the relation between the currents (6.13). We only neglect i_0 in (6.13), which order of magnitude is small compared to that of i_1 and i_2 . As mentioned, the system has an electrical power of $U_1 I_1 = U_2 I_2 = 40$ kVA.

6.2.2 Modeling

We present the geometry, the governing equations, the physical properties and the mesh used for our simulations.

Geometry

The coils are modeled by hollow cylinders of square section and made of pure copper. We denote by Ω the entire domain, Ω_{cr} the core domain, Ω_{cl}^p the primary coil domain, Ω_{cl}^s the secondary coil domain, Ω_f the fluid domain and Ω_t the tank domain. The boundary of each domain is denoted with a ∂ in front. The top, lateral and bottom boundaries of the entire domain are denoted by $\partial\Omega_{top}$, $\partial\Omega_{lat}$ and $\partial\Omega_{bot}$, respectively. For the magnetic field computation only, we consider a supplementary domain Ω_0 representing the air and the support around the tank, where the magnetic permeability is that of vacuum, μ_0 . The exterior boundary of Ω_0 is denoted by $\partial\Omega_{0,ext}$. Ω_0 is chosen large enough so that the boundary conditions applied on $\partial\Omega_{0,ext}$ have little influence. The notations are illustrated in Figure 6.4.

¹Current in each wire multiplied by the number of wires.

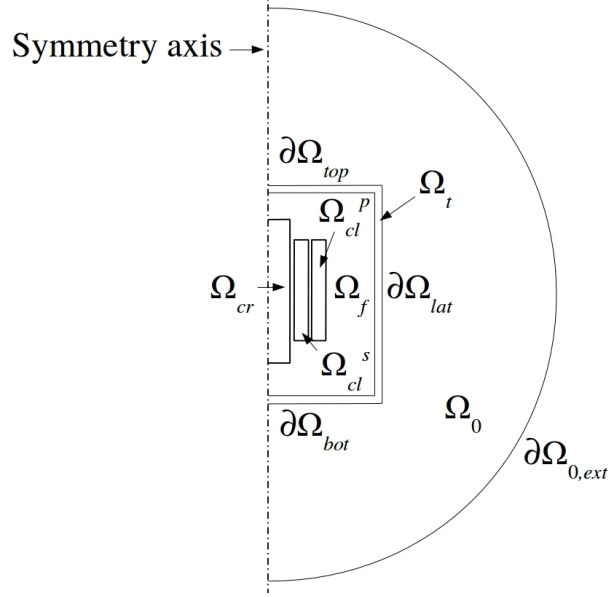


Figure 6.4: Subdomains in a meridian section. The domain Ω is composed of Ω_{cr} , Ω_{cl}^p , Ω_{cl}^s , Ω_f and Ω_t .

Governing equations

Section 5.2.4 shows that an AC current and a DC current with the same RMS value lead to an equivalent temperature rise in the immersed coil. We therefore consider a constant current density in the present modeling. The ferromagnetic core is assumed laminated; the eddy currents generated by the alternating magnetic field in the core are thus neglected. The currents in the coil are modeled by current densities $j_0 \mathbf{e}_\theta$ in the primary coil and $-j_0 \mathbf{e}_\theta$ in the secondary coil, with $j_0 = 2 \times 10^6 \text{ A/m}^2$.

The governing equations used in the previous chapter are adapted to this new configuration containing two coils. We recall the equations for the sake of clearness. Regarding the properties, the values taken in each subdomain are distinguished by the corresponding subscripts when needed.

The temperature equations are

$$\left\{ \begin{array}{ll} \rho c \partial_t T + \rho c \tilde{\mathbf{u}} \cdot \nabla T - \nabla \cdot (\lambda \nabla T) = f_T & \text{in } \Omega, \\ -\lambda_t \nabla T \cdot \mathbf{n} = h(T - T_0) & \text{on } \partial\Omega_{top} \cup \Omega_{lat}, \\ -\lambda_t \nabla T \cdot \mathbf{n} = 0 & \text{on } \partial\Omega_{bot}, \\ T|_{t=0} = T_0 & \text{in } \Omega. \end{array} \right. \quad (6.14)$$

$\tilde{\mathbf{u}}$ is the extension of the velocity in the entire domain defined by

$$\tilde{\mathbf{u}} = \begin{cases} \mathbf{u} & \text{in } \Omega_f, \\ 0 & \text{in } \Omega \setminus \Omega_f. \end{cases} \quad (6.15)$$

The source term f_T is defined by

$$f_T = \begin{cases} \rho_e j_0^2 & \text{in } \Omega_{cl}^p \cup \Omega_{cl}^s, \\ 0 & \text{in } \Omega \setminus (\Omega_{cl}^p \cup \Omega_{cl}^s), \end{cases} \quad (6.16)$$

where ρ_e is the electrical resistivity of the conductors. h is the convection coefficient at the top and lateral boundaries of the tank and T_0 is the initial temperature. The pyromagnetic coefficient term in the temperature equation of ferrofluids is not considered in this chapter.

The velocity and pressure equations for transformer oil cooling are

$$\left\{ \begin{array}{ll} \partial_t \mathbf{u} + (\nabla \times \mathbf{u}) \times \mathbf{u} + \nabla \left(\frac{p}{\rho_f} \right) - \nabla \cdot (2\nu_f \nabla^s \mathbf{u}) = \alpha_f (T - T_0) g \mathbf{e}_z & \text{in } \Omega_f, \\ \nabla \cdot \mathbf{u} = 0 & \text{in } \Omega_f, \\ \mathbf{u} = 0 & \text{on } \partial\Omega_f, \\ \mathbf{u}|_{t=0} = 0 & \text{in } \Omega_f. \end{array} \right. \quad (6.17)$$

If the transformer oil is replaced by transformer oil-based ferrofluid, we introduce the variation of the Kelvin force and the momentum equation becomes

$$\partial_t \mathbf{u} + (\nabla \times \mathbf{u}) \times \mathbf{u} + \nabla \left(\frac{p}{\rho_f} \right) - \nabla \cdot (2\nu_f \nabla^s \mathbf{u}) = \alpha_f (T - T_0) g \mathbf{e}_z + \frac{\mu_0}{\rho_f} (\chi(T) - \chi(T_0)) \nabla \left(\frac{H^2}{2} \right) \text{ in } \Omega_f. \quad (6.18)$$

Here, we use the change of variable $p \leftarrow p - \mu_0 \chi(T_0) H^2 / 2$. The pressure notation is not changed to avoid multiplying the variables. The susceptibility is given by an approximation of Langevin's law:

$$\chi(T) = \frac{\phi \mu_0 \pi d^3 M_{s,p}(T)^2}{18 k_B T}, \quad (6.19)$$

where ϕ is the volume fraction of magnetic material, d is the nanoparticle diameter, $M_{s,p}$ is the saturation magnetization of the magnetic nanoparticles and k_B is the Boltzmann constant. The saturation magnetization of the magnetic nanoparticles is function of the temperature and is described by Bloch's law, see (5.9), with a Curie temperature $T_C < \infty$.

Finally, the magnetic field equations are

$$\left\{ \begin{array}{ll} \nabla \times \mathbf{H} = \mathbf{j} & \text{in } \Omega \cup \Omega_0, \\ \nabla \cdot (\mu \mathbf{H}) = 0 & \text{in } \Omega \cup \Omega_0, \\ \mathbf{H} \times \mathbf{n} = 0 & \text{on } \partial\Omega_{0,ext}. \end{array} \right. \quad (6.20)$$

The current density \mathbf{j} is defined by

$$\mathbf{j} = \begin{cases} j_0 \mathbf{e}_\theta & \text{in } \Omega_{cl}^p, \\ -j_0 \mathbf{e}_\theta & \text{in } \Omega_{cl}^s, \\ 0 & \text{in } (\Omega \cup \Omega_0) \setminus (\Omega_{cl}^p \cup \Omega_{cl}^s). \end{cases} \quad (6.21)$$

The magnetic permeability μ is piecewise constant. It is equal to $\mu_0(1 + \chi(T_0))$ in the ferrofluid.

Physical properties

The thermophysical properties used in the simulations are presented in Table 6.2. The electrical resistivity of the coils is $\rho_e = 1.68 \times 10^{-8} \Omega \cdot m$ [117].

As in the article in Section 5.1, the dynamic viscosity of the transformer oil is approximated by using the expression

$$\eta(T) = A \exp \left(\frac{B}{T} \right), \quad (6.22)$$

where $A \simeq 1.3 \times 10^{-6} \text{ Pa} \cdot \text{s}$, $B \simeq 3.1 \times 10^3 \text{ K}$ and T in K. The thermophysical properties of the transformer oil-based ferrofluid are functions of that of the transformer oil and

Property	Copper	RO	MO	Steel	Iron
Density (kg/m ³)	8933	922	965	7850	7870
Thermal expansion (1/K)	-	7.4e-4	7.3e-3	-	-
Heat capacity (J/K · kg)	385	1970	1898	475	447
Thermal conductivity (W/m · K)	401	0.166	0.171	44.5	80.2

Table 6.2: Material properties. Copper and iron properties are from [107, pp. 983-984]. Regular oil (RO) properties are from the manufacturer (Midel). Magnetic oil (MO) properties are functions of the regular oil properties and the magnetite nanoparticles properties. Steel properties are from the COMSOL software.

that of magnetite, following the same laws (see Section 2.3 of the article for the detailed laws). The volume fraction of nanoparticles is $\phi = 1\%$ to maintain reasonable dielectric properties, see Section 2.4.2. The magnetite nanoparticles have the following properties: $\rho_p = 5.18 \times 10^3$ kg/m³ [111], $c_p = 630$ J/K · kg [112] and $\lambda_p = 6$ W/m · K [46]. As that of the transformer oil, the viscosity of the transformer oil-based ferrofluid is temperature-dependent.

The diameter of the magnetic nanoparticles is $d = 10$ nm, their saturation magnetization at 20°C is $M_{s,p}(20^\circ\text{C}) = 4.46 \times 10^5$ A/m [114] and their Curie temperature is $T_C = 580^\circ\text{C}$.

To enhance heat transfer, the transformer tanks are usually equipped with heat transfer fins, which form a larger exchange surface with the air. The convection coefficient can then be multiplied several times with respect to the coefficient with no fin (up to 20 in electronics for instance [118]). Based on the dimensions and the power of the present transformer, we can estimate that the convection coefficient at the top and lateral boundaries of the tank is approximately 6 W/m² · K in the absence of heat transfer fins, see Appendix E. In the following, we consider that the tank is equipped with such fins and we use the value $h = 150$ W/m² · K.

The relative magnetic permeability is $\mu_r = 100$ in the (steel) tank and $\mu_r = 5000$ in the (iron) ferromagnetic core.

Mesh

The mesh of the meridian section is presented in Figure 6.5. The mesh size in the coil is chosen so that three elements lay in the gap between the coils. The mesh size in the tank is chosen so that two elements lay in the wall thickness. Note that the figure does not show the large air domain around the tank, a half-disk of radius 1.23 m, used for the computation of the magnetic field only. Without the air domain, the mesh contains 10776 \mathbb{P}_1 nodes and 39105 \mathbb{P}_2 nodes.

Note that most of the computations reported here are performed assuming axisymmetry of the solution (only mode 0 is solved). Results in Section 6.3.4 show that the solution is quasi-axisymmetric and that the computations on mode 0 are valid.

6.3 Regular oil vs. magnetic oil cooling

In the simulations, the electromagnetic system is cooled either with the transformer oil or the transformer oil-based ferrofluid. In this section, the temperature and the velocity fields are compared to assess the benefit of ferrofluid cooling.

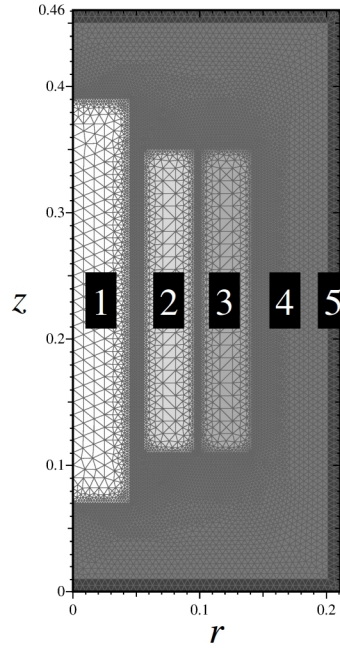


Figure 6.5: Mesh of the meridian section (symmetry axis on the left). Axes in meters. 1: ferromagnetic core, 2: secondary coil, 3: primary coil, 4: oil, 5: tank. The mesh size goes from 2×10^{-3} (center) to 10^{-2} m (boundary with the oil) in the coils and is 5×10^{-3} m in the tank.

6.3.1 Time evolutions

We are primarily interested in the operating configuration of the transformer, i.e., in the permanent regime of the system. Figure 6.6 shows the time evolution of the kinetic energy and the average temperature defined by

$$E_k = \int_{\Omega_f} \frac{1}{2} \rho_f u^2 dV, \quad \bar{T} = \sqrt{\frac{1}{V} \int_{\Omega} T^2 dV}, \quad (6.23)$$

where V is the volume of the system (solid part included). Even though the kinetic energy presents sustained oscillations, the average temperature has a smooth evolution. A steady state is reached around $t = 10000$ s for the temperature. Note that the time evolutions of the average temperature in the case of regular oil and magnetic oil cooling are very close. The magnetic nanoparticles seem to not affect the temperature in the system from a global point of view. Let us verify whether differences exist locally.

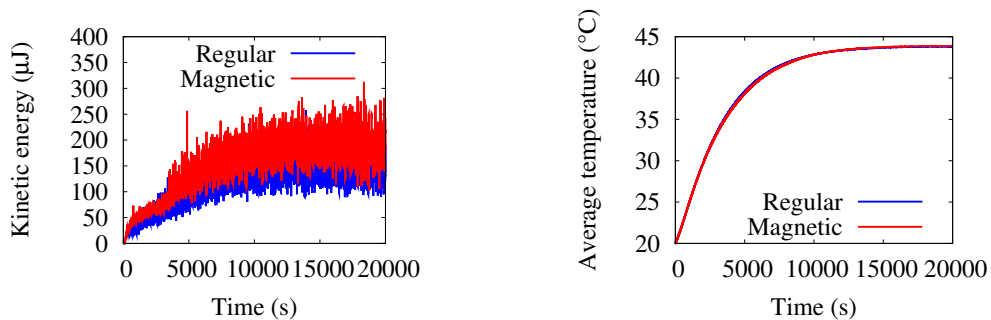


Figure 6.6: Kinetic energy (left panel) and average temperature (right panel) for regular oil and magnetic oil cooling.

We wish to assume the benefit of the ferrofluid in the hottest region of the transformer, i.e., the windings. In the model, the thermal conductivities in the subdomains corresponding to the ferromagnetic core and the coils are large (the coil subdomains are made of pure copper). The computed temperature in each of these components is therefore rather homogeneous. Figure 6.7 shows the time evolution of the temperature at the center of the core and the coils for regular oil and magnetic oil cooling. As expected, the temperature in the core (40-45°C) is lower than the temperature in the windings (55-60°C). At $t = 20000$ s, the temperature in the primary (secondary) coil is about 2°C (5°C) lower with magnetic oil than with regular oil. According to this figure, the cooling of the coils is more efficient with magnetic oil for the properties used in the simulations. Note that the temperature in the core is approximately 1°C higher with magnetic oil than with regular oil. It shows that the temperature is more homogeneous in the system when magnetic oil is used.

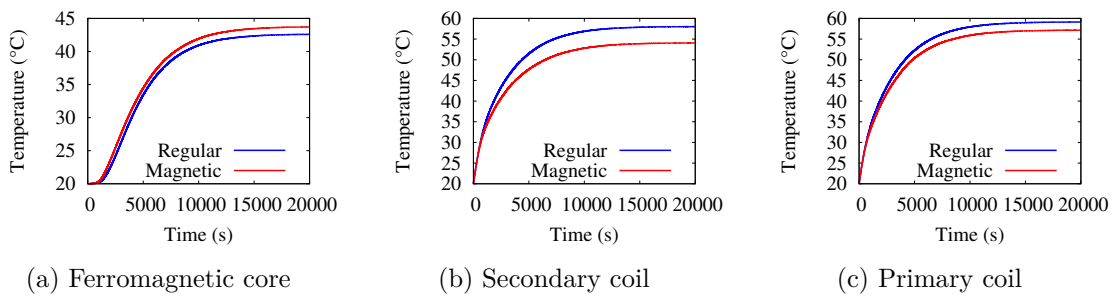


Figure 6.7: Temperature at the center of each component when regular oil is used versus when magnetic oil is used.

6.3.2 Temperature and velocity fields

The maximum temperature in the system can only be determined by observing the temperature field. Figure 6.8 compares the temperature fields in a meridian section at $t = 20000$ s when regular oil or magnetic oil is used. The temperature decrease when using magnetic oil instead of regular oil can be due to the change of the oil thermophysical properties and the thermomagnetic convection effect, see Chapter 5. The temperature field obtained with magnetic oil but a zero magnetic field (no magnetic interactions, only the thermophysical properties change) is also displayed.

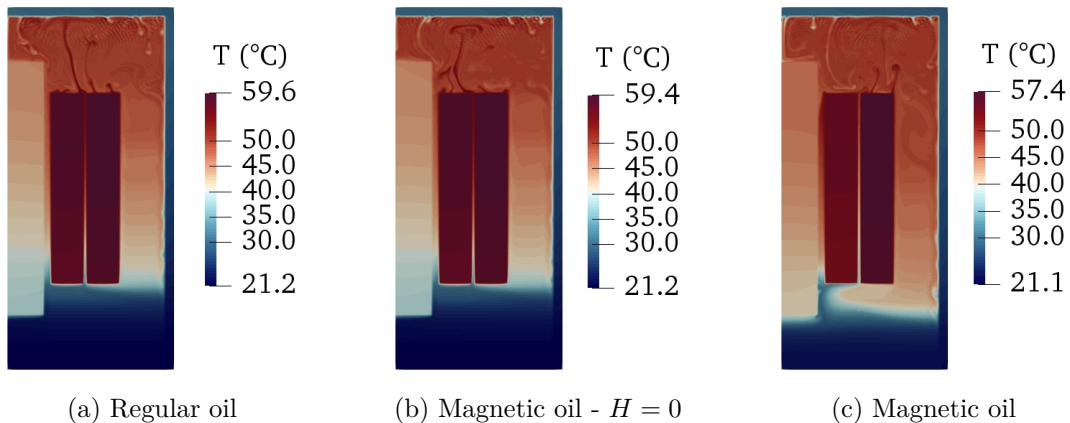


Figure 6.8: Temperature in a meridian section (symmetry axis on the left) at $t = 20000$ s.

According to this figure, the maximum temperature in the system is 59.6°C with regular

oil and 57.4°C with magnetic oil. The use of magnetic oil therefore reduces the maximum temperature by 2.2°C. The improvement of the cooling efficiency by the addition of magnetic nanoparticles to the transformer oil is confirmed by this result. The temperature distribution seems more homogeneous in the oil as well, see the region at the bottom of the coils in both panels. The maximum temperature in the system is 59.4°C with magnetic oil and a zero magnetic field, showing that the change of the thermophysical properties is only responsible for 0.2°C of the temperature decrease in this configuration.

We investigate the changes in the velocity flow due to thermomagnetic convection. Figure 6.9 shows the components of the velocity in a meridian section at $t = 20000$ s, in the regular oil and in the magnetic oil. The azimuthal component is zero in both cases and is therefore not displayed. No matter the kind of cooling, a strong convective flow is present in the fluid region above the core and the coils. This convective flow is different in the regular oil and magnetic oil cases: further visualizations of the meridian section show that the fluid turns clockwise in the regular oil and counter-clockwise in the magnetic oil. Thermomagnetic convection also modifies the flow by introducing an additional convection cell under the coils and by increasing the flow velocity in the gap between the coils (compare Figures 6.9b and 6.9d).

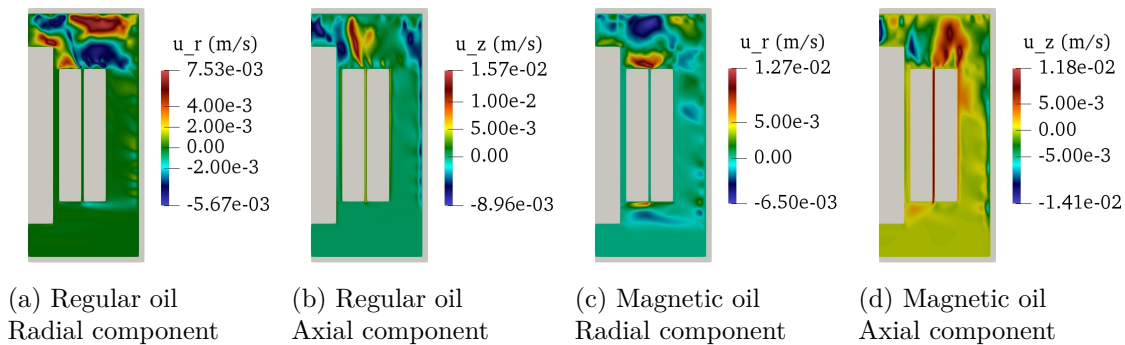


Figure 6.9: Components of the velocity in a meridian section (symmetry axis on the left) at $t = 20000$ s.

We want to verify that the axial velocity is stronger in the gap between the coils when magnetic oil is used. Figure 6.10 shows the axial velocity profile at $t = 20000$ s in the oil layer between the two coils. As observed, the velocity is much higher in this area when the magnetic oil is used. The maximum axial velocity is doubled in the presence of the magnetic oil (8 mm/s with magnetic oil against 4 mm/s with regular oil). This feature can help to dissipate more efficiently the heat generated by the windings.

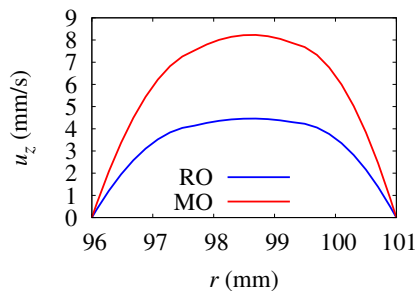


Figure 6.10: Axial velocity profile in the gap between the coils at mid-height ($z = 0.23$ m) at $t = 20000$ s, for regular oil (RO) and magnetic oil (MO).

6.3.3 Magnetic field

As mentioned, thermomagnetic convection relies on the magnetic field generated by the coils in the fluid region. Figure 6.11 shows the intensity of the magnetic field in the ferrofluid case (it is slightly different from that of the transformer oil case owing to the magnetic susceptibility of the ferrofluid). The magnetic field is localized in the gap between the coils and takes a weak value far from this area. As a matter of fact, the magnetic field is the sum of the magnetic fields generated by the coils (linearity of the magnetostatics equations), which carry opposite currents. Far from the coils, the magnetic fields generated by the coils are thus nearly opposite and their sum is zero.

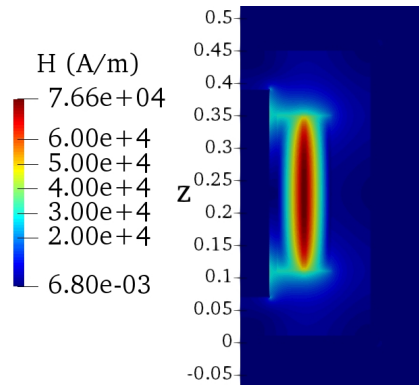


Figure 6.11: Magnetic oil cooling. Magnetic field intensity in a meridian section (symmetry axis on the left). The z axis is in meters.

To illustrate this statement, we show the profiles of the magnetic field components along two axes and for three cases: 1) the primary coil only is crossed by a current, 2) the secondary coil only is crossed by a current, 3) both coils are crossed by currents (configuration of the simulations), see Figure 6.12. The comparison of the profiles confirms that the magnetic fields generated by the coils separately cancel each other everywhere except in the fluid layer between the coils (see the area around $r = 0.1$ m in Figure 6.12c for instance). Note that the interface conditions between the tank ($\mu_r = 100$) and the ferrofluid ($\mu_r = 1.11$), and between the ferrofluid and the core ($\mu_r = 5000$), are respected on H_z in Figure 6.12a.

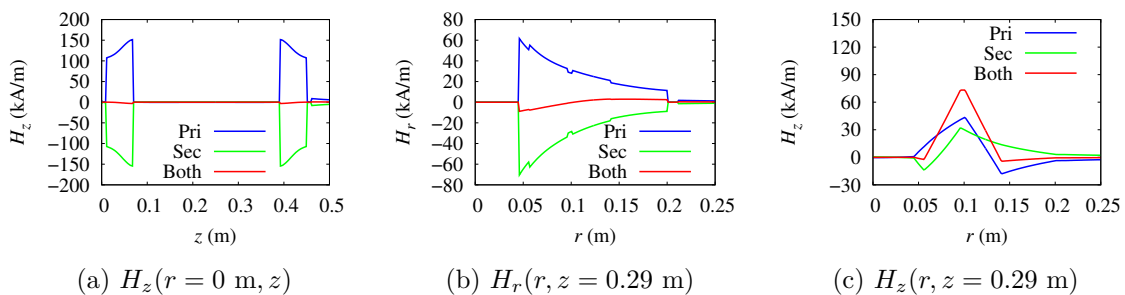


Figure 6.12: Magnetic oil cooling. Magnetic field profiles when the primary coil only is active, when the secondary coil only is active and when both are active.

The opposite direction of the currents in the coils is enforced by the principle of a transformer, as explained in Section 6.1. In this configuration, the magnetic fields generated by the coils cancel each other. The magnetic body force and the associated thermomagnetic convection effect might therefore be limited. It would be interesting to test other configurations to avoid this symmetry. Note that the intensity of the magnetic field in the gap

between the coils can explain the higher velocity in this region when the magnetic oil is used (Figure 6.10).

6.3.4 Three-dimensional study

Previous results are obtained with computations on mode 0 only, i.e., we have assumed that the solution is axisymmetric. To verify this assumption (as in Section 4.3.2), the computation is restarted at $t = 10000$ s by using 8 modes (0 to 7), with a perturbation of 10^{-3}C on temperature modes greater or equal to 1. Figures 6.13 and 6.14 present the time evolution of the modal kinetic energies, see definitions (4.19) and (4.20), and the modal average temperatures, see definitions (5.4) and (5.5), for regular oil and magnetic oil, respectively. The time evolutions are similar in both cases (regular or magnetic oil). The modal kinetic energy and the modal average temperature for modes greater or equal to 1 do not decay and are maintained at a constant level. Nevertheless, mode 0 dominates the other modes (mode 0 is approximately 10 times stronger than the others for the kinetic energy and 100 times stronger than the others for the average temperature). The velocity and the temperature are quasi-axisymmetric. We can conclude that the computations on mode 0 only give a good approximation of the three-dimensional solutions.

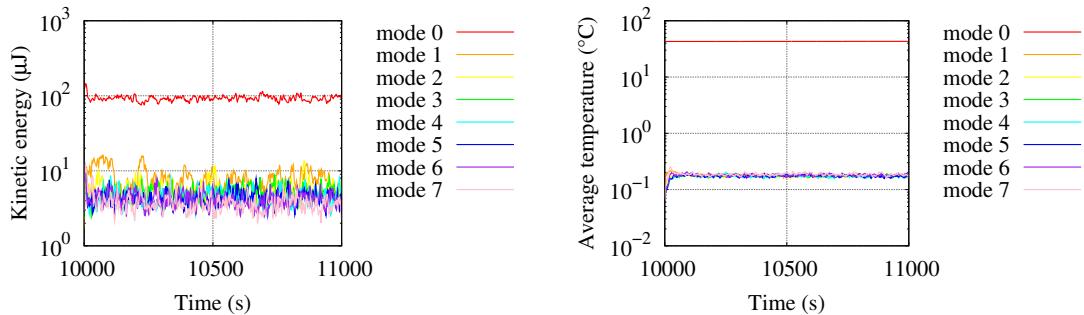


Figure 6.13: Regular oil cooling. Mode-by-mode time evolution of the global quantities after restart from the solution on mode 0 at $t = 10000$ s.

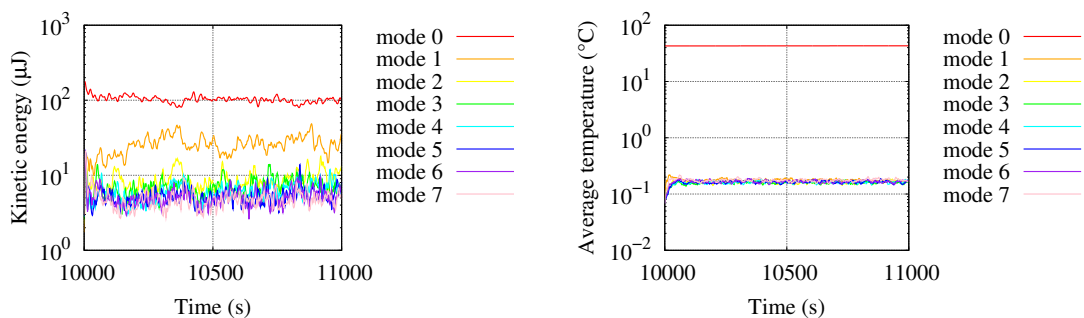


Figure 6.14: Magnetic oil cooling. Mode-by-mode time evolution of the global quantities after restart from the solution on mode 0 at $t = 10000$ s.

6.4 Variations of the model

This section aims at testing the influence of various parameters on the cooling efficiency of the magnetic oil. The results are shown at $t = 10000$ s because the previous simulations show that the temperature stabilize around this instant time.

6.4.1 Tank magnetic permeability

We study the impact of the relative magnetic permeability of the tank to test whether a ferromagnetic material can enhance or not the thermomagnetic convection effect. In addition to the standard computation with $\mu_r = 100$ in the tank (steel), we perform two computations with $\mu_r = 1$ (aluminium) and $\mu_r = 1000$ (iron) in the tank. The other properties of the tank stay the same to highlight the influence of the magnetic permeability. The temperatures at the center of each component of the active part obtained with the various relative magnetic permeabilities, are reported in Table 6.3. The temperature varies of 0.3°C maximum, showing that the impact of the tank magnetic permeability is limited. The temperature tends to slightly increase with the relative magnetic permeability. Apparently, the higher the magnetic permeability in the tank, the lower the thermomagnetic convection effect. These computations show that, with the parameters chosen in this study, ferromagnetic materials should be avoided. Materials having a weak magnetic permeability should on the contrary be preferred to maximize the thermomagnetic convection effect (even if the benefit appears to be low).

Component \ μ_r	1	100	1000
Ferromagnetic core	41.7	41.9	42.0
Secondary coil	52.6	52.8	52.9
Primary coil	55.8	55.9	55.9

Table 6.3: Magnetic oil cooling. Temperature (°C) at the center of each component at $t = 10000$ s with respect to the relative magnetic permeability in the tank.

6.4.2 Curie temperature

As shown in the immersed coil case (Section 5.3.1), the magnetic materials with a low Curie temperature can improve the cooling efficiency of ferrofluids by enhancing the thermomagnetic convection effect. We perform additional computations to observe the influence of the Curie temperature in the transformer case. In addition to the standard computation with $T_C = 580^\circ\text{C}$ (magnetite), we perform two computations with $T_C = 150^\circ\text{C}$ (Mn-Zn ferrites) and $T_C = 365^\circ\text{C}$ (average between 150 and 580°C). The rest of the ferrofluid parameters stays the same to highlight the effect of the Curie temperature. The temperatures at the center of each component of the active part obtained with the various Curie temperatures are reported in Table 6.4. In the coils, the temperature is lowered by a few 0.1°C from $T_C = 580^\circ\text{C}$ to $T_C = 365^\circ\text{C}$, but it is increased also by a few 0.1°C from $T_C = 365^\circ\text{C}$ to $T_C = 150^\circ\text{C}$. The temperature variations are such that, in the secondary coil, the temperature at the center is higher with $T_C = 150^\circ\text{C}$ than with $T_C = 580^\circ\text{C}$. In the core, the temperature is increased by a few degrees with $T_C = 150^\circ\text{C}$ compared to $T_C = 580$ and 365°C . As for the tank magnetic permeability, the temperature variations when the Curie temperature is modified are limited. Moreover, lowering the Curie temperature does not systematically improve the cooling as in the immersed coil system.

We verify that reducing the Curie temperature strengthen the magnetic body force. Figure 6.15 shows the variation of the Kelvin body force divided by the fluid density,

$$\frac{\mathbf{f}_m}{\rho_f} = \frac{\mu_0}{\rho_f} \Delta\chi(T) \nabla \left(\frac{H^2}{2} \right), \quad (6.24)$$

in a meridian section at the final time. The view is centred on the top region of the coils, where lays the maximum intensity of the magnetic body force. Note that the lower the Curie temperature, the higher the intensity of the magnetic body force, as expected.

Component	T_C		
	580°C	365°C	150°C
Ferromagnetic core	41.9	41.9	44.0
Secondary coil	52.8	52.2	53.0
Primary coil	55.9	55.4	55.5

Table 6.4: Magnetic oil cooling. Temperature (°C) at the center of each component at $t = 10000$ s with respect to the Curie temperature.

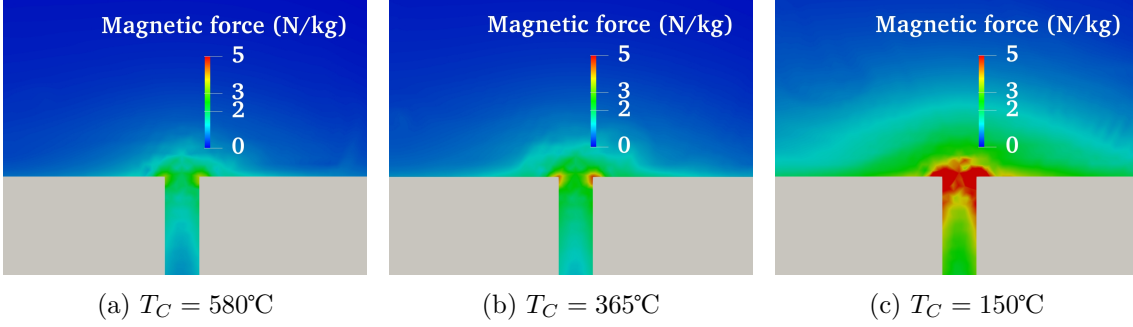


Figure 6.15: Intensity of the magnetic body force divided by the fluid density in a meridian section at $t = 10000$ s. The grey parts represent the top end of the coils.

This result is surprising because the literature agrees on the fact that the nanoparticles should be made of magnetic materials with a low Curie temperature in order to enhance thermomagnetic convection, see [77, 72, 4] for instance. It might show the limit of the linear magnetic material assumption for the ferrofluid. The magnetic field intensity in the gap between the coils (Figure 6.11) is such that the ferrofluid magnetization should saturate, while the model does not enable the magnetization saturation due to this assumption. If the magnetization intensity saturated close to the coils, the Kelvin body force would be weaker there and the thermomagnetic convection could be more important.

6.4.3 Size of the tank

There exists transformer geometries where the oil volume between the active part and the tank is weaker, see [115] for instance. The dimensions of our tank are actually quite arbitrary. We investigate the effect of the magnetic oil in two additional transformer geometries. In the new geometries, the tank radius and height take lower values so that the tank walls get closer to the active part and the oil volume is reduced. In the following, the original tank is called tank 1 and the additional tanks are called tanks 2 and 3. The radius and the height of tank 1 are $R_t = 0.211$ m and $H_t = 0.46$ m. The radius and the height of tank 2 are $R_t = 0.191$ m and $H_t = 0.42$ m. The radius and the height of tank 3 are $R_t = 0.171$ m and $H_t = 0.38$ m. The active part is still localized in the middle of the tank. The meshes used for each geometry are shown in Figure 6.16.

The maximum temperature in the system obtained for each tank is reported in Table 6.5. For regular oil cooling and magnetic oil cooling, the maximum temperature increases when the tank volume is reduced. As expected, reducing the oil volume decreases the heat transfer efficiency, no matter the kind of oil. The maximum temperature decreases when magnetic oil is used instead of regular oil in all tanks. The decrease of the maximum temperature is 2.2°C in the original tank (tank 1), 2°C in the middle-size tank (tank 2) and 3.2°C in the smaller tank (tank 3). According to this test, the size of the tank does not affect the positive influence of the magnetic nanoparticles. Reducing the tank even increases the temperature decrease with the magnetic oil (2.2°C \rightarrow 3.2°C).

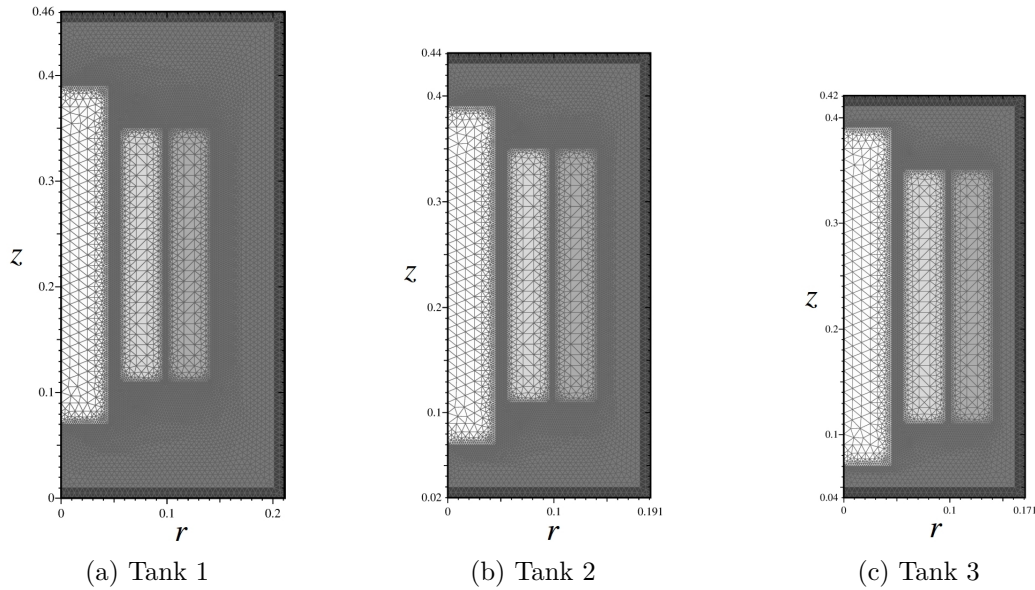


Figure 6.16: Mesh of the meridian section (symmetry axis on the left). Axes in meters. For every mesh, the mesh size goes from 2×10^{-3} to 10^{-2} m in the coil and is 5×10^{-3} m in the tank.

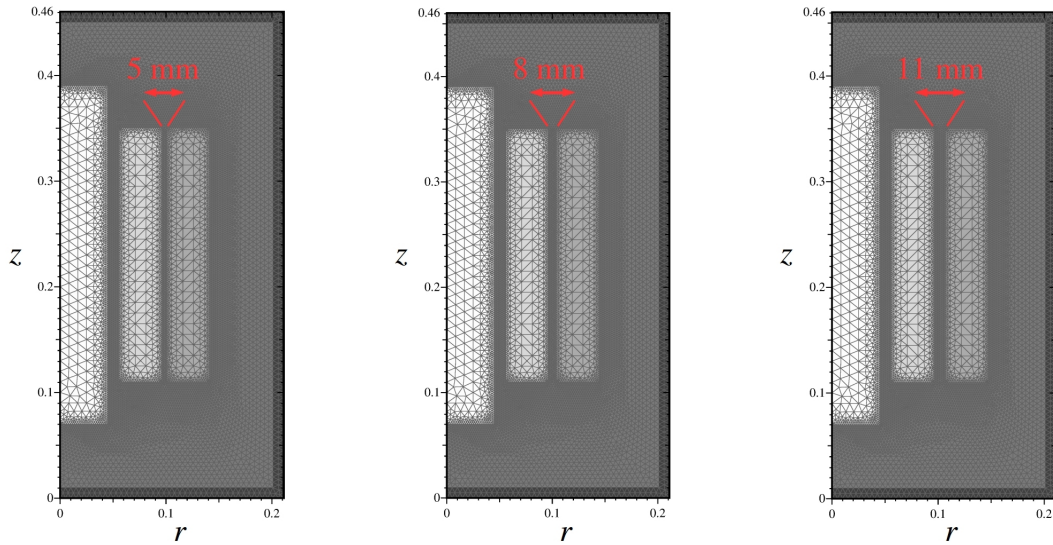
	Tank		
Oil	1	2	3
Regular	58.4	62.2	67.2
Magnetic	56.2	60.2	64.0

Table 6.5: Maximum temperature ($^{\circ}\text{C}$) in the system at $t = 10000$ s with respect to the tank size.

6.4.4 Distance between the coils

Thermomagnetic convection increases the flow velocity in the gap between the coils (Figure 6.10), which can enhance heat dissipation between the coils and the oil. Here, we try to maximize the thermomagnetic convection effect by increasing the distance between the coils. The distance between the coil is 5 mm in the original geometry. Additional computations are performed in geometries where this distance is either 8 or 11 mm. To obtain a larger gap, the primary coil is simply moved radially in the direction of the tank. The meshes used for each geometry are shown in Figure 6.17.

The maximum temperature in the system obtained for each geometry is reported in Table 6.6. For regular oil cooling or magnetic oil cooling, the maximum temperature increases when the distance between the coils is increased. We can explain this by considering that the volume of the primary coil increases when it is moved radially in the direction of the tank (its interior and exterior radii increase, leading to a larger volume). The Joule effect per unit volume being constant, the total Joule effect grows, i.e., more heat needs to be dissipated. The decrease of the maximum temperature when magnetic oil is used instead of regular oil is 2.2°C with the 5 mm original distance, 1.6°C with the 8 mm distance and 1.8°C with the 11 mm distance. Spacing the coils thus does not generate a major thermomagnetic convection effect.



(a) Gap between coils: 5 mm (b) Gap between coils: 8 mm (c) Gap between coils: 11 mm

Figure 6.17: Mesh of the meridian section (symmetry axis on the left). Axes in meters. For every mesh, the mesh size goes from 2×10^{-3} to 10^{-2} m in the coil and is 5×10^{-3} m in the tank.

Gap	5 mm	8 mm	11 mm
Oil			
Regular	58.4	59.5	59.8
Magnetic	56.2	57.9	58.0

Table 6.6: Maximum temperature ($^{\circ}\text{C}$) in the system at $t = 10000$ s with respect to the distance between the coils in the setup.

6.5 Conclusion of the chapter

The benefit of a transformer oil-based ferrofluid is studied in a 40 kVA (20 kV/400 V) transformer. An electromagnetic system composed of two concentric coils, representing the primary and secondary coils, wound around a cylindrical ferromagnetic core is considered. In a first step, a 3D model considering the whole ferromagnetic circuit is not used because this axisymmetric system gives a good approximation of the thermomagnetic convection and of the temperature rise that would be obtained in the transformer. The current densities in the model have realistic values and the volume fraction of nanoparticles is limited to 1% to maintain adapted dielectric properties.

The ferrofluid is shown to reduce the maximum temperature in the transformer compared to the transformer oil (2.2°C decrease), due to the change of the oil thermophysical properties and the thermomagnetic convection effect. When the ferrofluid is used, the flow velocity is increased in the space between the coils, enhancing heat dissipation. The flow is also modified in the rest of the fluid region by the appearance of additional convection cells. Because the currents in the coils are opposite, the linearity of the magnetostatics equations imposes that the magnetic field is negligible far from the coils. The computation of the magnetic field shows that the magnetic field intensity is weak in the fluid region, except in the space between the coils. It can explain the stronger flow velocity in this region with ferrofluid, but we can wonder whether thermomagnetic convection could be more efficient in another configuration of currents. These results are obtained with computations on mode 0 only but computations on several modes show that the temperature

and the velocity are dominated by mode 0 for the parameters used in this study.

The influence of various parameters (tank magnetic permeability, Curie temperature of the magnetic nanoparticles, size of the tank, space between the coils) are investigated but, while the ferrofluid cooling is more efficient than the transformer oil cooling in each configuration, no parameter notably affects the temperature decrease. It is globally not as high as we could expect (3.2°C at most). A temperature decrease of approximately 20°C was measured in a transformer prototype of similar power [2]. Nevertheless, the magnetic modeling of the ferrofluid could be improved in our simulations by considering the non-linear regime. Moreover, we have to consider that a few degrees of difference can strongly affect the lifetime of a transformer (multiplied by 2 for a temperature decrease of 6°C).

Chapter 7

Conclusion

7.1 Outcome

The goal of this PhD was to study the impact of the use of ferrofluids for the cooling of immersed transformers. Several tasks had to be completed: development of a model for the natural convection of ferrofluids, adaptation of the SFEMaNS code to solve such problem, validation of the model against experiments using an immersed coil, assessment and understanding of the benefit of ferrofluids for the cooling of electromagnetic systems. The performed work led to multiple findings.

Modeling. In a first step, we considered the ferrofluid as a continuum with Newtonian behavior and homogeneous properties. Owing to the tiny relaxation time, the ferrofluid magnetization was assumed collinear to the applied magnetic field. The temperature difference being relatively small in the considered applications, we worked under the Boussinesq approximation. We used the linearization of Langevin's law for the ferrofluid magnetization intensity, valid for a low magnetic field intensity. The ferrofluid magnetic susceptibility being quasi-constant in our applications, it was assumed constant to avoid a strong coupling with the magnetic problem. To summarize, we considered the magnetostatics equations, the Navier-Stokes equations, under the Boussinesq approximation and with the Kelvin (or Helmholtz) magnetic body force, and the temperature equation (of a regular Newtonian fluid). In addition, classical laws for the thermophysical properties of the ferrofluid as functions of the volume fraction of nanoparticles were used (Maxwell's model for the thermal conductivity and Rosensweig's model for the dynamic viscosity). We investigated the magnetic body force in ferrofluids. The literature mentions various expressions but several of them, including the most popular ones, are equal up to a gradient. This PhD numerically confirmed that these expressions in fact provide the same velocity and temperature solutions, and that we can therefore choose arbitrary any one of them to solve a convection problem.

Numerical method. New functionalities were brought to the SFEMaNS code to solve ferrohydrodynamics problems. The code is yet able to compute the temperature in mixed solid/fluid domains, to assess the impact of the convective flow on the temperature in a solid body. Various adaptations of the existing numerical schemes were carried out to include the Kelvin or Helmholtz body forces, a temperature-dependent viscosity in the momentum equation and the pyromagnetic coefficient term in the temperature equation of ferrofluids. These new coupling terms are made explicit due to their non-linearity but they preserve the time and space convergence rate of the code. Robin boundary conditions were also implemented to improve the comparison with experiments. Convergence

tests on manufactured solutions showed the correct behavior of the code with these new developments.

Comparison with the experiments. The numerical results were first compared with the experiments using pure transformer oil. By using a realistic tank/air convection coefficient in the model, we obtained a good match between the computed temperature and the measured temperature at various points. Oscillatory phenomena were observed in the experiments and the simulations but it was not clear whether they were of the same nature. The numerical results were then compared with the experiment using a transformer oil-based ferrofluid. The experiment confirmed the positive effect of thermomagnetic convection predicted by the simulations. Moreover, the measured temperature decrease was similar to the computed one. These convincing comparisons showed the relevance of our modeling choices, even if some aspects may be improved.

Cooling of electromagnetic systems with ferrofluid. In the simulations, the transformer oil-based ferrofluid was shown to be more efficient in terms of cooling than the transformer oil in any considered system. As a matter of fact, a maximum temperature decrease was consistently computed when the regular oil was replaced by the magnetic oil, even if this temperature decrease might be considered disappointing (2-3°C in the transformer, while some experimental works obtain more significant differences). The computations showed that two aspects of ferrofluids are responsible for this temperature decrease: thermomagnetic convection and the change of the thermophysical properties due to the presence of the magnetic nanoparticles. With the physical data and the laws considered in this study, the change of the thermophysical properties was sufficient (no need of the magnetic field) to reduce the maximum temperature in the system. When the magnetic field was activated, the convective flow was modified and the maximum temperature was further reduced. The simulations on the immersed coil showed that the use of ferromagnetic materials (for the nanoparticles) with a low Curie temperature enhances the heat transfer, because the ferrofluid then has a high pyromagnetic coefficient (as indicated by the literature). Nevertheless, it was not true in the simulations on the transformer, which might be due to the modeling.

7.2 Perspectives

Some questions were answered but others are still to be tackled and several perspectives can be listed in order to continue the work.

The comparison with the experiment using the ferrofluid was not fully completed due to a lack of time. By refining the ferrofluid parameters in the model, we may obtain a good quantitative agreement between the numerical and the experimental results. Ideally, we would need the actual thermophysical properties of the ferrofluid (measured over the temperature range of the experiment) to make use of a more realistic model.

The results obtained with the transformer showed a small impact of the magnetic nanoparticles on the temperature in the windings, contrary to some other results of the literature. In future works, one should try to understand this aspect. We can already think of one way to improve our results. A strong hypothesis of this PhD is the linearization of Langevin's law for the ferrofluid magnetization intensity. Nevertheless, the magnetic field intensity in some of the considered systems (including the transformer) is such that the ferrofluid magnetization intensity will locally saturate. It is difficult to assess how the saturation will affect the heat transfer but it might be in a positive way because the saturation will reduce the magnetic body force close to the source of heat (and therefore

possibly increase thermomagnetic convection). It would be interesting to implement the full law of Langevin and re-perform the simulations.

We can think of another limit of our model: the transformer geometry. For simplicity, we only considered an axisymmetric model, sufficient for the computation of the leakage magnetic field and of the Joule effect. The simulations should be re-performed with a three-dimensional model including the full magnetic circuit to confirm the results. Moreover, the considered transformer was simpler than an actual transformer. For instance, we did not model the solid insulation parts and the tank geometry was cylindrical. It would be interesting to perform the simulations with transformer oil and transformer oil-based ferrofluid in the geometry of an existing transformer (possibly of very high power). Let us also mention that we did not consider the induced currents in the ferromagnetic core and the tank, which could produce additional thermomagnetic convection.

Finally, one should investigate an optimal transformer design to maximize the ferrofluid benefit. The leakage magnetic flux is usually minimized to control the energy loss during the conversion, while thermomagnetic convection requires a magnetic field to develop. A patent suggests the use of permanent magnets to increase the magnetic field in the insulating liquid for instance. The setup of the coils could also be modified to avoid that their respective magnetic fields cancel each other.

Chapter 8

Résumé en français

8.1 Introduction

Les transformateurs sont des machines électriques qui permettent de modifier la tension entre deux branches d'un réseau électrique. Le refroidissement des transformateurs de forte puissance est assuré par la convection, naturelle ou forcée, du liquide isolant. Il s'agit en général d'huile minérale qui sert aussi à l'isolation électrique. Plusieurs équipes de recherche [1, 2, 3, 4] ont proposé d'améliorer les transferts thermiques en utilisant de l'huile de transformateurensemencée de nanoparticules magnétiques, c'est-à-dire du ferrofluide. En effet, la présence d'un champ magnétique et d'un gradient de température génère un phénomène dit de convection thermomagnétique dans ces fluides. Plusieurs avantages pourraient être obtenus, tels que des cuves plus petites, la suppression des pompes, l'augmentation de la durée de vie ou l'utilisation d'huile végétale.

Cependant, l'avantage d'un ferrofluide pour le refroidissement des transformateurs n'est pas bien expliqué dans la littérature. Se posent notamment les questions de la cohabitation des phénomènes de convection thermogravitationnelle et thermomagnétique, ou de l'effet du changement des propriétés thermophysiques de l'huile (densité, conductivité thermique, viscosité, etc.) avec l'ajout de nanoparticules. Pour étudier cette problématique, nous proposons une approche de modélisation numérique avec le code de recherche parallélisé SFEMaNS (Spectral/Finite Element for Maxwell and Navier-Stokes) pour des géométries axisymétriques, utilisant une décomposition spectrale dans la direction azimutale et des éléments finis de Lagrange dans le plan méridien. Après plusieurs développements, le code est d'abord appliqué au cas d'un dispositif expérimental. Il s'agit d'une bobine immergée dans un bain d'huile. Le code est ensuite appliqué au cas d'un transformateur pour vérifier si l'on peut étendre l'avantage des ferrofluides à cette application industrielle.

Les objectifs de cette étude sont de proposer un modèle pour la convection naturelle des ferrofluides, d'adapter le code SFEMaNS afin de pouvoir résoudre un tel problème, de valider le modèle avec les résultats expérimentaux sur la bobine immergée et d'étudier l'avantage des ferrofluides par rapport aux fluides classiques pour le refroidissement de systèmes électromagnétiques.

Après cette première section introductive, la seconde section présente l'étude bibliographique. La troisième section présente les développements dans SFEMaNS. La quatrième section présente les résultats numériques obtenus sur le dispositif expérimental. La cinquième section présente les résultats numériques obtenus sur un second dispositif expérimental (changement du matériau de la cuve), avec un modèle plus réaliste prenant en compte les vraies propriétés thermophysiques du ferrofluide. La sixième section présente les résultats numériques obtenus sur un transformateur de 40 kVA. La septième section présente les conclusions et les perspectives.

8.2 Etude bibliographique sur les ferrofluides

Nous présentons ici les ferrofluides, leur modélisation dans la littérature, le phénomène de convection thermomagnétique et les principaux travaux portant sur l'utilisation de ferrofluide pour refroidir les transformateurs.

8.2.1 Généralités

Les ferrofluides sont des suspensions constituées d'un liquide porteur et de nanoparticules (3-15 nm de diamètre) magnétiques [10, p. 7]. Les nanoparticules sont composées de matériaux ferromagnétiques (fer, nickel, cobalt) ou de leurs composés et alliages, ou de leurs oxydes (magnétite souvent : Fe_3O_4). Le liquide porteur peut être de l'eau, de l'huile ou du kérosène par exemple. Le mouvement Brownien et l'ajout d'un surfactant permettent d'éviter l'agglomération et la sédimentation des nanoparticules. Les ferrofluides se comportent ainsi comme des fluides monophasiques avec des propriétés magnétiques. Il existe quelques applications industrielles telles que les haut-parleurs et les joints liquides. D'autres applications, notamment bio-médicales, sont encore à l'état de recherche.

8.2.2 Modélisation

De par leur faible taille, les nanoparticules sont composées d'un unique domaine de Weiss et portent systématiquement un moment magnétique non nul. Les ferrofluides ont ainsi un comportement magnétique dit super-paramagnétique [10, pp. 55-61]. Leur magnétisation est fonction du champ magnétique et de la température, et l'intensité de la magnétisation est donnée par la loi de Langevin :

$$M = M_s L(\xi) = M_s \left(\coth(\xi) - \frac{1}{\xi} \right), \quad (8.1)$$

avec M_s la magnétisation à saturation définie par

$$M_s = \phi M_{s,p}, \quad (8.2)$$

où ϕ est la fraction volumique de nanoparticules et $M_{s,p}$ la magnétisation à saturation du matériau ferromagnétique, et ξ défini par

$$\xi = \frac{\pi \mu_0 M_{s,p} d^3 H}{6 k_B T}, \quad (8.3)$$

où μ_0 est la perméabilité magnétique du vide, d le diamètre des nanoparticules (considéré unique pour simplifier), H l'intensité du champ magnétique, k_B la constante de Boltzmann et T la température en Kelvin. Sous faible champ, l'intensité de la magnétisation peut être linéarisée¹ : $M = \chi H$ avec

$$\chi = \frac{\pi \mu_0 \phi M_{s,p}^2 d^3}{18 k_B T}. \quad (8.4)$$

Les ferrofluides sont généralement considérés comme des milieux continus avec un comportement newtonien, comme par exemple dans [33]. On utilise alors les équations de Navier-Stokes avec une densité de force magnétique en plus de la gravité au membre de droite. Il existe plusieurs expressions de densité de force magnétique, dont celle de Kelvin (la plus citée) et celle de Helmholtz :

$$\mathbf{f}_K = \mu_0 (\mathbf{M} \cdot \nabla) \mathbf{H}, \quad \mathbf{f}_H = -\frac{H^2}{2} \nabla \mu, \quad (8.5)$$

¹Hypothèse utilisée dans la thèse.

où \mathbf{M} est la magnétisation du ferrofluide, \mathbf{H} le champ magnétique et μ la perméabilité magnétique du ferrofluide. Par ailleurs, il est raisonnable de supposer que \mathbf{M} est colinéaire à \mathbf{H} car le temps de relaxation de la magnétisation est très faible dans les ferrofluides.

Les propriétés thermophysiques des ferrofluides (densité, chaleur spécifique, conductivité thermique, viscosité, coefficient d'expansion thermique) sont différentes de celles du fluide de base, même en l'absence de champ magnétique. La densité et la chaleur spécifique sont données par des lois de mélange [42]. Il existe de multiples modèles donnant la conductivité thermique et la viscosité des nanofluides (suspensions de nanoparticules) en fonction de ϕ , tels que celui de Maxwell [49] pour la conductivité,

$$\lambda_{\text{ff}} = \left(1 + \frac{3\phi(\lambda_p - \lambda_{\text{bf}})}{3\lambda_{\text{bf}} + (1 - \phi)(\lambda_p - \lambda_{\text{bf}})} \right) \lambda_{\text{bf}}, \quad (8.6)$$

où λ_{ff} est la conductivité du ferrofluide, λ_{bf} celle du fluide de base et λ_p celle des nanoparticules, et celui de Rosensweig [10, pp. 63-65] pour la viscosité,

$$\eta_{\text{ff}} = \left(1 - \frac{5}{2}\tilde{\phi} + \frac{5}{2}\frac{\tilde{\phi}_c - 1}{\tilde{\phi}_c^2}\tilde{\phi}^2 \right)^{-1} \eta_{\text{bf}}, \quad (8.7)$$

où η_{ff} est la viscosité dynamique du ferrofluide, η_{bf} celle du fluide de base, $\tilde{\phi}$ la fraction volumique de nanoparticules incluant le surfactant et $\tilde{\phi}_c = 0.74$.

8.2.3 Convection thermomagnétique

La convection thermomagnétique est un phénomène lié aux propriétés magnétiques des ferrofluides, qui se produit en présence d'un champ magnétique (appliqué ou induit) et d'un gradient de température. Cette instabilité est due à la variation de la magnétisation avec la température, ce qui crée des variations spatiales de la densité de force magnétique et peut entraîner un mouvement macroscopique du ferrofluide [17]. Ainsi, dans la configuration de la Figure 8.1, le bilan des forces est tel qu'une particule de ferrofluide qui s'éloignerait de sa position d'équilibre serait entraînée plus en avant dans son mouvement (situation instable). Ce phénomène est analogue à la convection naturelle classique liée à la variation de la densité avec la température.

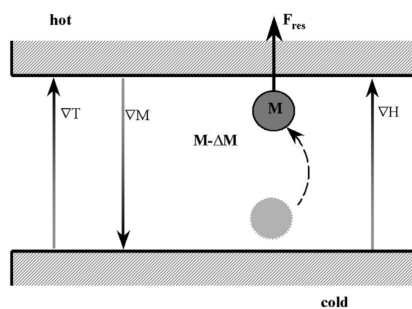


Figure 8.1: Configuration d'apparition de la convection thermomagnétique [12].

La convection thermomagnétique a été étudiée par de multiples auteurs de façon analytique [64], expérimentale [65, 67, 68], numérique [69, 70, 71] ou par approche couplée expérience et numérique [72, 73, 74, 75]. Ces études ont montré que divers facteurs entrent en ligne de compte : l'intensité et la direction du champ magnétique, le gradient de température et les propriétés magnétiques du ferrofluide. Les auteurs favorisent ainsi l'utilisation de matériaux ferromagnétiques à faible température de Curie (ferrites de Mn-Zn par exemple), car cela augmente le coefficient pyromagnétique du ferrofluide $-\partial M/\partial T$. Ces études ont également montré que la convection thermomagnétique peut améliorer les

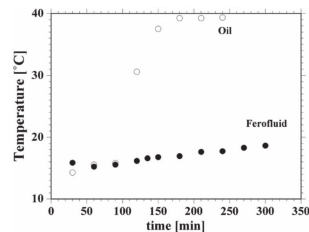
transferts de chaleur dans le ferrofluide de façon significative (multiplication par 2 ou 3 du nombre de Nusselt sans et avec champ magnétique dans [67] par exemple). Cependant, la plupart de ces études ne comparent pas les transferts thermiques avec ceux dans le fluide de base, alors que c'est ce qui nous intéresse particulièrement dans le cas du transformateur.

8.2.4 Refroidissement des transformateurs

Le refroidissement des transformateurs par ferrofluide a été l'objet de brevets en 1995 [77] et 1999 [89]. Le principe est d'exploiter le champ magnétique de fuite des bobinages pour provoquer de la convection thermomagnétique dans le liquide isolant ensemencé de nanoparticules magnétiques. Plusieurs groupes de recherche [1, 2, 3, 4] ont mené des travaux expérimentaux afin de quantifier l'avantage d'un tel mélange sur la température dans le système, en utilisant notamment des prototypes. Des différences de température significatives ont été obtenues entre l'utilisation d'huile de transformateur pure et celle de ferrofluide, voir Figure 8.2. Les études numériques sont cependant assez limitées.



(a) Prototype du transformateur



(b) Température dans la partie active

Figure 8.2: Expérience sur un transformateur de 40 kVA [2].

Par ailleurs, d'autres travaux ont porté sur l'impact des nanoparticules magnétiques sur les propriétés diélectriques du ferrofluide [79, 83, 85]. Étonnamment, la mesure de la tension de claquage du mélange a été trouvée supérieure à celle de l'huile de transformateur pure dans plusieurs études, voir Figure 8.3. Cette tendance s'expliquerait par la capture des électrons par les nanoparticules [88]. Il semble que la fraction volumique de nanoparticules doive cependant rester sous le seuil des 1% afin d'observer ce résultat. D'autres propriétés ont été étudiées, telle que la résistivité électrique, mais il reste des éléments à vérifier pour s'assurer que ce mélange remplit les obligations en termes de sûreté des transformateurs [92] (aspect non abordé dans cette thèse).

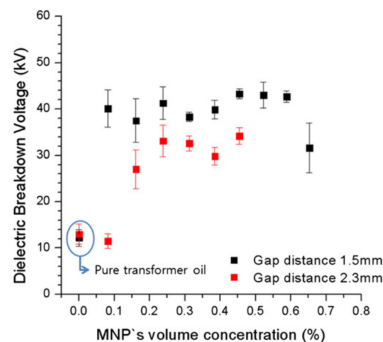


Figure 8.3: Mesure de la tension de claquage en fonction de la fraction volumique de nanoparticules [85].

8.3 Nouveaux développements dans SFEMaNS : applications de ferrohydrodynamique

Nous présentons ici le prototype de problèmes de ferrofluide que peut résoudre SFEMaNS et la méthode numérique en insistant sur les développements menés au cours de la thèse.

8.3.1 Problème physique

Les équations de la ferrohydrodynamique sont résolues dans un domaine axisymétrique $\Omega \subset \mathbb{R}^3$, partitionné en des régions fluide Ω_f et solide Ω_s . La température était originellement calculée dans Ω_f seul. Avec les développements, elle est aussi calculée dans Ω_s , en entier ou en partie. Le domaine de la température est noté Ω_T et on a toujours $\Omega_f \subset \Omega_T \subset \Omega$. La frontière de chaque domaine est dénotée avec un ∂ : $\partial\Omega$ pour la frontière de Ω par exemple. Les parties de ces frontières sur lesquelles sont imposées des conditions de Dirichlet, Neumann ou Robin sont dénotées par un indice d , n ou r , respectivement. Par ailleurs, Ω est partitionné en N sous-domaines Ω_i , $i \in \overline{1, N}$, qui représentent les différentes composantes du système physique. La perméabilité magnétique et les propriétés thermophysiques sont constantes dans chaque sous-domaine. On note Σ_μ l'interface entre ces sous-domaines. La Figure 8.4 représente un exemple type de domaine de calcul.

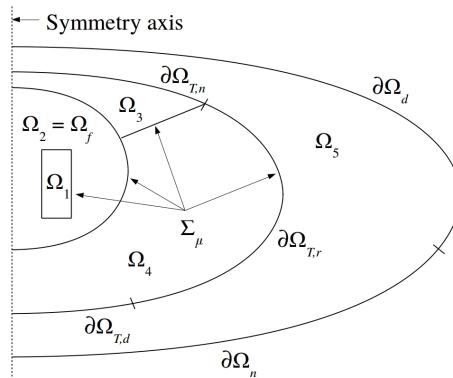


Figure 8.4: Section méridienne d'un exemple type de domaine de calcul Ω . Ω_T est composé des sous-domaines 1 à 4.

Le ferrofluide est considéré comme un milieu continu avec un comportement newtonien. On suppose que la magnétisation est colinéaire au champ magnétique et on se place dans le régime linéaire de la magnétisation. On a ainsi $\mathbf{M} = \chi(T)\mathbf{H}$ dans le ferrofluide, avec \mathbf{M} la magnétisation du ferrofluide, χ la susceptibilité magnétique, T la température et \mathbf{H} le champ magnétique. On note également \mathbf{u} la vitesse et p la pression.

Les équations de la température sont

$$\left\{ \begin{array}{ll} \rho c \partial_t T + \rho c \tilde{\mathbf{u}} \cdot \nabla T - \nabla \cdot (\lambda \nabla T) & \\ + \mu_0 T \frac{\partial \chi}{\partial T}(T) \left(\partial_t \left(\frac{H^2}{2} \right) + \mathbf{u} \cdot \nabla \left(\frac{H^2}{2} \right) \right) = f_T & \text{in } \Omega_f \times \mathbb{R}_+^* \\ \rho c \partial_t T + \rho c \tilde{\mathbf{u}} \cdot \nabla T - \nabla \cdot (\lambda \nabla T) = f_T & \text{in } (\Omega_T \setminus \Omega_f) \times \mathbb{R}_+^* \\ T = T_d & \text{on } \partial\Omega_{T,d} \times \mathbb{R}_+^*, \\ \partial_{\mathbf{n}} T = 0 & \text{on } \partial\Omega_{T,n} \times \mathbb{R}_+^*, \\ -\lambda \nabla T \cdot \mathbf{n} = h_c (T - T_r) & \text{on } \partial\Omega_{T,r} \times \mathbb{R}_+^*, \\ T|_{t=0} = T_0 & \text{in } \Omega_T, \end{array} \right. \quad (8.8)$$

où ρ est la densité, c la chaleur spécifique, λ la conductivité thermique, f_T le terme source, T_d la température imposée sur la frontière de Dirichlet, h_c le coefficient de convection, T_r

la température extérieure à la frontière de Robin et T_0 la température initiale. $\tilde{\mathbf{u}}$ est l'extension du champ de vitesse dans Ω_T . Le terme impliquant $\chi(T)$ est issu des travaux sur la modélisation des ferrofluides [33].

On se place dans l'approximation de Boussinesq. Les équations de la vitesse et de la pression sont

$$\left\{ \begin{array}{l} \partial_t \mathbf{u} + (\nabla \times \mathbf{u}) \times \mathbf{u} + \nabla \left(\frac{p}{\rho_f} \right) \\ -\nabla \cdot (2\nu_f(T) \nabla^s \mathbf{u}) = \alpha_f(T - T_*) g \mathbf{e}_z + \frac{\mathbf{f}_m}{\rho_f} + \frac{\mathbf{f}}{\rho_f} \quad \text{in } \Omega_f \times \mathbb{R}_+^*, \\ \nabla \cdot \mathbf{u} = 0 \quad \text{in } \Omega_f \times \mathbb{R}_+^*, \\ \mathbf{u} = \mathbf{u}_d \quad \text{on } \partial\Omega_f \times \mathbb{R}_+^*, \\ \mathbf{u}|_{t=0} = \mathbf{u}_0 \quad \text{in } \Omega_f, \end{array} \right. \quad (8.9)$$

où T_* est la température de l'approximation de Boussinesq, ρ_f la densité du fluide à T_* , ν_f la viscosité cinématique, α_f le coefficient d'expansion thermique, \mathbf{f}_m la densité de force magnétique, \mathbf{f} les densités de force non liées à la gravité ou la force magnétique, \mathbf{u}_d la vitesse à la frontière et \mathbf{u}_0 la vitesse initiale. On utilise la notation $\nabla^s \mathbf{u} = \frac{1}{2} (\nabla \mathbf{u} + (\nabla \mathbf{u})^T)$ pour le tenseur des taux de déformation. La densité de force magnétique est au choix celle de Kelvin²,

$$\mathbf{f}_K = \mu_0 \chi(T) \nabla \left(\frac{H^2}{2} \right), \quad (8.10)$$

ou celle de Helmholtz,

$$\mathbf{f}_H = -\mu_0 \frac{H^2}{2} \nabla \chi(T). \quad (8.11)$$

On se place dans l'approximation du régime quasi-stationnaire en électromagnétisme et on considère que la perméabilité magnétique du ferrofluide est constante. Les équations du champ magnétique sont

$$\left\{ \begin{array}{l} \nabla \times \mathbf{H} = \mathbf{j} \quad \text{in } \Omega \times \mathbb{R}_+^*, \\ \nabla \cdot (\mu \mathbf{H}) = 0 \quad \text{in } \Omega \times \mathbb{R}_+^*, \\ \mathbf{H} \times \mathbf{n} = \mathbf{H}_d \times \mathbf{n} \quad \text{on } \partial\Omega_d \times \mathbb{R}_+^*, \\ \mu \mathbf{H} \cdot \mathbf{n} = \mu \mathbf{H}_n \cdot \mathbf{n} \quad \text{on } \partial\Omega_n \times \mathbb{R}_+^*, \end{array} \right. \quad (8.12)$$

où \mathbf{j} est la densité de courant, \mathbf{H}_d le champ magnétique à la frontière de Dirichlet et \mathbf{H}_n le champ magnétique à la frontière de Neumann. Les conditions aux interfaces sur Σ_μ sont imposées dans la formulation faible par une méthode de pénalisation, voir [99].

Remarquons qu'il y a un couplage fort entre la température et la vitesse et des couplages faibles entre le champ magnétique et la température (terme de [33]) et entre le champ magnétique et la vitesse (force magnétique).

8.3.2 Méthode numérique

Le code SFEMaNS est basé sur les coordonnées cylindriques (r, θ, z) . La particularité de la méthode est la représentation de Fourier selon la direction θ des variables approchées. Ainsi, l'approximation f_h d'un champ scalaire f est sous la forme

$$f_h(r, \theta, z, t) = \sum_{m=0}^{m_{\max}} f_h^{m, \cos}(r, z, t) \cos(m\theta) + \sum_{m=1}^{m_{\max}} f_h^{m, \sin}(r, z, t) \sin(m\theta), \quad (8.13)$$

²Les hypothèses sur la magnétisation du ferrofluide mentionnées plus haut permettent de simplifier l'expression de \mathbf{f}_K dans (8.5).

où m_{\max} est le mode maximum considéré. Les coefficients $f_h^{\cos,m}$, $m \in \{0, \dots, m_{\max}\}$, et les coefficients $f_h^{\sin,m}$, $m \in \{1, \dots, m_{\max}\}$, sont approchés par des éléments finis de Lagrange, qui sont d'ordre 2 pour la température, la vitesse et le champ magnétique (et d'ordre 1 pour la pression).

L'algorithme en temps du problème est basé sur la méthode des lignes [100, p. 286], avec une approximation en temps par différences finies. Une itération du problème correspond à un incrément de temps τ du temps physique t . Les dérivées temporelles sont approchées par une formule d'ordre 2 tandis que les termes non-linéaires sont traités explicitement. Des approximations d'ordre 2 (ou 1) sont utilisées pour extrapoler les variables de couplages, notées avec un exposant * dans la suite. Les termes non-linéaires sont calculés dans l'espace physique, une méthode de *Fast Fourier Transform* faisant le lien entre le monde physique et le monde de Fourier. Le calcul des champs nécessite la résolution d'un système linéaire par composante dans la décomposition de Fourier (8.13). Chaque problème étant 2D, SFEMaNS reste plus efficace qu'un code classique 3D (pour un m_{\max} raisonnable). Notons enfin que le code a deux niveaux de parallélisme : résolution mode à mode et décomposition de domaines dans le plan méridien.

Nous présentons seulement les schémas numériques qui ont été modifiés pour traiter la ferrohydrodynamique. Pour chaque $n \in \{0, \dots, n_{\max}\}$, on note T_h^n , \mathbf{u}_h^n , p_h^n et \mathbf{H}_h^n l'approximation des champs à $t_n = n\tau$. Nous référons à la partie en anglais pour la définition des espaces d'approximation. L'itération $n \rightarrow n+1$ du schéma de la température³ consiste à résoudre : Trouver $T_h^{n+1} \in S_h$, tel que $T_h^{n+1} = T_d(t_{n+1})$ sur $\partial\Omega_{T,d}$ et

$$\begin{aligned} & \int_{\Omega_T} \rho c \frac{3T_h^{n+1}}{2\tau} s_h dV + \int_{\Omega_T} \lambda \nabla T_h \cdot \nabla s_h dV + \int_{\partial\Omega_{T,r}} h_c T_h^{n+1} s_h dS = \\ & \int_{\Omega_T} \left(\rho c \frac{4T_h^n - T_h^{n-1}}{2\tau} - \rho c \nabla \cdot (T_h^{*,n+1} \tilde{\mathbf{u}}_h^{*,n+1}) + f_T(x, t^{n+1}) \right) s_h dV \\ & - \int_{\Omega_f} \mu_0 T_h^{*,n+1} \frac{\partial \chi}{\partial T}(T_h^{*,n+1}) \left(\mathbf{H}_h^{*,n+1} \cdot \frac{\mathbf{H}_h^n - \mathbf{H}_h^{n-1}}{\tau} + \frac{1}{2} \mathbf{u}_h^{*,n+1} \cdot \nabla ((H_h^{*,n+1})^2) \right) s_h dV \\ & + \int_{\partial\Omega_{T,r}} h_c T_r s_h dS, \forall s_h \in S_h^0. \end{aligned} \tag{8.14}$$

Le schéma de la vitesse et de la pression utilise une méthode de projection en forme rotationnelle, avec élimination du champ de vitesse projetée⁴. L'itération $n \rightarrow n+1$ du schéma consiste à résoudre :

1. Trouver $\mathbf{u}_h^{n+1} \in \mathbf{V}_h$ tel que $\mathbf{u}_h^{n+1} = \mathbf{u}_d$ sur $\partial\Omega_f$ et

$$\begin{aligned} & \int_{\Omega_f} \frac{3\mathbf{u}_h^{n+1}}{2\tau} \cdot \mathbf{v}_h dV + \int_{\Omega_f} 2\bar{\nu}_f \nabla^s \mathbf{u}_h^{n+1} : \nabla \mathbf{v}_h dV + \int_{\Omega_f} c_{\text{div}} \bar{\nu}_f \nabla \cdot \mathbf{u}_h^{n+1} \nabla \cdot \mathbf{v}_h dV = \\ & \int_{\Omega_f} \left(\frac{4\mathbf{u}_h^n - \mathbf{u}_h^{n-1}}{2\tau} - (\nabla \times \mathbf{u}_h^{*,n+1}) \times \mathbf{u}_h^{*,n+1} + \frac{\mathbf{f}(t_{n+1})}{\rho_f} \right) \cdot \mathbf{v}_h dV \\ & - \int_{\Omega_f} \nabla \left(\frac{p^n}{\rho_f} + \frac{4\psi^n - \psi^{n-1}}{3} \right) \cdot \mathbf{v}_h dV - \int_{\Omega_f} 2\tilde{\nu}_f(T^{n+1}) \nabla^s \mathbf{u}_h^{*,n+1} : \nabla \mathbf{v}_h dV \\ & + \int_{\Omega_f} \left(\alpha_f (T_h^{n+1} - T_*) g \mathbf{e}_z + \frac{\mu_0}{\rho_f} \chi(T^{n+1}) \frac{1}{2} \nabla \cdot ((H_h^{*,n+1})^2) \right) \cdot \mathbf{v}_h dV, \forall \mathbf{v}_h \in \mathbf{V}_h^0. \end{aligned} \tag{8.15}$$

³Voir l'approximation de l'équation de la chaleur dans [100, pp. 279-300] par exemple.

⁴Voir l'approximation de l'équation de Stokes dans [100, pp. 300-312] par exemple.

2. Trouver $\psi_h^{n+1} \in M_h$ tel que

$$\int_{\Omega_f} \nabla \psi_h^{n+1} \cdot \nabla q_h dV = \frac{3}{2\tau} \int_{\Omega_f} \mathbf{u}_h^{n+1} \cdot \nabla q_h dV, \forall q_h \in M_h. \quad (8.16)$$

3. Trouver $\delta_h^{n+1} \in M_h$ tel que

$$\int_{\Omega_f} q_h \delta_h^{n+1} dV = \int_{\Omega_f} q_h \nabla \cdot \mathbf{u}_h^{n+1} dV, \forall q_h \in M_h. \quad (8.17)$$

4. Incrémenter p_h^{n+1} par

$$\frac{p_h^{n+1}}{\rho_f} = \frac{p_h^n}{\rho_f} + \psi_h^{n+1} - 2\bar{\nu} \delta_h^{n+1} - c_{\text{div}} \bar{\nu} \delta_h^{n+1}, \quad (8.18)$$

$$\frac{p_h^{n+1}}{\rho_f} \leftarrow \frac{p_h^{n+1}}{\rho_f} - \frac{1}{V_f} \int_{\Omega_f} \frac{p_h^{n+1}}{\rho_f} dV, \quad (8.19)$$

où V_f est le volume de Ω_f . Les variables $\bar{\nu}$ et $\tilde{\nu}$ sont définies comme la valeur maximale et la partie variable de la viscosité cinématique :

$$\bar{\nu} = \max_{T \in [T_{\min}, T_{\max}]} \{\nu(T)\}, \quad \tilde{\nu}(T) = \nu(T) - \bar{\nu}. \quad (8.20)$$

Le paramètre c_{div} permet de contrôler la divergence. ψ_h est le champ scalaire de la décomposition de Helmholtz. δ_h est l'approximation de la divergence, voir [96] pour plus de détails.

Les différents ajouts dans le code (calcul de la température dans la région solide, forces de Kelvin et de Helmholtz, terme supplémentaire dans l'équation de la température des ferrofluides, conditions de Robin, viscosité variable) ont été validés avec des tests de convergence présentés dans la partie en anglais.

8.4 Convection thermomagnétique dans un bain d'huile chauffé par un solénoïde

Le code est appliqué à l'expérience d'une bobine immergée dans un bain d'huile. Nous présentons ici la modélisation du problème, les résultats numériques sur la comparaison du refroidissement par ferrofluide versus par huile classique et un résultat sur les densités de force magnétique. De nombreux détails (dimensions, propriétés, etc.) sont précisés dans la version anglaise seulement.

8.4.1 Modélisation du problème

L'expérience consiste en une bobine alimentée en courant continu et immergée dans un bain d'huile de transformateur (cuve d'environ 10 cm de haut), voir Figure 8.5a. La température est mesurée localement aux points S_1 (bobine) et S_2 (huile) de la figure.

Le domaine de calcul Ω englobe la cuve (parois incluses). Les indices *inf*, *lat* et *sup* dénotent les parois inférieure, latérale et supérieure, respectivement. Les équations de la température sont (on omet de spécifier le domaine temporel) :

$$\left\{ \begin{array}{ll} \rho c \partial_t T + \rho c \tilde{\mathbf{u}} \cdot \nabla T - \nabla \cdot (\lambda \nabla T) = f_T & \text{dans } \Omega, \\ T = T_0 & \text{sur } \partial\Omega_{\text{inf}}, \\ -\lambda \nabla T \cdot \mathbf{n} = h(T - T_0) & \text{sur } \partial\Omega_{\text{lat}} \cup \partial\Omega_{\text{sup}}, \\ T|_{t=0} = T_0 & \text{dans } \Omega, \end{array} \right. \quad (8.21)$$

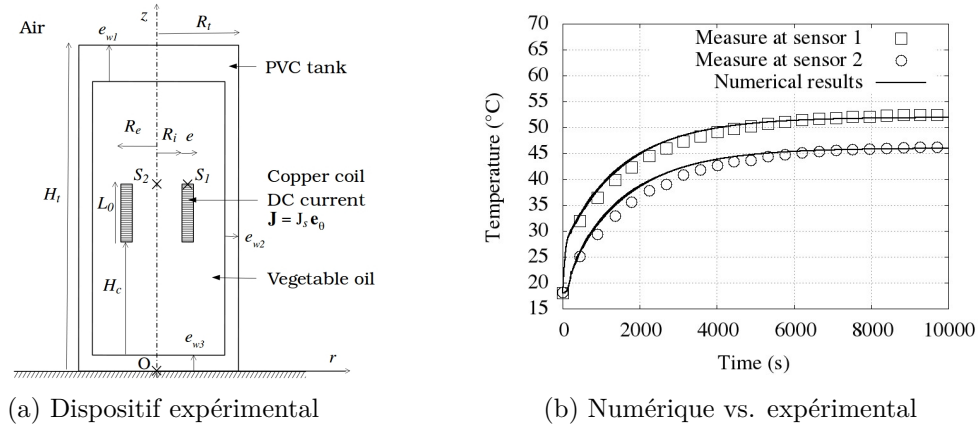


Figure 8.5: Simulation de l'expérience sur la bobine immergée.

où $\tilde{\mathbf{u}} = 0$ dans Ω_s , f_T est l'effet Joule dans la bobine (nul ailleurs) et h le coefficient de convection. Les équations de la vitesse et de la pression sont :

$$\left\{ \begin{array}{l} \partial_t \mathbf{u} + (\nabla \times \mathbf{u}) \times \mathbf{u} + \nabla \left(\frac{p}{\rho_f} \right) \\ -\nabla \cdot (2\nu_f \nabla^s \mathbf{u}) = \alpha_f (T - T_0) g \mathbf{e}_z + \frac{\Delta \chi(T)}{\rho_f} \nabla \left(\frac{H^2}{2} \right) \quad \text{dans } \Omega_f, \\ \nabla \cdot \mathbf{u} = 0 \quad \text{dans } \Omega_f, \\ \mathbf{u} = 0 \quad \text{sur } \partial\Omega_f, \\ \mathbf{u}|_{t=0} = 0 \quad \text{dans } \Omega_f, \end{array} \right. \quad (8.22)$$

où $\Delta \chi(T) = \chi(T) - \chi(T_0)$ et χ est donné par (8.4). On travaille avec la variation de la force de Kelvin pour éviter une instabilité numérique⁵. Les équations du champ magnétique sont :

$$\left\{ \begin{array}{l} \nabla \times \mathbf{H} = \mathbf{j} \quad \text{dans } \Omega, \\ \nabla \cdot (\mu \mathbf{H}) = 0 \quad \text{dans } \Omega, \\ \mathbf{H} \times \mathbf{n} = 0 \quad \text{sur } \partial\Omega, \end{array} \right. \quad (8.23)$$

où \mathbf{j} est la densité de courant dans la bobine (nulle ailleurs). Des calculs sur plusieurs modes montrent que la solution du régime permanent est axisymétrique, c'est-à-dire qu'un calcul sur le mode 0 suffit. Avec un coefficient de convection réaliste, $h = 17 \text{ W/m}^2 \cdot \text{K}$, on obtient des résultats très proches des mesures de température, voir Figure 8.5b, ce qui contribue à la validation du modèle thermo-hydrodynamique (pas d'interaction avec le champ magnétique).

8.4.2 Avantage du refroidissement par ferrofluide

Une simulation est réalisée en remplaçant l'huile classique par un ferrofluide à base d'huile, avec une fraction volumique $\phi = 10\%$ de nanoparticules en magnétite. Pour étudier l'effet de la force magnétique, nous considérons que les propriétés thermophysiques du ferrofluide sont celles de l'huile classique. Les champs de température et de vitesse obtenus dans le régime permanent sont présentés dans la Figure 8.6. On peut voir une diminution de la température maximale d'environ 3°C avec l'utilisation du ferrofluide, ce qui peut s'expliquer par la formation d'une cellule de convection supplémentaire au bas de la bobine

⁵Cela implique un changement de variable de la pression, le gradient de pression absorbant la partie gradient de la force magnétique.

lorsque la force magnétique est active. Des visualisations montrent que la force magnétique est dominante devant la force de Boussinesq et localisée sur les parois de la bobine, ce qui est cohérent avec la modification de l'écoulement dans le ferrofluide.

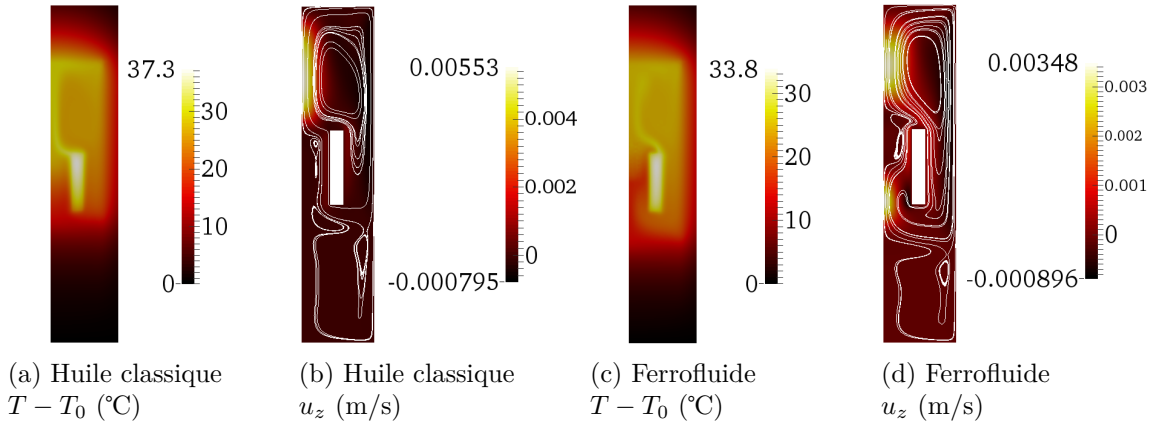


Figure 8.6: Vue d'une section méridienne (axe de symétrie à gauche) à $t = 10000$ s.

8.4.3 Comparaison des modèles de force de Kelvin et de Helmholtz

Il existe plusieurs expressions de la densité de force magnétique dans la littérature mais certaines sont égales à un gradient près. Par exemple, dans le cas des forces de Kelvin (8.10) et de Helmholtz (8.11), on peut écrire

$$\mathbf{f}_K = \mathbf{f}_H + \nabla\Phi, \quad \Phi = \mu_0\chi\frac{H^2}{2}. \quad (8.24)$$

Or, si (\mathbf{u}, p) est solution des équations de Navier-Stokes (8.9) avec $\mathbf{f}_m = \mathbf{f}_K$, $(\mathbf{u}, p - \Phi)$ est solution des mêmes équations avec $\mathbf{f}_m = \mathbf{f}_H = \mathbf{f}_K - \nabla\Phi$. Ces deux densités de force sont équivalentes en termes de vitesse (et de température), et l'on peut appliquer le même raisonnement à n'importe quelles autres expressions qui diffèrent d'un gradient. La Figure 8.7 montre à quel point les distributions de force sont différentes alors qu'on observe numériquement exactement le même champ de vitesse. Ce résultat répond en partie à la question du modèle de force à utiliser.

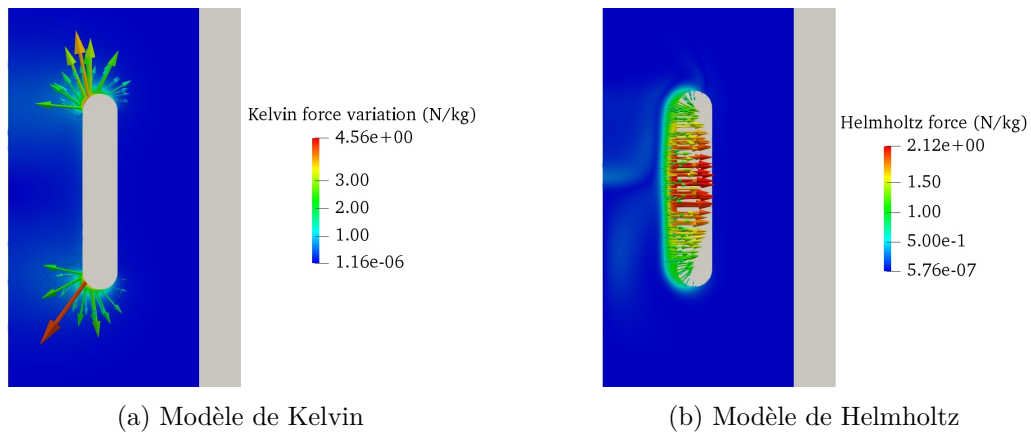


Figure 8.7: Vue d'une section méridienne (axe de symétrie à gauche) à $t = 10000$ s.

8.5 Vraies propriétés thermophysiques du ferrofluide

Une autre expérience est réalisée avec une cuve en aluminium pour plus de réalisme vis-à-vis des transformateurs. Nous présentons ici l'adaptation du modèle et les nouveaux résultats numériques associés. Le modèle du ferrofluide est amélioré en prenant en compte le changement des propriétés thermophysiques avec les nanoparticules.

8.5.1 Adaptation du modèle

La cuve en aluminium présente une forte conductivité thermique par rapport à celle en PVC. La condition de Dirichlet imposée sur $\partial\Omega_{inf}$, trop contraignante dans ce cas, est remplacée par une condition de Neumann homogène $\partial_{\mathbf{n}}T = 0$. De plus, on utilise une viscosité fonction de la température dans (8.22), ce paramètre étant fortement affecté par la température. En utilisant un coefficient de convection réaliste, $h = 8 \text{ W/m}^2 \cdot \text{K}$, on obtient un bon accord avec les nouvelles mesures de température (toujours sans interaction magnétique).

8.5.2 Résultats avec les propriétés modifiées

Dans les simulations, on remplace l'huile classique par du ferrofluide avec des fractions volumiques entre 1 et 7%. Comme dans la cuve en PVC, l'ajout de nanoparticules améliore les transferts thermiques puisqu'on observe une diminution de la température maximale, cette diminution de température croissant avec ϕ (Figure 8.8a). De plus, les simulations montrent que le changement des propriétés suffit à abaisser la température maximale (avec les lois et paramètres considérés dans cette étude). A nouveau, l'écoulement est modifiée par la convection thermomagnétique lorsque la force de Kelvin est active, ce qui améliore les transferts de chaleur (Figure 8.8b). A cause du changement des propriétés thermophysiques, la comparaison du nombre de Nusselt sans et avec nanoparticules n'est pas pertinente : mieux vaut se référer à la température maximale dans le système.

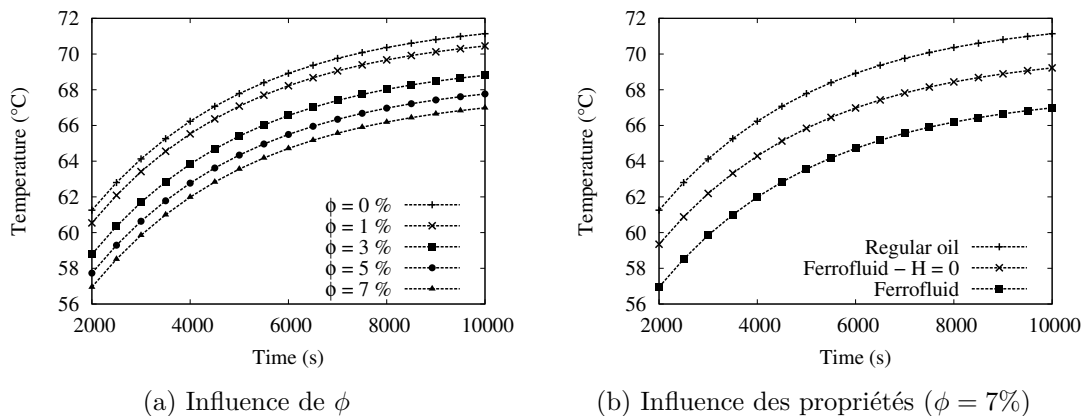


Figure 8.8: Température au point chaud de la bobine.

Un cœur ferromagnétique est ajouté dans le modèle, afin d'une part d'accroître le champ \mathbf{H} dans le fluide et d'autre part de se rapprocher d'une géométrie proche d'un transformateur. Avec le cœur, on observe une plus forte différence de température dans la bobine entre huile classique et ferrofluide (plus de 10°C d'écart pour $\phi = 7\%$). Le phénomène de convection thermomagnétique prend en effet plus d'ampleur grâce à l'intensité du champ magnétique accrue. Cependant, des estimations laissent à penser que l'approximation de matériau magnétique linéaire est discutable dans ce cas.

Des résultats expérimentaux sur un ferrofluide confirment la baisse de température avec la convection thermomagnétique. L'expérience consiste à inverser à intervalles réguliers le sens du courant dans l'un des fils du bobinage (bi-filaire), afin d'activer/désactiver le champ magnétique. Lorsque le champ magnétique est désactivé, la température mesurée à la bobine croît de 2°C environ (et inversement quand il est désactivé), signe que la convection thermomagnétique a un effet positif. L'expérience est reproduite avec une simulation de façon satisfaisante, voir Figure 8.9. Les paramètres du modèle ne permettent cependant qu'une comparaison qualitative.

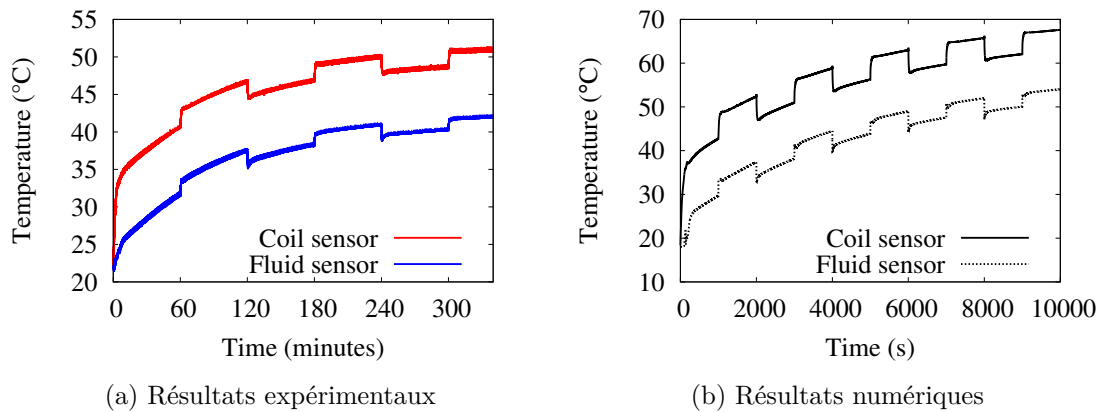


Figure 8.9: Température mesurée/calculée dans la cuve remplie de ferrofluide.

Afin de se rapprocher des conditions proches de celles rencontrées dans l'étude d'un transformateur, nous simulons le refroidissement de la bobine immergée en supposant un courant alternatif (50 Hz) plutôt que continu. Les résultats montrent que le type de courant n'a qu'un effet négligeable sur la montée en température de la bobine, du moment que la valeur efficace est la même. Cela peut justifier la modélisation thermique d'un dispositif alimenté par un courant AC (qui nécessite un pas de temps très petit et donc un très grand nombre d'itérations) en considérant un courant DC.

8.5.3 Amélioration de la modélisation du ferrofluide

Afin de vérifier l'intérêt des matériaux ferromagnétiques à faible température de Curie, nous prenons en compte la variation de la magnétisation à saturation des nanoparticules dans (8.4), par la loi de Bloch :

$$M_{s,p}(T) = \begin{cases} M_{s,p}(0) \left(1 - \left(\frac{T}{T_C}\right)^{1.5}\right) & \text{si } T \leq T_C, \\ 0 & \text{si } T \geq T_C, \end{cases} \quad (8.25)$$

où T_C est la température de Curie (Figure 8.10). Avec cette modélisation, plus T_C est faible, plus la dépendance en température de l'intensité de la magnétisation du ferrofluide est importante (renforcement du coefficient pyromagnétique). On constate numériquement que la température dans la bobine diminue, grâce à plus de convection thermomagnétique, lorsque T_C diminue (Figure 8.11), ce qui confirme les préconisations de la littérature [77].

Par ailleurs, nous observons que le terme additionnel impliquant χ dans l'équation de la température des ferrofluides (8.8) est négligeable dans le cas de la bobine immergée, au moins en courant continu, en utilisant des estimations des ordres de grandeur et des simulations.

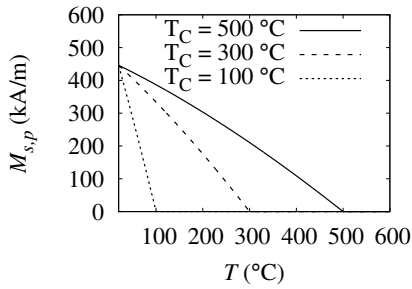
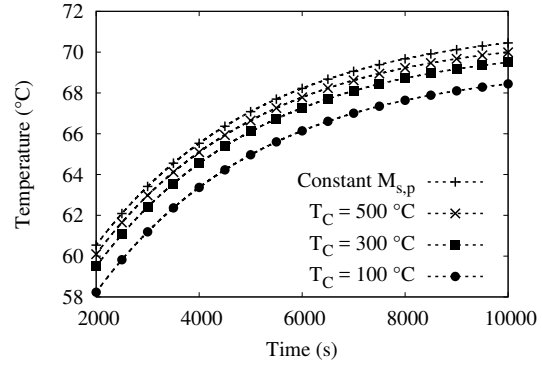


Figure 8.10: Loi de Bloch.


 Figure 8.11: Température au point chaud de la bobine ($\phi = 1\%$).

8.6 Convection thermomagnétique dans un transformateur

Nous souhaitons vérifier si les résultats positifs du ferrofluide dans le cas de la bobine immergée peuvent être étendus à un transformateur de 40 kVA (20 kV/400 V). Nous présentons ici la modélisation du transformateur ainsi que les résultats comparant l'efficacité de l'huile classique et du ferrofluide.

8.6.1 Modélisation du problème

Il est fréquent dans la communauté du génie électrique d'opter pour un modèle axisymétrique de transformateur, c'est-à-dire de ne pas modéliser le circuit ferromagnétique entier [115, 2, 116]. Cela permet d'obtenir une approximation raisonnable du champ magnétique de fuite et de l'effet Joule avec un calcul axisymétrique, et c'est ce parti que nous prenons ici afin d'étudier l'effet de la convection thermomagnétique. Le modèle du transformateur (46 cm de haut) est présenté dans la Figure 8.12. Les tensions et les intensités satisfont les relations imposées par le principe du transformateur (voir partie en anglais). En particulier, les ampère-tours sont égaux dans les deux bobines et les courants ont des sens opposés.

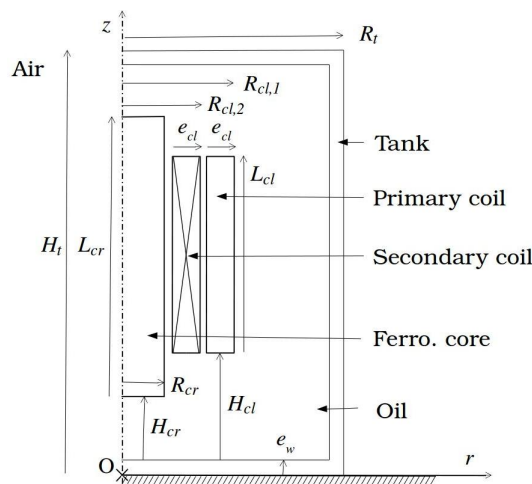


Figure 8.12: Section méridienne du transformateur (axe de symétrie à gauche).

Nous utilisons les équations de la bobine immergée, en adaptant les termes sources de la température et du champ magnétique de façon appropriée. Le courant est considéré continu dans le modèle, en vertu du résultat de la partie précédente sur le type de courant.

Des calculs sur plusieurs modes montrent que la solution en régime permanent est quasi-axisymétrique (le mode 0 domine nettement les autres modes). Ainsi, les calculs à temps long sont réalisés sur le mode 0 seul.

8.6.2 Refroidissement par huile classique versus par ferrofluide

Le système est refroidi avec de l'huile de transformateur ou un ferrofluide à base d'huile de transformateur (avec $\phi = 1\%$ pour limiter la détérioration des propriétés diélectriques de l'huile). Le système atteint un régime permanent autour de 10000 s. Les champs de température obtenus sont présentés dans la Figure 8.13. La température maximale est réduite de 2.2°C avec le ferrofluide. Le changement des propriétés thermophysiques n'est ici responsable que d'une diminution de 0.2°C de la température maximale.

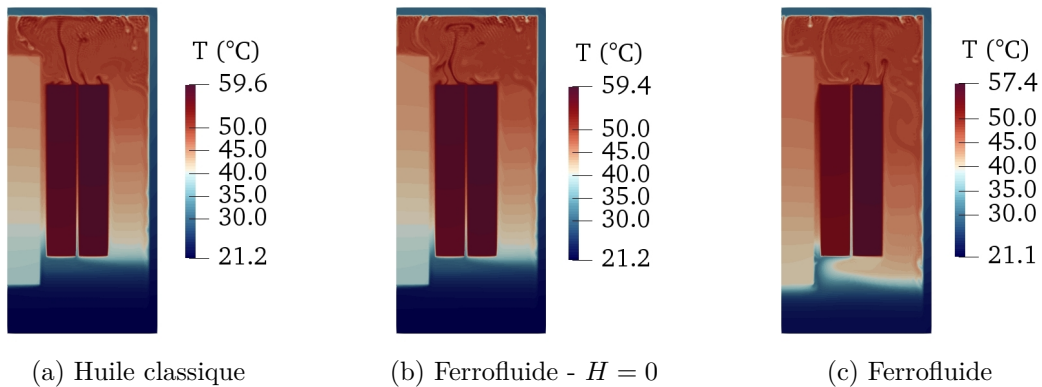


Figure 8.13: Température dans une section méridienne (axe de symétrie à gauche) à $t = 20000$ s.

La diminution de la température est principalement due à la convection thermomagnétique qui s'établit, en plus de la convection thermogravitationnelle. On peut notamment observer que l'écoulement vertical entre les bobinages est particulièrement plus fort dans le cas du ferrofluide (Figure 8.14), cette zone étant celle où se concentre l'intensité du champ magnétique (Figure 8.15).

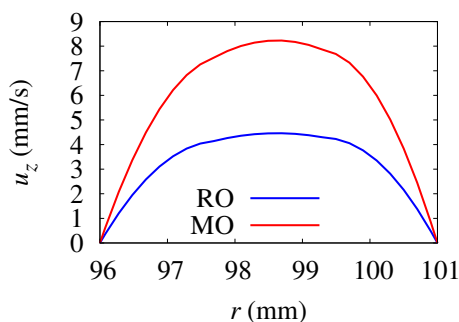


Figure 8.14: Profil de u_z entre les bobinages à mi-hauteur ($t = 20000$ s). RO : huile classique, MO : ferrofluide.

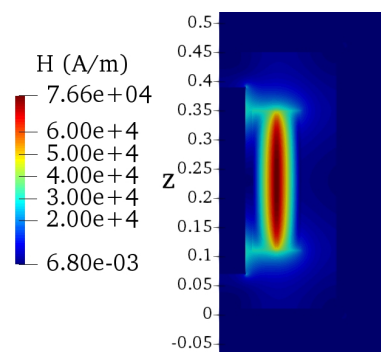


Figure 8.15: Intensité du champ magnétique dans une section méridienne (axe de symétrie à gauche)

Afin d'étudier l'impact de la température de Curie, nous nous la faisons varier (prise initialement à $T_C = 580^\circ\text{C}$ pour de la magnétite). Malgré l'intensité de la force magnétique accrue (Figure 8.16), la température des bobines ne diminue pas toujours avec l'abaissement de T_C à 365°C puis 150°C . Les variations de température avec T_C sont de toutes façons très faibles (quelques 0.1°C). Ce résultat, contraire aux attentes vis-à-vis

des matériaux ferromagnétiques à faible température de Curie, reste à être expliqué; il est peut-être dû à une limite du modèle magnétique linéaire du ferrofluide.

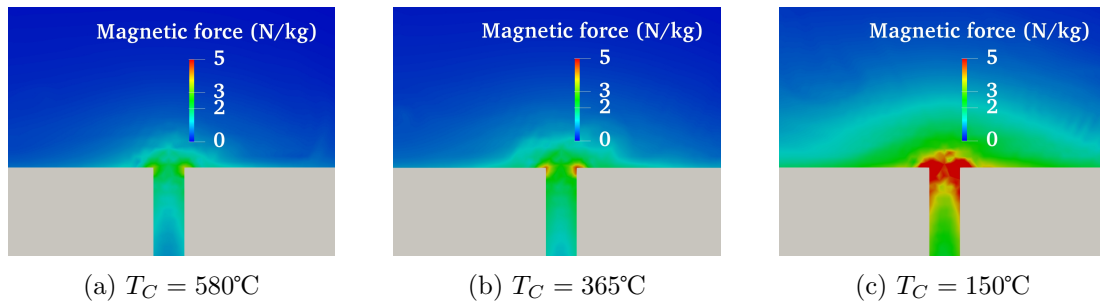


Figure 8.16: Intensité de la force magnétique à $t = 10000$ s (partie grise : partie supérieure des bobines).

Des variations de la géométrie du transformateur (taille de la cuve et espace entre les bobinages) sont testées mais, même si l'on observe systématiquement une diminution de la température dans les bobinages avec le ferrofluide, l'abaissement de température reste aux alentours de 2-3°C (alors que des travaux expérimentaux sur transformateur montrent des écarts de température plus significatifs).

8.7 Conclusion

8.7.1 Bilan

Dans une première étape, nous avons modélisé le problème de la convection naturelle des ferrofluides par les équations de la magnéto-statique, les équations de Navier-Stokes sous approximation de Boussinesq avec la densité de force de Kelvin (ou Helmholtz) pour prendre en compte l'action d'un champ magnétique et l'équation de la température (d'un fluide newtonien incompressible). Des lois classiques ont été utilisées pour modéliser les propriétés thermophysiques du ferrofluide. Les calculs ont confirmé que des densités de force magnétique qui sont égales à un gradient près donnent les mêmes solutions de vitesse et de température, ce qui donne une certaine liberté quant au choix du modèle de force.

Diverses fonctionnalités ont été apportées à SFEMaNS. Il est à présent possible de calculer la température dans des domaines mixtes solide/fluide, afin d'estimer l'impact d'un écoulement convectif sur la température d'un corps solide. Les développements incluent : les densités de force de Kelvin et Helmholtz, une viscosité dépendante de la température, le terme additionnel dans l'équation de la température des ferrofluides, des conditions de Robin pour la température. Ces développements ont été validés par des tests de convergence montrant le bon comportement du code.

Le modèle thermo-hydraulique a été validé en comparant les résultats obtenus numériquement à ceux de l'expérience sur une bobine immergée. Un bon accord qualitatif a été obtenu entre les résultats numériques et des résultats expérimentaux sur du ferrofluide, vis-à-vis de l'effet positif de la convection thermomagnétique.

Que ce soit dans les simulations sur la bobine immergée ou le transformateur, nous avons systématiquement observé une diminution de la température maximale lorsque l'huile classique était remplacée par du ferrofluide. Cette baisse de température s'explique par l'effet combiné du changement des propriétés thermophysiques et de la convection thermomagnétique. Les calculs sur la bobine immergée ont confirmé que les matériaux ferromagnétiques (pour les nanoparticules magnétiques) à faible température de Curie améliorent les transferts de chaleur, car le ferrofluide possède alors un coefficient pyromagnétique élevé.

8.7.2 Perspectives

Plusieurs pistes sont à envisager pour poursuivre cette thèse. Il serait intéressant de finaliser la comparaison avec l'expérience sur du ferrofluide, en utilisant les bons paramètres de celui-ci dans le modèle. L'abaissement de la température maximale due au ferrofluide dans le cas du transformateur est relativement faible par rapport à certains expérimentaux de la littérature. Cela peut-être une dû à une limite du modèle de matériau magnétique linéaire pour le ferrofluide. Afin d'améliorer nos résultats, il faudrait prendre en compte la non-linéarité de l'intensité de la magnétisation du ferrofluide, i.e., implémenter le modèle de Langevin non approché. Par ailleurs, on peut envisager de réaliser des simulations sur un modèle de transformateur plus réaliste, basé sur une géométrie existante (incluant les isolations solides) et prenant en compte les courants de Foucault. Finalement, il faudrait mener une réflexion sur un design de transformateur optimal pour la convection thermomagnétique (ajout d'aimant permanent, disposition des bobines différente).

Appendix A

Governing equations in fluid mechanics

This appendix is dedicated to the derivation of the governing equations in fluid mechanics. The case of a general fluid is first treated. The adaptation of the equations in the case of a Newtonian and incompressible fluid is then presented. The Boussinesq approximation, used in the whole thesis, and the equations under this approximation are finally described.

A.1 General equations

This section is dedicated to the governing equations of any fluid satisfying the principles of mass conservation and energy conservation.

We consider a control volume V always composed of the same fluid particles. Its surface is denoted by S and the outer unit normal vector is denoted by \mathbf{n} . The control volume follows the fluid in its movement. We should use the notations $V(t)$ and $S(t)$, where t is the time, but we use the notations V and S for simplicity.

A.1.1 Continuity equation

The continuity equation expresses the mass conservation principle. Since the control volume always contains the same amount of matter, its mass M is constant. We can thus write

$$\frac{dM}{dt} = 0. \quad (\text{A.1})$$

By re-writing the mass with the density ρ , we have the global form of the continuity equation:

$$\frac{d}{dt} \int_V \rho dV = 0. \quad (\text{A.2})$$

By using the Reynolds transport theorem, we can invert the time derivative and the integral. We obtain

$$\int_V \partial_t \rho dV + \int_S \rho \mathbf{u} \cdot \mathbf{n} dS = 0.$$

By using the divergence theorem, we can turn the integral over the surface into an integral over the volume. We have then

$$\int_V (\partial_t \rho + \nabla \cdot (\rho \mathbf{u})) dV = 0.$$

Since it is true for every control volume V , the quantity inside the integral is zero at every point. The local form of the continuity equation is

$$\partial_t \rho + \nabla \cdot (\rho \mathbf{u}) = 0. \quad (\text{A.3})$$

A.1.2 Momentum equation

The momentum equation expresses the fundamental principle of dynamics. By applying this principle to the control volume, we can write

$$\frac{d\mathbf{P}}{dt} = \mathbf{F}, \quad (\text{A.4})$$

where \mathbf{P} is the momentum of the control volume and \mathbf{F} is the sum of the forces acting on the control volume. These forces are of two kinds: the forces acting on the volume and the forces acting on the surface. In the following, we consider that the volume forces only consist in the gravity force. We should also consider the magnetic body force in a ferrofluid for instance. We can write

$$\mathbf{F} = \int_V \rho \mathbf{g} dV + \int_S [\sigma] \cdot \mathbf{n} dS, \quad (\text{A.5})$$

where \mathbf{g} is the gravity and $[\sigma]$ is the stress tensor. We introduce the decomposition

$$[\sigma] = -p[I] + [\sigma'], \quad (\text{A.6})$$

where p is the pressure, $[I]$ is the identity tensor and $[\sigma']$ is the tensor of viscous stress. By re-writing the momentum and the sum of the forces, the fundamental principle of dynamics applied to the control volume can be written as

$$\frac{d}{dt} \int_V \rho \mathbf{u} dV = \int_V \rho \mathbf{g} dV - \int_S p \mathbf{n} dS + \int_S [\sigma'] \cdot \mathbf{n} dS, \quad (\text{A.7})$$

which is the global form of the momentum equation.

By applying the Reynolds transport theorem to the component i of the momentum derivative on the left-hand side in (A.7) and by using the divergence theorem, we obtain

$$\frac{d}{dt} \int_V \rho u_i dV = \int_V (\partial_t(\rho u_i) + \nabla \cdot (\rho u_i \mathbf{u})) dV.$$

By using (A.3), we simplify the expression on the right-hand side:

$$\frac{d}{dt} \int_V \rho u_i dV = \int_V (\rho \partial_t u_i + \rho \mathbf{u} \cdot \nabla u_i) dV.$$

The derivative of the momentum is expressed by

$$\frac{d}{dt} \int_V \rho \mathbf{u} dV = \int_V (\rho \partial_t \mathbf{u} + \rho (\mathbf{u} \cdot \nabla) \mathbf{u}) dV.$$

The pressure term in (A.7) can be expressed with a volume integral by applying the divergence theorem to each component:

$$\int_S p \mathbf{n} dS = \int_V \nabla p dV.$$

The same treatment applied to the viscous stress term gives

$$\int_S [\sigma'] \cdot \mathbf{n} dS = \int_V \nabla \cdot [\sigma'] dV,$$

where $\nabla \cdot [\sigma']$ is the vector of the divergence of each line of $[\sigma']$, i.e., $\forall i, \{\nabla \cdot [\sigma']\}_i = \partial_j \sigma'_{ij}$. Finally, (A.7) can be expressed by

$$\int_V (\rho \partial_t \mathbf{u} + \rho (\mathbf{u} \cdot \nabla) \mathbf{u}) dV = \int_V \rho \mathbf{g} dV - \int_V \nabla p dV + \int_V \nabla \cdot [\sigma'] dV.$$

The equation being valid for every control volume V , we have the local form of the momentum equation:

$$\rho \partial_t \mathbf{u} + \rho (\mathbf{u} \cdot \nabla) \mathbf{u} = \rho \mathbf{g} - \nabla p + \nabla \cdot [\sigma']. \quad (\text{A.8})$$

A.1.3 Energy equation

The energy equation is based on the first principle of thermodynamics, also called the conservation of energy principle. According to the first principle of thermodynamics, the variation of the total energy (internal and kinetic energy) of the control volume is equal to the energy (work and heat) it exchanges with the environment. We can write

$$\frac{d}{dt}(E + E_k) = \frac{dW}{dt} + \frac{dQ}{dt}, \quad (\text{A.9})$$

where E is the internal energy, E_k is the kinetic energy, W is the exchanged work and Q is the exchanged heat. We can write

$$\frac{d}{dt}(E + E_k) = \frac{d}{dt} \int_V \rho \left(e + \frac{u^2}{2} \right) dV, \quad (\text{A.10})$$

where e is the internal energy by unit mass. The time derivative of the work is the power of the forces acting on the control volume and can be written as

$$\frac{dW}{dt} = \int_V \rho \mathbf{g} \cdot \mathbf{u} dV - \int_S (p\mathbf{n}) \cdot \mathbf{u} dS + \int_S ([\sigma'] \cdot \mathbf{n}) \cdot \mathbf{u} dS. \quad (\text{A.11})$$

The time derivative of the heat is the power exchanged with the environment of the control volume and can be written as

$$\frac{dQ}{dt} = \int_V q_v dV - \int_S \mathbf{q} \cdot \mathbf{n} dS, \quad (\text{A.12})$$

where q_v is a power source term per unit volume and \mathbf{q} is the heat flux vector. By replacing these expressions, we have the global form of the energy equation:

$$\begin{aligned} \frac{d}{dt} \int_V \rho \left(e + \frac{u^2}{2} \right) dV = \\ \int_V \rho \mathbf{g} \cdot \mathbf{u} dV - \int_S (p\mathbf{n}) \cdot \mathbf{u} dS + \int_S ([\sigma'] \cdot \mathbf{n}) \cdot \mathbf{u} dS + \int_V q_v dV - \int_S \mathbf{q} \cdot \mathbf{n} dS. \end{aligned} \quad (\text{A.13})$$

By using the Reynolds transport theorem, the divergence theorem and (A.3), we have

$$\frac{d}{dt} \int_V \rho \left(e + \frac{u^2}{2} \right) dV = \int_V \left(\rho \partial_t \left(e + \frac{u^2}{2} \right) + \rho \mathbf{u} \cdot \nabla \left(e + \frac{u^2}{2} \right) \right) dV.$$

By using the divergence theorem, we have

$$\int_S (p\mathbf{n}) \cdot \mathbf{u} dS = \int_V \nabla \cdot (p\mathbf{u}) dV.$$

A basic development and the divergence theorem provide the following results:

$$\int_S ([\sigma'] \cdot \mathbf{n}) \cdot \mathbf{u} dS = \int_S ([\sigma'] \cdot \mathbf{u}) \cdot \mathbf{n} dS = \int_V \nabla \cdot ([\sigma'] \cdot \mathbf{u}) dV.$$

The heat flux vector term can also be changed into a volume integral by using the divergence theorem:

$$\int_S \mathbf{q} \cdot \mathbf{n} dS = \int_V \nabla \cdot \mathbf{q} dV.$$

By replacing these expressions in (A.13), we obtain

$$\int_V \left(\rho \partial_t \left(e + \frac{u^2}{2} \right) + \rho \mathbf{u} \cdot \nabla \left(e + \frac{u^2}{2} \right) \right) dV = \int_V \rho \mathbf{g} \cdot \mathbf{u} dV - \int_S (p \mathbf{n}) \cdot \mathbf{u} dS + \int_V \nabla \cdot ([\sigma'] \cdot \mathbf{u}) dV + \int_V q_v dV - \int_V \nabla \cdot \mathbf{q} dV.$$

The equation being valid for every control volume V , we have the local form of the energy equation:

$$\rho \partial_t \left(e + \frac{u^2}{2} \right) + \rho \mathbf{u} \cdot \nabla \left(e + \frac{u^2}{2} \right) = \rho \mathbf{g} \cdot \mathbf{u} - \nabla \cdot (p \mathbf{u}) + \nabla \cdot ([\sigma'] \cdot \mathbf{u}) + q_v - \nabla \cdot \mathbf{q}. \quad (\text{A.14})$$

A.1.4 Theorem of the kinetic energy

The theorem of the kinetic energy is not based on a fundamental principle. It is a corollary of the momentum equation. By applying the inner product by \mathbf{u} to (A.8), we have

$$\rho \partial_t \mathbf{u} \cdot \mathbf{u} + \rho (\mathbf{u} \cdot \nabla) \mathbf{u} \cdot \mathbf{u} = \rho \mathbf{g} \cdot \mathbf{u} - \nabla p \cdot \mathbf{u} + \nabla \cdot [\sigma'] \cdot \mathbf{u}.$$

We can apply the basic reformulations

$$\partial_t \mathbf{u} \cdot \mathbf{u} = \partial_t \left(\frac{u^2}{2} \right) \quad \text{and} \quad (\mathbf{u} \cdot \nabla) \mathbf{u} \cdot \mathbf{u} = \mathbf{u} \cdot \nabla \left(\frac{u^2}{2} \right).$$

Moreover, the calculus shows that

$$-\nabla p \cdot \mathbf{u} = -\nabla \cdot (p \mathbf{u}) + p \nabla \cdot \mathbf{u}$$

and

$$\nabla \cdot [\sigma'] \cdot \mathbf{u} = \nabla \cdot ([\sigma'] \cdot \mathbf{u}) - [\sigma'] : \nabla \mathbf{u}.$$

By replacing with these expressions, we obtain the local form of the kinetic energy theorem:

$$\rho \partial_t \left(\frac{u^2}{2} \right) + \rho \mathbf{u} \cdot \nabla \left(\frac{u^2}{2} \right) = \rho \mathbf{g} \cdot \mathbf{u} - \nabla \cdot (p \mathbf{u}) + \nabla \cdot ([\sigma'] \cdot \mathbf{u}) + p \nabla \cdot \mathbf{u} - [\sigma'] : \nabla \mathbf{u}. \quad (\text{A.15})$$

We can integrate (A.15) over the control volume:

$$\int_V \left(\rho \partial_t \left(\frac{u^2}{2} \right) + \rho \mathbf{u} \cdot \nabla \left(\frac{u^2}{2} \right) \right) dV = \int_V \rho \mathbf{g} \cdot \mathbf{u} dV - \int_V \nabla \cdot (p \mathbf{u}) dV + \int_V \nabla \cdot ([\sigma'] \cdot \mathbf{u}) dV + \int_V p \nabla \cdot \mathbf{u} dV - \int_V [\sigma'] : \nabla \mathbf{u} dV.$$

By using (A.3), we obtain

$$\int_V \left(\rho \partial_t \left(\frac{u^2}{2} \right) + \rho \mathbf{u} \cdot \nabla \left(\frac{u^2}{2} \right) \right) dV = \int_V \left(\partial_t \left(\rho \frac{u^2}{2} \right) + \nabla \cdot \left(\rho \frac{u^2}{2} \mathbf{u} \right) \right) dV$$

The divergence theorem gives

$$\int_V \nabla \cdot \left(\rho \frac{u^2}{2} \mathbf{u} \right) dV = \int_S \rho \frac{u^2}{2} \mathbf{u} \cdot \mathbf{n} dS$$

By using the Reynolds transport theorem, we obtain

$$\int_V \partial_t \left(\rho \frac{u^2}{2} \right) dV + \int_S \rho \frac{u^2}{2} \mathbf{u} \cdot \mathbf{n} dS = \frac{d}{dt} \int_V \rho \frac{u^2}{2} dV.$$

By reversing the reasoning done for the energy equation, we have

$$\int_V \nabla \cdot (p\mathbf{u}) dV = \int_S p\mathbf{n} \cdot \mathbf{u} dS$$

and

$$\int_V \nabla \cdot ([\sigma'] \cdot \mathbf{u}) dV = \int_S ([\sigma'] \cdot \mathbf{n}) \cdot \mathbf{u} dS.$$

Finally, the global form of the theorem of the kinetic energy is

$$\begin{aligned} \frac{d}{dt} \int_V \rho \frac{u^2}{2} dV = \int_V \rho \mathbf{g} \cdot \mathbf{u} dV - \int_S (p\mathbf{n}) \cdot \mathbf{u} dS + \int_S ([\sigma'] \cdot \mathbf{n}) \cdot \mathbf{u} dS \\ + \int_V p \nabla \cdot \mathbf{u} dV - \int_V [\sigma'] : \nabla \mathbf{u} dV. \end{aligned} \quad (\text{A.16})$$

On the right-hand side,

- $\int_V \rho \mathbf{g} \cdot \mathbf{u} dV$ represents the power of the gravity force;
- $-\int_S p\mathbf{n} \cdot \mathbf{u} dS + \int_S ([\sigma'] \cdot \mathbf{n}) \cdot \mathbf{u} dS$ represents the power of the exterior surface forces;
- $\int_V p \nabla \cdot \mathbf{u} dV - \int_V [\sigma'] : \nabla \mathbf{u} dV$ represents the power of the interior surface forces.

A.1.5 Internal energy and temperature equations

By subtracting (A.16) to (A.13), we obtain the global form of the equation of the internal energy:

$$\frac{d}{dt} \int_V \rho e dV = - \int_V p \nabla \cdot \mathbf{u} dV + \int_V [\sigma'] : \nabla \mathbf{u} dV + \int_V q_v dV - \int_S \mathbf{q} \cdot \mathbf{n} dS. \quad (\text{A.17})$$

By subtracting (A.15) to (A.14), we obtain the local form of the equation of the internal energy:

$$\rho c \partial_t e + \rho \mathbf{u} \cdot \nabla e = -p \nabla \cdot \mathbf{u} + [\sigma'] : \nabla \mathbf{u} + q_v - \nabla \cdot \mathbf{q}. \quad (\text{A.18})$$

In condensed phases, we consider that the internal energy variations are proportional to the temperature variations. For infinitesimal variations, we have $de = cdT$, where c is the specific heat and T is the temperature. Fourier's law states that the heat flux vector is proportional to the gradient of the temperature: $\mathbf{q} = -\lambda \nabla T$, where λ is the thermal conductivity. By considering these elements, (A.18) leads to the (local) temperature equation:

$$\rho c \partial_t T + \rho c \mathbf{u} \cdot \nabla T - \nabla \cdot (\lambda \nabla T) = -p \nabla \cdot \mathbf{u} + [\sigma'] : \nabla \mathbf{u} + q_v. \quad (\text{A.19})$$

A.2 Incompressible Navier-Stokes equations

In this section, we derive the local forms of the continuity equation, the momentum equation and the temperature equation for a Newtonian and incompressible fluid.

A.2.1 Continuity equation

If the fluid is incompressible, ρ is a constant in (A.3), and we have the local form of the continuity equation for incompressible fluids:

$$\nabla \cdot \mathbf{u} = 0. \quad (\text{A.20})$$

Note that this equation is valid whether the fluid is Newtonian or not.

A.2.2 Momentum equation

In the case of a Newtonian and incompressible fluid, the viscous stress tensor is under the form

$$[\sigma'] = 2\eta \nabla^s \mathbf{u}, \quad (\text{A.21})$$

where η is the dynamic viscosity and

$$\nabla^s \mathbf{u} = \frac{1}{2} (\nabla \mathbf{u} + (\nabla \mathbf{u})^T) \quad (\text{A.22})$$

is the strain rate tensor. By introducing this expression in (A.8), we obtain the local form of the momentum equation for Newtonian and incompressible fluids:

$$\rho \partial_t \mathbf{u} + \rho (\mathbf{u} \cdot \nabla) \mathbf{u} + \nabla p - \nabla \cdot (2\eta \nabla^s \mathbf{u}) = \rho \mathbf{g}. \quad (\text{A.23})$$

A.2.3 Temperature equation

By using (A.20) and introducing (A.21) in (A.19), we have the temperature equation for Newtonian and incompressible fluids:

$$\rho c \partial_t T + \rho \mathbf{c} \mathbf{u} \cdot \nabla T - \nabla \cdot (\lambda \nabla T) = 2\eta \nabla^s \mathbf{u} : \nabla \mathbf{u} + q_v. \quad (\text{A.24})$$

A.3 Newtonian fluid under Boussinesq approximation

With this approximation, the density of the fluid is considered constant except in the gravitational term of the momentum equation. The Boussinesq approximation makes it possible to address thermal convection by using equations close to those of incompressible fluids.

A.3.1 Applicability of the approximation

Boussinesq approximation in the case of steady free convection is presented in [119, pp. 155-161]. The main condition of applicability is

$$\alpha \Delta T \ll 1, \quad (\text{A.25})$$

where α is the thermal expansion coefficient and ΔT is the characteristic temperature difference causing the flow. There exist other conditions but they are likely to be violated only in large-scale geophysical situations.

A.3.2 Governing equations

Let T_* be the temperature around which we use the approximation. We note ρ_* the density of the fluid at T_* . If (A.25) is satisfied, we can consider that the density is constant equal to ρ_* in the equations except in the gravitational term of the momentum equation. (A.20) is thus still valid. (A.23) can be adapted by modifying the gravity body force. In the gravity body force, we use the approximation

$$\rho(T) = \rho_*(1 - \alpha(T - T_*)). \quad (\text{A.26})$$

With the Boussinesq approximation, the momentum equation of a Newtonian fluid is then

$$\rho_* \partial_t \mathbf{u} + \rho_* (\mathbf{u} \cdot \nabla) \mathbf{u} + \nabla p - \nabla \cdot (2\eta \nabla^s \mathbf{u}) = \rho_* \alpha (T - T_*) g \mathbf{e}_z, \quad (\text{A.27})$$

where we have used the change of variable $p \leftarrow p + \rho_* g z$. We assume that the gravity is $\mathbf{g} = -g \mathbf{e}_z$. The constant part of the gravity body force is absorbed by the pressure gradient. Because the Boussinesq approximation is used in the whole thesis, we never use the notation ρ_* . We simply use ρ instead.

Appendix B

Approximations using Taylor expansions in SFEMaNS

Let us consider a scalar field $u(t)$, $t \in \mathbb{R}$. We introduce a time step τ , an integer $n_{\max} \in \mathbb{N}$ and the sequence $\{t_n\}_{n \in [-1, n_{\max}]}$ defined by $t_n = n\tau$, $\forall n$. We define $u^n = u(t_n)$, $\partial_t u^n = \partial_t u(t_n)$, $\partial_{tt} u^n = \partial_{tt} u(t_n)$ and $\partial_{t^3} u^n = \partial_{t^3} u(t_n)$, $\forall n \in [-1, n_{\max}]$. In the following, we consider a random $n \in [0, n_{\max}]$. The results can easily be extended to vectors.

B.1 Backward Difference Formula of second order (BDF2)

The Taylor expansions of u at time t_{n+1} for times t_n and t_{n-1} are:

$$u^n = u^{n+1} - \partial_t u^{n+1} \tau + \frac{1}{2} \partial_{tt} u^{n+1} \tau^2 - \frac{1}{6} \partial_{t^3} u^{n+1} \tau^3 + O(\tau^4), \quad (\text{B.1})$$

$$u^{n-1} = u^{n+1} - 2\partial_t u^{n+1} \tau + 2\partial_{tt} u^{n+1} \tau^2 - \frac{4}{3} \partial_{t^3} u^{n+1} \tau^3 + O(\tau^4). \quad (\text{B.2})$$

Note that $O(2\tau) = O(\tau)$. The sum 4 times (B.1) minus (B.2) gives

$$4u^n - u^{n-1} = 3u^{n+1} - 2\partial_t u^{n+1} \tau + \frac{2}{3} \partial_{t^3} u^{n+1} \tau^3 + O(\tau^4). \quad (\text{B.3})$$

(B.3) implies the BDF2

$$\partial_t u^{n+1} = \frac{3u^{n+1} - 4u^n + u^{n-1}}{2\tau} + O(\tau^2). \quad (\text{B.4})$$

B.2 Time extrapolation of second order

The sum 2 times (B.1) minus (B.2) gives

$$2u^n - u^{n-1} = u^{n+1} - \partial_{tt} u^{n+1} \tau^2 + O(\tau^3). \quad (\text{B.5})$$

(B.5) implies the time extrapolation of second order

$$u^{n+1} = 2u^n - u^{n-1} + O(\tau^2). \quad (\text{B.6})$$

B.3 Time extrapolation of first order

The sum (B.1) minus (B.2) gives

$$u^n - u^{n-1} = \partial_t u^{n+1} \tau + O(\tau^2). \quad (\text{B.7})$$

(B.7) implies the approximation of first order

$$\partial_t u^{n+1} = \frac{u^n - u^{n-1}}{\tau} + O(\tau). \quad (\text{B.8})$$

We can write

$$\partial_t \left(\frac{u^2}{2} \right) (t_{n+1}) = u^{n+1} \partial_t u^{n+1}. \quad (\text{B.9})$$

By replacing u^{n+1} and $\partial_t u^{n+1}$ on the right-hand side of (B.9) by using (B.6) and (B.8), respectively, we obtain the time extrapolation of first order

$$\partial_t \left(\frac{u^2}{2} \right) (t_{n+1}) = (2u^n - u^{n-1}) \frac{u^n - u^{n-1}}{\tau} + O(\tau). \quad (\text{B.10})$$

Appendix C

Additional convergence tests

This appendix presents more convergence tests relative to Section 3.3.

C.1 Magnetostatics

This test is similar to the first test in Section 3.3.2. The comments of the results are the same. This test is made with a small time step $\tau = 1/10$ and a large number of iterations $n = 500$ to reach a steady regime. In the other tests of Section 3.3.2, the time derivative is made zero and the solution is computed in one iteration.

The solution is

$$\mathbf{H}(r, \theta, z) = \frac{r^3}{4} e^{-z} \mathbf{e}_r + r^2 e^{-z} \mathbf{e}_z \text{ in } \Omega. \quad (\text{C.1})$$

The imposed current density is

$$\mathbf{j}(r, \theta, z) = - \left(\frac{r^3}{4} + 2r \right) e^{-z} \mathbf{e}_\theta \text{ in } \Omega. \quad (\text{C.2})$$

\mathbf{H}_d is set to match the solution.

The relative errors on \mathbf{H} and $\nabla \times \mathbf{H}$ in \mathbf{L}^2 -norm for the different mesh sizes are presented in Table C.1.

h	Rel. error	COC	Curl rel. error	COC
0.5	1.9822E-2	-	9.9344E-3	-
0.25	1.7803E-3	3.48	2.0952E-3	2.25
0.125	1.4509E-4	3.62	4.9644E-4	2.08
0.0625	1.8863E-5	2.94	1.1460E-4	2.12
0.03125	2.8061E-6	2.75	2.4742E-5	2.21
0.015625	4.4505E-7	2.66	5.3431E-6	2.21
0.0078125	7.2410E-8	2.62	1.1546E-6	2.21

Table C.1: Relative errors on \mathbf{H} and $\nabla \times \mathbf{H}$ in \mathbf{L}^2 -norm, and associated computed order of convergence.

C.2 Kelvin magnetic body force

Variations of the test presented in Section 3.3.4 are presented. The magnetic susceptibility law and the solution change. The comments of the results are the same.

C.2.1 Linear law of magnetic susceptibility

The law of the magnetic susceptibility is

$$\chi(T) = -T. \quad (\text{C.3})$$

The solution is

$$\begin{aligned} T(r, \theta, z, t) &= r^2(r - r_0)^2 \sin(z)(1 + \cos(\theta)) \cos(t) && \text{in } \Omega, \\ u_r(r, \theta, z, t) &= -(r - r_0)^2 \cos(z)(1 + \cos(\theta)) \cos(t) && \text{in } \Omega_f, \\ u_\theta(r, \theta, z, t) &= (r - r_0)^2 \cos(z)(1 + \cos(\theta)) \cos(t) && \text{in } \Omega_f, \\ u_z(r, \theta, z, t) &= \frac{r - r_0}{r} \sin(z)((3r - r_0)(1 + \cos(\theta)) + (r - r_0) \sin(\theta)) \cos(t) && \text{in } \Omega_f, \\ p(r, \theta, z, t) &= 0 && \text{in } \Omega_f, \\ H_r(r, \theta, z, t) &= 0 && \text{in } \Omega, \\ H_\theta(r, \theta, z, t) &= \frac{r}{2} && \text{in } \Omega_s, \\ H_\theta(r, \theta, z, t) &= \frac{r_0^2}{2r} && \text{in } \Omega_f, \\ H_z(r, \theta, z, t) &= 0 && \text{in } \Omega, \end{aligned} \quad (\text{C.4})$$

where $r_0 = 0.5$ is the limit between the solid and fluid parts.

The problem is solved on modes 0, 1 and 2. Eight processors are used in the meridian plane and three processors are used in the Fourier space.

The errors in L^2 -norm or \mathbf{L}^2 -norm on the temperature, the velocity, the pressure, the magnetic field and the curl of the magnetic field for the various mesh sizes and time steps are presented in Tables C.2, C.3, C.4, C.5 and C.6, respectively.

$h \backslash \tau$	0.01	0.005	0.0025	0.00125	0.000625
0.1	7.6078E-5	7.6288E-5	7.6342E-5	7.6356E-5	7.6359E-5
0.05	6.5649E-6	6.5375E-6	6.5546E-6	6.5604E-6	6.5619E-6
0.025	1.4294E-6	6.8004E-7	6.1754E-7	6.1695E-7	6.1779E-7
0.0125	1.3341E-6	3.3440E-7	9.4781E-8	5.3170E-8	5.0080E-8
0.00625	1.3358E-6	3.3329E-7	8.3239E-8	2.1094E-8	6.6396E-9

Table C.2: Relative L^2 -norm error on the temperature at $t = 1$.

$h \backslash \tau$	0.01	0.005	0.0025	0.00125	0.000625
0.1	1.3864E-5	1.3763E-5	1.3721E-5	1.3702E-5	1.3695E-5
0.05	1.2277E-6	1.1113E-6	1.1003E-6	1.0982E-6	1.0975E-6
0.025	5.1976E-7	1.5693E-7	9.6882E-8	9.1654E-8	9.1247E-8
0.0125	5.1064E-7	1.2696E-7	3.2493E-8	1.0882E-8	7.7219E-9
0.00625	5.1053E-7	1.2670E-7	3.1593E-8	7.9119E-9	2.0675E-9

Table C.3: Relative \mathbf{L}^2 -norm error on the velocity at $t = 1$.

$h \backslash \tau$	0.01	0.005	0.0025	0.00125	0.000625
0.1	3.7117E-4	3.6582E-4	3.6386E-4	3.6304E-4	3.6271E-4
0.05	5.8798E-5	5.2805E-5	5.2071E-5	5.1885E-5	5.1814E-5
0.025	2.5212E-5	9.3101E-6	7.2093E-6	7.0272E-6	7.0040E-6
0.0125	2.4066E-5	6.0081E-6	1.7454E-6	9.9263E-7	9.2278E-7
0.00625	2.4039E-5	5.9291E-6	1.4792E-6	3.8699E-7	1.5064E-7

Table C.4: L^2 -norm error on the pressure at $t = 1$.

$h \backslash \tau$	0.01	0.005	0.0025	0.00125	0.000625
0.1	3.3197E-4	3.3197E-4	3.3197E-4	3.3197E-4	3.3197E-4
0.05	5.1246E-5	5.1246E-5	5.1246E-5	5.1246E-5	5.1246E-5
0.025	6.9289E-6	6.9289E-6	6.9289E-6	6.9289E-6	6.9289E-6
0.0125	8.9720E-7	8.9720E-7	8.9720E-7	8.9720E-7	8.9720E-7
0.00625	1.1381E-7	1.1381E-7	1.1381E-7	1.1381E-7	1.1381E-7

Table C.5: Relative L^2 -norm error on the magnetic field at $t = 1$.

$h \backslash \tau$	0.01	0.005	0.0025	0.00125	0.000625
0.1	8.6838E-4	8.6838E-4	8.6838E-4	8.6838E-4	8.6838E-4
0.05	1.4026E-4	1.4026E-4	1.4026E-4	1.4026E-4	1.4026E-4
0.025	2.0712E-5	2.0712E-5	2.0712E-5	2.0712E-5	2.0712E-5
0.0125	3.0716E-6	3.0716E-6	3.0716E-6	3.0716E-6	3.0716E-6
0.00625	4.5559E-7	4.5559E-7	4.5559E-7	4.5559E-7	4.5559E-7

Table C.6: Relative L^2 -norm error on the curl of the magnetic field at $t = 1$.

C.2.2 Periodic solution

The solution is periodic in z . Periodic conditions on the top and bottom boundaries are enforced. The law of the magnetic susceptibility is

$$\chi(T) = -T^2. \quad (\text{C.5})$$

The solution is

$$\begin{aligned}
T(r, \theta, z, t) &= \frac{1}{\lambda} r^2 (r - r_0) \sin(2\pi z) (1 + \cos(\theta)) \cos(t) && \text{in } \Omega, \\
u_r(r, \theta, z, t) &= -2\pi (r - r_0)^2 \cos(2\pi z) (1 + \cos(\theta)) \cos(t) && \text{in } \Omega_f, \\
u_\theta(r, \theta, z, t) &= 2\pi (r - r_0)^2 \cos(2\pi z) (1 + \cos(\theta)) \cos(t) && \text{in } \Omega_f, \\
u_z(r, \theta, z, t) &= \frac{r - r_0}{r} \sin(2\pi z) (3r - r_0 + (3r - r_0) \cos(\theta) + (r - r_0) \sin(\theta)) \cos(t) && \text{in } \Omega_f, \\
p(r, \theta, z, t) &= 0 && \text{in } \Omega_f, \\
H_r(r, \theta, z, t) &= 2\pi r^3 \sin(2\pi z) (1 + \sin(\theta)) \cos(t) && \text{in } \Omega, \\
H_\theta(r, \theta, z, t) &= -2\pi r^3 \sin(2\pi z) (1 + \sin(\theta)) \cos(t) && \text{in } \Omega, \\
H_z(r, \theta, z, t) &= -r^2 \cos(2\pi z) (4 - \cos(\theta) + 4 \sin(\theta)) \cos(t) && \text{in } \Omega.
\end{aligned} \quad (\text{C.6})$$

The problem is solved on modes 0, 1, 2, 3 and 4. Five processors are used in the meridian plane and five processors are used in the Fourier space.

The errors in L^2 -norm or \mathbf{L}^2 -norm on the temperature, the velocity, the pressure, the magnetic field and the curl of the magnetic field for the various mesh sizes and time steps are presented in Tables C.7, C.8, C.9, C.10 and C.11, respectively.

$h \backslash \tau$	0.01	0.005	0.0025	0.00125	0.000625
0.1	2.1918E-4	2.1910E-4	2.1908E-4	2.1907E-4	2.1907E-4
0.05	1.8319E-5	1.8247E-5	1.8236E-5	1.8233E-5	1.8233E-5
0.025	1.9819E-6	1.6263E-6	1.5991E-6	1.5967E-6	1.5964E-6
0.0125	1.5395E-7	1.5395E-7	1.5395E-7	1.3663E-7	1.3536E-7
0.00625	1.1522E-6	2.8836E-7	7.3079E-8	2.1667E-8	1.2761E-8

Table C.7: Relative L^2 -norm error on the temperature at $t = 1$.

$h \backslash \tau$	0.01	0.005	0.0025	0.00125	0.000625
0.1	3.4189E-4	3.4069E-4	3.4018E-4	3.3997E-4	3.3988E-4
0.05	2.8251E-5	2.7092E-5	2.7021E-5	2.7012E-5	2.7008E-5
0.025	8.8727E-6	3.1652E-6	2.4256E-6	2.3767E-6	2.3746E-6
0.0125	8.5927E-6	2.1403E-6	5.6430E-7	2.3269E-7	1.9419E-7
0.00625	8.5915E-6	2.1325E-6	5.3180E-7	1.3406E-7	3.7507E-8

Table C.8: Relative \mathbf{L}^2 -norm error on the velocity at $t = 1$.

$h \backslash \tau$	0.01	0.005	0.0025	0.00125	0.000625
0.1	1.3269E-2	1.3256E-2	1.3250E-2	1.3247E-2	1.3245E-2
0.05	1.6200E-3	1.6086E-3	1.6084E-3	1.6084E-3	1.6083E-3
0.025	3.1435E-4	2.1663E-4	2.0986E-4	2.0957E-4	2.0957E-4
0.0125	2.3972E-4	6.4640E-5	3.1201E-5	2.7953E-5	2.7763E-5
0.00625	2.3847E-4	5.8836E-5	1.5101E-5	5.3847E-6	4.0935E-6

Table C.9: L^2 -norm error on the pressure at $t = 1$.

$h \backslash \tau$	0.01	0.005	0.0025	0.00125	0.000625
0.1	2.8695E-3	2.8695E-3	2.8695E-3	2.8695E-3	2.8695E-3
0.05	4.3654E-4	4.3654E-4	4.3654E-4	4.3654E-4	4.3654E-4
0.025	6.3670E-5	6.3670E-5	6.3670E-5	6.3670E-5	6.3670E-5
0.0125	9.7355E-6	9.7355E-6	9.7355E-6	9.7355E-6	9.7355E-6
0.00625	1.5499E-6	1.5499E-6	1.5499E-6	1.5499E-6	1.5499E-6

Table C.10: Relative \mathbf{L}^2 -norm error on the magnetic field at $t = 1$.

$h \backslash \tau$	0.01	0.005	0.0025	0.00125	0.000625
0.1	7.2268E-3	7.2268E-3	7.2268E-3	7.2268E-3	7.2268E-3
0.05	1.5647E-3	1.5647E-3	1.5647E-3	1.5647E-3	1.5647E-3
0.025	3.2669E-4	3.2669E-4	3.2669E-4	3.2669E-4	3.2669E-4
0.0125	6.5963E-5	6.5963E-5	6.5963E-5	6.5963E-5	6.5963E-5
0.00625	1.3774E-5	1.3774E-5	1.3774E-5	1.3774E-5	1.3774E-5

Table C.11: Relative \mathbf{L}^2 -norm error on the curl of the magnetic field at $t = 1$.

C.2.3 Periodic solution with non-zero pressure

The solution is periodic in z . Periodic conditions on the top and bottom boundaries are enforced. The law of the magnetic susceptibility is

$$\chi(T) = -T^2. \quad (\text{C.7})$$

The solution is

$$\begin{aligned}
T(r, \theta, z, t) &= \frac{1}{\lambda} r^2 (r - r_0) \sin(2\pi z) (1 + \cos(\theta)) \cos(t) && \text{in } \Omega, \\
u_r(r, \theta, z, t) &= -2\pi (r - r_0)^2 \cos(2\pi z) (1 + \cos(\theta)) \cos(t) && \text{in } \Omega_f, \\
u_\theta(r, \theta, z, t) &= 2\pi (r - r_0)^2 \cos(2\pi z) (1 + \cos(\theta)) \cos(t) && \text{in } \Omega_f, \\
u_z(r, \theta, z, t) &= \frac{r - r_0}{r} \sin(2\pi z) (3r - r_0 + (3r - r_0) \cos(\theta) + (r - r_0) \sin(\theta)) \cos(t) && \text{in } \Omega_f, \\
p(r, \theta, z, t) &= r^3 \sin(2\pi z) \cos(\theta) \cos(t) && \text{in } \Omega_f, \\
H_r(r, \theta, z, t) &= 2\pi r^3 \sin(2\pi z) (1 + \sin(\theta)) \cos(t) && \text{in } \Omega, \\
H_\theta(r, \theta, z, t) &= -2\pi r^3 \sin(2\pi z) (1 + \sin(\theta)) \cos(t) && \text{in } \Omega, \\
H_z(r, \theta, z, t) &= -r^2 \cos(2\pi z) (4 - \cos(\theta) + 4 \sin(\theta)) \cos(t) && \text{in } \Omega.
\end{aligned} \quad (\text{C.8})$$

The problem is solved on modes 0, 1, 2, 3 and 4. Five processors are used in the meridian plane and five processors are used in the Fourier space.

The errors in L^2 -norm or \mathbf{L}^2 -norm on the temperature, the velocity, the pressure, the magnetic field and the curl of the magnetic field for the various mesh sizes and time steps are presented in Tables C.12, C.13, C.14, C.15 and C.16, respectively.

$h \backslash \tau$	0.01	0.005	0.0025	0.00125	0.000625
0.1	2.2000E-4	2.1919E-4	2.1907E-4	2.1906E-4	2.1905E-4
0.05	2.5736E-5	1.9270E-5	1.8341E-5	1.8243E-5	1.8525E-5
0.025	1.8056E-5	6.3166E-6	2.4813E-6	1.6892E-6	1.6037E-6
0.0125	1.7967E-5	6.1025E-6	1.8991E-6	5.6567E-7	2.0321E-7
0.00625	1.7962E-5	6.0991E-6	1.8936E-6	5.4922E-7	1.5222E-7

Table C.12: Relative L^2 -norm error on the temperature at $t = 1$.

$h \backslash \tau$	0.01	0.005	0.0025	0.00125	0.000625
0.1	3.6382E-4	3.4328E-4	3.4074E-4	3.4036E-4	3.4026E-4
0.05	1.2493E-4	4.6802E-5	2.9144E-5	2.7175E-5	3.6450E-5
0.025	1.2184E-4	3.8338E-5	1.1304E-5	3.8347E-6	2.5028E-6
0.0125	1.2172E-4	3.8232E-5	1.1046E-5	3.0187E-6	8.1552E-7
0.00625	1.2170E-4	3.8223E-5	1.1041E-5	3.0121E-6	7.9310E-7

Table C.13: Relative \mathbf{L}^2 -norm error on the velocity at $t = 1$.

$h \backslash \tau$	0.01	0.005	0.0025	0.00125	0.000625
0.1	6.1696E-2	6.0449E-2	6.0064E-2	5.9947E-2	5.9911E-2
0.05	1.1791E-2	9.3564E-3	8.6836E-3	8.4983E-3	9.0489E-3
0.025	6.0131E-3	2.8343E-3	1.8778E-3	1.6178E-3	1.5488E-3
0.0125	5.0506E-3	1.7811E-3	7.3782E-4	4.3844E-4	3.5846E-4
0.00625	4.8285E-3	1.5537E-3	5.0154E-4	1.9298E-4	1.0871E-4

Table C.14: Relative L^2 -norm error on the pressure at $t = 1$.

$h \backslash \tau$	0.01	0.005	0.0025	0.00125	0.000625
0.1	2.8695E-3	2.8695E-3	2.8695E-3	2.8695E-3	2.8695E-3
0.05	4.3654E-4	4.3654E-4	4.3654E-4	4.3654E-4	4.3654E-4
0.025	6.3670E-5	6.3670E-5	6.3670E-5	6.3670E-5	6.3670E-5
0.0125	9.7355E-6	9.7355E-6	9.7355E-6	9.7355E-6	9.7355E-6
0.00625	1.5499E-6	1.5499E-6	1.5499E-6	1.5499E-6	1.5499E-6

Table C.15: Relative \mathbf{L}^2 -norm error on the magnetic field at $t = 1$.

$h \backslash \tau$	0.01	0.005	0.0025	0.00125	0.000625
0.1	7.2268E-3	7.2268E-3	7.2268E-3	7.2268E-3	7.2268E-3
0.05	1.5647E-3	1.5647E-3	1.5647E-3	1.5647E-3	1.5647E-3
0.025	3.2669E-4	3.2669E-4	3.2669E-4	3.2669E-4	3.2669E-4
0.0125	6.5963E-5	6.5963E-5	6.5963E-5	6.5963E-5	6.5963E-5
0.00625	1.3774E-5	1.3774E-5	1.3774E-5	1.3774E-5	1.3774E-5

Table C.16: Relative \mathbf{L}^2 -norm error on the curl of the magnetic field at $t = 1$.

C.2.4 Inverse law of magnetic susceptibility

The law of the magnetic susceptibility is

$$\chi(T) = \frac{10}{T + 1} \quad (\text{C.9})$$

and based on the law of Langevin of the ferrofluid magnetization. The solution is

$$\begin{aligned}
T(r, \theta, z, t) &= \frac{1}{\lambda} r^2 (r - r_0) \sin(2\pi z) \cos(\theta) \cos(t) && \text{in } \Omega, \\
u_r(r, \theta, z, t) &= -2\pi (r - r_0)^2 \cos(2\pi z) (1 + \cos(\theta)) \cos(t) && \text{in } \Omega_f, \\
u_\theta(r, \theta, z, t) &= 2\pi (r - r_0)^2 \cos(2\pi z) (1 + \cos(\theta)) \cos(t) && \text{in } \Omega_f, \\
u_z(r, \theta, z, t) &= \frac{r - r_0}{r} \sin(2\pi z) (3r - r_0 + (3r - r_0) \cos(\theta) + (r - r_0) \sin(\theta)) \cos(t) && \text{in } \Omega_f, \\
p(r, \theta, z, t) &= 0 && \text{in } \Omega_f, \\
H_r(r, \theta, z, t) &= 0 && \text{in } \Omega, \\
H_\theta(r, \theta, z, t) &= \frac{r}{2} && \text{in } \Omega_s, \\
H_\theta(r, \theta, z, t) &= \frac{r_0^2}{2r} && \text{in } \Omega_f, \\
H_z(r, \theta, z, t) &= 0 && \text{in } \Omega.
\end{aligned} \tag{C.10}$$

The problem is solved on modes 0, 1, 2 and 3. Eight processors are used in the meridian plane and four processors are used in the Fourier space.

The errors in L^2 -norm or \mathbf{L}^2 -norm on the temperature, the velocity, the pressure, the magnetic field and the curl of the magnetic field for the various mesh sizes and time steps are presented in Tables C.17, C.18, C.19, C.20 and C.21, respectively.

$h \backslash \tau$	0.01	0.005	0.0025	0.00125	0.000625
0.1	2.1388E-4	2.1383E-4	2.1382E-4	2.1382E-4	2.1382E-4
0.05	1.8190E-5	1.8121E-5	1.8110E-5	1.8108E-5	1.8107E-5
0.025	1.9497E-6	1.6197E-6	1.5942E-6	1.5919E-6	1.5916E-6
0.0125	1.1075E-6	3.0659E-7	1.5203E-7	1.3628E-7	1.3513E-7
0.00625	1.0978E-6	2.7399E-7	6.9390E-8	2.0833E-8	1.2643E-8

Table C.17: Relative \mathbf{L}^2 -norm error on the temperature at $t = 1$.

$h \backslash \tau$	0.01	0.005	0.0025	0.00125	0.000625
0.1	3.4057E-4	3.3915E-4	3.3812E-4	3.3794E-4	3.3777E-4
0.05	2.7806E-5	2.7035E-5	2.6954E-5	2.6934E-5	2.6927E-5
0.025	7.1280E-6	2.9839E-6	2.5026E-6	2.4420E-6	2.4149E-6
0.0125	6.6681E-6	1.6642E-6	4.5361E-7	2.1715E-7	1.9424E-7
0.00625	6.6664E-6	1.6549E-6	4.1283E-7	1.0796E-7	4.7519E-8

Table C.18: Relative \mathbf{L}^2 -norm error on the velocity at $t = 1$.

$h \backslash \tau$	0.01	0.005	0.0025	0.00125	0.000625
0.1	1.4720E-2	1.4691E-2	1.4670E-2	1.4667E-2	1.4660E-2
0.05	1.7333E-3	1.7185E-3	1.7178E-3	1.7166E-3	1.7170E-3
0.025	3.3190E-4	2.3080E-4	2.2371E-4	2.2213E-4	2.2199E-4
0.0125	2.5054E-4	6.7624E-5	3.3249E-5	3.0029E-5	2.9506E-5
0.00625	2.4909E-4	6.1431E-5	1.6833E-5	8.5649E-6	7.2570E-6

Table C.19: \mathbf{L}^2 -norm error on the pressure at $t = 1$.

$h \backslash \tau$	0.01	0.005	0.0025	0.00125	0.000625
0.1	3.3197E-4	3.3197E-4	3.3197E-4	3.3197E-4	3.3197E-4
0.05	5.1246E-5	5.1246E-5	5.1246E-5	5.1246E-5	5.1246E-5
0.025	6.9289E-6	6.9289E-6	6.9289E-6	6.9289E-6	6.9289E-6
0.0125	8.9720E-7	8.9720E-7	8.9720E-7	8.9720E-7	8.9720E-7
0.00625	1.1381E-7	1.1381E-7	1.1381E-7	1.1381E-7	1.1381E-7

Table C.20: Relative \mathbf{L}^2 -norm error on the magnetic field at $t = 1$.

$h \backslash \tau$	0.01	0.005	0.0025	0.00125	0.000625
0.1	8.6838E-4	8.6838E-4	8.6838E-4	8.6838E-4	8.6838E-4
0.05	1.4026E-4	1.4026E-4	1.4026E-4	1.4026E-4	1.4026E-4
0.025	2.0712E-5	2.0712E-5	2.0712E-5	2.0712E-5	2.0712E-5
0.0125	3.0716E-6	3.0716E-6	3.0716E-6	3.0716E-6	3.0716E-6
0.00625	4.5559E-7	4.5559E-7	4.5559E-7	4.5559E-7	4.5559E-7

Table C.21: Relative \mathbf{L}^2 -norm error on the curl of the magnetic field at $t = 1$.

C.3 Temperature-dependent viscosity

C.3.1 Polynomial temperature

The problem is solved in a cylinder of rectangular meridian section

$$\Omega = \{(r, \theta, z) \in \mathbb{R}^3; 0 \leq r < 1, 0 \leq \theta < 2\pi, -1 < z < 1\}.$$

We solve the equations of the temperature (3.52) and the equations of the fluid dynamics (3.55) in Ω . We have $\Omega_f = \Omega_T = \Omega$. The fluid is not a ferrofluid. The magnetic body force and the pyromagnetic coefficient term are absent from the momentum equation and the temperature equation, respectively ($C_p = C_m = 0$). The equation of the temperature uses a thermal diffusivity instead of the density, the heat capacity and the thermal conductivity:

$$\partial_t T + \tilde{\mathbf{u}} \cdot \nabla T - \kappa \Delta T = f_T, \quad (\text{C.11})$$

where κ is the dimensionless thermal diffusivity. We enforce only Dirichlet conditions on the temperature: $\partial\Omega_{T,d} = \partial\Omega_T = \partial\Omega$, $\partial\Omega_{T,n} = \partial\Omega_{T,r} = \emptyset$. The Boussinesq force is absent. The variable Reynolds number is defined by

$$\frac{1}{Re(T)} = \frac{1}{\overline{Re}} \left(1 - \frac{T}{2}\right), \quad (\text{C.12})$$

where \overline{Re} is the minimum Reynolds number. The values of the dimensionless coefficients are given in Table C.22.

Coefficient	Value
κ	3
\overline{Re}	0.5
C_g	0

Table C.22: Dimensionless coefficients.

The solution is

$$\begin{aligned}
T(r, \theta, z, t) &= \frac{r^2 + z^2}{2} \sin(t)^2 && \text{in } \Omega, \\
u_r(r, \theta, z, t) &= 0 && \text{in } \Omega, \\
u_\theta(r, \theta, z, t) &= r^2 \sin(t - z) && \text{in } \Omega, \\
u_z(r, \theta, z, t) &= 0 && \text{in } \Omega, \\
p(r, \theta, z, t) &= 0 && \text{in } \Omega.
\end{aligned} \tag{C.13}$$

The velocity satisfies $\nabla \cdot \mathbf{u} = 0$. The source terms are defined by

$$\begin{aligned}
f_T(r, \theta, z, t) &= \frac{r^2 + z^2}{2} \sin(2t) - 3\kappa \sin(t)^2 && \text{in } \Omega, \\
f_r(r, \theta, z, t) &= -3r^3 \sin(t - z)^2 && \text{in } \Omega, \\
f_\theta(r, \theta, z, t) &= r^2 \cos(t - z) + \frac{r^2 \sin(t)^2 (\sin(t - z) - z \cos(t - z))}{2\overline{R}_e} - \frac{(3 - r^2) \sin(t - z)}{R_e(T)} && \text{in } \Omega, \\
f_z(r, \theta, z, t) &= r^4 \cos(t - z) \sin(t - z) && \text{in } \Omega.
\end{aligned} \tag{C.14}$$

The problem is approximated with

$$h \in \left\{ \frac{1}{10}, \frac{1}{20}, \frac{1}{40}, \frac{1}{80}, \frac{1}{160} \right\}, \quad \tau \in \left\{ \frac{1}{100}, \frac{1}{200}, \frac{1}{400}, \frac{1}{800}, \frac{1}{1600} \right\}.$$

The mesh of the meridian section with $h = 1/10$ is shown in Figure C.1. The problem is solved on the mode 0 only. Four processors are used in the meridian plane and one processor is used in the Fourier space.

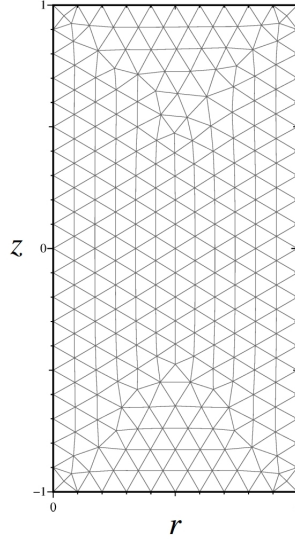


Figure C.1: Mesh of the meridian section with $h = 1/10$.

The evolution of the relative errors on T , \mathbf{u} and p in L^2 -norm or \mathbf{L}^2 -norm with the mesh size at fixed (small) time step is presented in Figure C.2. The error on the temperature does not decrease because the exact solution of the temperature is in the approximation space. The decrease of the error on the velocity follows the theoretical third-order convergence rate. The decrease of the error on the pressure is higher than the theoretical second-order convergence rate for the larger mesh sizes. For the smaller mesh sizes, the error is dominated by the time approximation error.

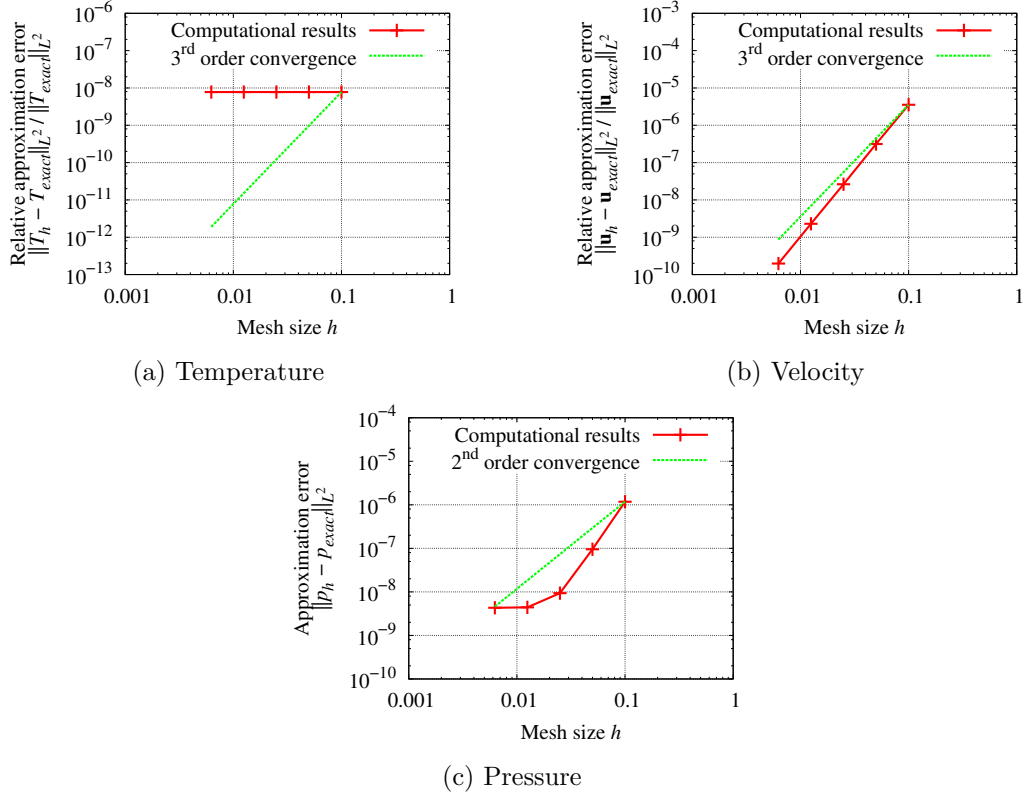


Figure C.2: Error in L^2 -norm or \mathbf{L}^2 -norm at $t = 10^{-2}$ with respect to mesh size for a fixed time step $\tau = 10^{-4}$ and comparison with the theoretical convergence.

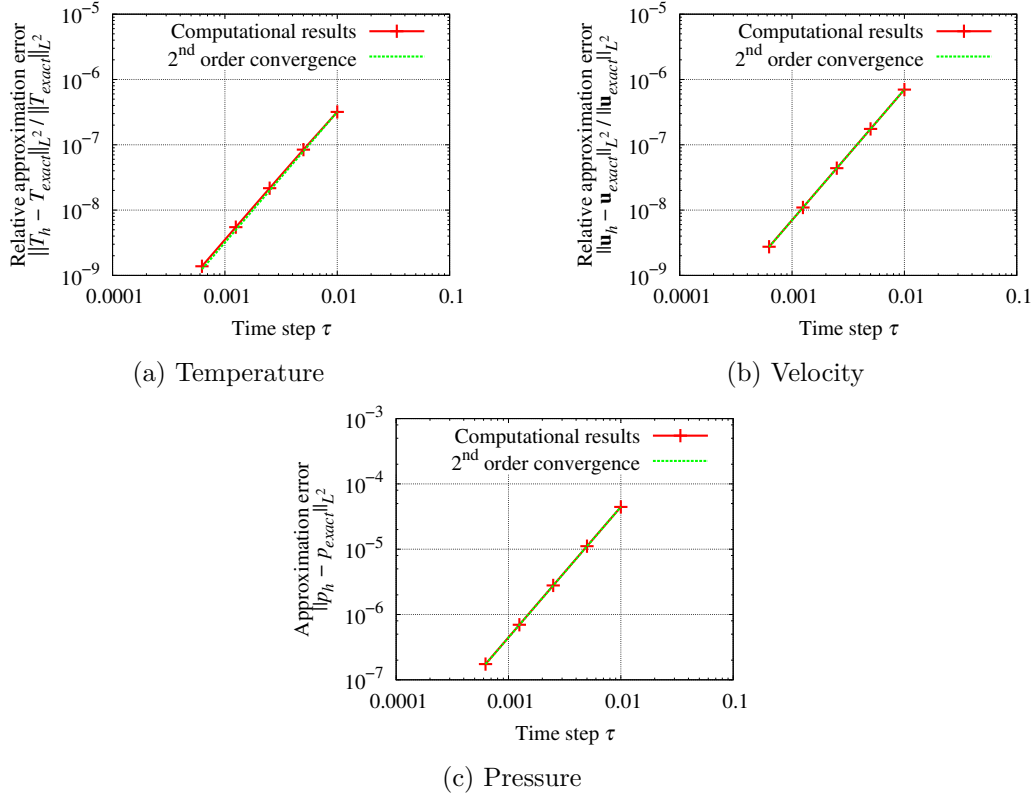


Figure C.3: Error in L^2 -norm or \mathbf{L}^2 -norm at $t = 0.1$ with respect to time step on the mesh with $h = 6.25 \times 10^{-3}$ and comparison with the theoretical convergence.

The evolution of the relative errors on T , \mathbf{u} and p in L^2 -norm or \mathbf{L}^2 -norm with the time step at fixed (small) mesh size is presented in Figure C.3. The decrease of the error on all fields follows the theoretical second-order convergence rate.

The evolution of the relative errors on T , \mathbf{u} and p in L^2 -norm or \mathbf{L}^2 -norm with the mesh size at fixed C_{CFL} is presented in Figure C.4. The decrease of the error on the temperature and the velocity is between the second-order (time step) and third-order (mesh) convergence rates.

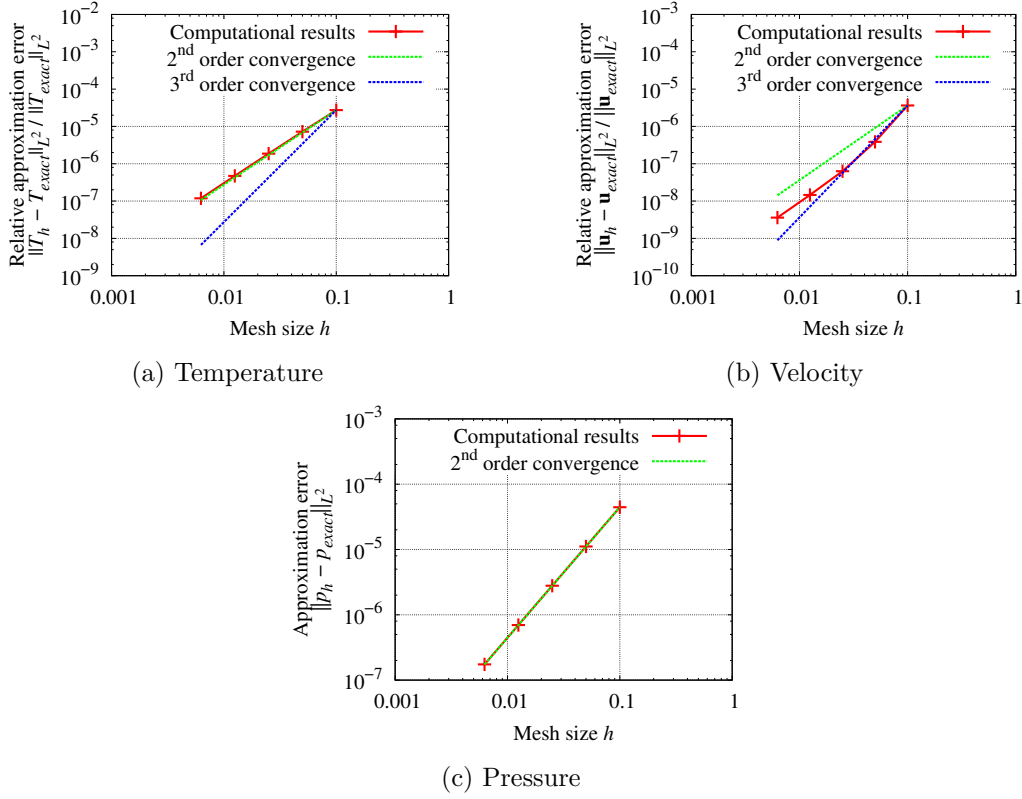


Figure C.4: Error in L^2 -norm or \mathbf{L}^2 -norm at $t = 0.1$ with respect to mesh size with constant ratio $\tau/h = 0.1$ and comparison with the theoretical spatial and time convergences.

C.3.2 Exponential temperature

The main difference with the previous test is the form of the temperature solution. In this test, the temperature solution is not in the approximation space. The other difference is $\overline{R_e} = 1/10$. The solution is

$$\begin{aligned}
 T(r, \theta, z, t) &= \frac{r^3 + e^z}{1 + e} \cos(t)^2 && \text{in } \Omega, \\
 u_r(r, \theta, z, t) &= 0 && \text{in } \Omega, \\
 u_\theta(r, \theta, z, t) &= r^2 \sin(t - z) && \text{in } \Omega, \\
 u_z(r, \theta, z, t) &= 0 && \text{in } \Omega, \\
 p(r, \theta, z, t) &= 0 && \text{in } \Omega.
 \end{aligned} \tag{C.15}$$

The source terms are defined by

$$\begin{aligned}
 f_r(r, \theta, z, t) &= -3r^3 \sin(t - z)^2 && \text{in } \Omega, \\
 f_\theta(r, \theta, z, t) &= r^2 \cos(t - z) + \frac{r^2 \cos(t)^2 (3r \sin(t - z) - e^z \cos(t - z))}{2(1 + e)R_e} - \frac{(3 - r^2) \sin(t - z)}{R_e(T)} && \text{in } \Omega, \\
 f_z(r, \theta, z, t) &= r^4 \cos(t - z) \sin(t - z) && \text{in } \Omega, \\
 f_T(r, \theta, z, t) &= -\frac{r^3 + e^z}{1 + e} \sin(2t) - \frac{\kappa}{1 + e} (9r + e^z) \cos(t)^2 && \text{in } \Omega.
 \end{aligned} \tag{C.16}$$

The evolution of the relative errors on T , \mathbf{u} and p in L^2 -norm or \mathbf{L}^2 -norm with the mesh size at fixed (small) time step is presented in Figure C.5. The decrease of the error on the temperature and the velocity follows the theoretical third-order convergence rate. The decrease of the error on the pressure is higher than the theoretical second-order convergence rate for the larger mesh sizes. For the smaller mesh sizes, the error is dominated by the time approximation error.

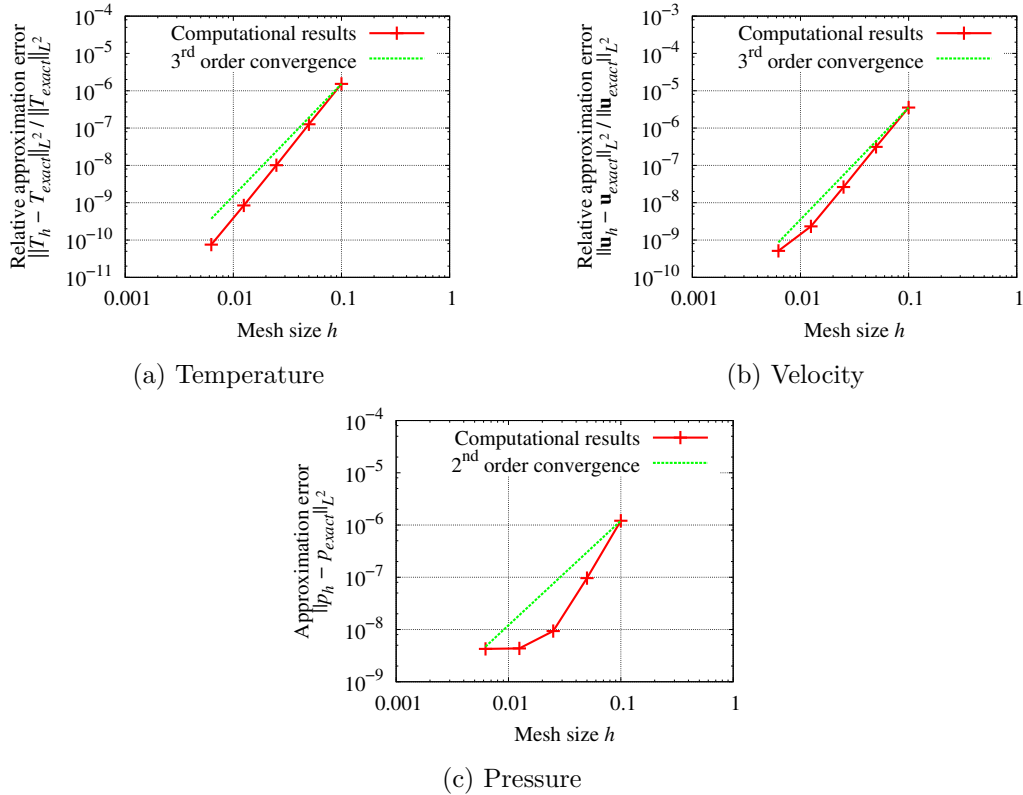


Figure C.5: Error in L^2 -norm or \mathbf{L}^2 -norm at $t = 10^{-2}$ with respect to mesh size for a fixed time step $\tau = 10^{-4}$ and comparison with the theoretical convergence.

The evolution of the relative errors on T , \mathbf{u} and p in L^2 -norm or \mathbf{L}^2 -norm with the time step at fixed (small) mesh size is presented in Figure C.6. The decrease of the error on all fields follows the theoretical second-order convergence rate.

The evolution of the relative errors on T , \mathbf{u} and p in L^2 -norm or \mathbf{L}^2 -norm with the mesh size at fixed C_{CFL} is presented in Figure C.7. The decrease of the error on the temperature and the velocity is between the second-order (time step) and third-order (mesh) convergence rates.

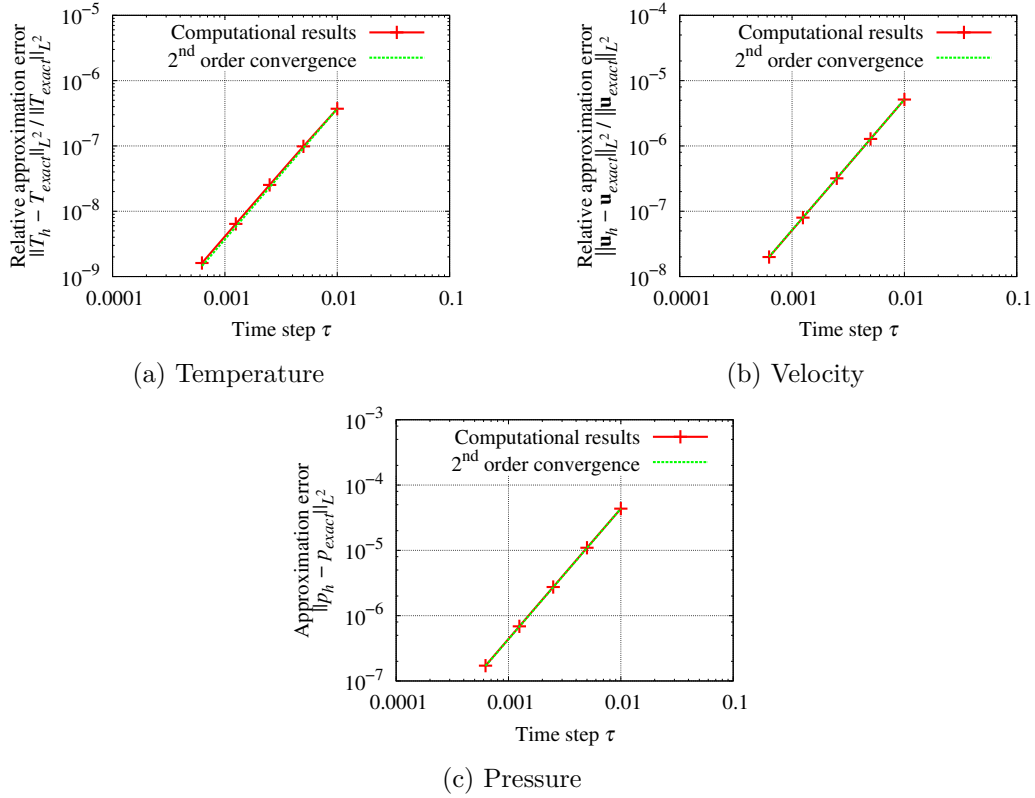


Figure C.6: Error in L^2 -norm or \mathbf{L}^2 -norm at $t = 0.1$ with respect to time step on the mesh with $h = 6.25 \times 10^{-3}$ and comparison with the theoretical convergence.

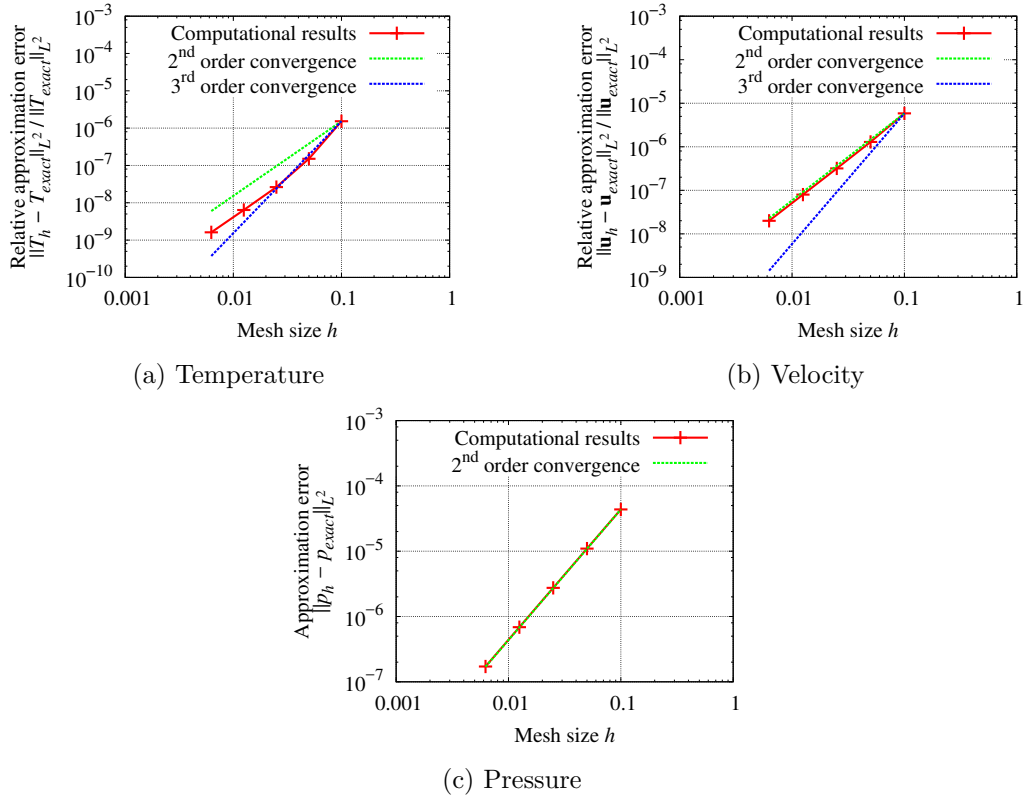


Figure C.7: Error in L^2 -norm or \mathbf{L}^2 -norm at $t = 0.1$ with respect to mesh size with constant ratio $\tau/h = 0.1$ and comparison with the theoretical spatial and time convergences.

Appendix D

Preparatory study for the design of the experiment

This appendix is dedicated to the simulations performed in order to design the experimental setup of the immersed coil. The goal of these simulations was to predict the temperature difference in the coil when transformer oil or transformer oil-based ferrofluid is used as coolant. This difference of temperature had to be sufficient to be observed during the experiment.

D.1 Modeling

Figure D.1 presents the experimental setup considered for these simulations. The coil is made of two layers of wires to maximize the temperature rise. The walls are made of PVC to facilitate the work of the experimenters. The dimensions are $H_t = 4$ cm, $R_t = 3$ cm, $R_i = 0.9$ cm, $R_e = 1.1$ cm, $e = 0.2$ cm, $L_0 = 2$ cm and $e_w = 0.5$ cm.

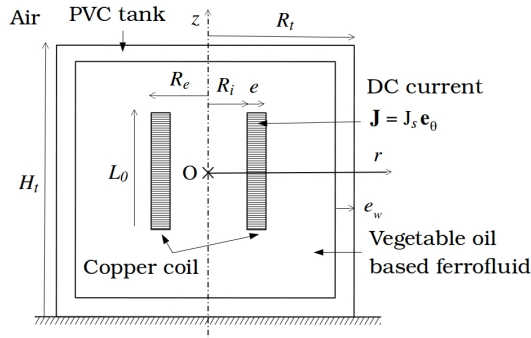


Figure D.1: Experimental setup.

The governing equations are that of the article in Chapter 4, except for the boundary conditions on the temperature: Dirichlet conditions ($T = T_0$) are used instead of Robin conditions on the top and lateral walls of the tank.

In the model, the coil is made of pure copper. The properties of the materials considered in the simulations are reported in Table D.1. The transformer oil and the ferrofluid have the same properties to highlight the Kelvin body force effect. The electrical conductivity of copper is $\sigma_{cl} = 6.0 \times 10^7$ $1/\Omega \cdot \text{m}$ [117].

The exterior temperature is $T_0 = 293$ K. The ferrofluid characteristics are $\phi = 0.07$, $d = 10$ nm and $M_0 = 446$ kA/m [114]. The enforced current is 10 A and the corresponding current density is $J_s = 10^7$ A/m². For the magnetostatics equations, the magnetic permeability is $\mu = \mu_0$ everywhere for simplicity.

Property	Copper	Transformer oil	PVC
Density (kg/m ³)	8933	922	1400
Heat capacity (J/K · kg)	385	1970	1000
Thermal conductivity (W/m · K)	401	0.166	0.16
Kinematic viscosity (m ² /s)	-	6.7×10^{-5}	-
Thermal expansion coefficient (1/K)	-	7.4×10^{-4}	-

Table D.1: Material properties. Copper properties are from [107, p. 983]. The oil is the vegetable transformer oil eN 1215 from Midel company. Oil properties are taken at 20°C and furnished by the manufacturer. PVC properties are from [108, p. 68].

The mesh of the meridian section is shown in Figure D.2. As for the mesh of the actual setup (see Section 4.2.4), the mesh size is chosen considering the thickness of the boundary layers for the velocity and the temperature at the coil, denoted by δ and δ_T , respectively. Based on the dimensions of the coil and the current density, we can estimate that the heat flux across the coil walls is

$$q_S = \frac{\frac{J_s^2}{\sigma_{cl}} \pi L_0 (R_2^2 - R_i^2)}{2\pi(L_0(R_i + R_e) + R_e^2 - R_i^2)} \simeq 1.5 \times 10^3 \text{ W/m}^2. \quad (\text{D.1})$$

The Rayleigh number (case of an enforced flux q_S) is

$$Ra = \frac{g \alpha_f q_S L_0^4}{\kappa_f \nu_f \lambda_f} \simeq 1.7 \times 10^7, \quad (\text{D.2})$$

where g is the gravity, α_f is the thermal expansion coefficient, κ_f is the thermal diffusivity, ν_f is the kinematic viscosity and λ_f is the thermal conductivity. The thickness of the thermal boundary layer is estimated by $\delta_T = L_0 (Pr Ra)^{-\frac{1}{5}} \simeq 3.0 \times 10^{-4}$ m. The mesh size in the coil being at most 4×10^{-4} m, it is sufficient to observe the variations of the velocity along δ and that of the temperature along δ_T .

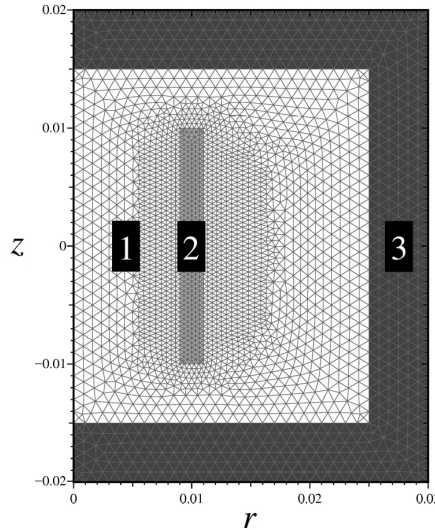


Figure D.2: Mesh of the meridian section (symmetry axis on the left). Axes in meters. 1: fluid, 2: coil, 3: tank. The mesh size is 4×10^{-4} m in the coil and 10^{-3} m in the tank.

The simulations are performed on mode 0 only, assuming the axisymmetry of the solution.

D.2 Results

The system reaches a steady regime in about 1 h of physical time. The magnetic field (Figure D.3) impacts the ferrofluid flow. Because of the Kelvin body force, a strong upward flow appears at the symmetry axis and leads to an additional convection cell that cools down the coil, as shown in Figure D.4.

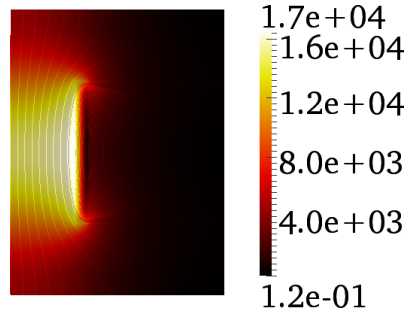


Figure D.3: Magnetic field intensity H (A/m) and field lines in a meridian section (symmetry axis on the left) for transformer oil and ferrofluid.

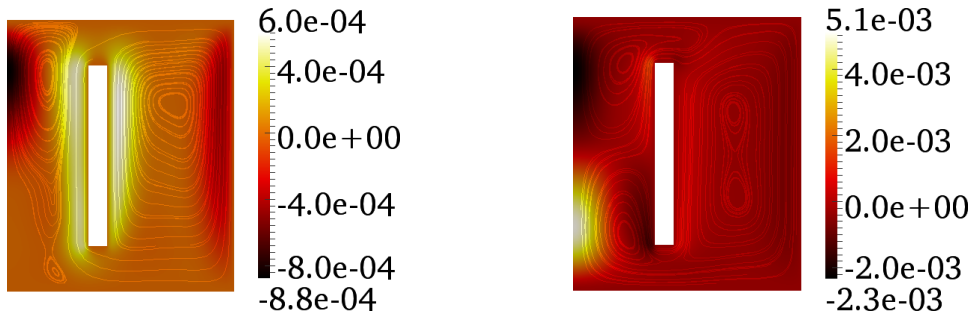


Figure D.4: Axial velocity u_z (m/s) and current lines in a meridian section (symmetry axis on the left) at $t = 5000$ s for transformer oil (left panel) and ferrofluid (right panel).

Thermomagnetic convection improves the heat removal in the ferrofluid system. The temperature increment $T - T_0$ in the coil goes from 34.4°C with transformer oil to 30.7°C with ferrofluid, see Figure D.5. Thanks to the nanoparticles, the increase of temperature in the coil is reduced by about 11%.

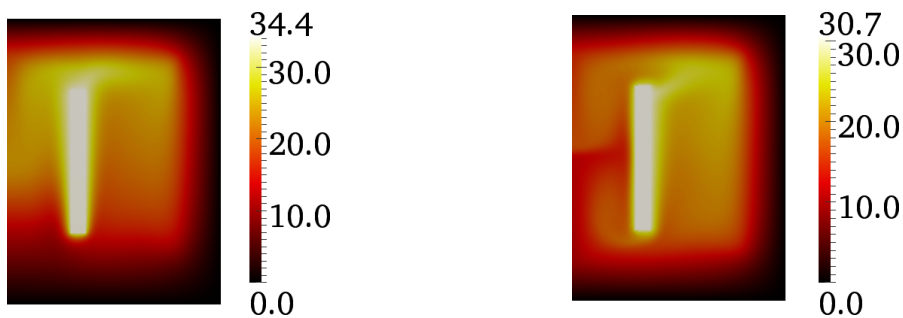


Figure D.5: Temperature increment $T - T_0$ ($^\circ\text{C}$) in a meridian section (symmetry axis on the left) at $t = 5000$ s for transformer oil (left panel) and ferrofluid (right panel).

The few degrees of difference in the coil between the cooling with transformer oil and the cooling with ferrofluid were considered sufficiently important to be measured during the experiment.

Appendix E

Transformer case: estimation of the convection coefficient in the absence of heat transfer fins

This appendix is dedicated to the calculus of the convection coefficient on the top and lateral boundaries of the transformer considered in Chapter 6. In this calculus, we assume that there is no heat transfer fins. The simulations are performed with an aluminium tank, which properties are close to that of steel.

E.1 Theory

The transformer is basically as high as it is large. None of its dimensions greatly exceeds all the others and it has thus a small aspect ratio. The handbook of heat transfer [120, pp. 4.8,4.25,4.26] suggests the following correlations in the case of external free convection and a body with small aspect ratio:

$$N_u^T = G\bar{C}_l R_a^{\frac{1}{4}}, \quad (\text{E.1})$$

$$N_{u,l} = ((N_{u,\text{COND}})^n + (N_u^T)^n)^{\frac{1}{n}}, \quad (\text{E.2})$$

$$N_{u,t} = \bar{C}_t R_a^{\frac{1}{3}}, \quad (\text{E.3})$$

$$N_u = (N_{u,l}^m + N_{u,t}^m)^{\frac{1}{m}}. \quad (\text{E.4})$$

$N_{u,\text{COND}}$ is the Nusselt number corresponding to the case $R_a \rightarrow 0$ (conduction only case). N_u^T is the Nusselt number in laminar regime, in the approximation of a thin boundary layer. $N_{u,l}$ and $N_{u,t}$ are the Nusselt numbers in laminar and turbulent regimes, respectively. Finally, the definition of N_u fits any case, laminar or turbulent regime. The coefficient \bar{C}_l depends on the Prandtl number of the fluid. The Prandtl number of air is about 0.71 at room temperature and the associated value is $\bar{C}_l = 0.515$. The coefficients G , \bar{C}_t , $N_{u,\text{COND}}$, n and m depend on the shape of the object. For a short vertical cylinder such that height / diameter = 1, these coefficients take the following values: $N_{u,\text{COND}} = 1.59$, $G = 0.839$, $n = 1.11$, $\bar{C}_t = 0.092$ and $m = 10$. The Rayleigh number is defined by

$$R_a = \frac{g\alpha\Delta T D^3}{\kappa\nu}, \quad (\text{E.5})$$

where g is the gravity, α is the thermal expansion coefficient, ΔT is the temperature difference generating the convective flow, D is the diameter of the cylinder, κ is the thermal diffusivity and ν is the kinematic viscosity. The thermophysical properties are

that of the fluid flowing around the body. The convection coefficient is related to the Nusselt number through

$$Nu = \frac{hD}{\lambda}, \quad (\text{E.6})$$

where λ is the thermal conductivity.

To estimate the convection coefficient, we need to calculate in the following order: the Rayleigh number through (E.5), the Nusselt number through (E.1)-(E.4) and finally h through (E.6). The air properties used to calculate the Rayleigh number and the convection coefficient are reported in Table E.1. The diameter of the transformer is $D = 2R_t = 0.422$ m. The only unknown is the temperature difference ΔT in the Rayleigh number.

Property	Value	Comment
Thermal expansion coefficient (1/K)	3.35×10^{-3}	at 25 °C, from [121]
Thermal conductivity (W/m · K)	26.3×10^{-3}	at 300 K, from [107]
Thermal diffusivity (m ² /s)	22.5×10^{-6}	at 300 K, from [107]
Kinematic viscosity (m ² /s)	15.89×10^{-6}	at 300 K, from [107]

Table E.1: Air properties.

E.2 Computations

To estimate the increment of temperature ΔT , we first run a simulation by using Dirichlet conditions on all the boundaries of the tank ($T = T_0 = 20^\circ\text{C}$). The convection is not taken into account by cancelling the Boussinesq force. As a matter of fact, the permanent solution of the conduction problem can be obtained quickly and it offers a satisfying approximation. The permanent solution of the convection problem would not change significantly the convection coefficient estimate owing to the exponent 1/4 in (E.1). A very large time step of $\tau = 10^{20}$ s is used to reach the permanent regime with one iteration. According to the simulation, the maximum temperature in the system is 757°C in the permanent regime, see Figure E.1. By using $\Delta T = 737^\circ\text{C}$, we obtain $R_a \simeq 5.09 \times 10^9$, $Nu \simeq 159$ and $h \simeq 9.91 \text{ W/m}^2 \cdot \text{K}$.

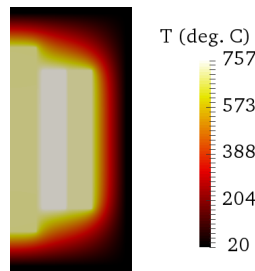


Figure E.1: Dirichlet boundary conditions on every external boundary. Temperature in a meridian section (symmetry axis on the left).

This value of the convection coefficient is used to simulate the temperature in the conduction only case in permanent regime, with Robin boundary conditions at the tank / air interfaces (and homogeneous Neumann boundary condition at the bottom of the tank). The results are shown in Figure E.2. On the top boundary, the temperature reaches approximately 122°C . On the lateral boundary it reaches approximately 133°C . With $\Delta T = 102^\circ\text{C}$, we obtain $R_a \simeq 7.05 \times 10^8$, $Nu \simeq 83.7$ and $h \simeq 5.22 \text{ W/m}^2 \cdot \text{K}$ for

the top boundary. By using $\Delta T = 113^\circ\text{C}$, we obtain $R_a \simeq 7.81 \times 10^8$, $N_u \simeq 86.5$ and $h \simeq 5.39 \text{ W/m}^2 \cdot \text{K}$ for the lateral boundary.

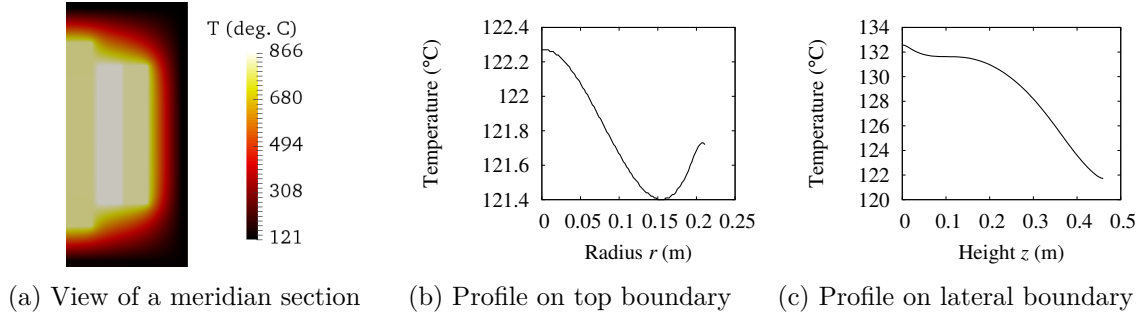


Figure E.2: Robin conditions at the top and lateral boundaries with $h = 9.91 \text{ W/m}^2 \cdot \text{K}$, homogeneous Neumann condition at the bottom boundary.

These values of the convection coefficient are used to re-run the previous computation, see Figure E.3. On the top boundary, the temperature reaches approximately 213°C . On the lateral boundary it reaches approximately 224°C . Convection coefficients are estimated once again. With $\Delta T = 193^\circ\text{C}$, we obtain $R_a \simeq 1.33 \times 10^9$, $N_u \simeq 103$ and $h \simeq 6.40 \text{ W/m}^2 \cdot \text{K}$ for the top boundary. By using $\Delta T = 204^\circ\text{C}$, we obtain $R_a \simeq 1.41 \times 10^9$, $N_u \simeq 104$ and $h \simeq 6.51 \text{ W/m}^2 \cdot \text{K}$ for the lateral boundary.

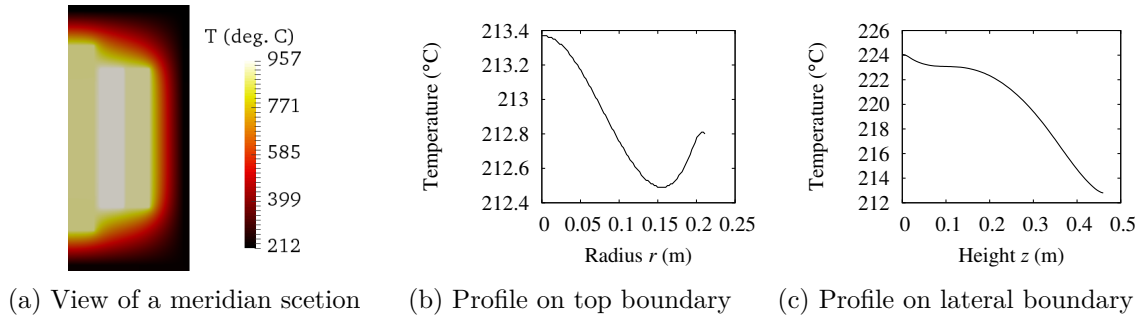


Figure E.3: Robin at the top and lateral boundaries with $h_{\text{top}} = 5.22 \text{ W/m}^2 \cdot \text{K}$ and $h_{\text{lat}} = 5.39 \text{ W/m}^2 \cdot \text{K}$, homogeneous Neumann condition at the bottom boundary.

The same process is applied one more time to converge, see Figure E.4. On the top boundary, the temperature reaches approximately 179°C . On the lateral boundary it reaches approximately 190°C . Convection coefficients are estimated once again. By using $\Delta T = 159^\circ\text{C}$, we obtain $R_a \simeq 1.10 \times 10^9$, $N_u \simeq 96.4$ and $h \simeq 6.01 \text{ W/m}^2 \cdot \text{K}$ for the top boundary. By using $\Delta T = 170^\circ\text{C}$, we obtain $R_a \simeq 1.17 \times 10^9$, $N_u \simeq 98.5$ and $h \simeq 6.14 \text{ W/m}^2 \cdot \text{K}$ for the lateral boundary. Observing that the maximum temperatures in the system found in the last two steps are close (957 and 923°C), and that it leads to close convection coefficients (around $6 \text{ W/m}^2 \cdot \text{K}$), we stop here the iterations.

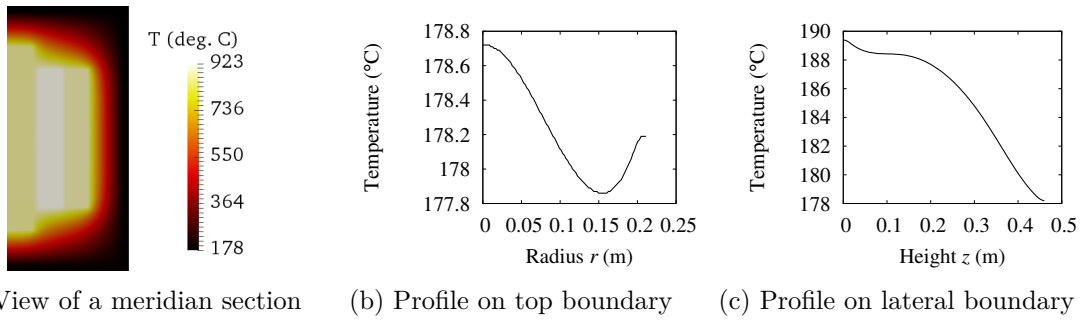


Figure E.4: Robin conditions at the top and lateral boundary with $h_{\text{top}} = 6.40 \text{ W/m}^2 \cdot \text{K}$ and $h_{\text{lat}} = 6.51 \text{ W/m}^2 \cdot \text{K}$, homogeneous Neumann condition at the bottom boundary.

E.3 Conclusion

By using conduction only computations and correlations from the literature, we estimate that the convection coefficient on the top and lateral boundaries of the transformer is approximately $6 \text{ W/m}^2 \cdot \text{K}$ in the absence of heat transfer fins.

Bibliography

- [1] V. Segal and K. Raj. An investigation of power transformer cooling with magnetic fluids. *Indian Journal of Engineering & Materials Science*, 5:416–422, 1998.
- [2] L. Pîslaru-Danescu, A. M. Morega, M. Morega, V. Stoica, O. M. Marincia, F. Nouras, N. Paduraru, I. Borbàth, and T. Borbàth. Prototyping a Ferrofluid-Cooled Transformer. *IEEE Transaction on Industry Applications*, 49(3):1289–1298, 2013.
- [3] G.-Y. Jeong, S. P. Jang, H.-Y. Lee, J.-C. Lee, S. Choi, and S.-H. Lee. Magnetic-Thermal-Fluidic Analysis for Cooling Performance of Magnetic Nanofluids Comparing With Transformer Oil and Air by Using Fully Coupled Finite Element Method. *IEEE Transactions on Magnetics*, 49(5):1865–1868, 2013.
- [4] J. Patel, K. Parekh, and R. V. Upadhyay. Prevention of hot spot temperature in a distribution transformer using magnetic fluid as a coolant. *International Journal of Thermal Sciences*, 103:35–40, 2016.
- [5] Y. Bertrand and L. C. Hoang. Vegetable Oils as Substitute for Mineral Oils. In *Proceedings of the 7th International Conference on Properties and Applications of Dielectric Materials International Conference on Properties and Applications of Dielectric Materials*, pages 491–494, 2003.
- [6] G. J. Pukel, R. Schwarz, F. Baumann, H. M. Muhr, R. Eberhardt, B. Wieser, and D. Chu. POWER TRANSFORMERS with environmentally friendly and low flammability ester liquids. In *CIGRE 2012*, 2012.
- [7] Y. Bertrand and P. Lauzevis. DEVELOPMENT OF A LOW VISCOSITY INSULATING LIQUID BASED ON NATURAL ESTERS FOR DISTRIBUTION TRANSFORMERS. In *22nd International Conference on Electricity Distribution (CIRED 2013)*, 2013.
- [8] B. H. Sitorus. *The Study of Jatropha Curcas Oil-Based Biodegradable Insulation Materials For Power Transformer*. PhD thesis, Ecole Centrale de Lyon, 2015.
- [9] J. M. G. Evangelista Jr., F. E. Bortot Coelho, J. A. O. Carvalho, E. M. R. Araújo, T. L. S. Miranda, and A. Salum. Development of a New Bio-Based Insulation Fluid from *Jatropha curcas* Oil for Power Transformers. *Advances in Chemical Engineering and Science*, 7:235–255, 2017.
- [10] R. E. Rosensweig. *Ferrohydrodynamics*. Cambridge University Press, 1985.
- [11] R. Massart, J.-C. Bacri, and R. Perzynski. Liquides magnétiques ou ferrofluides. *Techniques de l'Ingénieur*, pages 1–9, June 1995. Reference: D2180 V1.
- [12] S. Odenbach. *Magnetoviscous Effect in Ferrofluids*. Springer-Verlag, Berlin, Heidelberg, 2002.

- [13] M. Petit. *Contribution à l'étude des systèmes de refroidissement basés sur le couplage magnétothermique dans les ferrofluides à faible température de Curie : mise en place d'outils de caractérisation et de modélisation*. PhD thesis, Université de Grenoble, 2012.
- [14] D. Wen, G. Lin, S. Vafaei, and K. Zhang. Review of nanofluids for heat transfer applications. *Particuology*, 7:141–150, 2009.
- [15] P. G. Huray. *Maxwell's Equations*. John Wiley & Sons, Hoboken, NJ, 2010.
- [16] E. Du Trémolet de Lacheisserie, D. Guignoux, and M. Schlenker. *Magnetism: Fundamentals*. Springer-Verlag, New York, 2005.
- [17] S. Odenbach. Magnetic fluids - suspensions of magnetic dipoles and their magnetic control. *Journal of Physics: Condensed Matter*, 15:1497–1508, 2003.
- [18] I. Milosevic, L. Motte, and F. Mazaleyrat. Ferrofluides - Nanoparticules superparamagnétiques. *Techniques de l'Ingénieur*, pages 1–14, April 2011. Reference: N4590 V1.
- [19] M. Bahiraei and M. Hangi. Flow and heat transfer characteristics of magnetic nanofluids: a review. *Journal of Magnetism and Magnetic Materials*, 374:125–138, 2015.
- [20] S. S. Papell and O. C. Faber Jr. Zero- and Reduced-Gravity Simulation on a Magnetic-Colloid Pool-Boiling System, 1966. NASA technical note D-3288.
- [21] G. W. Reimers and S. E. Khalafalla. Production of magnetic fluids by peptization techniques, 1974. US Patent 3843540.
- [22] J. Perrin. Mouvement brownien et réalité moléculaire. *Annales de Chimie et de Physique, Huitième série, Tome XVIII*, pages 5–114, 1909.
- [23] H. C. Hamaker. THE LONDON-VAN DER WAALS ATTRACTION BETWEEN SPHERICAL PARTICLES. *Physica*, 4(10):1058–1072, 1937.
- [24] National Institute of Standards and Technology. The NIST Reference on Constants, Units, and Uncertainty. physics.nist.gov/cuu/index.html. Data from the Physical Measurement Laboratory of NIST. Accessed in 2016.
- [25] Ferrotec company. Ferrotec. <https://ferrofluid.ferrotec.com>. Accessed in 2018.
- [26] S. Baglio, P. Barrera, and N. Savalli. Novel Ferrofluidic Inertial Sensors. In *IMTC 2006 – Instrumentation and Measurement Technology Conference*, pages 2368–2372, 2006.
- [27] B. Andò, A. Ascia, S. Baglio, and N. Savalli. A Novel Ferrofluidic Inclinometer. *IEEE Transactions on Instrumentation and Measurement*, 56(4):1114–1123, 2007.
- [28] L. J. Love, J. F. Jansen, T. E. McKnight, Y. Roh, T. J. Phelps, L. W. Yeary, and G. T. Cunningham. Ferrofluid Field Induced Flow for Microfluidic Applications. *IEEE/ASME Transaction on Mechatronics*, 10(1):68–76, 2005.
- [29] S. Odenbach. *Colloidal Magnetic Fluids: Basic, Development and Application of Ferrofluids*. Springer-Verlag, Berlin, Heidelberg, 2009. Lect. Notes Phys. 763.

- [30] J. Patel, K. Parekh, and R. V. Upadhyay. Performance of Mn-Zn ferrite magnetic fluid in a prototype distribution transformer under varying loading conditions. *International Journal of Thermal Sciences*, 114:64–71, 2017.
- [31] R. E. Rosensweig. MAGNETIC FLUIDS. *Annual Reviews of Fluid Mechanics*, 19:437–463, 1987.
- [32] R. W. Chantrell, J. Popplewell, and S. W. Charles. MEASUREMENTS OF PARTICLE SIZE DISTRIBUTION PARAMETERS IN FERROFLUIDS. *IEEE Transaction on Magnetics*, 14(5):975–977, 1978.
- [33] J. L. Neuringer and R. E. Rosensweig. Ferrohydrodynamics. *The Physics of Fluids*, 7(12):1927–1937, 1964.
- [34] R. E. Rosensweig. Basic Equations for Magnetic Fluids with Internal Rotations. In S. Odenbach, editor, *Ferrofluids: Magnetically Controllable Fluids and Their Applications, LNP 594*, pages 61–84. Springer-Verlag, Berlin, Heidelberg, 2002.
- [35] M. I. Shliomis. Ferrohydrodynamics: Retrospective and Issues. In S. Odenbach, editor, *Ferrofluids: Magnetically Controllable Fluids and Their Applications, LNP 594*, pages 85–111. Springer-Verlag, Berlin, Heidelberg, 2002.
- [36] T. H. Boyer. The force on a magnetic dipole. *American Journal of Physics*, 56:688–692, 1988.
- [37] A. Bossavit. On Forces in Magnetized Matter. *IEEE Transaction on Magnetics*, 50(2), 2014.
- [38] J. R. Melcher. *Continuum Electromechanics*. MIT Press, Cambridge, MA, 1981.
- [39] A. Bossavit. Virtual Power Principle and Maxwell’s tensor: Which comes first? *COMPEL International Journal of Computations and Mathematics in Electrical and Electronic Engineering*, pages 1–6, 2011.
- [40] S. Afkhami, Y. Renardy, M. Renardy, J. S. Riffle, and T. St Pierre. Field-induced motion of ferrofluid droplets through immiscible viscous media. *Journal of Fluid Mechanics*, 610:363–380, 2008.
- [41] A. Bossavit. Un tenseur de Maxwell non linéaire et symétrique. *European Journal of Electrical Engineering*, 18(3-4):169–177, 2016.
- [42] X.-Q. Wang and A. S. Mujumdar. A REVIEW ON NANOFUIDS - PART I: THEORETICAL AND NUMERICAL INVESTIGATIONS. *Brazilian Journal of Chemical Engineering*, 25(4):613–630, 2008.
- [43] S. M. S. Murshed, K. C. Leong, and C. Yang. Investigations of thermal conductivity and viscosity of nanofluids. *International Journal of Thermal Sciences*, 47:560–568, 2008.
- [44] C. Choi, H. S. Yoo, and J. M. Oh. Preparation and heat transfer properties of nanoparticle-in-transformer oil dispersions as advanced energy-efficient coolants. *Current Applied Physics*, 8:710–712, 2008.
- [45] B. LotfizadehDehkordi, S. N. Kazi, M. Hamdi, A. Ghadimi, E. Sadeghinezhad, and H. S. C. Metselaar. Investigation of viscosity and thermal conductivity of alumina nanofluids with addition of SDBS. *Heat and Mass Transfer*, 49(8):1109–1115, 2013.

- [46] V. E. Fertman, L. E. Golovicher, and N. P. Matusevich. THERMAL CONDUCTIVITY OF MAGNETITE MAGNETIC FLUIDS. *Journal of Magnetism and Magnetic Materials*, 65:211–214, 1987.
- [47] M. J. Pastoriza-Gallego, L. Lugo, J. L. Legido, and M. M. Pineiro. Enhancement of thermal conductivity and volumetric behavior of Fe_xO_y nanofluids. *Journal of Applied Physics*, 110(014309):1–9, 2011.
- [48] A. Karimi, M. Goharkhah, M. Ashjaee, and M. B. Shafii. Experimental investigation on thermal conductivity of MFe_2O_4 ($\text{M} = \text{Fe}$ and Co) magnetic nanofluids under influence of magnetic field. *Thermochimica Acta*, 598:59–67, 2014.
- [49] J. Eapen, R. Rusconi, R. Piazza, and S. Yip. The Classical Nature of Thermal Conduction in Nanofluids. *Journal of Heat Transfer*, 132(102402):1–14, 2010.
- [50] A. Vatani, P. L. Woodfield, and D. V. Dao. A survey of practical equations for prediction of effective thermal conductivity of spherical-particle nanofluids. *Journal of Molecular Liquids*, 211:712–733, 2015.
- [51] J. Philip, P. D. Shima, and B. Raj. Enhancement of thermal conductivity in magnetite based nanofluid due to chainlike structures. *Applied Physics Letters*, 91(203108):1–3, 2007.
- [52] M. Rabaud. Notes de cours d'hydrodynamique (2014-2015), 2014. Magistère Formation Interuniversitaire de Physique, Université Paris-Sud.
- [53] S. W. Lee, S. D. Park, S. Khang, I. C. Bang, and J. H. Kim. Investigation of viscosity and thermal conductivity of SiC nanofluids for heat transfer applications. *International Journal of Heat and Mass Transfer*, 54:433–438, 2011.
- [54] P. D. Shima, J. Philip, and B. Raj. Synthesis of Aqueous and Nonaqueous Iron Oxide Nanofluids and Study of Temperature Dependence on Thermal Conductivity and Viscosity. *J. Phys. Chem. C*, 114:18825–18833, 2010.
- [55] L. S. Sundar, M. K. Singh, and A. C. M. Sousa. Investigation of thermal conductivity of Fe_3O_4 nanofluid for heat transfer applications. *International Communications in Heat and Mass Transfer*, 44:7–14, 2013.
- [56] A. Malekzadeh, A. R. Pouranfard, N. Hatami, A. Kazemnejad Banari, and M. R. Rahimi. Experimental Investigations on the Viscosity of Magnetic Nanofluids under the Influence of Temperature, Volume Fractions of Nanoparticles and External Magnetic Field. *Journal of Applied Fluid Mechanics*, 9(2):693–697, 2016.
- [57] A. Einstein. Eine neue Bestimmung der Moleküldimensionen. *Annalen der Physik*, 324:289–306, 1906.
- [58] A. Einstein. Berichtigung zu meiner Arbeit: "Eine neue Bestimmung der Moleküldimensionen". *Annalen der Physik*, 339:591–592, 1911.
- [59] S. M. Sohel Murshed and P. Estellé. A state of the art review on viscosity of nanofluids. *Renewable and Sustainable Energy Reviews*, 76:1134–1152, 2017.
- [60] J. P. McTague. Magnetoviscosity of Magnetic Colloids. *The Journal of Chemical Physics*, 51(1):133–136, 1969.
- [61] W. F. Hall and S. N. Busenberg. Viscosity of Magnetic Suspensions. *The Journal of Chemical Physics*, 51(1):137–144, 1969.

- [62] M. I. Shliomis. Effective Viscosity of Magnetic Suspensions. *Soviet Physics JETP*, 34(6):1291–1294, 1972.
- [63] S. Odenbach and K. Raj. THE INFLUENCE OF LARGE PARTICLES AND AGGLOMERATES ON THE MAGNETOVISCOUS EFFECT IN FERROFLUIDS. *Magnetohydrodynamics*, 36(4):312–319, 2000.
- [64] B. A. Finlayson. Convective instability of ferromagnetic fluids. *Journal of Fluids Mechanics*, 40:753–767, 1970.
- [65] L. Schwab, U. Hildebrandt, and K. Stierstadt. MAGNETIC BENARD CONVECTION. *Journal of Magnetism and Magnetic Materials*, 39:113–114, 1983.
- [66] S. Odenbach. Microgravity experiments on thermomagnetic convection in magnetic fluids. *Journal of Magnetism and Magnetic Materials*, 149:155–157, 1995.
- [67] A. A. Bozhko and G. F. Putin. Magnetic action on convection and heat transfer in ferrofluid. *Indian Journal of Engineering & Materials Sciences*, 11:309–314, 2004.
- [68] M. T. Krauzina, A. A. Bozhko, P. V. Krauzin, and S. A. Suslov. The use of ferrofluids for heat removal: Advantage or disadvantage? *Journal of Magnetism and Magnetic Materials*, 431:241–244, 2017.
- [69] M. S. Krakov and I. V. Nikiforov. To the influence of uniform magnetic field on thermomagnetic convection in square cavity. *Journal of Magnetism and Magnetic Materials*, 252:209–211, 2002.
- [70] S. M. Snyder, T. Cader, and B. A. Finlayson. Finite element model of magnetoconvection of a ferrofluid. *Journal of Magnetism and Magnetic Materials*, 262:269–279, 2003.
- [71] M. Ashouri and M. Behshad Shafii. Numerical simulation of magnetic convection ferrofluid flow in a permanent magnet-inserted cavity. *Journal of Magnetism and Magnetic Materials*, 442:270–278, 2017.
- [72] H. Yamaguchi, I. Kobori, Y. Uehata, and K. Shimada. Natural convection of magnetic fluid in a rectangular box. *Journal of Magnetism and Magnetic Materials*, 201:264–267, 1999.
- [73] H. Yamaguchi, X.-D. Niu, X.-R. Zhang, and K. Yoshikawa. Experimental and numerical investigation of natural convection of magnetic fluids in a cubic cavity. *Journal of Magnetism and Magnetic Materials*, 321:3665–3670, 2009.
- [74] D. Zablotsky, A. Mezulis, and E. Blums. Surface cooling based on the thermomagnetic convection: numerical simulation and experiment. *International Journal of Heat and Mass Transfer*, 52:5302–5308, 2009.
- [75] H. Yamaguchi, X.-R. Zhang, X.-D. Niu, and K. Yoshikawa. Thermomagnetic natural convection of thermo-sensitive magnetic fluids in cubic cavity with heat generating object inside. *Journal of Magnetism and Magnetic Materials*, 322:698–704, 2010.
- [76] J. M. D. Coey. *Magnetism and Magnetic Materials*. Cambridge University Press, 2010.
- [77] K. Raj and R. Moskowitz. Ferrofluid-cooled electromagnetic device and improved cooling method, 1995. US Patent 5462685. Assignee: Ferrofluidics Corporation, Nashua, New Hampshire, USA.

- [78] M. I. Shliomis and B. L. Smorodin. Convective instability of magnetized ferrofluids. *Journal of Magnetism and Magnetic Materials*, 252:197–202, 2002.
- [79] V. Segal, A. Hjortsberg, A. Rabinovich, D. Nattrass, and K. Raj. AC (60 Hz) and IMPULSE BREAKDOWN STRENGTH OF A COLLOIDAL FLUID BASED ON TRANSFORMER OIL AND MAGNETITE NANOPARTICLES. In *Conference Record of the 1998 IEEE International Symposium on Electrical Insulation*, pages 619–622, 1998.
- [80] P. Kopcansky, L. Tomco, K. Marton, M. Koneracka, I. Potocova, and M. Timko. The experimental study of the DC dielectric breakdown strength in magnetic fluids. *Journal of Magnetism and Magnetic Materials*, 272-276:2377–2378, 2004.
- [81] P. Kopcansky, L. Tomco, K. Marton, M. Koneracka, M. Timko, and I. Potocova. The DC dielectric breakdown strength of magnetic fluids based on transformer oil. *Journal of Magnetism and Magnetic Materials*, 289:415–418, 2005.
- [82] P. P. C. Sartoratto, A. V. S. Neto, E. C. D. Lima, A. L. C. Rodrigues de Sá, and P. C. Morais. Preparation and electrical properties of oil-based magnetic fluids. *Journal of Applied Physics*, 97(10Q917):1–3, 2005.
- [83] J. Kudelcik, P. Bury, P. Kopcansky, and M. Timko. Dielectric breakdown in mineral oil ITO 100 based magnetic fluid. *Physics Procedia*, 9:78–81, 2010.
- [84] J.-C. Lee, W.-H. Lee, S.-H. Lee, and S. Lee. Positive and negative effects of dielectric breakdown in transformer oil based magnetic fluids. *Materials Research Bulletin*, 47:2984–2987, 2012.
- [85] J.-C. Lee and W.-Y. Kim. Experimental study on the dielectric breakdown voltage of the insulating oil mixed with magnetic nanoparticles. *Physics Procedia*, 32:327–334, 2012.
- [86] J. Ghasemi, S. Jafarmadar, and M. Nazari. Effect of magnetic nanoparticles on the lightning impulse breakdown voltage of transformer oil. *Journal of Magnetism and Magnetic Materials*, 389:148–152, 2015.
- [87] M. Nazari, M. H. Rasoulifard, and H. Hosseini. Dielectric breakdown strength of magnetic nanofluid based on insulation oil after impulse test. *Journal of Magnetism and Magnetic Materials*, 399:1–4, 2016.
- [88] J. G. Hwang, M. Zahn, F. M. O’Sullivan, L. A. A. Petterson, O. Hjortstam, and R. Liu. Effects of nanoparticle charging on streamer development in transformer oil-based nanofluids. *Journal of Applied Physics*, 107(014310):1–17, 2010.
- [89] V. Segal. Colloidal insulating and cooling fluid, 1999. US Patent 5863455. Assignee: ABB Power T&D Company, Raleigh, North Carolina, USA.
- [90] V. Segal, D. Nattrass, K. Raj, and D. Leonard. Accelerated thermal aging of petroleum-based ferrofluids. *Journal of Magnetism and Magnetic Materials*, 201:70–72, 1999.
- [91] V. Segal, A. Rabinovich, D. Nattrass, K. Raj, and A. Nunes. Experimental study of magnetic colloidal fluids behavior in power transformers. *Journal of Magnetism and Magnetic Materials*, 215-216:513–515, 2000.

- [92] S. Chaudhari, S. Patil, R. Zambare, and S. Chakraborty. Exploration on Use of Ferrofluid in Power Transformers. In *2012 IEEE 10th International Conference on the Properties and Applications of Dielectric Materials*, 2012.
- [93] R. Laguerre. *Approximation des équations de la MHD par une méthode hybride spectrale-éléments finis nodaux : application à l'effet dynamo*. PhD thesis, Université Paris VII, 2006.
- [94] A. Ribeiro. *Approche spectrale/éléments finis pour des problèmes de magnétohydrodynamique non-linéaires*. PhD thesis, Université Paris-Sud, 2010.
- [95] F. Luddens. *Theoretical and numerical analysis of the magnetohydrodynamics equations : application to dynamo action*. PhD thesis, Université Paris-Sud, 2012.
- [96] L. Cappanera. *Nonlinear stabilization of magnetohydrodynamics equations and application to multiphase flows*. PhD thesis, Université Paris-Sud, 2015.
- [97] D. Castanon Quiroz. *Solving the MHD Equations in the Presence of Non-Axisymmetric Conductors Using the Fourier-Finite Element Method*. PhD thesis, Texas A&M University, 2016.
- [98] C. Nore. *La MagnétoHydroDynamique-Description fluide*, 2014. Université Paris-Sud.
- [99] J.-L. Guermond, J. Léorat, F. Luddens, C. Nore, and A. Ribeiro. Effect of discontinuous magnetic permeability on magnetodynamic problems. *Journal of Computational Physics*, 230:6299–6319, 2011.
- [100] A. Ern and J.-L. Guermond. *Theory and Practice of Finite Elements*, volume 159 of *Applied Mathematical Sciences*. Springer Science+Business Media, New York, 2004.
- [101] J. L. Guermond and J. Shen. ON THE ERROR ESTIMATES FOR THE ROTATIONAL PRESSURE-CORRECTION PROJECTION METHODS. *Mathematics of Computation*, 73(248):1719–1737, 2003.
- [102] J.-L. Guermond, P. Mineev, and J. Shen. An overview of projection methods for incompressible flows. *Comput. Methods Appl. Mech. Engrg.*, 195, 2006.
- [103] J.-L. Guermond, R. Laguerre, J. Léorat, and C. Nore. An interior penalty Galerkin method for the MHD equations in heterogeneous domains. *Journal of Computational Physics*, 221:349–369, 2007.
- [104] J.-L. Guermond, R. Laguerre, J. Leorat, and C. Nore. Nonlinear magnetohydrodynamics in axisymmetric heterogeneous domains using a Fourier/finite element technique and an interior penalty method. *Journal of Computational Physics*, 228:2739–2757, 2009.
- [105] A. Nait Djoudi. Etude multiphysique d'un système de refroidissement d'un dispositif électromagnétique à base d'huile végétale et de ferrofluide. Master's thesis, Université Paris-Sud, 2017. Internship at GeePs laboratory (Gif-sur-Yvette, France).
- [106] W. T. Perrins, D. R. McKenzie, and R. C. McPhedran. Transport properties of regular arrays of cylinders. *Proceedings of the Royal Society of London. Series A, Mathematical and Physical Sciences*, 369(1737):207–225, 1979.
- [107] T. L. Bergman, A. S. Lavine, F. P. Incropera, and D. P. Dewitt. *Fundamentals of Heat and Mass Transfer*. John Wiley & Sons, Hoboken, NJ, 2011.

- [108] W. V. Titow. *PVC Technology*. Elsevier Applied Science Publishers, London, New York, fourth edition, 1984.
- [109] C. Garnier. *Modélisation numérique des écoulements ouverts de convection naturelle au sein d'un canal vertical asymétriquement chauffé*. PhD thesis, Université Pierre et Marie Curie, 2014.
- [110] S. Nasser El Dine. Etudes numérique et expérimentale du refroidissement par bain de ferrofluide d'un système électromagnétique simple : mise en place d'outils de caractérisation et de modélisation. Master's thesis, Ecole Centrale de Lille, 2018. Internship at GeePs laboratory (Gif-sur-Yvette, France).
- [111] L. Blaney. Magnetite (Fe_3O_4): Properties, Synthesis, and Applications. *Lehigh Review*, 15, 2007.
- [112] National Institute of Standards and Technology. NIST Chemistry WebBook, SRD 69, magnetite page. <http://webbook.nist.gov/cgi/cbook.cgi?ID=C1309382&Type=JANAFS&Plot=on>. Accessed in 2017.
- [113] I. M. Obaidat, B. Issa, B. A. Albiss, and Y. Haik. Temperature Dependence of Saturation Magnetization and Coercivity in $\text{Mn}_{0.5}\text{Zn}_{0.5}\text{Gd}_{0.02}\text{Fe}_{1.98}\text{O}_4$ Ferrite Nanoparticles. *IOP Conf. Series: Materials Science and Engineering*, 92(012012):1–7, 2015.
- [114] L. Vékàs, D. Bica, and O. Marinica. MAGNETIC NANOFUIDS STABILIZED WITH VARIOUS CHAIN LENGTH SURFACTANTS. *Romanian Reports in Physics*, 58(3):257–267, 2006.
- [115] N. El Wakil, N.-C. Chereches, and J. Padet. Numerical study of heat transfer and fluid flow in a power transformer. *International Journal of Thermal Sciences*, 45:615–626, 2006.
- [116] Y. B. Zhang, Y. L. Xin, T. Qian, X. Lin, W. H. Tang, and Q. H. Wu. 2-D Coupled Fluid-Thermal Analysis of Oil-Immersed Power Transformers Based on Finite Element Method. In *2016 IEEE Innovative Smart Grid Technologies - Asia (ISGT-Asia)*, pages 1060–1064, 2016.
- [117] R. A. Matula. Electrical Resistivity of Copper, Gold, Palladium, and Silver. *Journal of Physical and Chemical Reference Data*, 8(4):1147–1298, 1979.
- [118] AREELIS Technologies and LUSAC (Laboratoire Universitaire des Sciences Appliquées de Cherbourg). Dissipation thermique dans les composants/systèmes électroniques. Un enjeu pour la fiabilité des composants/systèmes électroniques. Quelles solutions technologiques ?, 2015. Internal report.
- [119] D. J. Tritton. *Physical Fluid Dynamics*. Van Nostrand Reinhold Company, 1977.
- [120] W. M. Rohsenow, J. P. Hartnett, and Y. I. Cho. *Handbook of Heat Transfer*. McGraw-Hill, New York, third edition, 1998.
- [121] Microelectronics Heat Transfer Laboratory. Fluid Properties Calculator. <http://www.mhtl.uwaterloo.ca/old/onlinetools/airprop/airprop.html>, 1997.

Titre : Convection thermomagnétique dans les ferrofluides : approximation par éléments finis et application au refroidissement des transformateurs

Mots clés : ferrofluide, modélisation numérique, convection thermomagnétique, méthode des éléments finis, couplage multiphysique, transformateur électrique

Résumé : Nous proposons d'exploiter la convection thermomagnétique, phénomène caractéristique des ferrofluides, pour améliorer les transferts de chaleur dans les transformateurs. Les équations régissant le système se composent des équations de Navier-Stokes dans l'approximation de Boussinesq, de l'équation de la conservation de l'énergie et des équations de la magnéto-statique. Les simulations sont menées avec notre code de recherche parallélisé SFEMaNS (Spectral/Finite Element for Maxwell and Navier-Stokes) pour des géométries axisymétriques, utilisant une décomposition spectrale dans la direction azimutale et des éléments finis de Lagrange dans le plan méridien. Afin de résoudre ce problème spécifique, divers développements sont apportés à SFEMaNS, tels que l'implémentation des forces magnétiques de Kelvin et de Helmholtz. Le code est d'abord appliqué au refroidissement d'un solénoïde dans une cuve cylindrique contenant de l'huile de transformateur ou un ferrofluide à base d'huile de transformateur. Les résultats

montrent que l'utilisation du ferrofluide diminue la température maximale du système grâce à la convection thermomagnétique et au changement des propriétés thermophysiques du fluide. L'influence de différents paramètres (fraction volumique de nanoparticules, présence d'un cœur ferromagnétique, propriétés magnétiques des nanoparticules) est étudiée. En particulier, les simulations confirment l'intérêt des nanoparticules magnétiques à faible température de Curie. Nous montrons également sur cet exemple que deux densités de force magnétique égales à un gradient près, telles que les forces de Kelvin et de Helmholtz, donnent le même écoulement. Un bon accord qualitatif est trouvé entre les résultats numériques et expérimentaux utilisant de l'huile de transformateur ou du ferrofluide. Le code est ensuite appliqué au refroidissement d'un système proche d'un transformateur de 40 kVA (20 kV/400 V). Les résultats montrent à nouveau une réduction de la température maximale grâce au ferrofluide.

Title : Thermomagnetic convection in ferrofluids: finite element approximation and application to transformer cooling

Keywords : ferrofluid, numerical modeling, thermomagnetic convection, finite element method, multiphysics coupling, electrical transformer

Abstract : We propose to make use of thermomagnetic convection, a characteristic phenomenon of ferrofluids, to improve heat transfer in transformers. The governing equations consist in the Navier-Stokes equations under the Boussinesq approximation, the energy conservation equation and the magnetostatics equations. The simulations are performed with the in-house parallel code SFEMaNS (Spectral/Finite Element for Maxwell and Navier-Stokes) for axisymmetric geometries, using a spectral decomposition in the azimuthal direction and Lagrange finite elements in the meridian plane. In order to solve this specific problem, various developments are brought to SFEMaNS, such as the implementation of the Kelvin and Helmholtz magnetic forces. The code is first applied to the cooling of a coil in a cylindrical tank containing either transformer oil or transformer oil-based ferrofluid. The results show that the use of the ferrofluid

reduces the maximum temperature in the system due to thermomagnetic convection and the change of the fluid thermophysical properties. The influence of different parameters (volume fraction of nanoparticles, presence of a ferromagnetic core, nanoparticle magnetic properties) is investigated. In particular, the simulations confirm the benefit of magnetic nanoparticles with a low Curie temperature. We also show on this example that two magnetic body forces equal up to a gradient, such as the Kelvin and Helmholtz forces, give the same flow. A good qualitative agreement is found between the numerical and experimental results using transformer oil or ferrofluid. The code is then applied to the cooling of an electromagnetic system close to a 40 kVA (20 kV/400 V) transformer. The results show again a reduction of the maximum temperature when using ferrofluid.

